

The Metallogenesis of the Skorpion Non-Sulphide Zinc Deposit, Namibia

Dissertation



zur Erlangung des akademischen Grades

doctor rerum naturalium (Dr. rer. nat.)

vorgelegt der

Mathematisch-Naturwissenschaftlich-Technischen Fakultät
(mathematisch-naturwissenschaftlicher Bereich)
der Martin-Luther-Universität Halle-Wittenberg

von Frau Katrin Kärner

geb. am 21.09.1973 in Halberstadt

Gutachter:

1. Prof. Dr. Gregor Borg
2. Prof. Dr. Murray Hitzman

Halle (Saale), 04. Juli 2006

urn:nbn:de:gbv:3-000011368

[<http://nbn-resolving.de/urn/resolver.pl?urn=nbn%3Ade%3Agbv%3A3-000011368>]

Acknowledgements

Above all, I would like to thank both the Geological Department of the Martin Luther University Halle-Wittenberg (MLU) and Anglo American (AAC) for providing the resources and funding for research throughout this PhD.

There are also lots of people I would like to thank for a huge variety of reasons.

Firstly, I would like to thank my supervisor Gregor Borg. His vast experience and knowledge of southern Africa opened many doors that may otherwise have remained closed. Without his continual support and encouragement over the last few years I would not have been able to accomplish this work, nor would I have experienced kite flying in the desert. Thanks a lot.

To all my colleagues at the institute that kept the working climate light, progressive and insightful, I thank you for your constant support and ceaseless encouragement.

Although I have thanked Anglo American in general, I would like to personally thank Roy Corrans for initiating this research project, Nick Franey, Ian Willis and Mike Buxton and the staff of the Anglo Exploration Division for their support and encouragement. The discussions and workshops in Johannesburg and at the Skorpion mine site were very inspiring and contributed greatly to my understanding of the Skorpion deposit and non-sulphide zinc deposits in general.

Early thanks go to Eckardt Freyer, Ken Hart and Karl Hartmann of Ambase Exploration Namibia, for introducing me to the Skorpion geology and for the enjoyable time I spent with them at the Exploration camp during the field campaigns.

From Anglo's Skorpion Zinc Mine, Dirk Harney, Senior Mine Geologist, and his family made life for me in Rosh Pinah enjoyable, with occasional "Doppelkopf" evenings which included Marcus Schafer, exploration geologist and card player extraordinaire. On the work front though, Dirk was invaluable. His genuine interest and continual motivation, even after his departure from Skorpion, helped ratify a belief in myself that carries on today. He also afforded me the opportunity to work in a practical manner on the mine, which led to a deeper understanding of the Skorpion ore body. At this point I also would like to thank Jaco Engelbrecht and Rob Botha, who provided many stimulating discussions about the genesis of the Skorpion deposit.

Thanks to Thomas Oberthür and his team from the Federal Institute for Geosciences and Natural Resources in Hanover, for their provision of resources and incredible generosity during my electron microprobe studies.

I would also like to thank Harald Strauss at the University of Munster and Albert Gilg at the Technical University of Munich for carrying out the stable isotope analyses.

Special thanks go to my dear friend Uwe, who more than anyone else in the world, held me together when I needed to be held together and prescribed 'obliteration' when that was the medicine required, at that time, to see this journey to its end.

Much appreciation goes to my family, who have been very tolerant over the years and never doubted me, even when my recurring claims of 'I'll be finished soon', ensued for more than the allotted time that the word 'soon' implies.

Finally, I thank a special Aussie just for being him.

Swakopmund, February 2006

Table of Contents

Table of Mineral Names and Formulas	1
Summary	2
1 Introduction	2
1.1 Non-sulphide Zinc Deposits Worldwide	2
1.2 Purpose and Scope of this Study	6
1.3 Outline of this Study	6
1.4. Methodology	7
1.4.1 Sampling	7
1.4.2 Analytics	7
1.4.3 GIS work	9
1.5 Previous Work	10
2 Regional Geological Setting	12
2.1 Introduction	12
2.2 Gariep Belt	13
2.2.1 Geological Framework	13
2.2.2 Tectonic Evolution	14
2.2.3 Stratigraphy and Lithology	15
3 The Skorpion Deposit	19
3.1 Exploration and Mining History	19
3.2 Geographical Overview	19

3.2.1 Present Geomorphology	19
3.2.2 Climate and Vegetation	20
3.3 Geological Framework	21
3.4 Lithology of Host Rocks	23
3.5 Petrography and Geochemistry of Host Rock and Wall Rock Lithotypes	26
3.5.1 Pre-Gariepian Basement	26
3.5.2 Gariepian Cover Rocks	27
3.5.2.1 Introduction	27
3.5.2.2 Marble	28
3.5.2.2.1 Petrography	28
3.5.2.2.2 Geochemistry	30
3.5.2.3 Felsic Metavolcanic Rocks	32
3.5.2.3.1 Petrography	32
3.5.2.3.2 Geochemistry	36
3.5.2.4 Amphibolites	44
3.5.2.4.1 Petrography	44
3.5.2.4.2 Geochemistry	45
3.5.2.5 Metasiliciclastic Rocks	49
3.5.2.5.1 Petrography	49
3.5.2.5.2 Geochemistry	54
3.6.3 Covering Sediments	63
3.7 Ore Minerals, Textures, and Styles of Mineralisation	65
3.7.1 Introduction	65
3.7.2 The Shape of the Supergene Ore Body	66
3.7.3 Primary Hypogene Ore Minerals	69
3.7.4 Secondary Supergene Ore Minerals	72
3.7.4.1 Supergene Sulphide Minerals	72
3.7.4.2 Supergene Non-Sulphide Minerals	75
3.7.4.2.1 Sauconite	75
3.7.4.2.2 Hemimorphite	76
3.7.4.2.3 Smithsonite	77

3.7.4.2.4 Hydrozincite	81
3.7.4.2.5 Zn-bearing Phosphates	81
3.7.4.2.6 Cu-bearing Minerals	82
3.7.4.2.7 Manganese Oxides	83
3.7.4.2.8 Iron Hydroxides	83
3.8 Rock Weathering and the Formation of the Supergene Ore	88
3.8.1 Weathering and Profile Development	88
3.8.2 Parent Rock and Profile Development	89
3.8.2.1 Dissolution of Sulphides from Host Rocks	89
3.8.2.2 Dissolution of Calcite	91
3.8.2.3 Dissolution of Feldspar	92
3.8.2.4 Dissolution of Mica	94
3.8.2.5 Dissolution of Apatite	94
3.8.2.6 Precipitation of Supergene Ore Minerals	95
3.8.2.6.1 Solubility of Metals	95
3.8.2.6.2 Supergene Metal Zonation Pattern	96
3.8.2.6.3 Supergene Mineral Zonation Pattern	101
3.9 Climate Regime and Development of the Weathering Profile	105
3.10 Geomorphology and Development of the Weathering Profile	106
3.10.1 Regional Geomorphological Evolution	106
3.10.2 Geomorphological Evolution and Development of the Weathering Profile at the Skorpion Deposit	112
4 Conclusions	119
References	123

List of Mineral Names

atacamite	$\text{Cu}_2\text{Cl}(\text{OH})_3$
barite	BaSO_4
brunckite	ZnS
chalcopyrite	CuFeS_2
chalcocite	Cu_2S
chalcophanite	$(\text{Zn, Fe, Mn})\text{Mn}_3\text{O}_7 \cdot 3\text{H}_2\text{O}$
chrysocolla	$\text{CuSiO}_3 \cdot n\text{H}_2\text{O}$
galena	PbS
goethite	FeOOH
gorceixite	$\text{BaAl}_3(\text{PO}_4)_2(\text{PO}_3\text{OH})(\text{OH})_6$
greenockite	CdS
hematite	Fe_2O_3
hemimorphite	$\text{Zn}_4\text{Si}_2\text{O}_7(\text{OH})_2 \cdot \text{H}_2\text{O}$
hydrozincite	$\text{Zn}_5(\text{OH})_6(\text{CO}_3)_2$
hydrohetearylite	$\text{Zn}_2\text{Mn}_4\text{O}_8 \cdot \text{H}_2\text{O}$
magnetite	Fe_3O_4
malachite	$\text{Cu}_2(\text{CO}_3)(\text{OH})_2$
manganomelane	synonym of wad (generic name for Mn oxides/hydroxides)
psilomelane	barium manganese oxide hydroxide (no fixed formula)
pyrite	FeS_2
pyrrhotite	Fe_{1-x}S ($x = 0$ to $x = 0.2$)
sauconite	$\text{ZnAl}[(\text{OH})_2 / \text{AlSi}_3\text{O}_{10}] (0.5 \text{ Ca, Na})_{0.3}(\text{H}_2\text{O})_4$
scholzite	$\text{CaZn}[\text{PO}_4]_2 \cdot 2\text{H}_2\text{O}$
skorpionite	$\text{Ca}_3\text{Zn}_2(\text{PO}_4)_2\text{CO}_3(\text{OH})_2 \cdot \text{H}_2\text{O}$
sphalerite	ZnS
smithsonite	ZnCO_3
tarbuttite	$\text{Zn}_2[\text{OH}/\text{PO}_4]$
zincolibithenite	$\text{CuZn}(\text{PO}_4)\text{OH}$

Summary

The supergene Skorpion non-sulphide zinc deposit is located approximately 40 km north of the Orange River in the southernmost Namib Desert, Namibia. It comprises a significant non-sulphide ore body (24.6 Mt @ 10.6 % Zn) and subordinate amounts of primary hypogene base metal sulphide mineralisation, which underlies the non-sulphide ores at depth. The mining commenced in October 2001 with the stripping of the overburden and exposure of the ore body.

The present metallogenic study is based mainly on drill core data from Anglo American's exploration drilling programme in 1999, since the study and the sampling for it was initiated prior to the opening of the mine. Investigations carried out on drill core samples include: i) light microscopy, XRD, and SEM-EDX in order to determine the mineralogy, ii) XRF, ICP-MS, electron microprobe technique and stable isotope analyses in order to determine the geochemistry of the ore body and its host rocks. Additionally, geochemical results from the exploration and infill drilling programme of the Skorpion Mine in 2004 were used in order to describe the supergene metal zonation pattern.

The Neoproterozoic host rocks of the Skorpion deposit are part of a volcano-sedimentary rock sequence within the Gariep Belt. The Neoproterozoic sequence has been affected by upper greenschist-/lowermost amphibolite metamorphism as well as complex deformation, which has resulted in folding and intensive thrusting during the Pan-African Orogeny at approximately 550 – 545 Ma. This event was followed by low-temperature retrograde metamorphism, uplift, fracturing, near-surface and surface weathering. The latter resulted in the formation of the supergene zinc deposit at Skorpion.

The hypogene Late Proterozoic hybrid VH(M)S/SH(M)S Zn-(Cu) protore of the Skorpion non-sulphide zinc ore body has formed in an initial continental rift system between the Kalahari cratonic province and the Rio de la Plata cratonic province. Bi-modal volcanism, anomalously high heat flow and hydrothermal activity have been significant controls for the hypogene ore formation. The Late Proterozoic rift sequence also contains siliciclastic and carbonate sediments, which were deposited in both shallow and deeper water environments.

The supergene non-sulphide ores have formed by oxidation of the base metal sulphide protore by wall rock replacement and in-situ oxidation. The non-sulphide ore minerals comprise predominantly saunonite (Zn-smectite), substantial amounts of hemimorphite and smithsonite, and subordinate amounts of hydrozincite, tarbuttite and chalcophanite. The supergene ore minerals form mainly euhedral and subhedral crystals and occur as open space fillings in inter- and intragranular voids, fractures and breccias.

The supergene non-sulphide ore body is hosted mainly by metasiliciclastic rocks, which are composed of meta-arkoses and –subarkoses, and subordinately by felsic metavolcanic rocks and their volcanoclastic equivalents. The ore body is irregularly shaped, transgressive to sedimentary layering and major tectonic features. It displays a relatively flattop, which is covered by a blanket of unmineralised overburden consisting of alluvial sediments, calcrete and Recent sand dunes.

The supergene ore body is laterally zoned displaying a pronounced supergene lateral metal zonation pattern, which has developed as a result of differences in metal solubilities. Iron and copper zones represent the leached part of the supergene ore body that corresponds to the location of the sulphide protore. The more mobile zinc has precipitated away from the iron and copper zones forming a markedly supergene zinc enrichment zone.

Even if the non-sulphide ore body and its lateral metal zonation are transgressive to a major Mesozoic fault system, the supergene deposit is partly controlled by it. The fault system

opened abundant dilatational joints and fractures, which increased the permeability of the host rocks. Thus, meteoric fluids were channeled and were able to percolate along the fault system and to oxidise the hypogene sulphide ores to several hundreds of meters depth. Palaeo-morphological features and palaeo-climatic conditions indicate that the supergene ore body must have formed during Early Tertiary. Subsequently, the uppermost part of the Skorpion ore body has been eroded and alluvial sediments have been deposited on top of the erosional palaeo-surface in Late Tertiary.

1 Introduction

1.1 Non-sulphide Zinc Deposits Worldwide

With the development of solvent-extraction (SX) and electro-winning (EW) processes, there has been a renewed economic interest for non-sulphide zinc deposits, also called 'zinc oxide deposits' throughout the world (e.g. Large 2001, Boni & Large 2003, Borg et al. 2003, Hitzman et al. 2003).

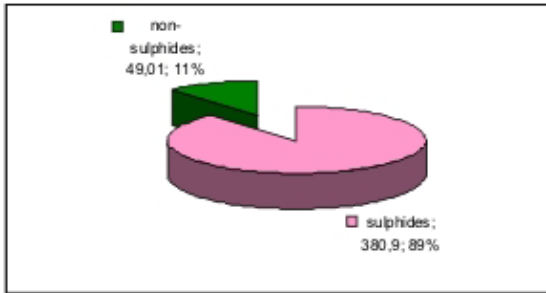


Fig. 1: The proportion of global zinc metal from non-sulphide and sulphide ores, Zn [Mt]. Data from BGR and several internet pages (2002).

The commercial exploitation of "zinc oxides" deposits has rapidly become an important source of metallic zinc. Within the foreseeable future the annual production of zinc from oxide ores could reach about 11 % of the global zinc metal production (Fig. 1). The attraction of these deposits includes the scale economy, as individual projects mostly exceed 1.000.000 tons zinc metal (Fig. 2), and the projected low processing costs for the production of zinc metal or high-grade zinc oxide on site (Large 2001).

The majority of the non-sulphide zinc deposits have formed mainly by the oxidation of zinc sulphide deposits in a near surface environment. Besides these supergene deposits there are a few hypogene non-sulphide zinc deposits known, which are characterised by a hydrothermal origin. Fig. 3 shows the location of the most important supergene and hypogene non-sulphide zinc deposits worldwide.

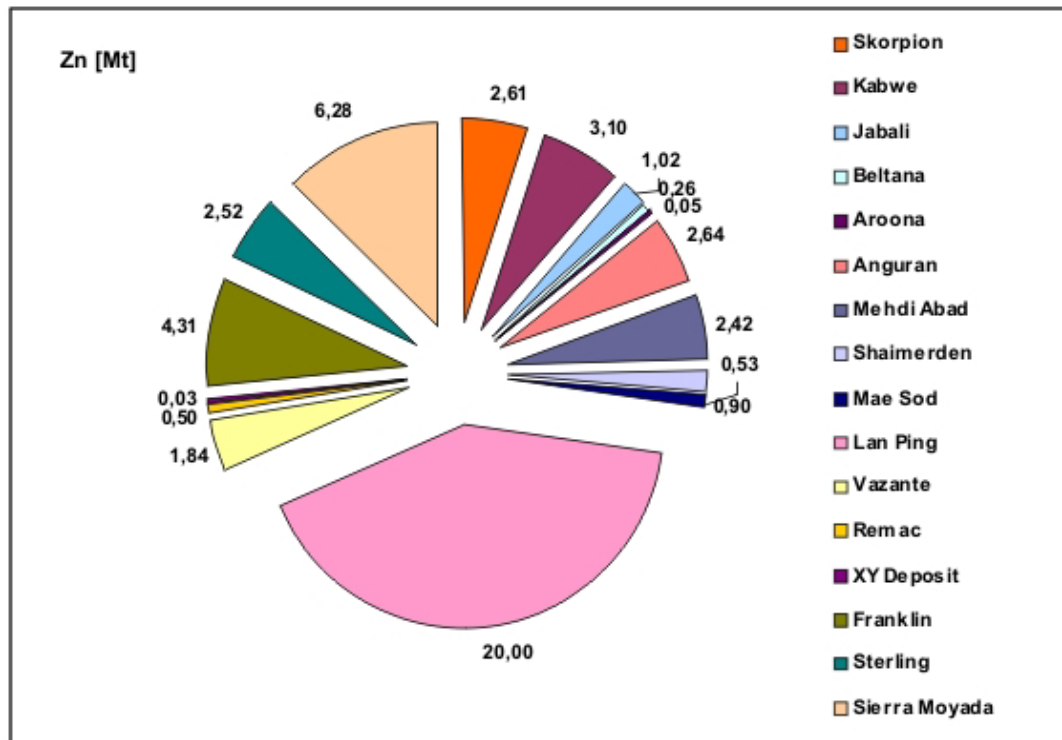


Fig. 2: Tonnes of zinc metal in non-sulphide zinc projects. Data from several internet pages, 2002.

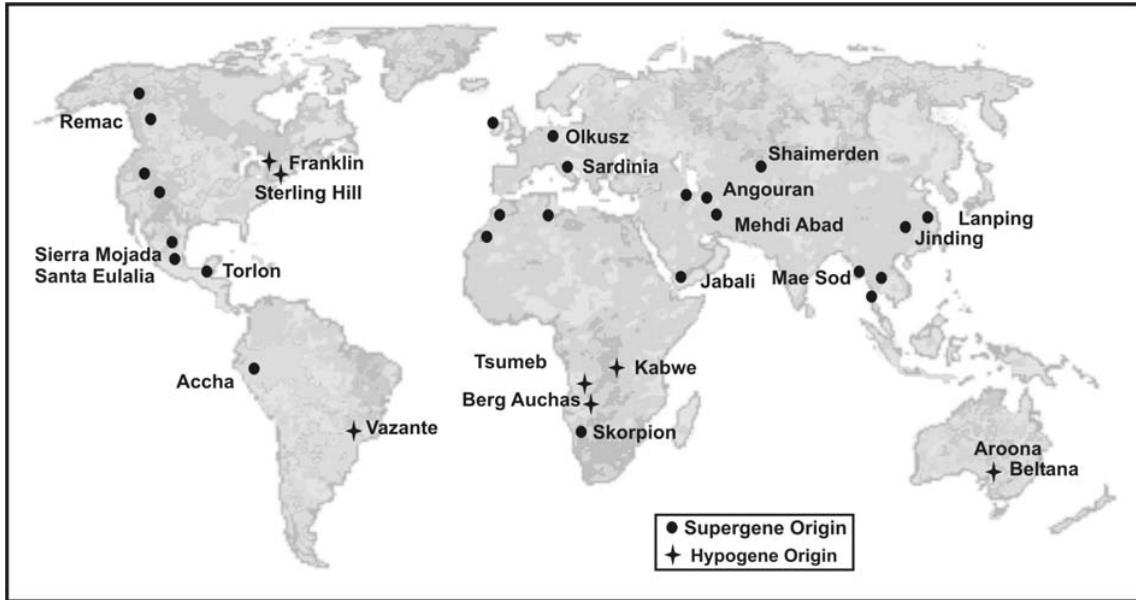


Fig. 3: Location of the most important non-sulphide zinc deposits worldwide.

Tonnages of non-sulphide zinc deposits range from less than 1 Mt to more than 200 Mt with grades of 7 % to more than 40 % Zn (Fig. 4). Deposits of this size include Skorpion (Namibia), Mae Sod (Thailand), Lan Ping (China), Angouran (Iran), Mehdi Abad (Iran), Shaimerden (Kazakhstan), Jabali (Yemen), Sierra Mojada (Mexico) and Franklin/Sterling Hill (USA). In addition, there are a number of other mines producing relatively small tonnages of non-sulphide zinc ores in Vietnam (Cho Dien), Turkey, China, Morocco and Egypt. For completeness, one should add to the total the high tonnages recovered in formerly exploited districts, like SW Sardinia, Belgium and Ireland, as well as in the areas where the non-sulphide zinc concentrations are not considered a resource, like in Upper Silesia (Poland) (Boni & Large 2003).

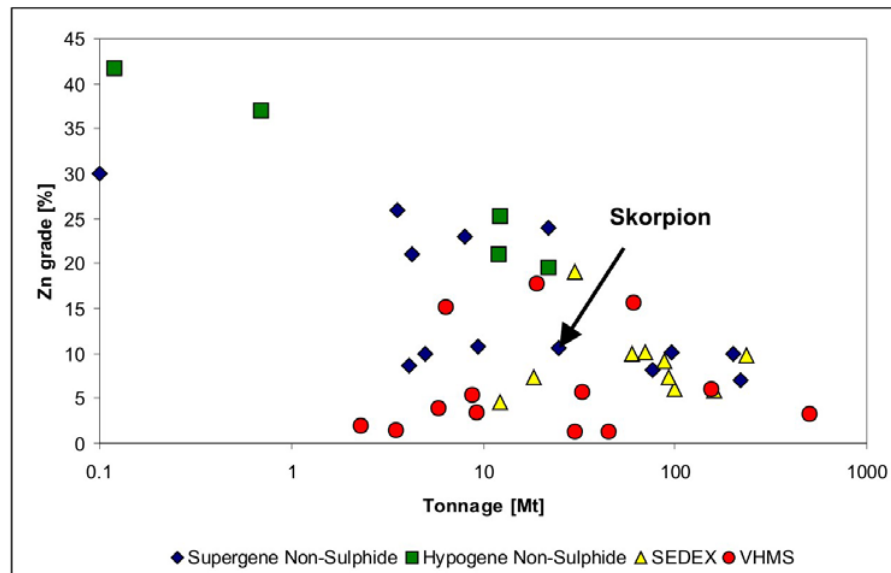


Fig. 4: Tonnages of both supergene and hypogene non-sulphide zinc deposits worldwide compared to sediment- and volcanic-hosted zinc sulphide deposits.

1.2 Purpose and Scope of this Study

The study commenced in July 2000. At that time the genesis of the non-sulphide Skorpion deposit was controversially discussed. Two opposing main genetic models existed envisaging as either supergene oxidised primary Zn-sulphides or hypogene primary Zn-non-sulphides. Corrans et al. (1993) assumed a supergene origin for the non-sulphide ores, however, without carrying out any further detailed investigations of the metallogenesis. Therefore, the present metallogenic study has been undertaken in order to investigate the origin of the non-sulphide ore body in detail.

The present study is focused mainly on ore petrology, geochemistry, and metallogenesis of the Skorpion deposit, based on data from drill core of Anglo American's exploration drilling programme in 1999, but also on some limited surface outcrop samples prior to a more extensive exposure of the ore body in the open pit. The study also uses geochemical information from Anglo American's long-term exploration programme of the area, which was provided by Anglo American in a Microsoft Access database. Additionally, geochemical results from the drilling campaign of the Skorpion Mine in 2004 have entered into the present study.

The investigations carried out on drill core samples as well as on surface outcrop samples include microscopic techniques, e.g. light-microscopy and SEM-EDX technique, as well as geochemical methods, e.g. XRF, ICP-MS, XRD and electron microprobe techniques.

Between July 2000 and September 2002 three field campaigns were undertaken in order to get familiarised with the regional geology, to sample drill core from the Skorpion deposit and to study the uppermost part of the Skorpion ore body after the mining had commenced in October 2001.

The early stages of investigation during this research project had revealed that the Skorpion ore body must have formed by supergene weathering of a primary sulphide deposit. Therefore, it is not the aim of this study to discuss the opposing main genetic models mentioned above. The overall aim of the present study is to formulate a metallogenic model for the supergene Skorpion non-sulphide ore body and particularly focus on the petrographical and geochemical characteristics of ores and their host rocks in order to elucidate the processes, which led to the formation of the supergene ore body. Additionally, the thesis seeks to provide a discussion about the timing and definition of the ore-forming events.

1.3 Outline of this Study

The thesis has been divided into four chapters. The first chapter introduces the study presenting the Skorpion deposit within a global framework and including previous work done on non-sulphide zinc deposits worldwide. Aim and purpose of the present study are formulated and the methodology is described.

The chapter two familiarizes the reader with the regional geological setting of southern Namibia and serves as an introduction to the geology of the Skorpion area.

The Skorpion deposit itself is presented in chapter three. This chapter forms the main part of the thesis. The ore body and its host rocks are described petrographically and geochemically and ore-forming processes are discussed. This chapter also reviews the geomorphological evolution of southern Namibia and applies regional published data to the Skorpion area.

The final chapter summarises the outcome of this research and presents ideas for future work.

Two appendices, which are filed on a CD, conclude the study. Appendix one includes borehole logs as well as maps showing the location of boreholes and surface samples.

Analytical results, such as XRF and ICP-MS data, but also electron microprobe- and SEM-EDX analyses are contained in appendix two. Appendix two also includes a sample list.

1.4. Methodology

1.4.1 Sampling

A first field campaign has been undertaken in July 2000 in order to sample drill core from diamond cored boreholes of the Skorpion deposit. After consulting the exploration geologists working on the Skorpion deposit at that time (K. Hart, K. Hartmann), drill cores of 10 representative boreholes from different parts of the Skorpion ore body have been selected, namely SD03, SD07, SD08, SD20, SD24, SD39, SD48, SD65, SD80, and BH70 (App. 1, map 1). The drill cores from the selected boreholes were already geologically logged. Thus, the geological information, which is included in the borehole logs (App. 1) correspond to the lithological interpretation of the Anglo American's exploration geologists at that time.

Some 300 samples were taken ensuring that the different lithological units and their mineralised horizons are covered (App. 1). Intervals containing the rather unobtrusive non-sulphide zinc mineralisation were identified using a zinc indicator solution, called 'Zinc Zap' (Tab. 1). The sample numbers refer to certain intervals, which are depicted in the lithological borehole logs. These logs also contain information about analytical methods that were applied to each sample.

Tab. 1: Zinc Zap reaction according to Skorpion Zinc Mine.

Zinc Zap reaction	Description
Non	Solution stays clear or turns green (no or almost no zinc present)
Weak	Solution turns light orange (about 4 – 9 % Zn)
Moderate	Solution turns orange-red (about 9 -13 % Zn)
Good	Solution turns red (about 13 – 20 % Zn)
Blood red	Solution turns dark red (about > 20 % Zn)

Another two field campaigns have been undertaken in February 2001 and September 2002 in order to collect reference samples from surface outcrops of the wider Skorpion area and samples from the uppermost part of the Skorpion ore body after the mining had commenced. A corresponding sample list is included in the appendix (App. 2).

Taken all samples into account including drill core samples and surface samples, the present study is based mainly on the investigation of 150 thin sections and some 180 XRF-, 70 ICP-MS (19 by courtesy of Anglo American Corporation)-, 100 XRD-analyses and several SEM-EDX-, electron microprobe-, and stable isotope analyses.

1.4.2 Analytics

Light Microscopy

Polished thin sections covering the various lithological units and different mineralisation styles were prepared for petrographic observations. Thin sections were investigated using light microscopy techniques under both reflected and transmittal light.

X-ray Fluorescence Spectrometry

Major and minor element concentrations in bulk rock samples were determined using conventional X-ray fluorescence spectrometry (XRF) at the Geological Department of the Martin-Luther-University Halle-Wittenberg.

Rock samples were crushed and then pulverised. The grinding equipment was cleaned between each sample by using SiO₂-sand as well as acetone in order to avoid contamination of sample material. However, at this point it also has to be stressed that those samples, which were ground with wolfram-bearing grinding equipment, display contaminations of wolfram and minor cobalt.

Samples were analysed as pressed powder resin pellets by Siemens-XRF SRS 3000, after determination of loss of ignition (LOI). Crystals used for refraction were LIF(200), PET and TIAP, measuring time was 20 seconds per line (approx. 90 minutes for a complete spectrum) at a minimum acceleration voltage of 20 kV and 10 mA current. Calibration was performed by using certified international standards. LOI was determined by roasting each sample at 1000°C for 2 hours.

ICP-MS

Trace, including rare earth, element concentrations have been analysed by Activation Laboratories Ltd. using ICP-MS techniques.

X-ray-Diffractometry

Powder XRD technique was applied on whole rock samples in order to investigate the mineralogy of host rocks and ore paragenesis. Samples were crushed and milled and bulk powder specimens were prepared. In some cases, minerals were hand-picked from the whole rock samples in order to investigate rare mineral phases in detail. The separated mineral specimen was ground and placed on a silicon plate. The specimens were analysed on a Philips X-ray diffractometer using Cu-K α radiation measuring from 3° to 90° (2 θ) at the Geological Department of the Martin-Luther-University Halle-Wittenberg.

SEM-EDX

Scanning electron microscopy technique coupled with an energy dispersive spectrometer has been carried out on selected samples using a GEOL JSM6300 at the Geological Department of the Martin-Luther-University Halle-Wittenberg. Minerals, which could not be identified under the light microscope due to their size, were analysed semi-quantitative using SEM-EDX technique. Thin sections and rock samples were coated with carbon before they were placed in the vacuum chamber of the scanning microscope. Additionally, high resolution backscattered images as well as secondary electron images have been taken in order to show ore textures.

Electron Microprobe Technique

The analyses of samples using the electron microprobe technique have been carried out at the Federal Institute for Geosciences and Natural Resources, Hanover.

Focus of the study was the determination of major and trace elements in both primary sulphides and secondary non-sulphides and sulphides. The measurements have been carried out by using a CAMECA SX 100. This microprobe is equipped with 5 wavelength dispersive (WDS) spectrometers and fully integrated energy dispersive spectrometer. The WDS spectrometers have been used to conduct quantitative analyses on individually selected points, but also on traverses and point grids. High resolution backscattered images have been taken in order to show ore textures.

Stable Isotope Analyses

Carbon and oxygen isotope studies have been carried out at the Technical University of Munich, Germany by A. Gilg in order to determine their concentrations in samples of smithsonite from the metasiliciclastic host rock and of calcite from the marble unit. The extraction of CO₂ from carbonates has been done at 72°C with water-free phosphoric acid in individual reaction tubes (GasBench II; ThermoFinnigan). The measurements of isotope ratios have been carried out by using a ThermoFinnigan Delta^{plus}-mass spectrometer with a 'continuous flow' system that uses helium as carrier gas. The correction of the oxygen isotope fractionation between CO₂ and smithsonite, released from the reaction with phosphoric acid, has been done according to Gilg et al. (2001). All C and O isotope compositions are reported in δ-notation in per mil (‰) relative to the PDB and V-SMOW standards, respectively, and show an absolute error of 0.1 ‰.

Sulphur isotope analyses have been undertaken by H. Strauss at the University Of Munster, Germany in order to determine their concentrations in sulphide samples from felsic metavolcanic rocks that occur in the footwall of the non-sulphide Skorpion deposit. The sulphides minerals were hand-picked from the crushed whole rock samples and analysed by coupling of mass spectrometer and elementary analyser. All S isotope compositions are reported in δ-notation in per mil (‰) relative to the V-CDT standards, and show an absolute error of 0.3 ‰.

1.4.3 GIS work

The GIS ArcView 3.2 has been used as a database for storing borehole and sample information as well as geochemical data. Regional geological data were provided by Anglo American. Maps containing sample and borehole locations (App. 1) are generated by ArcView 3.2 using Anglo American's geological information as background data.

Additionally, the Spatial Analyst extension for ArcView 3.2 was used in order to discover and understand spatial relationships in geochemical data. The Spatial Analyst was used to create cell-based raster data from geochemical vector data of the Skorpion ore body. The vector data from the Skorpion ore body include geochemical data produced in the course of the present study, but also geochemical results from several drilling campaigns by courtesy of Anglo American Corporation and Skorpion Mine. Grids interpolated from vector data include maps showing the palaeo-morphology of the Skorpion area, the present morphology of the Skorpion area, the thickness of young cover sediments (overburden), but also the lateral metal distribution patterns within the Skorpion ore body for base metals (Zn, Cu), Mn and Fe. Additionally, grids of single-metal distribution patterns were contoured and metal contours were laid on top of each other in order to elucidate the spatial relationships between them. Lithological and structural data from the Skorpion open pit (as of June 2004), compiled by Dirks (2004), have been used as background information for the metal distribution maps in order to understand the relationship between metal distribution, lithology and structure.

At this point, it should also be pointed out that regional maps have been created using UTM coordinates (map datum WGS84). However, maps showing the Skorpion open pit area are generally created using the local mine grid, which is offset 29° west of true north and 18.3° west of magnetic north, respectively. The different ways of data presentation are the result of the different databases, which entered into the present study.

1.5 Previous Work

Since non-sulphide zinc deposits have recently become technically and economically important again, the research on non-sulphide zinc deposits was reinforced and focused on several economic deposits throughout the world.

An attempt of a general compilation of data on non-sulphide deposits worldwide based on their mineralogy and geological characteristics, including some sketchy information on Skorpion, has been published by Large (2001). He subdivided non-sulphide zinc occurrences into:

- *Type I* characterised by MVT or CRD/manto Zn mineralisation with smithsonite, hemimorphite, and hydrozincite, e.g. Mehdi Abad, Mae Sod, Lanping
- *Type II* associated with major structures in Late Proterozoic – Early Cambrian sedimentary successions with willemite, hemimorphite, and smithsonite, e.g. Vazante, Beltana, Kabwe, (Franklin and Sterling Hill)
- *Type III* oxidised sulphide ores, preserved by an overlying cover with sauconite, hemimorphite and smithsonite, e.g. Skorpion, Shaimerden.

A more genetic classification has been published by Hitzman (2001) and Hitzman et al. (2003) based on Heyl & Bozion (1960). The classification includes:

- *Supergene* zinc oxide deposits, e.g. Mehdi Abad, Mae Sod, Lanping, Skorpion, Shaimerden
- *Hypogene* zinc oxide deposits, e.g. Vazante, Beltana, Kabwe
- *Metamorphic* zinc oxide deposits, e.g. Franklin, Sterling Hill

As mentioned above, the pioneering work regarding non-sulphide zinc deposits was carried out by Heyl & Bozion (1960). They published first a classification of non-sulphide zinc deposits including hypogene, supergene, and metamorphic non-sulphide zinc deposits. Furthermore, they subdivided the group of the supergene deposits into three main types according to their formation processes as follows:

- direct replacement deposits,
- wall rock replacement deposits, and
- saprolitic accumulations.

Direct replacement types are formed by in-situ oxidation of primary zinc ores essentially in place, without major migration of the zinc in solution. The host rocks of the precursor sulphide ore body are also host to the supergene non-sulphide ore body. Direct replacement deposits are more complex and richer in precious metals than deposits formed by the replacement of wall rock.

Wall rock replacement deposits are the result of leaching of primary ores, migration of zinc in solution, and redeposition of zinc by replacement of nearby carbonate or siliciclastic wall rocks.

Saprolitic accumulations are typically a mixture of (i) thoroughly decomposed earthy but untransported rock and oxidised zinc minerals, (ii) residual masses of clay, smithsonite, and hemimorphite that have slumped vertically and collected in solution pockets of decomposed limestone between buried pinnacles of unweathered limestone, and (iii) zinc carbonates and silicates that were deposited near the limestone walls in the bottoms of the solution pockets

by reaction of descending zinc-bearing solutions that formed from the weathering of the mineralised pinnacles and leaching of the saprolites above.

The classification of supergene non-sulphide zinc deposits is very helpful in order to explain genetic processes. However, it has to be taken into account that a supergene deposit can form by more than one of the processes described above, and thus hybrid systems are likely to occur.

During the last few years, research on non-sulphide zinc deposits including hypogene, metamorphic and supergene deposits, was mainly focussed on the major economic occurrences worldwide, e.g. Shaimerden, Kazakhstan (Schaffalitzky & Boland 2001, Boland et al. 2003, Kärner 2003a), Beltana, Australia (Muller 1972, Groves et al. 2003, Hitzman et al. 2003), Angouran, Iran (Hirayama 1986, Daliran & Borg 2003, Gilg et al. 2003), Vazante, Brazil (Monteiro et al. 1999, Hitzman et al. 2003), but also on older mining districts containing smaller, historically exploited deposits, e.g. Kabwe, Zambia (Kortmann 1972, Kamona & Friedrich 1994), Franklin/Sterling Hill, New Jersey (FrondeL, C. & Bam 1974, Johnson & Skinner 2003) and Sardinia (Boni et al. 2003, Boni & Large 2003).

Geological information from the Skorpion deposit *sensu stricto* has been scarce (e.g. Corrans et al. 1993, Borg et al. 2003) due to restricted access to Namibia's Diamond Area No. 1, the 'Sperrgebiet', where the deposit is situated and because of a competitive local exploration environment. However, the general geology of the region and the regional geochemistry of the supracrustal magmatic rocks have been described in detail by authors such as Söhne and Villiers (1947), McMillan (1968), Davies and Coward (1982), von Veh (1993), Alchin (1993), Frimmel et al. (1996a, b), and Frimmel (2000a, b). Additionally, a regional-scale data compilation and interpretation of the distribution patterns of base metal occurrences and their relationship to early crustal structures within the branches of the Pan-African fold belts of Namibia, including limited information from the Gariep belt, has been compiled by Borg (2000).

2 Regional Geological Setting

2.1 Introduction

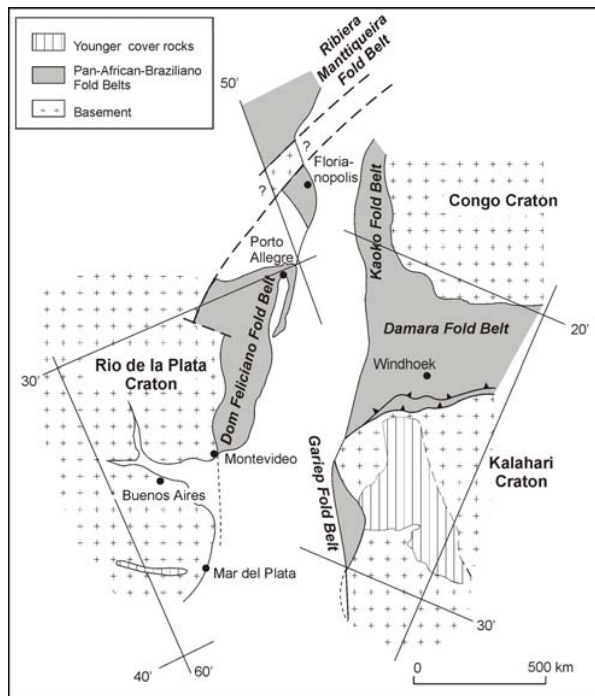


Fig. 5: Regional location of the Neoproterozoic Gariiep Belt in south-western Africa, illustrated within the framework of the Pan-African-Brasiliano fold belts (modified after Porada 1989, Tankard et al. 1982, Trompette 1994).

A network of Late Proterozoic to Early Palaeozoic orogenic belts is the prominent regional tectonic fabric of western Gondwana (Frimmel et al. 1996).

In south-western Africa, the Damara Belt separates the Congo and Angola Cratons from the Kalahari Craton, whereas the Gariiep Belt forms the southern coastal branch of the orogen and extends also northward into the Kaoko Belt (Fig. 5).

The Gariiep and Kaoko Belts originated as a Late Proterozoic suture between the South American Craton and the cratons of southern Africa. The rifting between the Kalahari and Rio de la Plata plates was initiated around 781 Ma ago and lasted some 40 Ma. It was accompanied by the formation of the Adamastor Ocean and oceanic crust (e.g. Frimmel et al. 1996, Frimmel & Frank 1996). The inversion from extension to compression led to a successive closure of first the northern Adamastor ocean (Kaoko Belt), followed by the Khomas sea (intracontinental Damara Belt), and finally the southern Adamastor ocean (Gariiep Belt) (Fig. 6).

Continental collision and thrusting of the internal onto external zones of the tectonic Gariiep Belt culminated between 547 – 543 Ma (Frimmel & Frank 1998).

The Late Proterozoic Pan-African orogeny was followed by a long period of tectonic stability. The break-up of Gondwana and thus, rifting in the South Atlantic was initiated in the Permian-Triassic and continued until the end of the Early Cretaceous. Rifting overlapped with the Cape Orogeny and the development of the Karoo foreland (Gilchrist et al. 1994). Igneous activity was widespread and spanned the period of rifting and into the Tertiary. A series of intrusive complexes in north-western Namibia is related to the Etendeka lavas, which were extruded during rifting. Suites of kimberlite pipes and alkaline plugs also intruded from the Late Cretaceous to the Early Tertiary. Terrestrial sedimentation was extensive in the continental interior and along the coast, represented by the Kalahari and Namib sediments respectively (Gilchrist et al. 1994).

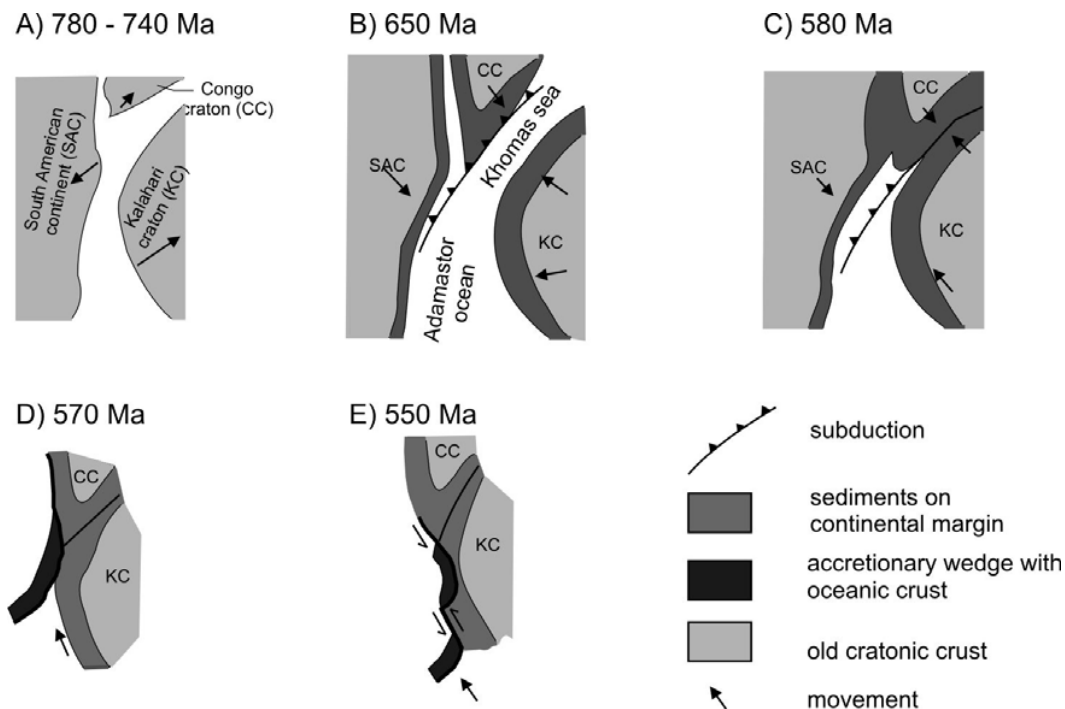


Fig. 6: Schematic diagram showing successive stages of the tectonic evolution that led to the development of the Gariep Belt: (A) rifting, followed by the opening of the Adamastor ocean and the Khomas sea; (B) closure of the Khomas sea and north-westward subduction; (C) continent-continent collision in the Damara Belt and formation of an accretionary wedge further southwest (Chameis Complex); (D) obduction of accretionary wedge; and (E) oblique collision in the Gariep Belt (Frimmel & Frank 1998).

2.2 Gariep Belt

2.2.1 Geological Framework

The Late Proterozoic Gariep Belt is regarded as the southern extension of the Damara orogenic front of central and northern Namibia (Davies & Coward 1982, Reid et al. 1991, Stanistreet et al. 1991, Gresse 1994, Frimmel 2000b, Jasper et al. 2000).

It is subdivided into an eastern para-autochthonous zone, the so-called Port Nolloth Zone (PNZ), which evolved from an intracontinental rift to a passive continental margin on the western edge of the Kalahari Craton (Jasper et al. 2000), and a western allochthonous zone, the Marmora Terrane (Fig. 7).

The Skorpion deposit is situated within the Port Nolloth Zone, which comprises a variety of siliciclastic and chemical sediments and bi-modal volcanic rocks, which have been strongly folded, faulted and overprinted by lower amphibolite facies metamorphism (e.g. Frimmel et al. 1995).

The rocks of the Port Nolloth zone contain stratiform Zn-Pb-Cu-Ag-(± Ba)-sulphide mineralisation in syn-rift sediments and felsic metavolcanic rocks, e.g. Rosh Pinah Pb-Zn mine, and Skorpion Zn mine (e.g. van Vuuren 1986, Alchin & Moore 2005). These base metal mineralisations were formed in an extensional environment during a phase of increased volcanogenic-hydrothermal activity between 740 and 754 Ma. The age of volcanogenic-hydrothermal activity is supported by isotopic SHRIMP age of zircons from a Skorpion meta-rhyolitic flow that gave 751.9 ± 5.5 Ma (Borg & Armstrong 2002).

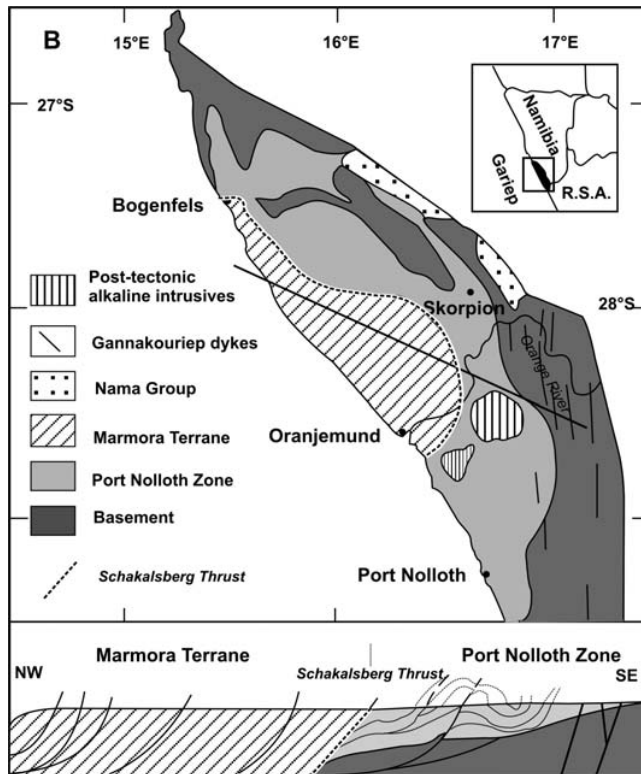


Fig. 7: Distribution of tectono-stratigraphic units of the Gariep Belt with a NW-SE cross-section. After Frimmel & Frank (1998).

cover rocks. The dyke swarm has been dated at 717 ± 11 Ma (Reid et al. 1991), marking the final stretching of the continental crust prior to the opening of the Adamastor Ocean in the West (Jasper et al. 2000).

Several post-orogenic intrusive bodies of alkali granite and syenite cross-cut the main tectonic fabrics and lithological contacts in the central part of the Gariep Belt. They occur along the so-called Kuboos-Bremen line, which strikes SW-NE, south of the Orange River. The Kuboos pluton is clearly younger (507 ± 6 Ma) than the main phase of deformation in the Gariep Belt (545 ± 2 Ma). While the earlier 545 Ma tectonothermal event is explained by the closure of the Adamastor Ocean between the Kalahari and the Rio de la Plata cratons, the younger 500 Ma tectonic pulse is linked to subduction beneath the western margin of Gondwana (Frimmel 2000b).

2.2.2 Tectonic Evolution

The tectonic evolution of the Gariep Belt is subdivided into an earlier sinistral transpressive phase (Davies & Coward 1982, Gresse 1994) with south-southeastwards directed thrusting and a later easterly to northeasterly verging deformation that affected the western part of the Gariep Belt (Gresse 1994). The earlier Gariepian deformation phase (G_1) is dated at between 542 ± 4 Ma and 546 ± 10 Ma by Onstott et al. (1986) and Reid et al. (1991); using a metamorphic overprint age on earlier Gannakouriep dykes that predates the deposition of the Gariep Sequence. The later (G_2) event is correlated to the late Pan African/Brasiliano event (at approx. 500 Ma) that affected the Nama foreland deposits up to 50 km farther towards the east at the Neint Nababeep Plateau (Gresse 1994).

The extensional phase ended with the deposition of the glaciogenic Numees Formation between 590 and 564 Ma, which correlates with the Varangerian glacial episode (Jasper et al. 2000).

After the deposition of the Gariep group ceased, the closure of the Adamastor Ocean resulted in continental collision, and thus in deformation and metamorphism. The compressional history ceased at about 500 Ma, followed by the deposition of predominantly siliciclastic Nama Group sediments into peripheral foreland basins (Stanisstreet et al. 1991, Germs & Gresse 1991, Jasper et al. 2000).

A number of pre-, syn-, and post-tectonic intrusions occur throughout the Gariep Belt. The 100 km wide N- to NE-trending, mafic /ultramafic Gannakouriep dyke and sill swarm intruded both Palaeo-Proterozoic basement rocks, which are part of the 1.0 Ga old Namaqua-Natal Metamorphic Belt, and late Proterozoic Gariep

The structural style of the G_1 event is dominated by thrust structures that strike north-northeast to south-southwest in the central and northern part of the belt and northeast-southwest in the southern part of the belt. The most prominent structure is the Schakalsberg thrust that represents a major terrane boundary (Fig. 7), juxtaposing the oceanic allochthonous Marmora Terrane (towards the west) with the continental para-autochthonous Port Nolloth Zone towards the east (Davies & Coward 1982, Hartnady & von Veh 1990, Frimmel 2000b, Jasper et al. 2000).

The initial stages of the southeastwards directed thrusting imparted shallow north-north-westerly dipping planar fabrics in high-strain zones. Upper greenschist facies metamorphic assemblages define the fabrics. The transport direction of the thrusting is defined by the axial orientation of sheath folds and the strained long axes of pre-tectonic shape fabrics. The early formed thrust structures and associated planar fabrics became subsequently deformed during the later stages of the same deformation event. This event produced fold structures that are defined by the foliation/bedding and thrusts that affected both the Gariep Sequence and underlying basement rocks. The folds verge towards the east and southeast, and in the Rosh Pinah area, towards the west. The variable vergence of the folds is explained in terms of a progressive shear model where the initial folds form with axial orientations at large angles to the transport direction and that are then rotated by subsequent shear in either a clockwise or anti-clockwise sense, thus producing folds with an easterly vergence as well as folds with a westerly vergence. Thus, it is important to note that apparent westerly- or easterly-directed thrusting in west-east cross sections commonly has a major south-southeasterly directed thrust component attached to it.

Effects of the later G_2 event are restricted to the presence of slickensides from an area south of Port Nolloth (Gresse 1994), the presence of northeast-verging folds from the northern part of the belt (Davies & Coward 1982), the folding of the Nama sediments farther towards the west and perhaps a general tightening of earlier folds. No large-scale thrusting was observed.

2.2.3 Stratigraphy and Lithology

Regional stratigraphic correlations of the Late Proterozoic rock sequence within the Gariep Belt have been subject of considerable debate and several stratigraphic schemes have been proposed by different authors, e.g. SACS (1980), von Veh (1993), Frimmel (2000), and Alchin et al. (2005) (Fig. 8). This unsatisfactory situation is a result of poor, isolated outcrops, the complexly deformed rock sequence, rapid lateral facies changes of both meta-sedimentary and metavolcanic rock types.

Due to the on-going controversial discussion about the stratigraphical positions of the different lithotypes, this metallogenic study uses lithological terms rather than stratigraphical terms. The stratigraphical terms are also avoided, since this study is based mainly on drill core data that did not allow a reliable stratigraphic classification. However, the different stratigraphic units are summarised below in order to give a general overview of the occurrence of the different Late Proterozoic lithotypes and their possible stratigraphic positions.

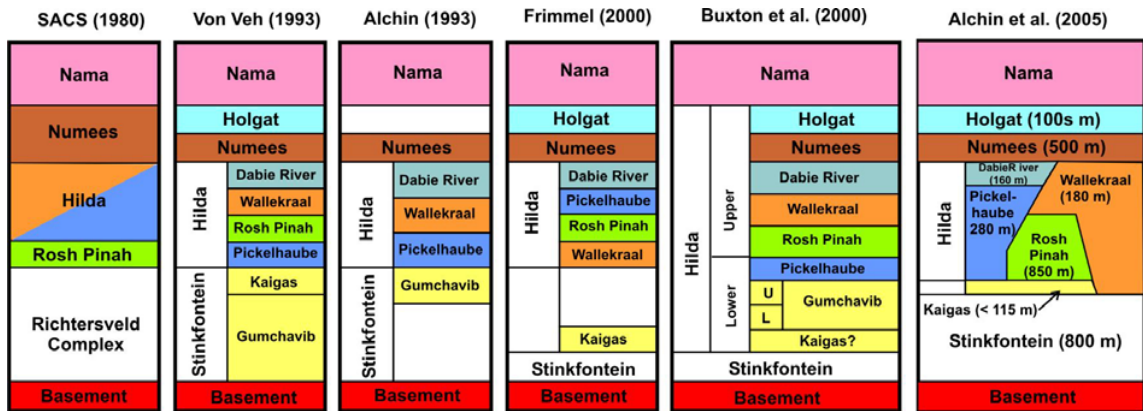


Fig. 8: Schematic stratigraphic schemes for the Late Proterozoic Gariep sequence.

The basement, on which the rocks of the Port Nolloth Zone rest, is part of the some 1.0 Ga old Namaqua-Natal Metamorphic Belt and includes 1730 - 1900 Ma Vioolsdrift Suite granites and 2000 Ma volcanics of the Haib Subgroup (von Veh 1993, Alchin 1993).

The Late Proterozoic Gariep cover rocks, which lie in most places tectonically on the Palaeoproterozoic basement rocks, approximately correspond to sequences assigned regionally to Stinkfontein and Hilda Subgroups, including Gumchavib, Pickelhaube, and Rosh Pinah Formations (Fig. 8). However, no reliable correlation is presently possible because these formations are characterised by rapid lateral facies changes and multiple deformation. Genetically, the Gariep sequence is related to progressive opening of a failed intracratonic rift graben in the east (Rosh Pinah/Skorpion Graben) that was separated by a basement horst from a half graben to the west (Fig. 9), which developed into the Adamastor ocean (Alchin et al. 2005).

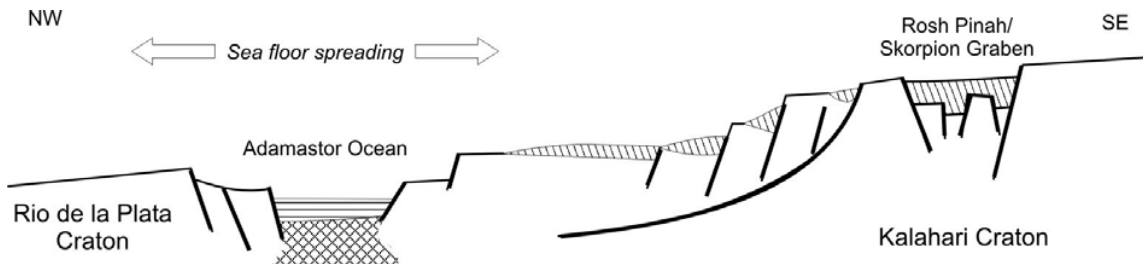


Fig. 9: Position of the Rosh Pinah Graben in thinning and breaking Mesoproterozoic continental crust around 700 Ma, after Alchin et al. (2005).

The Stinkfontein Subgroup is exposed mainly in South Africa along the southern and south-eastern front of the Gariep Belt (Frimmel 2000b). Northward thinning of the subgroup is believed to be due to stratigraphic onlap. The Stinkfontein Subgroup contains siliciclastic sediments in its lower part, containing mainly quartzarenites, feldspatic arenites and conglomerates of the so-called Lekkersing Formation. The Lekkersing Formation is conformably overlain by the Vredefontein Formation, which includes feldspatic arenites and minor metamorphosed felsic volcanic rocks (Frimmel 2000b, Alchin et al. 2005).

The Hilda Subgroup, containing a mixed sequence of shallow marine siliciclastic and carbonate sedimentary rocks with intercalated volcanic rocks, rests either unconformably on

Palaeo-Proterozoic basement rocks or para-conformable, on the Stinkfontein Subgroup or Kaigas Formation, though recently published stratigraphic schemes by Alchin et al. (2005) consider at least the Kaigas Formation to be the lowermost part of the Hilda Subgroup.

The Lower Hilda Subgroup consists mainly of fine- to medium-grained meta-arkoses, -subarkoses, - and sandstones (von Veh 1993, Alchin 1993) of the so-called Gumchavib Formation (Fig. 10). Some distal fine-grained deposits of this formation are apparently exposed some 15 km SSE of the Skorpion deposit (Buxton et al. 2000). Debris flow deposits of the Kaigas Formation might represent a basin marginal deposit, and thus a proximal Gumchavib facies (Buxton et al. 2000). However, the existence of the Gumchavib Formation is still controversially discussed as chemostratigraphic data (Fölling et al. 1998) indicate that the Gumchavib Formation might be a facies equivalent of the Pickelhaube Formation in the Hilda Subgroup (Frimmel 2000b).

Extensive carbonate rocks appeared the first time at the base of the Upper Hilda Subgroup (von Veh 1993, Alchin 1993, and Buxton et al. 2000), though according to Frimmel (2000b), these carbonates form the uppermost part of the Upper Hilda Subgroup. The stratigraphic scheme published by Frimmel (2000b) is based on an age dating of marbles from the lower Pickelhaube Formation (Fig. 10), which yielded $^{207}\text{Pb}/^{206}\text{Pb}$ isochron ages of 728 ± 32 and 545 ± 13 Ma for the carbonate and residue fractions, respectively. The former is interpreted as dating early diagenesis, whereas the latter refers to the metamorphic event. Thus, ages obtained from the marble by Frimmel (2000b) indicate that it is younger than the felsic volcanic metavolcanic rocks from the Rosh Pinah Formation (see below). However, the absolute isochron ages of the marbles from the Pickelhaube Formation have been re-interpreted recently by Frimmel & Lane (2005) as representing a more distal facies that was deposited contemporaneously with the Rosh Pinah Formation. In fact, the bulk of the Rosh Pinah Formation is correlated with the lower Pickelhaube Formation in those areas that were not affected by rift volcanism (Alchin et al. 2005).

Regionally, the carbonates of the Pickelhaube Formation consist of extensive calcitic marble, which rest either directly upon basement or gradationally upon the siliciclastic rocks of the Gumchavib Formation (Alchin 1993, Buxton et al. 2000). It is agreed that the marble of the Pickelhaube Formation represents an extensive shallow water carbonate sequence probably developed during shallow water sub-tropical conditions. The marble that forms an antiform on the eastern side of the Skorpion deposit, most likely belongs to the Pickelhaube Formation.

Bi-modal metavolcanic rocks and siliciclastic metasediments of the Rosh Pinah Formation (Fig. 10) rest on top of the carbonates of the Pickelhaube Formation according to von Veh (1993) and Buxton et al. (2000). Conversely, the comparison of isotopic ages of metarhyolite of the Rosh Pinah Formation (Borg & Armstrong 2002) and marble of the Pickelhaube Formation (Frimmel 2000) indicates that the Rosh Pinah Formation is older and thus might underlie the Pickelhaube Formation. However, the latest stratigraphic research shows that the Rosh Pinah Formation has been laid down around the same time as the Pickelhaube Formation (Alchin et al. 2005), which also finds support in a Pb-Pb carbonate age of 728 ± 32 Ma obtained on the latter (Frimmel & Lane (2005).

The lower part of Rosh Pinah Formation consists mainly of metarhyolite, rhyolitic agglomerates and ignimbrites. The upper part of the Rosh Pinah Formation consists predominantly of meta-tuffites, impure, marly metacalcarenite and largely dolomitic marble beds. Additionally,

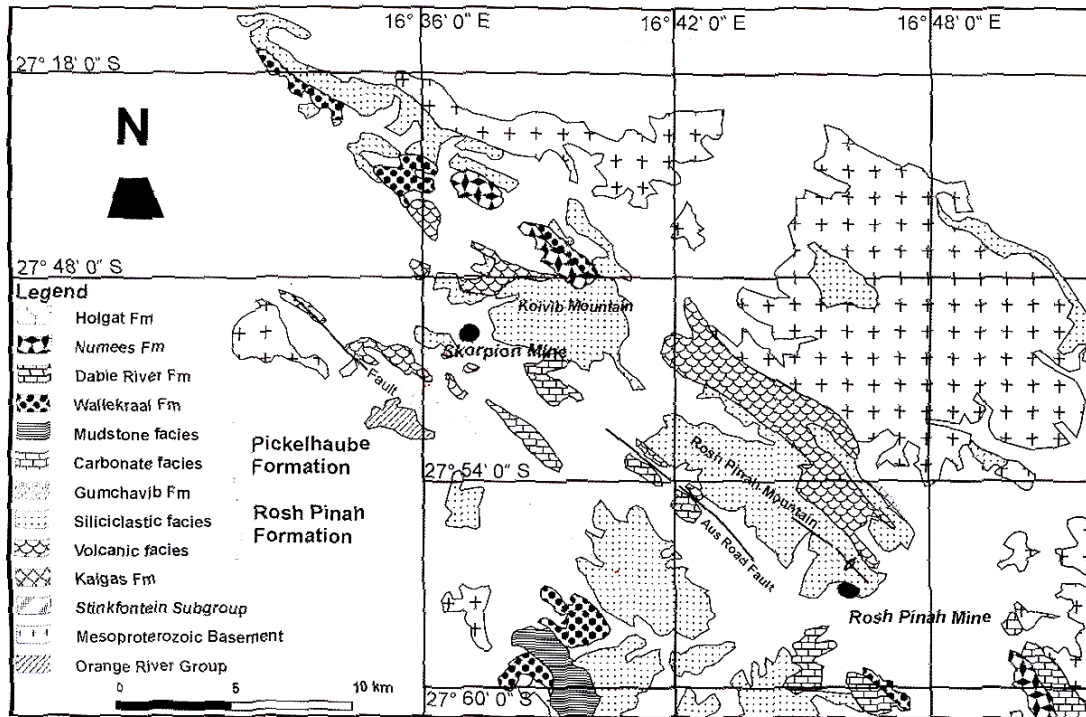


Fig. 10: Simplified geological map indicating the stratigraphy of the Rosh Pinah/Skorpion area. From Alchin & Moore (2005).

two black shale horizons occur in the middle and upperparts of the sequence, respectively, with the lower one being rich in sulphides. In its lower part, the Rosh Pinah Formation hosts the stratiform Pb-Zn-Cu sulphide bodies of the Rosh Pinah mine (Alchin et al. 2005). The sulphide precursor of the non-sulphide Skorpion deposit and remnants thereof are most likely also hosted by rocks of the Rosh Pinah Formation as they consist mainly of felsic metavolcanic rocks, e.g. metarhyolites and meta-tuffites, which make up a significant part of the Rosh Pinah Formation.

The Rosh Pinah Formation is overlain by the so-called Wallekraal Formation (von Veh 1993, Buxton et al. 2000), though it is also regarded as a lateral and time equivalent of the Rosh Pinah Formation (Alchin 1993, Alchin et al. 2005). The siliciclastic-dominated Wallekraal Formation consists generally of well sorted quartz-pebble conglomerate and feldspathic meta-arenite grading into metapelites in upward-fining sequences and is exposed some 25 km SSE of the Skorpion deposit (Buxton et al. 2000). The siliciclastic metasediments, which host a significant portion of the Skorpion non-sulphide ore body, might be equivalents of either Wallekraal Formation or the metasedimentary part of the Rosh Pinah Formation described above.

There is a general agreement that massive dolomitic limestone and/or dolomite, assigned to the Dable River Formation, forms the uppermost part of the Hilda Subgroup. The rocks of the Dable River Formation are only exposed close to the Orange River and are distinguished from the other carbonates in the subgroup by the presence of stromatolites, pisolites and oolites (Frimmel 2000b, Alchin et al. 2005).

The Hilda Subgroup is overlain by a diamictite with banded iron formation. The so-called Numees Formation is largely exposed about 30 km SE and SSE of the Skorpion deposit (Buxton et al. 2000). Metacalciturbites and metasiliciclastic rocks of the Holgat Formation, which are exposed about 15 km SW of the Skorpion deposit (Buxton et al. 2000), rest on top of the Numees Formation.

3 The Skorpion Deposit

3.1 Exploration and Mining History

The Skorpion zinc deposit, owned by Anglo American, is located approximately 40 km north of the Orange River and some 15 km north-northwest of Rosh Pinah Mine in the southernmost Namib Desert, Namibia (Fig. 10). It is hosted by a volcano-sedimentary succession of Neoproterozoic age, the so-called Hilda Sequence (Von Veh 1993, Alchin 1993, Frimmel 2000b, Buxton et al. 2000).

The Skorpion deposit is situated rather remotely in the restricted 'Sperrgebiet No. 1' (Diamond restricted area) of southern Namibia. This protected status of the area persisted until 1975, when Anglo American Prospecting Services (AAPS) and Consolidated Diamond Mines (CDM) entered into an agreement to explore the 'Sperrgebiet' for base metals. The Skorpion prospect was discovered during an exploration programme by Erongo Exploration and Mining Co. Ltd. in 1976-77, which included geochemical drainage and gossan sampling. A small outcrop of a crudely banded barite/iron-hydroxide gossan west of Skorpion, the so-called 'discovery outcrop' yielded anomalous metal values of 0.1 – 0.3 % Cu, 0.1 – 2.9 % Pb, 0.1 – 4.1 % Zn, 0.3 – 13.0 % Mn, and 2 – 50 ppm Ag (Corrans et al. 1993). Drainage samples in the area gave elevated values of Pb (250 ppm) and Zn (115 ppm) against background values for Pb, Cu and Zn of 20 - 40 ppm (Corrans et al. 1993).

The initial diamond drilling programme proved a measured and indicated resource of 8.3 Mt @ 10.9 % Zn (Corrans et al. 1993). An initial bulk sample pit was excavated in 1979 yielding ore grading approximately 20 % Zn. However, metallurgical testing, at the time, was unable to recover the zinc satisfactorily and the Skorpion prospect was 'mothballed'. Subsequently in 1996, Anglo American and Reunion Mining formed a joint venture within which Reunion carried out a new and major diamond and RC-drilling campaign during 1997/98. This programme increased the proven resource to 17.5 Mt @ 10.4 % Zn. Between 1996 and 1998, Reunion Mining commissioned a tailor-made solvent-extraction electro-winning (SX-EW) treatment process from Technicas Reunidas of Spain (the SX component) and Union Minière of Belgium, now Umicore (the EW component). This technological break-through converted the resource into a minable reserve. Reunion Mining was taken over by Anglo American in 1999 and as a result Anglo American again became the sole owner of the Skorpion deposit. Mining commenced in October 2001 with the stripping of the overburden and exposure of the ore body, which had a resource of 24.6 Mt at 10.6 % Zn by then (Mining Journal 2000). The first zinc metal was produced on site in May 2003.

3.2 Geographical Overview

3.2.1 Present Geomorphology

The Skorpion deposit is located within the south-eastern part of the Namib Desert within the 100 km-wide coastal zone west of the Great Escarpment. This desert, which is one of the world's most arid regions, is underlain by sands of a proto-Namib phase, which started to develop 35 million years ago. The Namib Desert stretches along the entire Atlantic coast and rises to a level of approximately 800 m at the foot of the Great Escarpment in the east. With differences in altitude of more than 1000 m, the Great Escarpment marks the transition to the Central Plateau east of the desert (Christelis & Struckmeier 2001).

The Skorpion area consists of undulating sand and gravel plains, isolated rock outcrops, and ranges of rocky hills (Fig. 11). The area is poorly drained, with a few ephemeral drainages

radiating away from higher lying features. The area lies about 650 m above sea level. The escarpment lies about 22 km east of the Skorpion area, where the land rises steeply to 800 – 1200 m above sea level. The surface of the current mining area is relatively flat and dips slightly to SE from 665 m in the north to 655 m in the south and forms a wide valley striking NW-SE. The subdued relief of the area with isolated outcrops and inselbergs is the result of the infilling of a rugged palaeo-topography by alluvial and colluvial sediments derived from the retreating escarpment and eroding valley sides as well as more recently, aeolian sand. These alluvial/colluvial sediments rest unconformable on the late Proterozoic host rocks of the Skorpion deposit. Additionally, ancient massive to nodular pedogenic calcrete horizons occur near the surface, although calcite is disseminated through most of the overburden profile as well. Iron-rich silcrete lenses are found locally above the erosional bedrock contact.



Fig. 11: Rock outcrop, sand plains and rocky hills in the Skorpion area. Red sands are part of the valley infill.

Fig. 12: Sparse vegetation in the Skorpion area.

3.2.2 Climate and Vegetation

The area is extremely arid and has mean annual rainfall of less than 100 mm per annum, usually concentrated from March to July. Sometimes, coastal fog from the Atlantic Ocean reaches this part of the Namib Desert, and thus contributes to the very limited precipitation in this area. Mean daily minimum and maximum temperatures range between 4°C and 20°C in July and 15° and 32°C in January, respectively.

Aeolian sedimentation processes are active in the southern Namib Desert, where dunes and flat sand plains prevail as the main morphological features. Chemical weathering and soil formation is hampered, mostly due to the lack of moisture. The scarce vegetation consists of grasses, shrubs and succulents growing on the sand plains (Fig. 12).

3.3 Geological Framework

The current mining activities exposed the rock sequence of the uppermost part of the supergene Skorpion ore body and thus tectonic structures within the Late Proterozoic sequence. The structures display a high intensity of deformation including folding, faulting, and thrusting in the mining area as a result of a multi-stage deformation process in different periods since the Late Proterozoic. This chapter summarises the main concepts based on studies undertaken by Corrans et al. (1993), Borg et al. (2004), and Dirks (2004).

Corrans et al. (1993) described the dominance of Pan-African deformation features like NNW-trending folds, here with a persistent moderate northerly plunge (31°) and related this to thrusting from the west during the late Pan-African event. Additionally, they found major, some of them probably still active, NW-trending faults, which displace the Late Proterozoic Gariiep sequence, interpreted as being originally related to the break-up of Gondwana and been in part responsible for the extreme oxidation and deep weathering of the primary sulphide ore zones, locally to more than 800 m depth (Corrans et al. 1993).

Two major separate deformational events have also been defined by Borg et al. (2004) and Dirks (2004). The earlier, ductile one, has been related to the main Pan-African deformation event, when the Skorpion precursor ore body was buried and metamorphosed to lower amphibolite facies grade, and has been accompanied by lateral sinistral transpression and pronounced SSE-ward thrusting, which was associated with the closure of the Adamastor ocean around 545 Ma ago (Borg et al. 2004). This multi-stage Pan-African deformation event led to the development of bedding-parallel thrust horizons, and therefore caused a duplication of the stratigraphic pile in places (Fig. 13, Dirks 2004). Additionally, E-verging, tight to isoclinal F_1 -folds were formed, which have been re-folded by W-verging, open F_2 -folds (Fig. 14) with a dominant, penetrative E-dipping cleavage. Fold axes of both F_1 - and F_2 -folds and prolate tectonic features (rodding) have a shallow to moderate plunge towards NNW (Borg et al. 2004), which is in agreement with Corrans et al. (1993). These early folds have been affected by wide and open D_3 -crossfolding with NE-SW-striking fold axes with a steep to moderate plunge that caused regional gentle “whale back-type” doubly plunging anticlines exposed prominently in the Skorpion and Rosh Pinah area. Both F_2 - and F_3 -folds feature strongly, although in smaller dimensions, in the open pit (Borg et al. 2004).



Fig. 13: Duplex arrays and intrafolial, recumbent fold packages wrapped by low-angle truncation planes mark Pan-African high-strain, thrust horizons. Skorpion open pit. Photo from Dirks (2004).



Fig. 14: Pan-African open F_2 -fold, Skorpion open pit, 630 m level.

The Pan-African deformed rock sequence has been affected by a later brittle-ductile deformation event in a transpressive shallow crustal regime (Borg et al. 2004), which might be correlated to the opening of the South Atlantic Ocean in the Jurassic (Dirks 2004). The Skorpion host rocks have been dissected by steeply dipping brittle-ductile shear zones, which show movement indicators for dip slip, oblique slip, and reverse slip shearing. In plan view of the pit area, this NW- to N-trending brittle ductile shear zone is the most prominent feature forming an anastomosing array (Fig. 16).

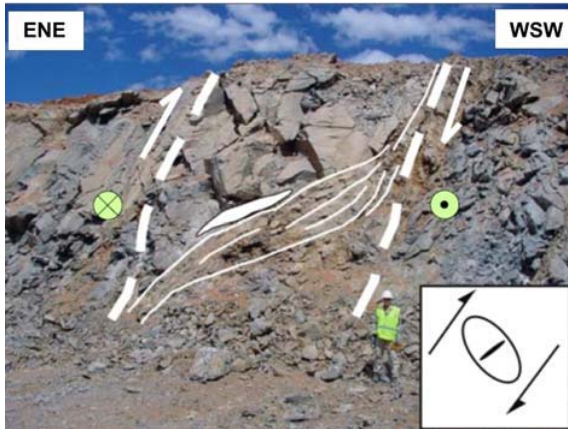


Fig. 15: View of the southern pit wall showing a dextral reverse fault set with a sigmoidal shear body and an extensional quartz vein as an example for the reverse oblique-slip fault zones as part of a positive flower structure. Photo from Borg et al. (2004).

feature forming an anastomosing array (Fig. 16).

Commonly, extensional quartz veins mark the centre of some of these shear zones. They are variable folded, boudinaged, and recrystallised (Borg et al. 2004, Dirks 2004). These zones have been interpreted by Borg et al. (2004) as the upper, marginal part of a dextral wrench fault system, which might be part of a positive flower structure (Fig. 15). Almost identical flower structures with a similar sense of movement have recently been identified offshore in seismic sections through the Orange Basin (Viola et al. 2005)

The youngest tectonic features, which are found within the Skorpion open pit, are most likely associated with the development of Namibia's continental margin (Tertiary to Recent) (Corrans et al. 1993).

The extensional crustal regime, which prevails since then, produces NE- and NW-trending normal faults (Dirks 2004), which partly occur to recent surface levels, also displacing Miocene boulder beds. These normal faults have either been newly formed or represent reactivated older fault structures (Borg et al. 2004).

Dirks (2004) subdivided the Late Proterozoic rock sequence, which is exposed in the open pit area, into five structural domains (Fig. 16) based on the distribution pattern of the Mesozoic brittle-ductile shear zones, which correspond to the dextral wrench fault system defined by Borg et al. (2004).

The westernmost domain (Domain I) consists mainly of felsic metavolcaniclastic rocks and metasiliciclastic rocks (e.g. argillaceous and arenitic meta-arkoses, metasubarkoses, meta-sand- and siltstones). Argillitic meta-arkoses as well as mylonitic metavolcaniclastic rocks (*mining term: sheared-sericite-schist*) and very minor marble occur within Domain II, which follows to the east. Within the northernmost part of the Skorpion open pit, metasiliciclastic rocks form a separate domain (Domain III). Felsic metavolcaniclastic and metavolcanic rocks (*mining term: quartz-sericite-schist*) are the main rock types within Domain IV, whereas Domain V consists exclusively of marble (*mining term: limestone*).

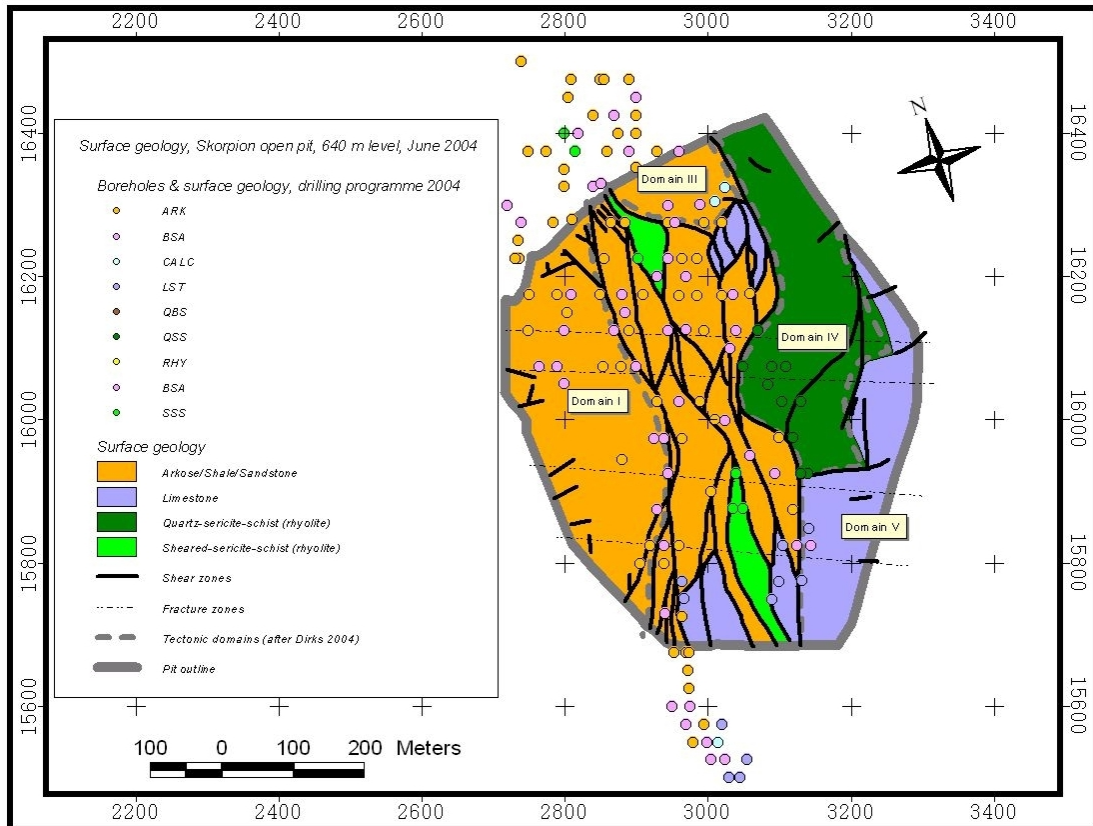


Fig. 16: Structural domains in the Skorpion open pit after Dirks (2004). Domain boundaries are defined by Mesozoic brittle-ductile shear zones. Later Cenozoic fracture zones (dashed lines) appear to transect the domains (Dirks 2004).

3.4 Lithology of Host Rocks

This present study uses metamorphic rock nomenclature rather than pseudo-sedimentary classification that has been used in mine records, since the Skorpion sulphide precursor has been modified by the Pan-African metamorphic event, and therefore has been undergone greenschist-/amphibolite facies metamorphism.

However, the pseudo-sedimentary classification, which has been used in mine records in order to classify host- and wall rocks of the Skorpion deposit petrographically, is listed in Tab. 2 and compared to the metamorphic nomenclature in order to allow a comparison of the two classification schemes.

Tab. 2: Classification schemes and protoliths for the Skorpion host rocks and wall rocks.

Mine Classification	Metamorphic Classification	Protolith
Overburden (OVB)	N/A	Sand-supported boulder beds and calcrete
Arkose (ARK)	Mainly psammitic siliciclastic meta-sediments	Arkose, subarkose, arkose sandstone to grey wacke, tuffite
Banded shale and arkose (BSA)	Mainly semipelitic siliciclastic meta-sediments	Siltstone, shale, minor arkose and arkose sandstone, tuffite
Black shale (SHB)	Metapelite	Black shale
Sheared-sericite schist (SSS)	Felsic metavolcanic rock (High-strain, mylonitic zone in the central part of the Skorpion ore body, highly sheared, well foliated felsic metavolcanic rock, sericite alteration)	Felsic volcanic rock (including felsic hyalo- and pyroclastic rocks)
Quartz-sericite-schist (QSS)	Felsic metavolcanic rock (Low-strain zone, foliated to massive felsic metavolcanic rock within the eastern portion of the Skorpion ore body, sericite alteration)	Felsic volcanic rock (including felsic hyalo- and pyroclastic rocks)
Rhyolite (RHY)	Felsic metavolcanic rock	Felsic volcanic rock
Amphibolite (AMP)	Metabasalt	Mafic volcanic rock (basalt)
Quartz-biotite-schist (QBS)	Felsic metavolcanic rock (Biotite alteration)	Felsic volcanic rock (including felsic hyalo- and pyroclastic rocks)
Limestone (LST)	Marble	Limestone
Calcarenite (CALC)	Marble	Impure limestone & calcarenite

Tab. 2 shows that the host rocks to the blind non-sulphide ore body and relict sulphide mineralisation are characterised by the presence of bimodal metavolcanic rocks, but also siliciclastic and chemical metasediments. Genetically, these rocks have formed in a failed intracratonic rift graben between the Kalahari cratonic province and the Rio de la Plata cratonic province (Borg et al. 2003).

During early rifting, sedimentation in the sub-ordered Skorpion/Rosh Pinah graben started with the sedimentary deposition of siliciclastic and carbonate sediments within both shallow and deep water environments. These protoliths consisted of arkose, limestone, calcarenite, silt- and mudstone, but also a large variety of volcanic and pyroclastic rocks related to bimodal, but predominantly felsic magmatism. Subsequently, three major events marked the evolution history of the Late Proterozoic rock sequence, namely: i) the Pan-African metamorphic event, ii) Mesozoic faulting, and iii) near-surface supergene weathering.

The supergene overprint led the formation of a deep weathering profile, composed of Late Proterozoic metamorphic rocks with varying degrees of weathering. In order to describe the degree of weathering, a supergene nomenclature can be used in addition to the metamorphic rock nomenclature. Rocks, in which less than 20 % of the weatherable minerals are altered, are referred to as saprock, whereas rocks, in which more than 20 % of the weatherable minerals are altered, are referred to as saprolite (Taboada & Garcia 1999).

The stratigraphic position of the different lithological units described above has been a controversial subject in the recent years. Hartmann et al. (2000) proposed that a major fault zone occurs between the felsic metavolcaniclastic, -volcanic footwall rocks within the western part of the deposit and the metasiliciclastic host rocks within the eastern part of the deposit (Fig. 17). This fault zone has been recognised in drill core by change in lithology and dip angles as well as by the occurrence of breccia zones, graphitic zones and core loss in boreholes. Starting from this thrust zone, site geologists recorded an upward younging in the western package compared to the constant downward younging in the eastern package, also indicating the occurrence of a major thrust zone in between (Hartmann et al. 2000).

The same observation was made by Dirks (2004) considering the distribution pattern of the lithological units as well as available younging indicators such as graded bedding (i.e. fining upward), and syn-sedimentary, cm-scale extensional structures. The younging indicators imply that in Structural Domains II-V the stratigraphic pile youngs W-ward and is overturned, whereas in Domain I the sequence appears to be largely right-way up. The two packages are separated by a brittle-ductile shear zone, which trends NNW-SSE through the central part of the Skorpion open pit.

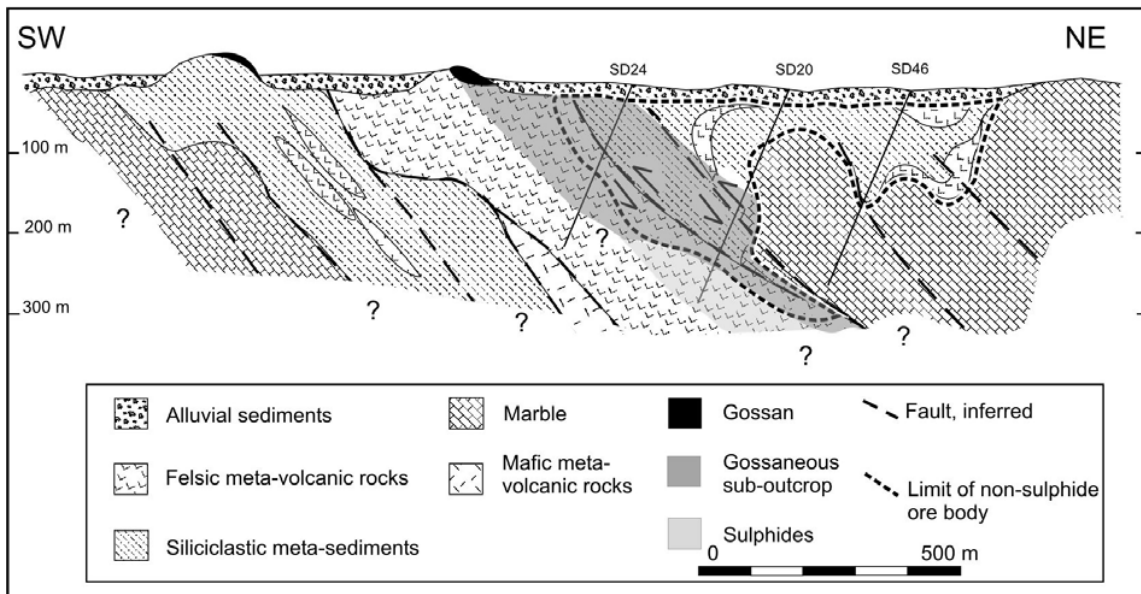


Fig. 17: Cross section through the Skorpion non-sulphide deposit as interpreted from borehole information. Ore-grade mineralisation occurs mainly in the metasiliciclastic rocks and subordinately in felsic metavolcanic rocks. Supergene mineralisation crosscuts sedimentary bedding within this package of rocks. The marble unit is generally devoid of mineralisation. A dashed line indicates the approximate limit of the non-sulphide ore body.

To conclude, there is sufficient evidence that the marble occurs at the base of the stratigraphic sequence at the Skorpion deposit, overlain by felsic metavolcanic rocks and metasiliciclastic rocks, which form the uppermost part of the Late Proterozoic sequence. This

stratigraphic scheme coincides with regional stratigraphic models of the Gariep sequence (e.g. Von Veh 1993, Buxton et al. 2000), in which marble of the Pickelhaube Formation occurs below volcanic and siliciclastic rocks of the Rosh Pinah Formation as part of the Hilda Sequence. It does not correspond to the stratigraphic scheme proposed by Frimmel (2000b), according to which the marble of the Pickelhaube Formation rests on top of the Rosh Pinah Formation (Fig. 8).

3.5 Petrography and Geochemistry of Host Rock and Wall Rock Lithotypes

3.5.1 Pre-Gariepian Basement

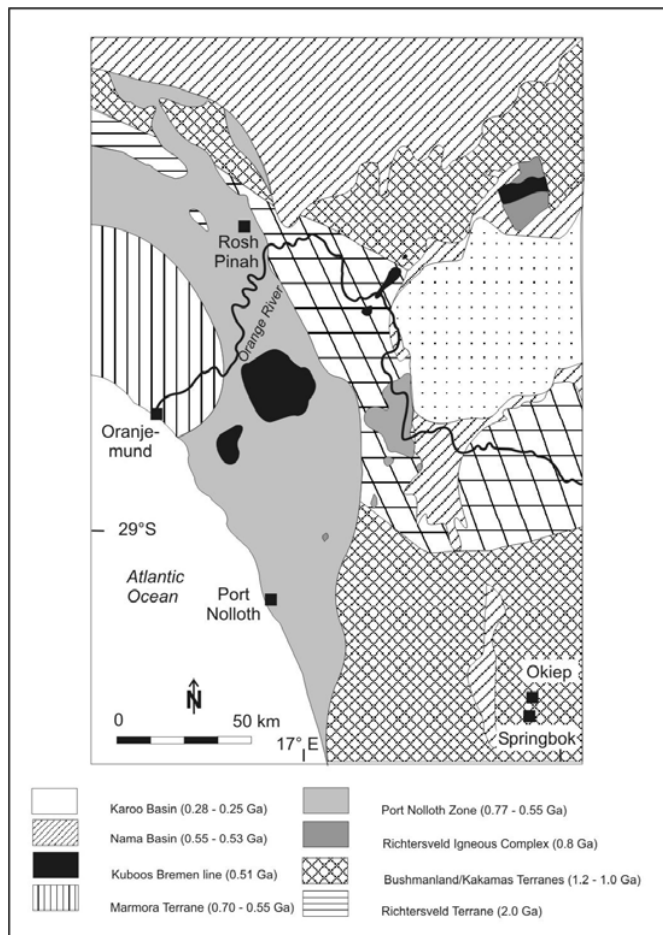


Fig. 18: Distribution of basement complexes within the Gariep Belt. Modified after Frimmel et al. (2004).

The Pre-Gariepian Eburnean basement underlies the Gariepian cover rocks, and therefore the host rocks of the Skorpion deposit. The basement is divided into three different types (Fig. 18, Frimmel et al. 2004):

i) A central, northeast-southwest trending, low-grade metamorphic Palaeoproterozoic (Eburnean) island arc (2.0 – 1.7 Ga Richtersveld Terrane) that comprises the Vioolsdrift Suite, consisting of gabbros, tonalites, granodiorites, and granites, and the predominantly volcanic Orange River Group.

ii) High-grade metamorphic, mixed volcano-sedimentary successions of Mesoproterozoic supracrustal rocks, reworked Palaeoproterozoic arc material and a series of intrusive bodies to the south (Bushmanland Terrane) and to the north (Kakamas Terrane) of the Richtersveld Terrane.

These two metamorphic terranes document the accretion of a 1.2 Ga island arc, the intrusion of 1.1 Ga extension-related granites and low-

pressure, high-temperature metamorphism and extensive magmatism around 1.06 – 1.03 Ga. The third basement type is younger and consists of iii) 830 – 770 Ma alkali granite and syenite bodies of the Richtersveld Suite (Frimmel et al. 2001).

Basement outcrops of the Richtersveld Terrane occur north and northeast of the Skorpion deposit (Rooiberg, Aurusberg) consisting of granitic orthogneiss, which intruded garnet-bearing paragneiss. Additionally, the granitic orthogneisses have been truncated by mafic dykes, which have been deformed together with the orthogneiss. The country rocks to the

leucocratic intrusive bodies have been intruded by pegmatites, which are locally highly folded, boudinaged, and sheared.

Major basement outcrops occur about 15 km east of the Skorpion deposit. However, at the Skorpion deposit itself, the depth of the top of the Eburnean basement is unknown. The deepest boreholes, which were drilled within the Skorpion area, reach depths up to 800 m and end in Gariepian cover rocks.

3.5.2 Gariepian Cover Rocks

3.5.2.1 Introduction

The Pre-Gariepian basement formed highs of horst and graben structures in the North (Aurusberg, Rooiberg), East and West (Boesmanberg) during the deposition of the Gariep sequence. The basal Gariep sequence, which was deposited within the graben structures, consists of a basal conglomerate or metaarenite.

The contact between the underlying ortho- and paragneisses of the Richtersveld Terrane and the basal Gariep Sequence is developed as either erosional/sedimentary or in-situ regolithic. The erosional/sedimentary contact is characterised by the occurrence of polymictic boulderbeds, though the clasts derived mainly from the adjacent ortho- and paragneisses. A mixed siliciclastic-carbonate sequence follows on top of the basal conglomerate. The distribution of basement areas as well as the detrital composition of the siliciclastic part of the Gariep sequence suggests that the siliciclastic erosional debris has been derived from local sources, such as adjacent basement areas (Borg 2001).

Subsequently, an extensive shallow water carbonate sequence developed, which rests directly upon basement in north and west and gradationally upon the basal siliciclastic rocks in the central portion of graben structures. The occurrence of stromatolites and accretionary lapillis within these carbonates has been reported by Borg (2001).

Felsic volcanism occurred along the host and graben structures; and multistage volcanic activity was probably triggered by renewed tectonic activity. The felsic volcanism is characterised by a wide variety of volcanic rocks, e.g. rhyolitic flows, pyroclastites, hyaloclastites, and tuffites.

The mixed carbonate-siliciclastic sequence of the Skorpion basin alternates stratigraphically both on a large and on a small scale, suggesting a rapid change in depositional environment. Periods of extreme siliciclastic sediment influx alternated with periods of relative quiescence during which low energy siliciclastics and chemical carbonates have been deposited in relatively shallow water environments. The rapid change between high-energy and low-energy depositional environments gives evidence of an episodic extensional tectonic activity with uplift of the hinterland, the formation of graben structures, periods of increased erosion and clastic sediment influx.

Subsequent to its deposition, the Gariep rock sequence has been affected by a major tectono-metamorphic event during the Pan African/Brasiliano Orogeny at approximately 550 – 545 Ma. Metamorphism reached uppermost greenschist to lowermost amphibolite facies (Frimmel & Frank 1998). The complex deformational style of the region is the result of intense faulting, folding and thrusting.

3.5.2.2 Marble

3.5.2.2.1 Petrography

The calcitic marble forms an antiform in the eastern part of the Skorpion non-sulphide ore body (Fig. 17). It is commonly blue-grey, fine- to medium-grained and thinly to thickly bedded (Fig. 19). The metamorphosed limestone shows generally no secondary fabrics, though an indistinct cleavage, indicated by orientated mica, can be seen in impure marble. Additionally, the marble is characterised by a strong to very strong rock strength. It is moderately to closely jointed. In places, joints and fractures are filled by euhedral calcite or have iron hydroxide veneers. Along fractures and joints but also along the contact to the non-sulphide mineralised metasiliciclastic unit, the marble is commonly highly weathered indicated by higher clay content and a weak to very weak rock strength. Weathered marble is discoloured and usually light- to medium-grey, and partly tan-coloured (Fig. 20).

The marble unit is characterised by a very low porosity and permeability. However, fractures and joints provide minor open space, which makes a very limited groundwater flow possible. Nevertheless, the marble unit must be regarded as an aquiclude or aquitarde.

The marble unit most likely represents a shallow water carbonate deposited on a continental shelf during an advanced stage of the Pan-African tectonic cycle. The deposition of the shallow marine platform carbonates within the Rosh Pinah/Skorpion graben was also influenced by tectonic activity during the Late Proterozoic rifting, by sea-level fluctuations, by reworking processes and the nature of the preserved sedimentation record. These processes influenced the composition of the marble, which is impure in many places containing a siliciclastic component. Partly, proper siliciclastic beds are intercalated, which are a common constituent in tectonically active rift graben (Levell 1980). They typically represent a shallow-marine but high-energy environment. Additionally, mud- and silt-layers occur irregularly distributed. The incursion of terrigenous clay and silt onto the ancient platform suggests that alternating energy conditions prevailed, as the very fine grained terrigenous material has most likely deposited in a low-energy environment. In some places mud layers show soft sediment deformation but also reworked features as disrupted bands and mud flakes (Fig. 19).

The marble is barren and contains neither significant hypogene sulphide nor supergene non-sulphide mineralisation. However, disseminated hypogene pyrite is abundant in fresh or slightly weathered marble (Fig. 21 & 22). Additionally, traces of sphalerite have been found in marble, which occurs north of the Skorpion deposit at depth (Fig. 23 & 24).

Supergene mineralisation within the marble is usually not existent; however, elevated zinc values along fractures and joints but also along the contact to the non-sulphide-mineralised metasiliciclastic unit are common. The uppermost part of the marble antiform is highly brecciated and calcretised. Additionally, mining operations exposed a karst cave have in the Skorpion open pit, which will be discussed in relation to palaeomorphological aspects and palaeoclimatic conditions later in this study.



Fig. 19: Photograph of drill core showing slightly weathered blue-grey marble with silt- and mud layers. Borehole SD07, depth 151.0 m.



Fig. 20: Photograph of drill core showing highly weathered and discoloured light-grey to tan-coloured marble. Borehole SD07, depth 119.0 m.

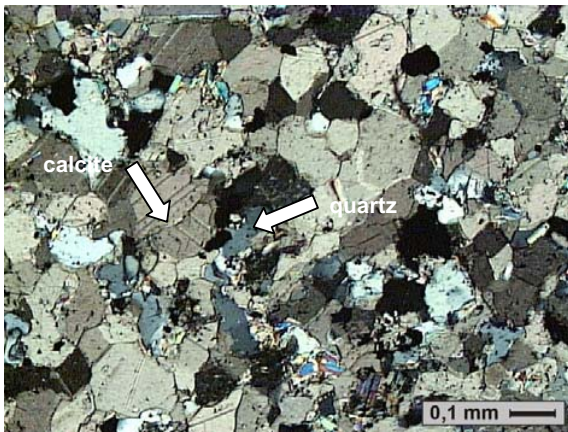


Fig. 21: Photograph of a thin section showing fine-grained, fresh marble. Borehole SD07, sample 0738, depth 146.4 m. XN.

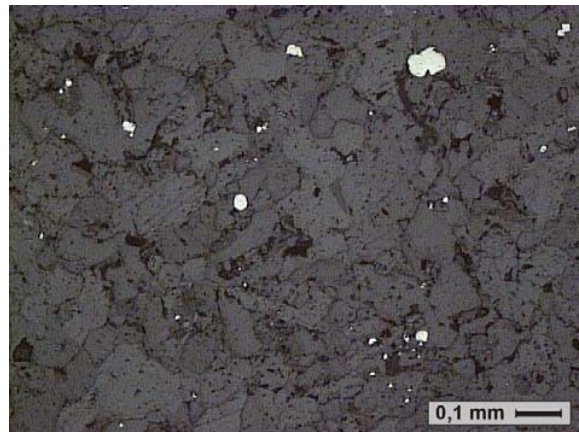


Fig. 22: Same frame as Fig. 21. Disseminated, very fine-grained anhedral pyrite in marble. Reflected light.

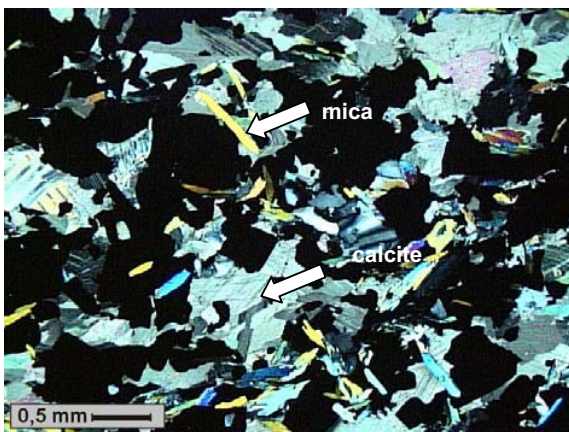


Fig. 23: Photograph of a thin section showing marble with euhedral pyrite and anhedral sphalerite. Borehole SD104, sample SD10402, depth 701.35 m. XN.

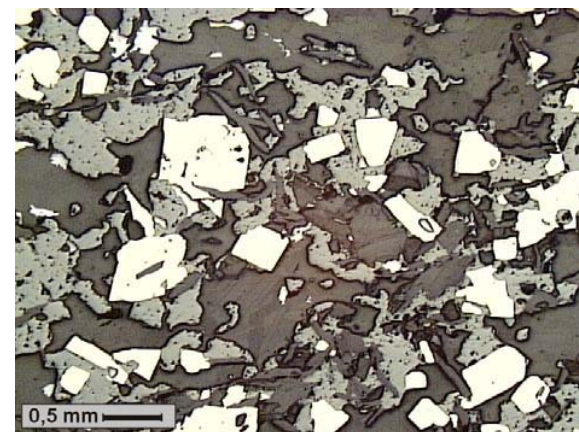


Fig. 24: Same frame as Fig. 23. Euhedral pyrite (whitish/light yellow) and anhedral sphalerite (light-grey) in marble. Reflected light.

3.5.2.2.2 Geochemistry

The calcitic marble is impure and contains various amounts of detrital quartz but also metamorphic mica, which leads to an average SiO₂ content of 20.4 %. Additionally, the marble contains minor Al₂O₃ averaging at 5.7 %, as well as minor MgO and K₂O, averaging at 1.5 % and 2.3 %, respectively. The amount of Al₂O₃ within the marble is higher along the contact to the siliciclastic unit. High concentrations of Al₂O₃ are coincident with elevated zinc values, which are more than 50 times higher than the background values, averaging out at 2709 ppm compared to 50 ppm for the background. The relationship between Al and Zn within the commonly highly weathered contact zones indicate the occurrence of Zn-bearing clay, which have formed during the weathering. The occurrence of SiO₂, K₂O and Al₂O₃ most likely represents the siliciclastic components within the marble in the form of quartz, mica, and minor feldspar. The general impurity of marbles has also been reported from dolomitic marbles from the Rosh Pinah area by Frimmel & Lane (2005) averaging at 11.3 % SiO₂, 1.2 % Al₂O₃ and 0.6 % K₂O.

In addition to the analysis of major elements using XRF techniques, two C-, O-isotope analyses have been carried out. The carbon-isotopic compositions of carbonates within the Damara basin provide a potentially useful tool for the correlation of units from the Kalahari Craton but also between the Kalahari and Congo cratons (Fölling et al. 2000, Kaufmann et al. 1991), since isotopic compositions of carbonates have not been affected by deformation and metamorphism (Kaufmann et al. 1991).

δ¹³C reflect variations in global changes in the isotopic composition of the Late Proterozoic sea. Investigations on carbon isotopes of carbonates in the Late Proterozoic succession of the Gariiep Belt have been carried out particularly by Kaufmann (e.g. Kaufmann et al. 1991) and Fölling (e.g. Fölling et al. 2000). Frimmel (2000b) has shown that carbonates in the Hilda Subgroup, which are chemical precipitates, are progressively enriched in δ¹³C. This trend reaches a maximum δ¹³C of 8 ‰ in the Upper Pickelhaube Formation and in the Dabie River Formation. Further up-section follows a rapid drop in δ¹³C towards the contact with the overlying Numees Formation diamictite (Frimmel 2000b).

The two marbles samples from the Skorpion ore body have shown that the Skorpion marble is enriched in δ¹³C and displays 5.82 ‰ and 8.09 ‰ (PDB), respectively. This signature is in agreement with results from Frimmel (2000b), indicating that the Skorpion marble is part of the Hilda Subgroup in the Gariiep Group (Fig. 25 & 26), and belongs most likely to the upper part of the Pickelhaube Formation (Fig. 25). This assumption is supported by Kaufmann et al. (1991), who also determined highly positive δ values for marble from the Hilda Subgroup. Additionally, recently published data by Frimmel & Lane (2005) have shown that negative primary δ¹³C ratios correlate to the Lower Pickelhaube Formation being at the same stratigraphic level as the Rosh Pinah Formation. However, considerably higher δ¹³C values, like the Skorpion marble displays, most likely reflect a higher stratigraphic position (Frimmel & Lane 2005), and thus the Upper Pickelhaube Formation. The apparent wide range of δ¹³C within the marbles of the Hilda Subgroup is explained by a change from global icehouse (low δ¹³C) to greenhouse conditions (high δ¹³C) (Frimmel et al. 2002). The correspondence between ice ages and negative δ¹³C values may reflect the effects of lowered sea levels; enhanced circulation of deep, cold, O₂-rich seawater; and/or the upwelling of δ¹³C-depleted deep water (Kaufmann et al. 1991). The Hilda Subgroup with its extensive carbonate sedimentation, especially the Upper Pickelhaube Formation, is therefore interpreted as an interglacial period relative to the Kaigas and Numees formations (Kaufmann et al. 1991). However, the enrichment in ¹³C does not necessarily reflect global climate changes but could also be an indication of chemical precipitate (Frimmel 2000b) and elevated evaporation rates

in a restricted basin, because the heavier isotope becomes concentrated in the remaining water body during evaporation (Frimmel & Lane 2005).

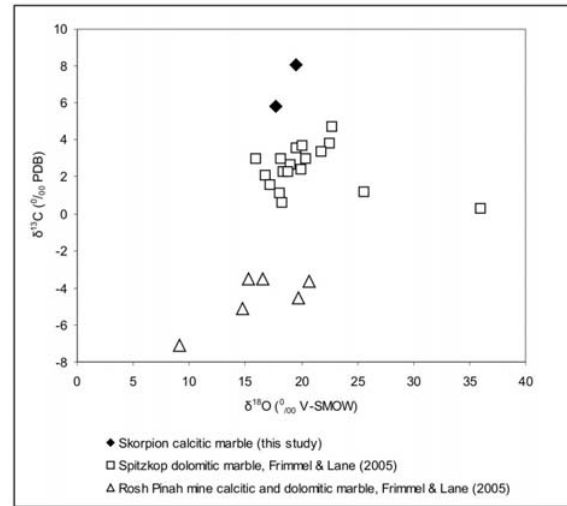
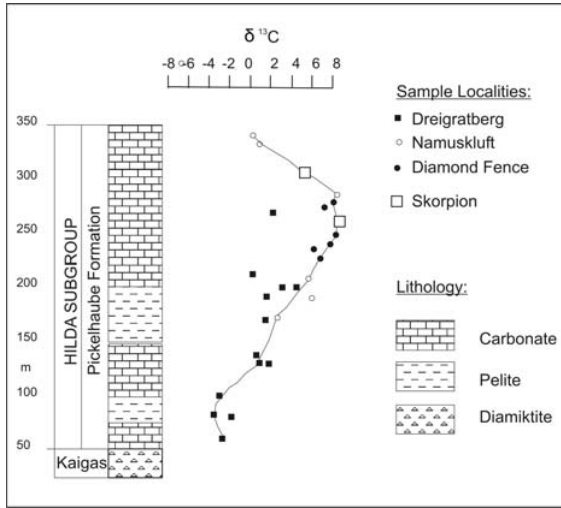


Fig. 25: Variations in $\delta^{13}\text{C}$ versus stratigraphical depth for carbonate deposits from the Gariep Belt in Namibia (from Fölling et al. 2000) including a proposed stratigraphic position for the Skorpion marble based on its $\delta^{13}\text{C}$ composition.

Fig. 26: $\delta^{13}\text{C}$ versus $\delta^{18}\text{O}$ diagram showing dolomitic and calcitic marble from the Rosh Pinah area, which are interpreted to belong to the Rosh Pinah Formation, and thus represent the stratigraphically equivalent Lower Pickelhaube Formation (Frimmel & Lane 2005). The Skorpion marble shows clearly a different isotopic composition, and thus, is interpreted to represent a higher stratigraphic position.

Tab. 3: C, O isotope analyses of two marble samples from the Skorpion ore body.

Sample No.	Borehole	Depth [m]	Mineral, rock type	$\delta^{13}\text{C}_{\text{VPDB}}$	$\delta^{18}\text{O}_{\text{VSMOW}}$
0721	SD07	245.15	Calcite, marble	8.09	19.48
8001	SD80	171.84	Calcite, marble	5.82	17.70

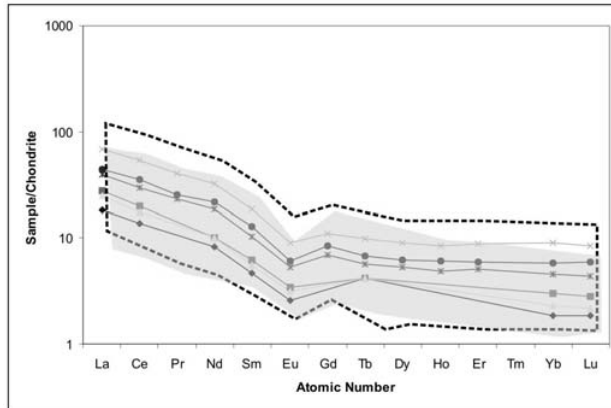


Fig. 27: Chondrite-normalised (Boynnton 1984) REE pattern of Skorpion marble (n = 6) compared to marble from the wider Skorpion (n = 6, dashed outline, this study) and the Rosh Pinah areas (n= 15, shaded area, Frimmel & Lane 2005).

The Skorpion calcitic marble displays enrichment in light REE when normalised against chondrite, with La/Lu ratios ranging between 72 and 110, averaging at 89 (Fig. 27). This distribution is similar in marble some kilometers south of the Skorpion deposit. These marbles are thought to represent stratigraphic equivalents of the Skorpion marble and show La/Lu ratios ranging between 62 and 166, and averaging at 72, respectively. Dolomitic and calcitic marbles from the Rosh Pinah area (Frimmel & Lane 2005), which represent a stratigraphic lower position according to their ¹³C composition, display La/Lu ratios ranging from 37 to 126 and averaging

at 96. Therefore, the La/Lu ratios seem to be very similar throughout the marbles of the Hilda Subgroup.

The low REE concentrations in the calcitic marble from the Skorpion deposit but also in calcitic and dolomitic marbles from the Rosh Pinah area are typical for chemical marine sediments (Frimmel & Lane 2005) and thus, expected to occur in the Late Proterozoic marbles. Some elevated REE concentrations could be attributed to contamination with detrital minerals (Frimmel & Lane 2005). Indeed, microscopic studies but also the analysis of major elements from the Skorpion marble has shown that the Skorpion marble is generally impure and contains a certain amount of detrital material in the form of mica, quartz and/or feldspar. The weak negative Eu-anomaly, which can be identified in the different marbles, averages at 0.15 for the Skorpion calcitic marble, 0.19 for calcitic marble south of the Skorpion deposit, and 0.24 for dolomitic/calcitic marble from the Rosh Pinah area (Frimmel & Lane 2005). This anomaly could well be a result of the detrital input, as the Late Proterozoic metasiliciclastic rocks from the Skorpion deposit display well-defined negative Eu-anomalies (see chapter 3.5.2.5.2).

3.5.2.3 Felsic Metavolcanic Rocks

3.5.2.3.1 Petrography

A wide variety and large volumes of felsic metavolcanic rocks occurs within the Skorpion area. The main felsic volcanic centres featuring rhyolitic domes occur east and southeast of the Skorpion deposit, e.g. Anninaub, Trekkport, and Spitzkop.

The felsic metavolcanic rocks, which are found in the footwall of the non-sulphide Skorpion deposit, host hypogene sulphides. Different mining terms exist for the felsic metavolcanic rocks, mainly depending on the degree of deformation.

Mining terms representing the felsic metavolcanic rocks at the Skorpion deposit include the so-called 'sheared sericite schist' (SSS), 'quartz-sericite schist' (QSS) and rhyolite (RHY) (Tab. 2). The volcanic origin of the highly strained and altered mylonitic sericite schist and the more massive and less foliated quartz-sericite schist was proven by Kärner (2003b) and subsequently confirmed by Dirks (2004). Primary pre-deformational features can hardly be identified in the felsic metavolcanic rocks due to post-deformational hydrothermal alteration,

subsequent Pan-African deformation and medium-grade metamorphism but also Tertiary supergene alteration that has formed schists with different textures, mineralogy, and grain size.

However, despite the predominance of deformative features and the subsequent supergene overprint the attempt has been made to classify the different volcanic facies types (Tab. 4).

Tab. 4: Felsic volcanic facies and their associated mineralisation at the Skorpion deposit, following the classification for mixed felsic facies typically for VHMS deposits from Allen et al. (1996).

Volcanic Facies	Petrographic Description	Metamorphic Nomenclature	Mineralisation
Massive felsic lavas	Undifferentiated rhyolitic metavolcanic rocks with metamorphic texture (no recognisable primary volcanic texture)	Metarhyolite and so-called 'quartz-sericite schist' (QSS) and 'sheared sericite schist' (SSS)	Pyrite, sphalerite; brunckite
Rhyolitic ash-siltstone	Fine grained, quartz-feldspar rich, well sorted, thin bedded to massive; settled subaqueous suspension (syn- and posteruptive)	Metatuffite ('quartz-biotite schist' (QBS), 'sheared sericite schist' (SSS))	Pyrite, sphalerite, chalcopyrite, (galena); sauconite, malachite, goethite
Rhyolitic accretionary lapilli tuff	Well-sorted accretionary lapilli (2 – 10 mm) in finer grained, well sorted siliciclastic matrix; planar bedded, beds internally massive or planar stratified, air fall or water-settled air fall (subaerial or shallow-marine), syneruptive; mm to dm thick beds	Metatuffite	Hemimorphite (replacing lapillis)
Rhyolitic stratified lithic sandstone and breccia	Planar to cross stratified, locally massive, moderate to well sorted, non-systematic grain-size variations; subaerial or shallow-water traction sedimentation; mainly post-eruptive	Metasandstone, meta-arkose	Sauconite, hemimorphite, smithsonite

The predominant felsic metavolcanic facies includes volcanic flows, hyaloclastites, and minor thin pyroclastic ash layers in metasediments. Additionally, well-sorted rhyolitic accretionary lapilli meta-tuff occurs as mm- to dm-thick layers both in meta-arkose and in metasandstone. The great abundance of non-welded pyroclastic debris, which can easily be mistaken as siliciclastic sediments, and paucity of definite welded pyroclastic deposits are indicative for a deposition in a subaqueous environment (Cas & Wright 1987). Alchin et al. (2005) propose a near-shore setting for the volcanic edifice, containing both subaerial and submarine deposited volcanic rocks.



Fig. 28: Rhyolitic columns at Eccles Ridge, south of the Skorpion deposit.

The massive medium- to light-grey felsic metavolcanic host rocks (volcanic flows) are commonly slightly to moderately weathered. They are characterised by high rock strength, which can be explained by the commonly high SiO₂ content that indicates a secondary silification. The process of secondary silification will be discussed separately. Porosity and permeability are very low in these rocks. The low degree of weathering is interpreted to have resulted from the availability of only limited open space due to the massive nature of this rock type, which prevented a high fluid run-through and thus deep oxidation. It is worth mentioning that outcropping

rheologically competent metarhyolitic flows locally display well-preserved columnar jointing, which can be seen west and south of the Skorpion deposit (Fig. 28).

Hypogene sulphide mineralisation or remnants thereof occur in all different volcanic facies types. Massive, partially silicified felsic flows may contain commonly pyritic stringers or finely disseminated pyrite (Fig. 29). Particularly, the metarhyolitic hyaloclastic rocks (quartz-sericite schist, quartz-biotite schist), structurally underlying the Skorpion non-sulphide deposit towards the west, are host to semi-massive, stringer-type, but also banded and abundant disseminated base metal sulphides (Fig. 30) including foliation-parallel elongated pyrite, sphalerite, minor chalcopyrite, and traces of galena. Alchin et al. (2005) have proposed that the Late Proterozoic rift volcanism provided the heat engine that was necessary for the convection of metal-bearing hydrothermal fluids through the rift-floor, however, the bulk of the base metals in the Late Proterozoic felsic metavolcanic rocks has most likely derived from the underlying basement (e.g. Frimmel 2004).



Fig. 29: Photograph of drill core showing pyritic stringer mineralisation in metarhyolite. Borehole SD 20, sample SD2031, depth 329.9 m.

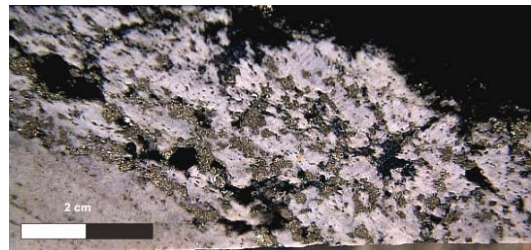


Fig. 30: Photograph of drill core showing semi-banded and disseminated pyrite-sphalerite mineralisation in felsic metavolcanic rock. Borehole SD20, sample SD2034, depth 337.7 m.

Felsic metavolcanic rocks that have contain hypogene sulphide mineralisation show evidence of a supergene overprint either by the occurrence of undeformed, low temperature sulphide and non-sulphide minerals (Fig. 31 – 33) or by the occurrence of extensive gossaneous zones (Fig. 34).



Fig. 31: Photograph of drill core showing accretionary lapilli metatuffite. Individual lapillis have been replaced by hemimorphite. Borehole BH70, sample BH7015, depth 97.95 m



Fig. 32: Same drill core as Fig. 31. The zinc indicator solution 'Zinc Zap', which turns red reacting to zinc-bearing minerals, was applied in order to show the inconspicuous hemimorphite mineralisation. The deep red colour indicates that the zinc concentration is > 20 %.

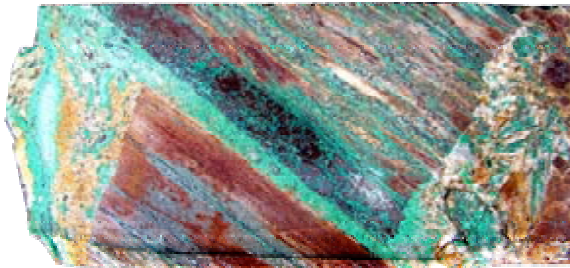


Fig. 33: Photograph of drill core showing mylonitic and brecciated felsic metavolcanic rock (mining term: quartz sericite schist) with a cm-thick band of supergene hematite and impregnations of malachite along the foliation planes. The sample indicates that in-situ oxidation took place, since former sulphide laminae have been completely replaced by hematite. Borehole SD65, sample 6510, depth 118.35 m. Length of drill core 12 cm.

The gossaneous felsic metavolcanic rocks feature colourful weathering colours ranging from white to light-grey, tan to pink and red brown to orange (Fig. 34). The advanced stage of weathering might be explained by the strong foliation, which enhanced a supergene fluid through-flow along the foliation planes and thus, increased the process of oxidation. Additionally, the occurrence of weatherable minerals like sulphides, and minor feldspar, biotite must have accelerated the oxidation process.



Fig. 34: Typical drill core of a gossaneous and malachite-stained metarhyolite from the footwall of the Skorpion non-sulphide ore body. Red brown to orange and white to pink colours as well as weak rock strength indicate a high degree of weathering. Foliation is well developed. SKGT2 (E 2689.5, N 16000), 65.11 – 70.22 m.

3.5.2.3.2 Geochemistry

At least three major events have overprinted the felsic metavolcanic rocks since their deposition, namely: i) hydrothermal alteration, ii) greenschist/amphibolite facies metamorphism, and iii) supergene weathering. All these events have led to several modifications of the primary mineral assemblage as a result of changing temperature and pressure conditions, but also changing Eh/pH conditions. The major problem, which arises from the complex alteration history, is a geochemical signature, which is often difficult to interpret as it may contain features, such as the enrichment or the depletion of certain elements, which could have resulted from at least three different processes.

The fact of the interference of hydrothermal, metamorphic and supergene alteration signatures also complicates the classification of the felsic metavolcanic rocks. In order to eliminate the effects of supergene alteration on the composition of the felsic metavolcanic rocks, least weathered felsic metavolcanic equivalents from the Skorpion/Rosh Pinah area (Frimmel 1996a, Borg et al. 2003, this study) were plotted in classification diagrams and then compared with the highly (supergene) altered felsic metavolcanic rocks from the Skorpion deposit (Fig. 35).

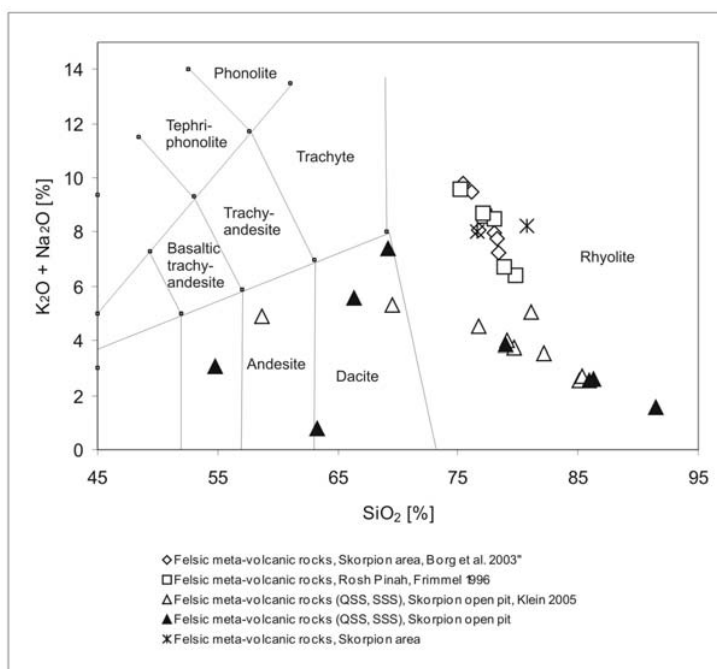


Fig. 35: TAS diagram, classification of felsic metavolcanic rocks, Na₂O + K₂O versus SiO₂ with field boundaries after LeMaitre et al. (1989).

(Fig. 35).

The TAS diagram after LeMaitre et al. (1989) | Fig. 35 shows that the least altered felsic metavolcanic rocks from the Skorpion/Rosh Pinah area belong to the group of rhyolites. The TAS diagram also shows that their highly deformed and supergene altered equivalents from the Skorpion deposit have apparently lost both sodium and potassium (post-metamorphically), which will be discussed more detailed later in this chapter. Additionally, some of them have apparently partly lost some silica and thus, plot erroneously within the field of andesite and dacite. Their erratic distribution in the

TAS diagram indicates that this classification cannot be applied to the supergene felsic metavolcanic rocks from the Skorpion deposit.

The K₂O versus SiO₂ diagram with boundaries after LeMaitre et al. (1989) shows that the least supergene weathered felsic metavolcanic rocks fall into the field of high-K rhyolite (Fig. 36). However, the harker diagram in Fig. 37 shows that only the felsic metavolcanic rocks from the Rosh Pinah area should be classified as high-K rhyolites, since the Skorpion felsic metavolcanic rocks have apparently undergone extensive K-metasomatism. K-metasomatism is related to high K₂O/Na₂O ratios, which results from the occurrence of ubiquitous sericite (Eastoe et al. 1987). This phenomenon has been reported from volcanic-hosted massive sulphide deposits elsewhere (Eastoe et al. 1987, Cooke et al. 1998 and

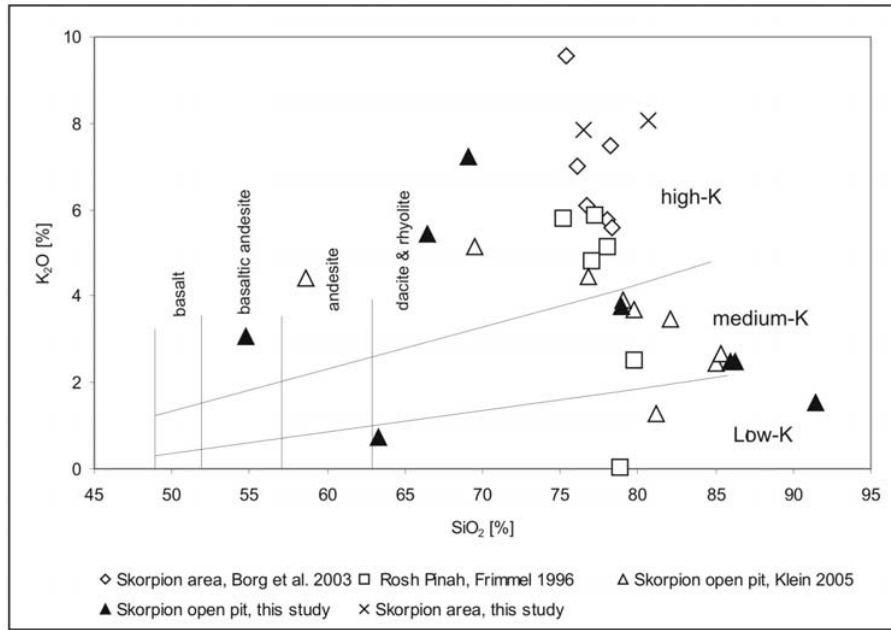


Fig. 36: K_2O versus SiO_2 with boundaries after LeMaitre et al. (1989) shows that the least supergene altered felsic metavolcanic rocks from the Skorpion and Rosh Pinah areas (Borg et al. 2003, Frimmel 1996a) fall into the field of high-K rhyolites. Their highly supergene altered equivalents from the Skorpion deposit plot erratically, which results from the advanced weathering stage.

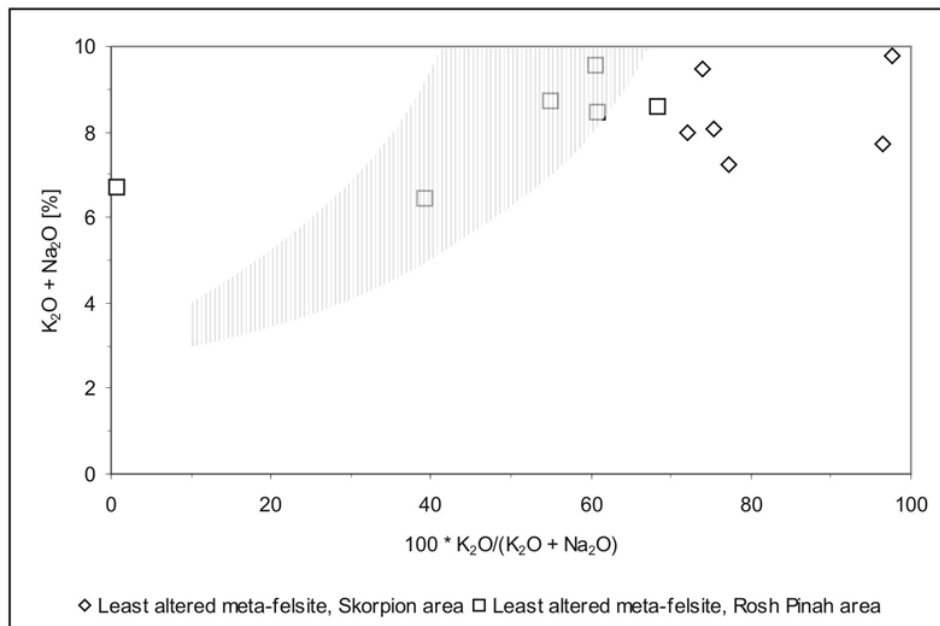


Fig. 37: Harker diagram showing alkali metasomatism of least supergene altered felsic metavolcanic rocks from Skorpion (Borg et al. 2003) and Rosh Pinah areas (Frimmel 1996a). Points outside of the normal range after Hughes (1973) have undergone alkali exchange reactions. K-enriched samples lying to the right and Na-enriched rocks to the left of this field.

The highly supergene altered felsic equivalents from the Skorpion open pit are not depicted in this plot, since they show an erratic distribution within the TAS diagram due to their advanced stage of weathering.

Rougvi & Sorensen 2002). Microscopic investigations on felsic metavolcanic rocks that have undergone K metasomatism have shown that these samples are characterised by the occurrence of abundant sericite (Fig. 34 – 35), which is in agreement with observations from massive sulphide deposits elsewhere.

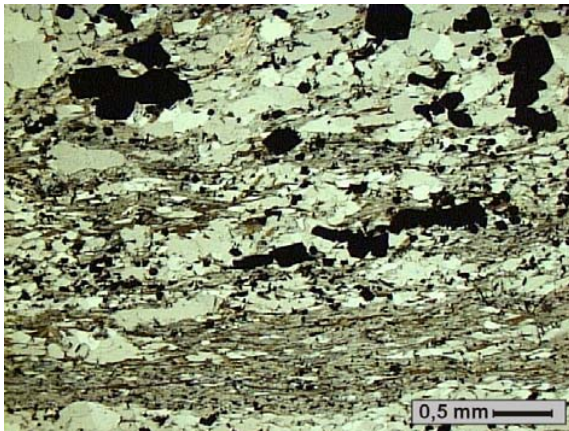


Fig. 34: Microscopic photograph of a thin section showing sericite alteration within sulphide-mineralised felsic metavolcanic rock from the footwall of the non-sulphide Skorpion deposit. High K_2O/Na_2O ratios as well as the occurrence of sericite indicate that K-metasomatism must have taken place. Borehole SD49, depth 325.8 m, sample 4962. LLP.

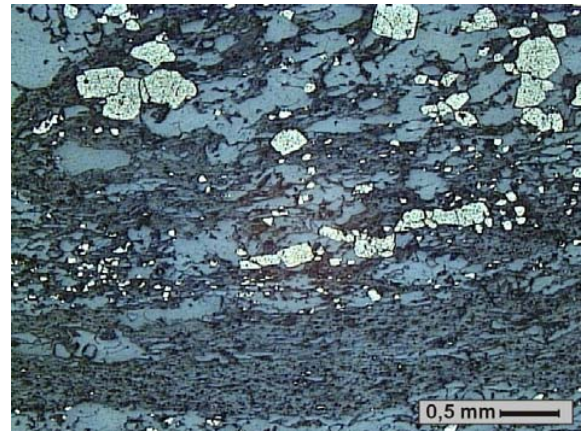


Fig. 35: Same frame as Fig. 34. Disseminated subhedral pyrite (light-yellow). Microscopic photograph, reflected light.

In order to quantify gains and losses of potassium, sodium but also other elements, the least altered felsic metavolcanic rocks are graphically compared with their most altered equivalents in the so-called isocon diagram according to Grant (1986) (Fig. 36). The 'isocon' defines the simultaneous graphical solution for all components that show no relative gain or loss of mass. On a graph of the concentrations in the altered rock against those in the original, an isocon is a straight line through the origin. The slope of the isocon defines the mass change in the alteration, and the deviation of a data point from the isocon defines the concentration for the corresponding component (Grant 1986).

Before using the isocon diagram for interpretation it has to be pointed out that the two groups, which are compared in this diagram are: i) fresh/least supergene altered felsic metavolcanic rocks from the Skorpion area (Borg et al. 2003) as they are thought to have a composition, which is closest to the original composition and ii) highly supergene altered felsic metavolcanic rocks from the Skorpion deposit. Therefore, any gain or losses of a certain element could result from either hydrothermal alteration, metamorphic mineral reactions or supergene alteration.

The isocon diagram for the felsic metavolcanic rocks (Fig. 36) shows that the majority of HREE's as well as SiO_2 behave collinear, and therefore are thought to represent the best-fit isocon (Grant 1986) corresponding to hypotheses of constant mass and constant volume. The effect of silification, which was mentioned above, is concealed, and indicates that the compared groups must have both undergone silification. The most significant mass changes can be reported for Ba and Mg (Tab. 5). Microscopic investigations as well as semiquantitative SEM-EDX analyses have shown that barium is primarily bounded to orthoclase. However, it has been subsequently released from feldspar by supergene fluids and precipitated as secondary barite (Fig. 37). The apparent enrichment of Mg is most likely the result of the

occurrence of chlorite in the felsic metavolcanic rocks. Chlorite is found in layers of schistose, chloritised metatuffite intercalated with the quartz-sericite schist (Fig. 38a). It is interpreted to represent remnants of a hydrothermal alteration paragenesis, since chlorite and biotite in felsic metatuffite are known to represent hydrothermal alteration facies in volcanogenic massive sulphide deposits elsewhere (Eastoe et al. 1987, Kranidiotis & MacLean 1987, Tiwary & Deb 1997). In particular, the concurrent enrichment of MgO and depletion of Na₂O, which can be observed in the felsic metavolcanic rocks from the Skorpion deposit (Tab. 5), indicates that the main reaction was chloritisation of plagioclase feldspar (Tiwary & Deb 1997).

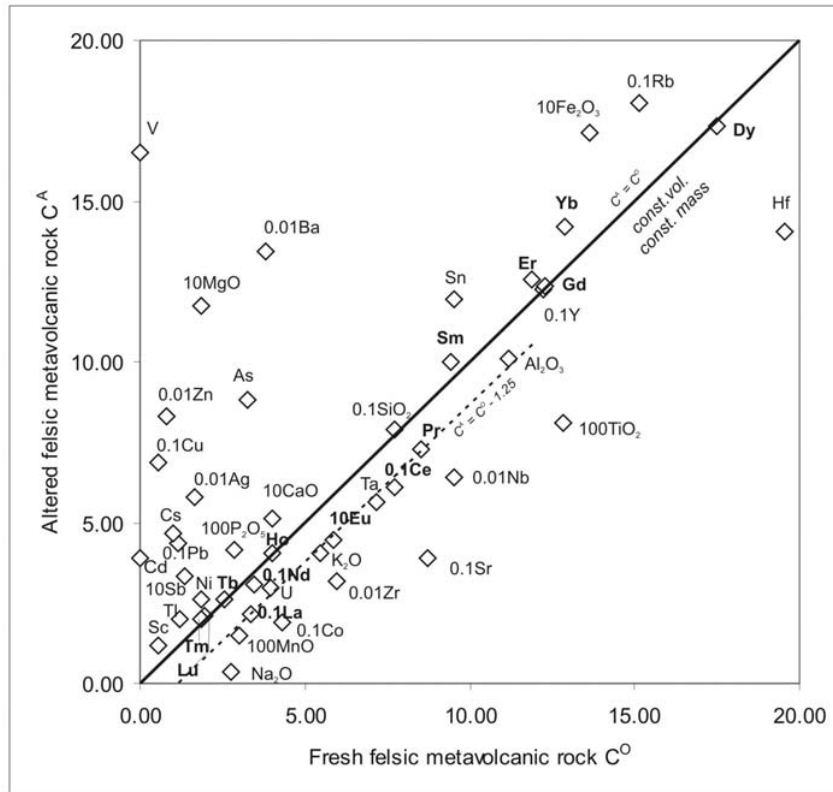


Fig. 36: Isocon diagram after Grant (1986) for average analyses of least altered felsic metavolcanic rocks ($n = 12$, Borg et al. 2003, Frimmel 1996a) and highly altered felsic metavolcanic rocks from the Skorpion deposit ($n = 16$). Oxides are plotted in weight percent, elements in ppm. The majority of HREE's is collinear, and therefore represent the best-fit isocon corresponding to hypotheses of constant mass and constant volume. LREE's as well as K₂O and Al₂O₃ plot on a line parallel to the isocon indicating a constant ΔC_i .

Tab. 5: Concentration changes in altered felsic metavolcanic rock corresponding to a constant mass/constant volume isocon. Calculation according to Grant (1986).

Component	SiO ₂	Al ₂ O ₃	Fe ₂ O ₃	MnO	MgO	CaO	Na ₂ O	K ₂ O	TiO ₂	P ₂ O ₅
$\Delta C_i/C_i^O$	+0.02	-0.10	+0.26	-0.50	+5.36	+0.28	-0.87	-0.26	-0.37	+0.47

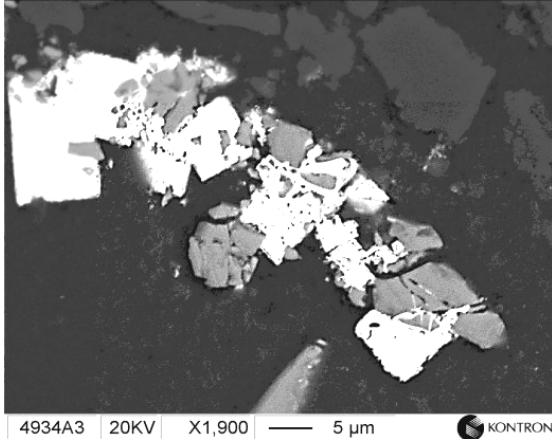


Fig. 37: BSE-photograph of barite (white) replacing pyrite cubes (dark grey) in metarhyolite. Borehole SD49, sample 4934, depth 316.40 m.

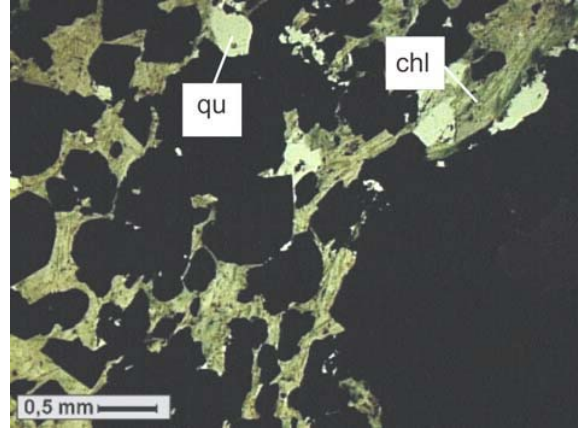


Fig. 38a: Chloritised felsic metavolcanic rock. Borehole SD20, depth 344.92 m. Sample 2037. Microscopic photograph, LLP.

Additionally, the occurrence of garnet-bearing quartz-biotite schists (Fig. 38b & 39) within the felsic metavolcanic rocks could well represent a hydrothermal assemblage, evolved from a quartz-chlorite-sericite assemblage, at higher than lower to middle greenschist facies metamorphism, as it has been reported by Eastoe et al. (1987) from Mt. Read, Tasmania.

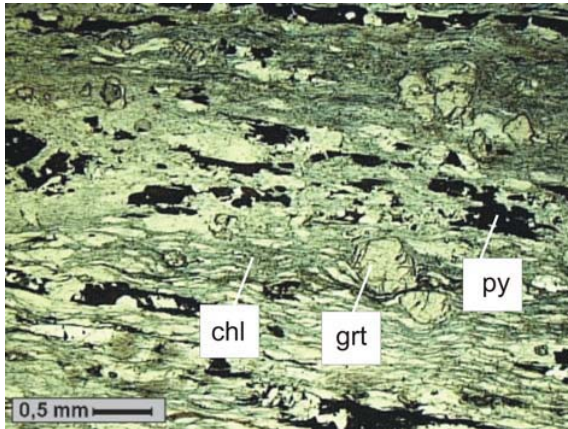


Fig. 38b: Photomicrograph of a thin section showing garnet (grt)-bearing quartz-chlorite (chl)-sericite-schist with disseminated pyrite (py). Borehole SD49, sample 4925, depth 306.00 m.

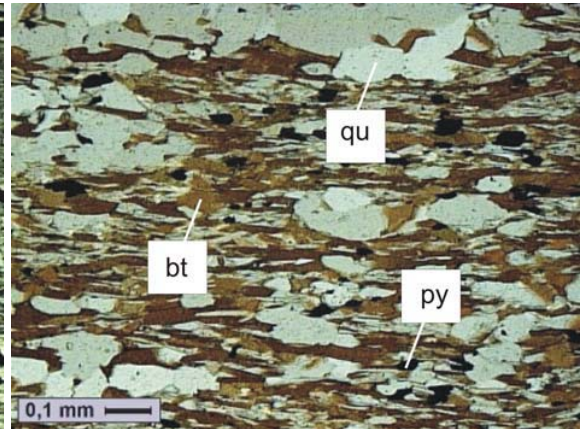


Fig. 39: Photomicrograph of a thin section showing quartz (qu)-biotite (bt)-schist with disseminated pyrite (py). Borehole SD20, sample 2042, depth 349.75 m, XN.

It has been shown above that the Skorpion felsic metavolcanic rocks, both highly supergene altered and least supergene altered, have undergone K metasomatism. Therefore, the loss of some K_2O , which is depicted in the isocon diagram, must be the result of a supergene alteration rather than hydrothermal alteration. There is microscopic evidence that the depletion in K_2O within the highly supergene altered felsic metavolcanic rocks results from potassium feldspar that has been altered to sericite and kaolinite.

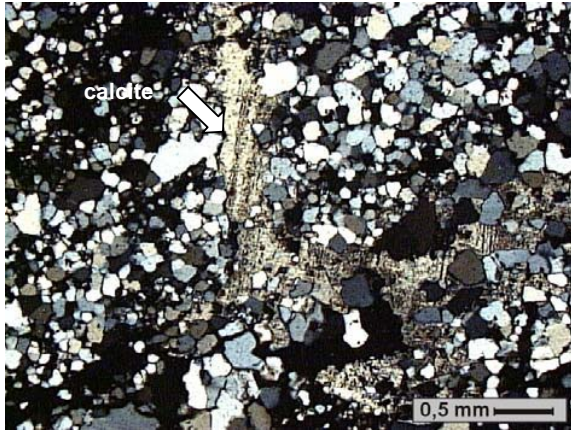


Fig. 40: Photomicrograph of a thin section showing felsic metavolcanic rock with secondary calcite filling voids. Borehole SD49, sample 4934, depth 316.4 m. XN.

Additionally, CaO must have been depleted, since felsic volcanic rocks are likely to contain more than 1 % CaO initially (Ewart 1979). However, both least and highly supergene altered felsic metavolcanic rocks display CaO concentrations averaging out far less than 1 %.

The loss of CaO could have resulted from hydrothermal alteration as shown by Barrett et al. (1993). They reported an important gain of MgO during hydrothermal alteration with a concomitant significant loss of Na₂O and CaO from the footwall rhyolite of the Noranda massive sulphide deposit. A similar gain/loss balance for these elements can be reported from the Skorpion felsic metavolcanic rocks.

Since CaO is depleted in both least and highly supergene altered felsic metavolcanic rocks, the loss of CaO cannot be depicted in the isocon diagram. In fact, the isocon diagram shows a gain of some CaO in the most altered felsic metavolcanic rocks (Tab. 5). Microscopic investigations have shown that the gain in CaO results from secondary calcite that precipitated along fractures or voids (Fig. 40).

The incompatible element plot (Fig. 41) shows that both least and highly supergene altered felsic metavolcanic rocks plot in the same range, indicating relatively inertia of incompatible elements towards chemical weathering and hydrothermal alteration (K metasomatism). Due to the immobile behaviour of the incompatible elements, their ratios can potentially serve as proxy of the geochemical character of the source rock (Tiwary & Deb 1997). Thus, the Ta-Yb tectonic discrimination diagram for granitic rocks of Pearce et al. (1984) gives reliable evidence of the source of the felsic metavolcanic rocks regardless their degrees of alteration (Fig. 42). Accordingly, the felsic metavolcanic rocks have formed in a 'within-plate granite setting', which has already been stated by Borg et al. (2003).

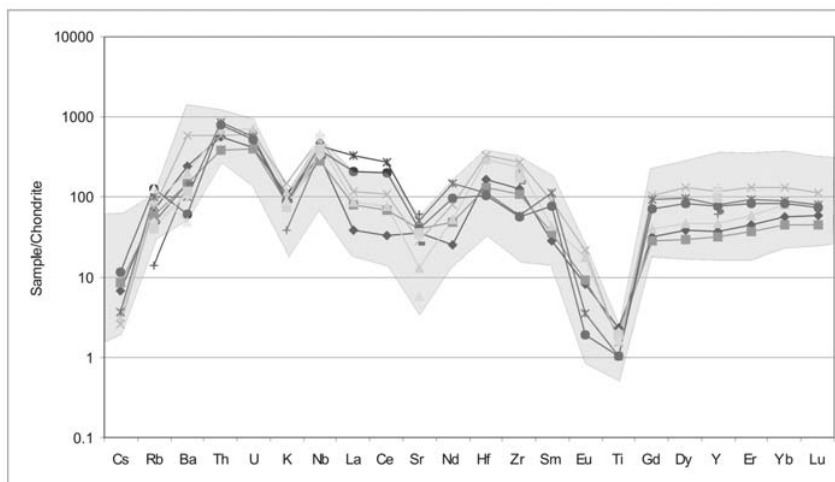


Fig. 41: Chondrite-normalised (Sun & McDonough 1995) spider diagram for fresh/least supergene altered felsic metavolcanic rocks of the Skorpion/Rosh Pinah area. The grey outline shows the distribution of trace elements within the highly altered felsic metavolcanic rocks (*mining terms*: QSS, SSS) of the Skorpion deposit.

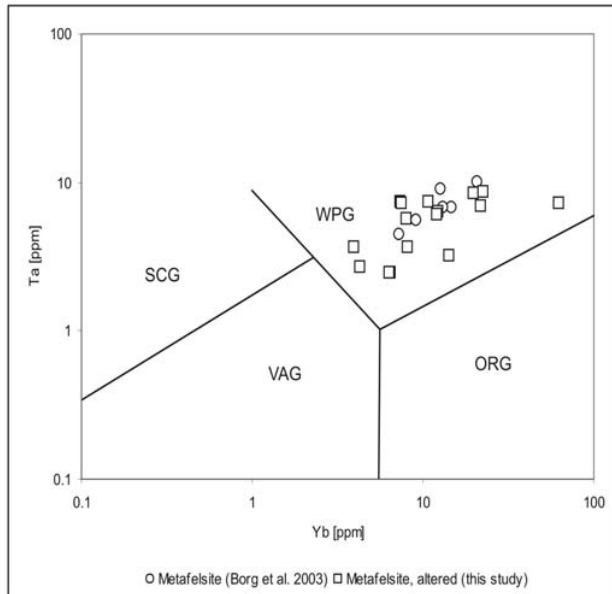


Fig. 42: Ta-Yb tectonic discrimination diagram for granitic rocks of Pearce et al. (1984) showing felsic metavolcanic rocks are from a within plate granite (WPG) setting. SCG = syn-collision granites, VAG = volcanic arc granites, ORG = ocean ridge granites.

The spider diagram in Fig. 41 indicates that REE's have behaved inert towards chemical weathering, and thus supergene alteration. Indeed, the REE patterns of both least supergene altered (Borg et al. 2003) and highly altered felsic metavolcanic rocks are coincident (Fig. 43a). However, the effects of hydrothermal alteration as well as regional metamorphism on REE's (Tiwary & Deb 1997) cannot be discussed as both least and highly supergene altered metavolcanic rocks have undergone hydrothermal alteration and metamorphism and thus possible effects thereof are hampered. The post-metamorphic concentration of REE's within metarhyolite samples from the Skorpion deposit ranges from 20 to 200 times more than that of C1 chondrite. They are characterised by very strong to strong negative Eu anomalies with Eu/Eu^* averaging at 0.21 (range 0.03 – 0.43). These

pronounced negative Eu/Eu^* are very similar to those reported from hydrothermally altered felsic metavolcanic rocks elsewhere (Fig. 43b, Tiwary & Deb 1997).

Robertson & Condie (1989) as well as Tiwary & Deb (1997) reported a considerable LREE/HREE fractionation (Fig. 43b & c) for metamorphosed and hydrothermally altered felsic volcanic rocks, respectively. However, the Skorpion felsic metavolcanic rocks do not display a considerable LREE/HREE fractionation resulting in conspicuously flat profiles except for distinct depletion in Eu (Eu/Eu^*). The least supergene altered samples (Borg et al. 2003) display $[\text{La}/\text{Yb}]_n$ ranging between 1 and 5.3 and averaging at 2.6. The highly supergene altered samples also lack a significant enrichment of LREE over HREE and are characterised by $[\text{La}/\text{Yb}]_n$ ranging between 0.2 and 4, and averaging at 1.8. The lack of a pronounced LREE/HREE fractionation seems to be a regional feature within the Late Proterozoic felsic metavolcanic rocks within the Rosh Pinah and Skorpion areas, as the felsic metavolcanic rocks from the Rosh Pinah area show a similar nonsignificant LREE/HREE fractionation. (Fig. 43d, pers. comm. C. Gauert).

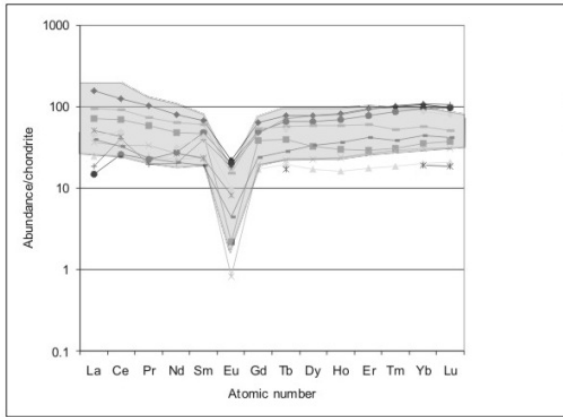


Fig. 43a: Chondrite-normalised (Boynton 1984) REE pattern of supergene altered felsic metavolcanic rocks (*mining terms*: SSS, QSS) compared to their least/non-altered equivalents from the Skorpion area (grey outline, data from Borg et al. 2003).

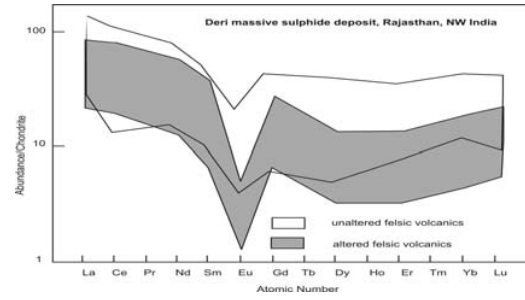


Fig. 43b: Chondrite-normalised REE pattern of unaltered and hydrothermally altered (grey outline) felsic volcanic rocks from a massive sulphide deposit in India. Data from Tiwary & Deb (1997). The wide range of REE concentrations in hydrothermally altered rocks is mainly due to the mass changes during alteration and do not reflect pre-alteration heterogeneity of their magmatic sources (MacLean 1988).

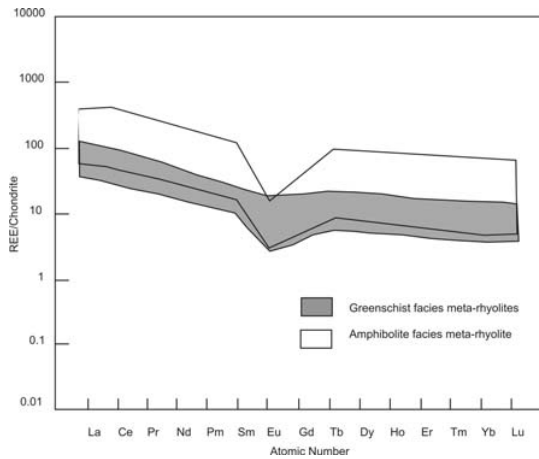


Fig. 43 c: Chondrite-normalised REE pattern of metarhyolites, which have been overprinted by greenschist- and amphibolite facies metamorphism, respectively. Data from Robertson & Condie (1989).

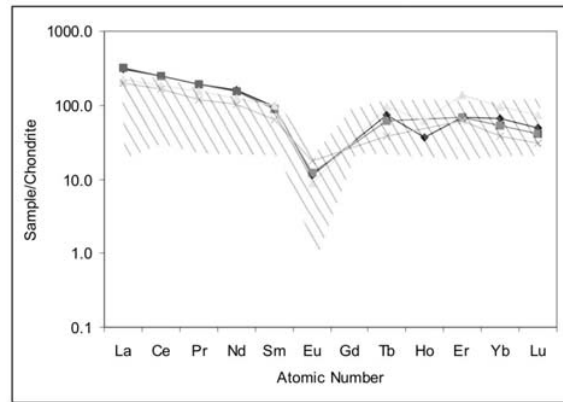


Fig. 43 d: Chondrite-normalised REE pattern (Boynton 1984) of felsic metavolcanic rocks from Spitzkopf (Rosh Pinah area). The shaded area shows the REE distribution within the Skorpion felsic metavolcanic rocks as depicted in Fig. 43a. Data for the Spitzkopf felsic metavolcanic rocks by courtesy of C. Gauert.

The Skorpion felsic metavolcanic rocks and their pyroclastic and hydroclastic equivalents are host to the remnants of the primary sulphide paragenesis with pyrite, sphalerite, minor chalcopyrite and traces of galena. In order to prove the volcanogenic origin of the sulphides an initial sulphur isotope study was carried out on three samples of the felsic metavolcanic unit from the Skorpion footwall rocks. The sulphide isotope composition ranges from +0.7 to 4.0 ‰, and thus averages at 2.7 ‰ (Tab. 6). Indeed, these ^{34}S compositions imply a volcanogenic origin (Rollison 1993) and are very similar to sulphur isotope data from the Iberian Pyrite Belt (Yamamoto et al. 1993), where many polymetallic massive sulphide deposits occur, which are related in space and time to submarine felsic volcanism. From the sulphide-mineralised felsic metavolcanic rocks and their tuffitic equivalents as well as the sulphur isotope signature of the sulphides, these rocks are host to, it can be concluded that the primary hypogene sulphide mineralisation has formed in a proximal to distal volcanic environment.

Tab. 6: Sulphur isotope data of sulphide minerals from the Skorpion felsic metavolcanic host rock.

Sample number	Borehole	Depth [m]	Mineral	$\delta^{34}\text{S}$ (‰, V-CDT)
2018	SD20	288.0	pyrite (in quartz-biotite schist)	+3.5
2034	SD20	337.8	sphalerite (in metarhyolite)	+4.0
2038	SD20	342.44	pyrite (in meta-pyroclastic rock)	+0.7
<i>Average</i>				+2.7

3.5.2.4 Amphibolites

3.5.2.4.1 Petrography



Fig. 44: Photograph of drill core showing a coarse-grained amphibolite from the vicinity of the Skorpion deposit. Borehole UTEM, depth 103.1 m.

Besides the felsic metavolcanic rocks, mafic metavolcanic rocks are found in the form of amphibolites within the Skorpion area (Fig. 44), but also in the footwall of the Skorpion non-sulphide ore body (Fig. 45). Amphibolites from the vicinity of the ore body are commonly slightly weathered or even fresh and usually contain disseminated magnetite (Fig. 46 & 47). Additionally, minor sulphides have been observed in the form of diffuse banded and disseminated pyrrhotite and pyrite, and locally chalcopyrite.

Amphibolites from the footwall of the Skorpion non-sulphide ore body are commonly highly weathered and characterised by a weak to very weak rock strength. They apparently underlie conformably the felsic metavolcanic rocks in the western part of the deposit (Fig. 45). Primary sulphides within these amphibolites are completely oxidised, and thus only pseudomorphs of iron hydroxides after sulphides as well as semi-massive goethites, mainly consisting of iron hydroxides, are found (Fig. 45). The advanced stage of weathering is associated with a change in rock colour from dark to pale green.



Fig. 45: Light-grey, buff to olive amphibolite in drill core from the western part of the Skorpion deposit (borehole SKGT5 (E 2850, N 15925)). Contact metarhyolite (white, tan to red) and amphibolite at 127.31 m. Both rock types are characterised by a strong foliation. The contact between felsic and mafic metavolcanic rocks is gradual.

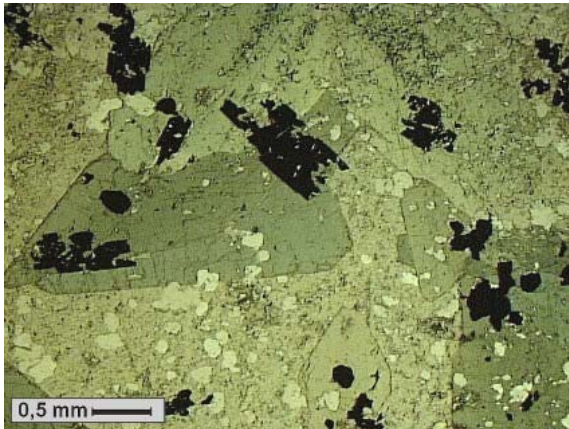


Fig. 46: Photomicrograph of a thin section showing coarse-grained amphibolite from the vicinity of the Skorpion deposit with disseminated magnetite and pyrrhotite. Borehole UTEM, depth 103.31 m. LLP.

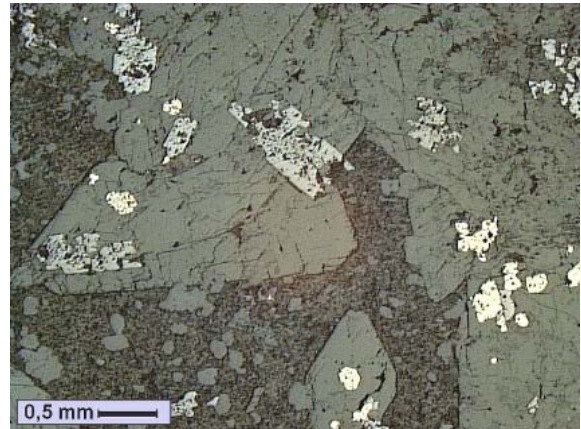


Fig. 47: Same frame as Fig. 46. Reflected light.

3.5.2.4.2 Geochemistry

The geochemistry of the amphibolites in the Skorpion area has been previously investigated by Borg et al. (2003). Additionally, Frimmel (1996a) studied the composition of amphibolites in the Rosh Pinah area. This study revises these data but does not provide new data, as the geochemical research of this study was concentrated mainly on metasedimentary and felsic metavolcanic rocks as they represent the host rocks of the Skorpion sulphide and non-sulphide mineralisations.

The classification of the amphibolites according to their immobile element distribution after Pearce (1996) shows that the amphibolites derived from basalts, which have had a relatively homogeneous composition, discernable by the narrow range of data points (Fig. 48).

Additionally, the mafic metavolcanic rocks plot in the 'within plate' fields of a Zr versus Zr/Y diagram respectively (Fig. 49), which is coincident with the 'within plate' tectonic environment of the felsic metavolcanic rocks (Fig. 42).

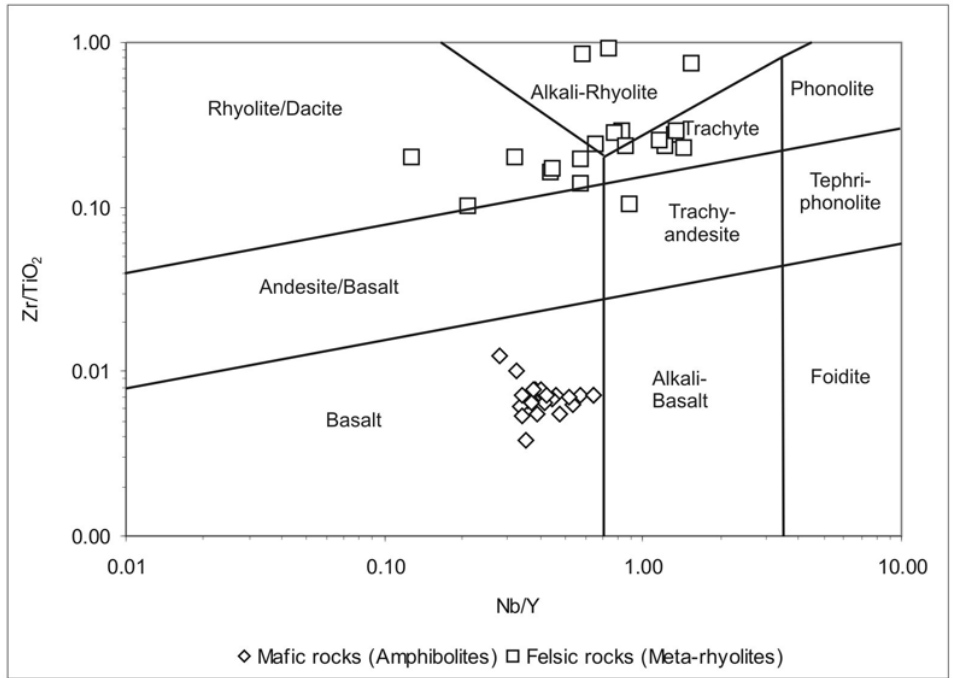


Fig. 48: Classification of mafic and felsic metavolcanic rocks from the Skorpion area according to their immobile element distribution. Classification diagram after Pearce (1996).

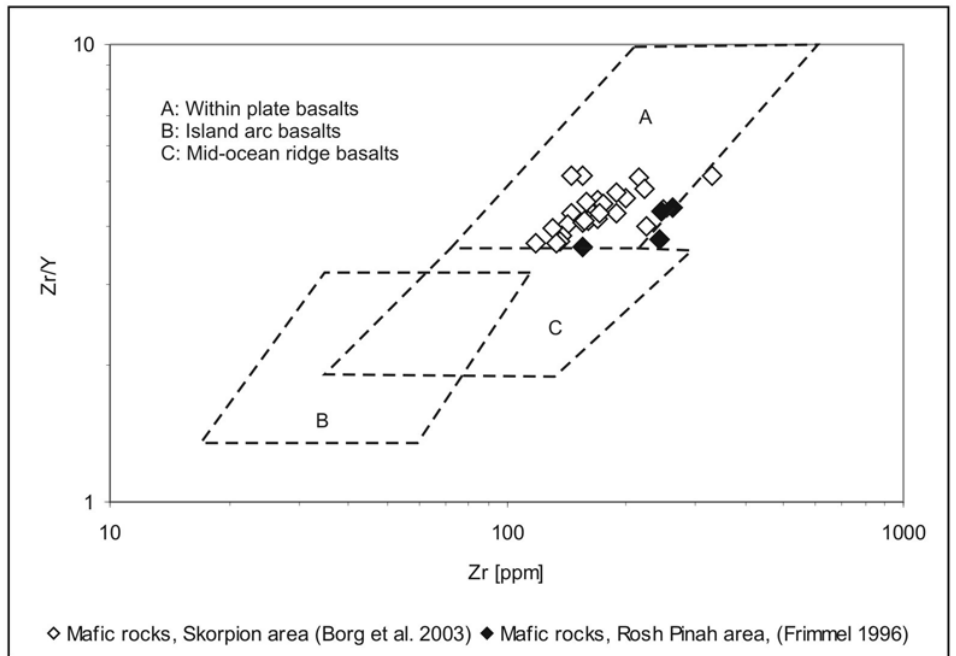


Fig. 49: Zr versus Zr/Y diagram after Pearce & Norry (1979), showing the within-plate tectonic environment of the Skorpion/Rosh Pinah mafic rocks (amphibolites).

The REE patterns of amphibolites from the Skorpion and Rosh Pinah areas are very homogeneous (Fig. 50). They are flat without displaying any significant Eu anomalies ($\text{Eu}/\text{Eu}^* = 0.94$ for samples from the Skorpion area, $\text{Eu}/\text{Eu}^* = 1.05$ for samples from the Rosh Pinah area). They are characterised by a lack of a significant LREE/HREE fractionation featuring $[\text{La}/\text{Yb}]_n$ ratios that average at 2.6 and 2.9 for samples from the Rosh Pinah and Skorpion areas, respectively. Such REE distribution patterns and the concurrent lack of a significant Eu anomaly are typical for amphibolites elsewhere (Fig. 51, Grauch 1991). Fig. 50 also shows that the amphibolites from the Skorpion/Rosh Pinah area are enriched in LREE and HREE compared to MORB compositions, and show LREE concentrations similar to compositions of the upper and lower crust, respectively.

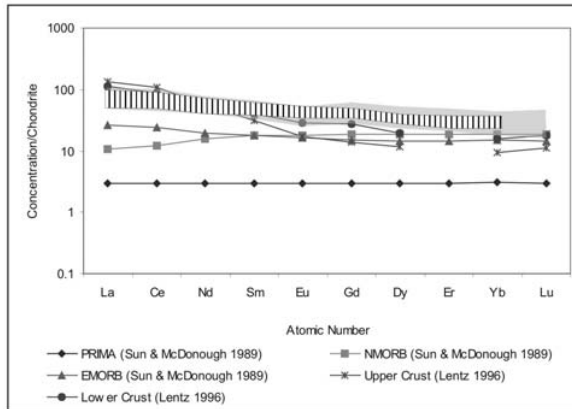


Fig. 50: Chondrite-normalised (Boynton 1984) REE pattern of amphibolite facies basalts from the Skorpion (grey outline, data from Borg et al. 2003) and Rosh Pinah areas (striped outline, data from Frimmel 1996a).

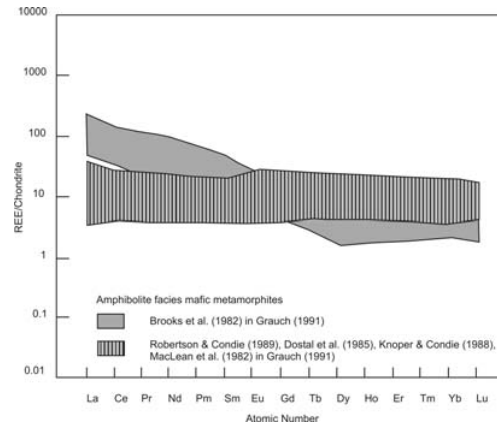


Fig. 51: Chondrite-normalised REE pattern for amphibolite facies mafic metamorphites. Modified after Grauch (1991).

The immobile element plot in Fig. 52 plot shows that the absolute abundances of trace elements in felsic metavolcanic rocks and amphibolites from the Skorpion area overlap. This precludes the possibility that the protolith of the felsic metavolcanic rocks (rhyolite) was derived from fractional crystallisation of the protolith of the amphibolite (basalt) (Barresi & Dostal 2005). Therefore, the Late Proterozoic rhyolites must have had a different source than the basalts. Indeed, the Late Proterozoic within-plate tectonic and magmatic setting is in agreement with the occurrence of two separate magma systems inferring an initial continental rift environment with bimodal volcanism (Barresi & Dostal 2005).

The mafic (basaltic) melts most likely derived from a mantle source and were formed due to decompression melting caused by crustal thinning in the course of rifting. They have ascended along zones of crustal weakness like faults zones. Additionally, the trace element distribution including REE's (Fig. 53) in amphibolites from the Skorpion area indicates that the mafic melts must have been contaminated by crustal material, since the distribution patterns as well as absolute concentrations of trace elements within the amphibolites resemble the composition of continental crust (Fig. 53).

Unlike the mafic magmas, the felsic melts have most likely been generated by heat provided by mafic magmas and subsequent partial melting of the continental crust of the rift flanks. Rift-related faulting might have allowed these magmas to erupt with minimal mixing, which accounts for the bimodality of the volcanic suite (Barresi & Dostal 2005).

Zr vs. Hf- and Ce vs. Nd-plots were used by Tiwary & Deb (1997) in order to determine the origin of felsic magmas. They concluded that a constancy of these incompatible element

ratios in rocks from basalt through andesite to rhyolite suggests a formation of felsic magmas by fractional crystallisation of the parental mafic magma. Skorpion's metavolcanic rocks, however, do not show these fractionation trends; they either form individual population trends (Fig. 54) or show interfering populations (Fig. 55). Therefore, a formation of the felsic magmas by fractional crystallisation of mafic magmas is precluded, which is in agreement with the inferred genetic relationship to continental rifting.

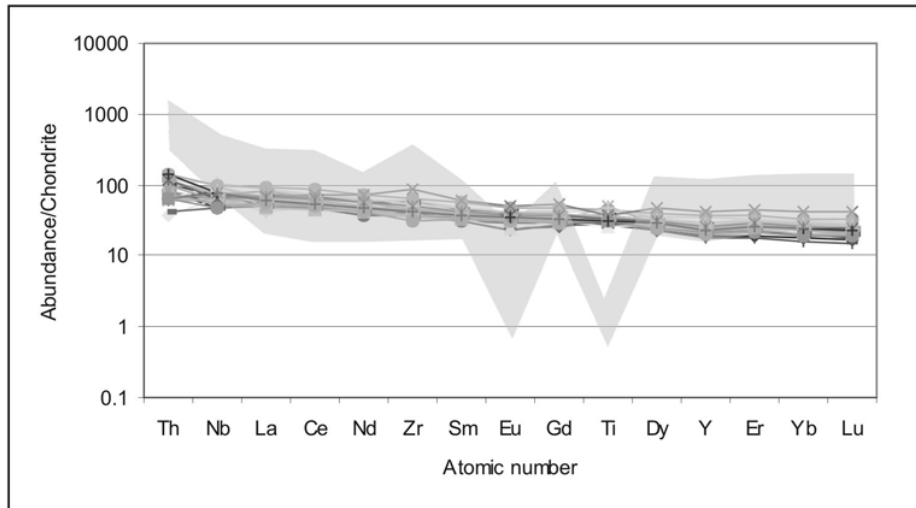


Fig. 52: Chondrite-normalised (Sun & McDonough 1995) immobile element plot showing the overlap in element concentrations for mafic (amphibolites) and felsic (metarhyolites) rocks (grey outline). Amphibolite data from Borg et al. (2003).

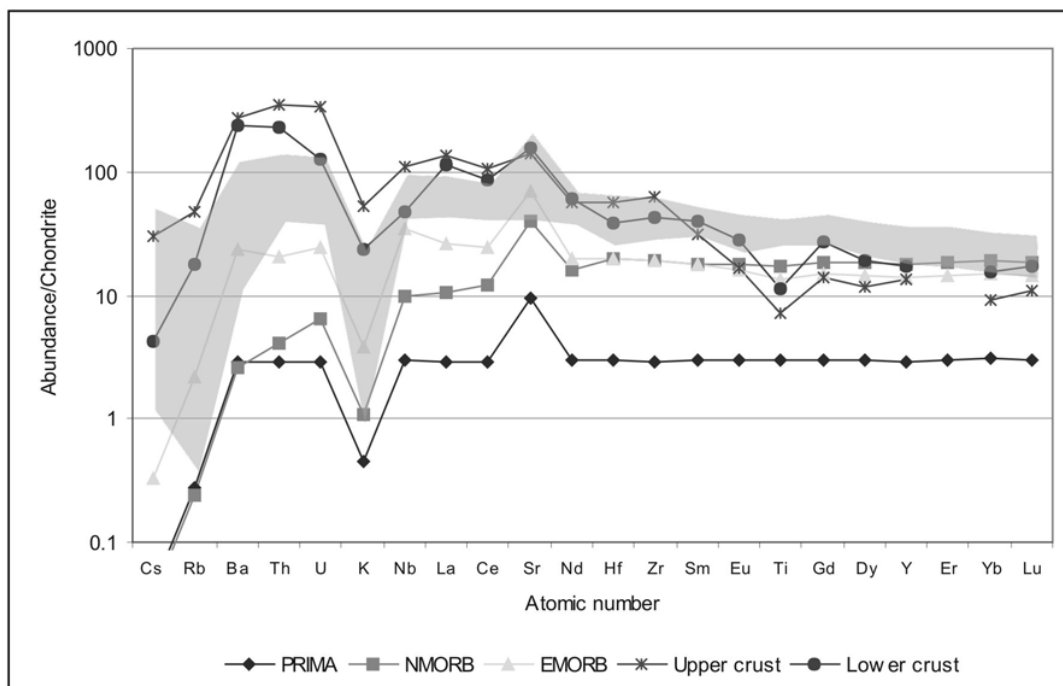


Fig. 53: Chondrite-normalised (Sun & McDonough 1995) spider diagram for amphibolites of the Skorpion area (grey outline). Distribution of trace elements in PRIMAs (Sun & McDonough 1995), MORBs (Sun & McDonough 1995), and continental crust (Lentz 1996) are given for comparison.

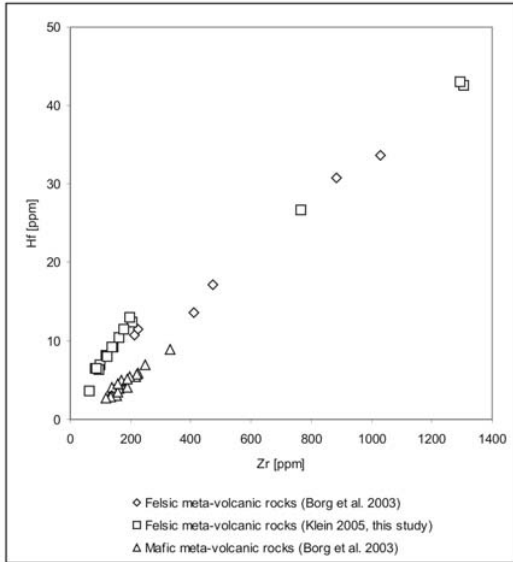


Fig. 54: Zr versus Hf plot. Note the different populations of felsic and mafic metavolcanic rocks. Individual populations are characterised by near-perfect linear trends.

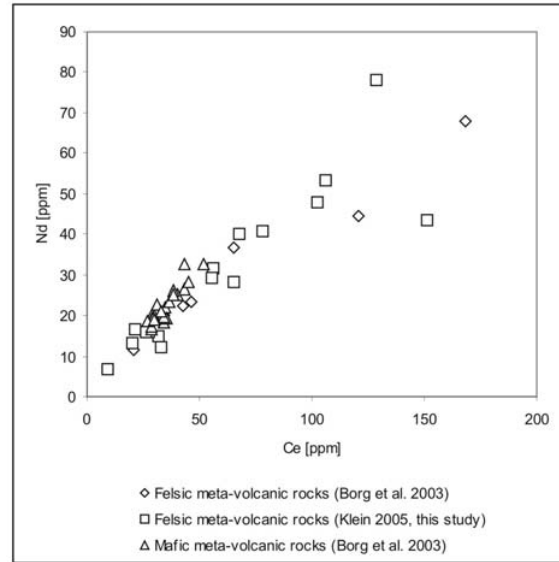


Fig. 55: Ce versus Nd plot. Crosscutting trends. However, individual populations show moderate linear trends.

3.5.2.5 Metasiliciclastic Rocks

3.5.2.5.1 Petrography

The siliciclastic metasediments, which will be discussed in the following chapter, are host to the major portion of the non-sulphide ore body. Although they have been affected by regional metamorphism and deformation, sedimentary structures can be identified. Macroscopic structures, which are considered to be primarily sedimentary in origin, include planar laminations/bedding, graded bedding, and slump structures (soft sediment deformation).

Additionally, the metasediments are highly brecciated in places. Some of these breccias are of sedimentary origin; they are usually matrix-supported and contain angular to subrounded sedimentary breccia clasts that display a polymict composition. However, the majority of the breccias is most likely of tectonic origin. The tectonic breccias are commonly clast-supported. The angular breccia clasts feature a monomict composition and display jigsaw textures in places (Fig. 56 & 57). The tectonic breccias pre-date the mineralising supergene event, which can be concluded from the fact that non-sulphide minerals, e.g. smithsonite, are found replacing both breccia matrix and breccia clasts (Fig. 56 – 57). The breccias are generally well mineralised, probably resulting from the higher permeability, which was provided by the brecciation.



Fig. 56: Smithsonite/sauconite-mineralised breccia. The breccia is most likely of tectonic origin (brittle ductile shear zone); since jig saw texture can be seen. Non-sulphide zinc mineralisation post-dates the breccia formation, as zinc-bearing are found in both breccia clasts and matrix. Breccia clasts consists of metasubarkose, borehole BH 70, sample BH7007, depth 59.8 m.



Fig. 57: Same picture of drill core as Fig. 56. A zinc indicator solution, which turns red, reacting to zinc-bearing minerals, was used in order to set off the unobtrusive non-sulphide zinc mineralisation. The red colour indicates more than 20 % Zn.

A third type of breccias that occur at the Skorpion deposit are solution collapse breccias. These breccias are monomict composed and contain subangular breccia clasts. They were formed when groundwater migrated through the mainly calcitic cemented metasediments, dissolving the calcitic cement and causing chunks of rock to fall into caves or open spaces. The breccia matrix commonly contains non-sulphide minerals. Typical mineralisation styles include the crystal growing in open spaces, displaying a colloform texture. At least some of the solution collapse breccias post-date the earlier stages of supergene non-sulphide mineralisation, since breccias were found containing different styles of non-sulphide mineralisation in breccia matrix and breccia clasts (Fig. 58 & 59).



Fig. 58: Solution-collapse breccia. Smithsonite-impregnated breccia clasts are cemented by green tarbuttite and dark-grey colloform chalcophanite. Surface sample (15 x 15 cm), Skorpion open pit, 645 m level.



Fig. 59: Solution-collapse breccia. Smithsonite-impregnated breccia clasts are cemented by white scholzite. Surface sample (15 x 15 cm), Skorpion open pit, 645 m level.

The tan- to orange coloured, but also grey psammitic siliciclastic metasediments are fine- to medium- (0.05 – 0.1 mm), locally coarse-grained and are commonly poorly to moderately sorted (Fig. 60 – 64). The detrital material consists mainly of quartz and potassium feldspar, minor sodium feldspar and traces of apatite. The matrix takes up between 10 and 50 volume % and consists mainly of calcite (Fig. 65 – 66) and sericite. However, within the mineralised metasediments, the matrix contains the zinc-bearing ore minerals consisting mainly of sauconite (Fig. 67 – 68), smithsonite, and minor hemimorphite. Calcite has not been found in the mineralised metasediments. The psammitic metasediments are typically thinly bedded to bedded or massive (Fig. 60). They are characterised by an extremely weak to weak rock strength, which results from their advanced weathering stage. Secondary deformation features include foliation, which is typically vague to moderately well developed. The psammitic metasediments are mined as 'arkoses' (ARK) and represent the major portion of the siliciclastic metasediments.



Fig. 60: Photograph of drill core from the western part of the Skorpion deposit showing weakly foliated tan to orange psammitic meta-arkoses. Manganese and iron hydroxides are found along the foliation planes. Borehole SKGT11 (E 2700.5, N 16152), depth 29.53 – 36.74 m, mining term 'arkose'.



Fig. 61: Coarse-grained meta-arkose with disseminated goethite. Borehole SD20, depth 70.0 m, length of drill core 15 cm.



Fig. 62: Close-up of Fig. 61. Zn-indicator solution 'Zinc Zap' turns light-orange indicating a zinc concentration of about 5 % Zn. Length of drill core is about 6 cm.



Fig. 63: Foliated saumonite-mineralised metasubarkose (K-feldspar-bearing quartz-sericite schist). Sample BH7001, borehole BH70, depth 26.90 m.



Fig. 64: Same drill core as Fig. 63. Zn-indicator solution 'Zinc Zap' turns blood-red indicating more than 20 % Zn.

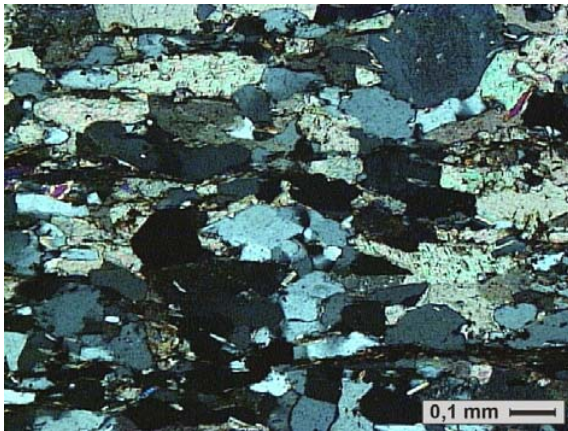


Fig. 65: Photomicrograph of a thin section showing a poorly cleaved metasandstone. Detrital quartz as well as grains of calcite cement are elongated. Sample 3906, borehole SD39, depth 76.55 m. LLP.

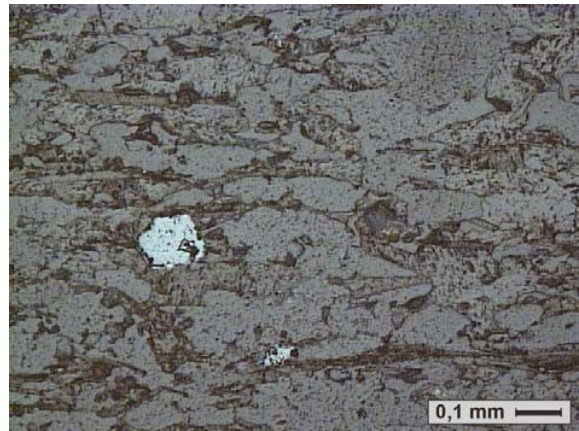


Fig. 66: Same frame as Fig. 65 under reflected light showing the occurrence of disseminated iron hydroxides (light-grey).

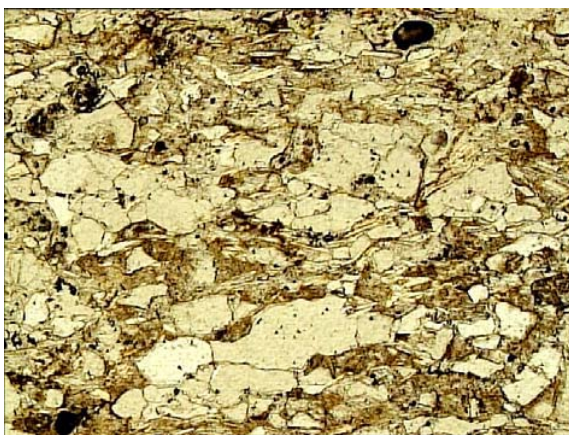


Fig. 67: Photomicrograph of a thin section showing a foliated saumonite-mineralised metasubarkose. Sample BH7001, BH70, depth 26.09 m. LLP. 1 cm = 0.1 mm.

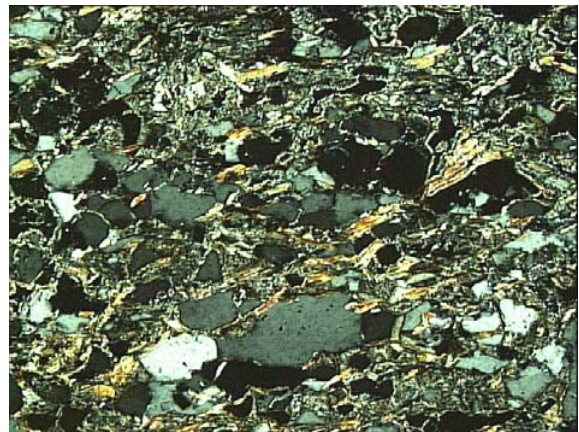


Fig. 68: Same frame as Fig. 67 under XP. Saumonite fills intragranular pore space. Sample BH7001, borehole BH70, depth 26.09 m. XP. 1 cm = 0.1 mm.

In order to classify the psammitic metasediments petrographically, the $\log \text{Fe}_2\text{O}_3/\text{K}_2\text{O}$ vs. $\log \text{SiO}_2/\text{Al}_2\text{O}_3$ (Herron 1988, Pettijohn et al. 1972) has been used (Fig. 69). Regional samples of siliciclastic metasediments are plotted for comparison, since the metasediments that host the non-sulphide ore body are highly weathered and thus do not display their original composition. The regional samples, which were taken some kilometers west and southwest of the Skorpion deposit (App. 1, map 2 – 4), plot mainly within the field of arkoses. However, metasediments from the Skorpion deposit plot mainly in the field of wackes as a result of their advanced stage of weathering, which led to an enrichment of Al_2O_3 and Fe_2O_3 . The gain and loss of major and trace elements will be discussed separately in detail. Higher amounts of aluminium shifted the Skorpion metasediments to the field of wackes. Still, the least altered metasediments from the Skorpion deposit plot within the field of arkoses. Therefore, it is reasonable to assume that the highly altered equivalents have originally had an arkosic composition as well. This classification is coincident with results from metasediments of the Rosh Pinah area, where metasediments also consist mainly of meta-arkoses (pers. comm. C. Gauert).

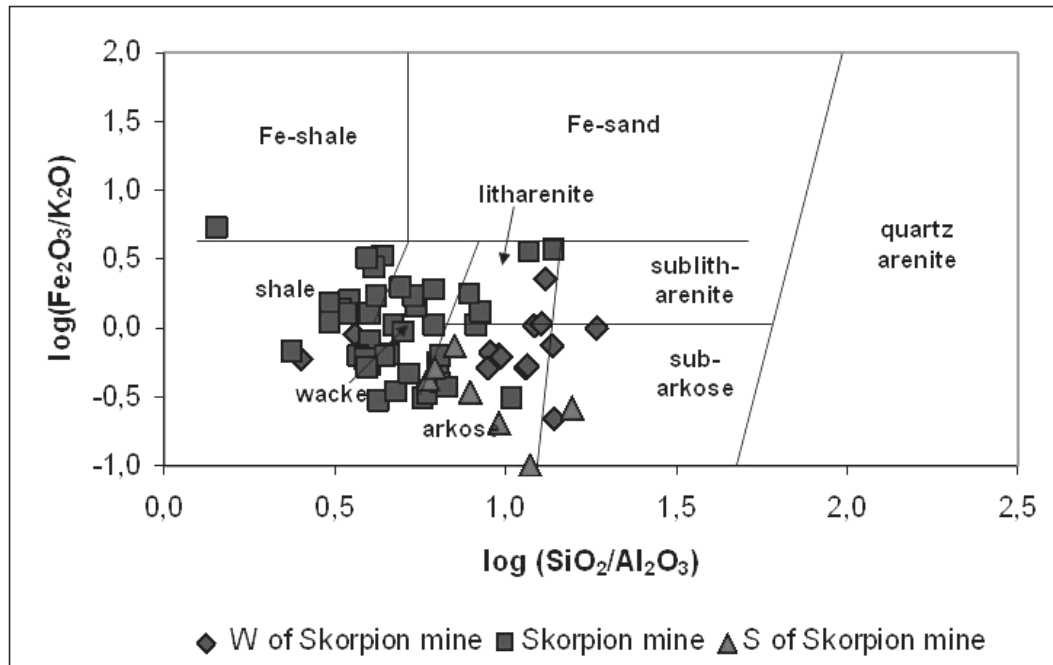


Fig. 69: The classification of metasiliciclastic host rocks (rectangle) using $\log(\text{Fe}_2\text{O}_3/\text{K}_2\text{O})$ vs. $\log(\text{SiO}_2/\text{Al}_2\text{O}_3)$ by Herron (1988) after Pettijohn et al. (1972). Samples of metasiliciclastic rocks from the vicinity of the ore body are depicted for comparison (triangle, diamond).

In addition to the dominant psammitic meta-arkoses, semipelitic to pelitic siliciclastic metasediments, locally with psammitic intercalations, occur within the metasedimentary pile of the Skorpion deposit. The so-called 'banded shale and arkose' unit, mining term BSA, is laminated to very thinly bedded (Fig. 70). The light-grey, white and black laminated, but also medium to dark-grey, tan to orange and red brown metasediments are very fine to fine grained, and contain only locally medium- to coarse-grained material. Additionally, they are characterised by a well-developed foliation and an extremely weak to very weak rock strength due to the advanced stage of weathering.



Fig. 70: Photograph of drill core from the western part of the Skorpion deposit showing semipelitic siliciclastic metasediment with psammitic intercalations. Borehole SKGT2 (E 2689.5, N 16000), depth 19.38 to 26.77 m.

There are also macroscopic and microscopic petrographic constraints, which support that some of the metasediments were derived from volcanic activity. Lack of coarser-grained fragments and absence of sedimentary features such as cross-bedding or slump structures are typical features of tuffaceous ashfall deposits of distal volcanic origin (Floyd & Winchester 1978). Indeed, the possible occurrence of ashfall deposits at the Skorpion deposit is in agreement with the inferred Late Proterozoic near-shore setting for the deposition of the siliciclastic sediments containing both proximal and distal volcanic deposits (Alchin et al. 2005).

3.5.2.5.2 Geochemistry

The distribution of major elements within the meta-arkoses allows a petrographic classification, which was presented in the previous chapter (Fig. 69). Additionally, the major elements can be used to describe the stage of supergene alteration. The chemical index of alteration (CIA, Nesbitt & Young 1982, 1989) has been applied in order to prove the higher degree of weathering of the Skorpion meta-arkoses, and thus supergene alteration, compared to the meta-arkoses in the wider Skorpion area. The CIA is calculated as $CIA = [Al_2O_3 / (Al_2O_3 + CaO + Na_2O + K_2O)] \times 100$, where Ca denotes the calcium content of the terrigenous fraction of the sample (Nesbitt & Young 1982). However, within the Skorpion meta-arkoses calcium is mainly incorporated in calcite, which forms the cement. Thus, the CIA monitors the progressive alteration of plagioclase and potassium feldspars to clay minerals, but also the alteration and dissolution of calcite. However, it must be stressed that the CIA is burdened with some uncertainty due to the heterogeneity of both metasiliciclastic host and wall rocks. Additionally, local redistribution of elements during the weathering process and a subsequent precipitation of supergene minerals, e.g. Ca and calcite, can distort the CIA values. Therefore, not all samples of meta-arkoses were suitable for CIA calculations. In spite of these limitations, the CIA values of the siliciclastic metasediments give evidence of the degree of weathering. High CIA values reflect the removal of mobile cations (e.g. Ca^{2+} , Na^+ , K^+) relative to stable residual constituents (Al^{3+} , Ti^{4+}) during weathering (Nesbitt & Young 1982).

The least weathered meta-arkoses occur in a distance from the Skorpion non-sulphide ore body. Their CIA values average at 53 (range 51 – 56), which indicate a low degree of weathering (Nesbitt & Young 1982, Slack & Höy 2000). In contrast, CIA values of the meta-arkoses that host the non-sulphide ore body average at 63 (range 53 – 85), and have therefore undergone moderate chemical weathering (Nesbitt & Young 1982). The general modest degree of weathering is mineralogically supported by the occurrence of smectite in the metasediment matrix, which is represented by sauconite. In fact, sauconite makes up a significant portion of the supergene ore body. Smectite, and thus sauconite would be destroyed under strong chemical weathering conditions (Nesbitt & Young 1982).

However, some samples also show evidence of strong chemical weathering and are highly altered. Their CIA values average at 75, but ranging from 58 – 97. These samples are mainly composed of kaolinite, quartz, and iron hydroxides and thus form the gossaneous iron-rich part of the Skorpion deposit.

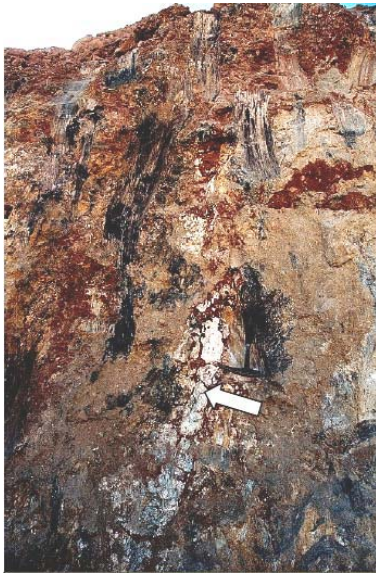


Fig. 71: Photograph showing the uppermost part of meta-arkoses in the Skorpion open pit. Meta-arkoses are fractured and brecciated. Fractures are partly filled by white kaolinite (arrow).

Fluctuations in CIA values in both moderate and highly weathered rocks results most likely from the heterogeneity of the metasediments. Heterogeneity is associated with different porosity and permeability properties, which cause variations in the fluid through-flow (Velde 1984). Fractured zones and fissures are characterised by a variable and intermittent fluid content, which is generally higher than in the surrounding sediment. The increased water/rock ratios in those zones can enhance the process and the degree of weathering. Thus, it is likely to find kaolinite and gibbsite in these oxidised zones, rather than smectites (Velde 1984). Indeed, brecciated meta-arkoses with kaolinite-filled fractures are exposed in the Skorpion open pit (Fig. 71).

The triangular plot in Fig. 72 shows that two alteration trends are recognisable within the siliciclastic metasediments. These proposed alteration trends are in agreement with microscopical observations. Alteration trend I, and thus loss of Ca results from the dissolution of calcite cements during the supergene weathering. Additionally, the Skorpion meta-arkoses have lost significant amounts of Na and K, mainly due to the breakdown of plagioclase and orthoclase. The breakdown of feldspars is depicted as alteration trend II in Fig. 72.

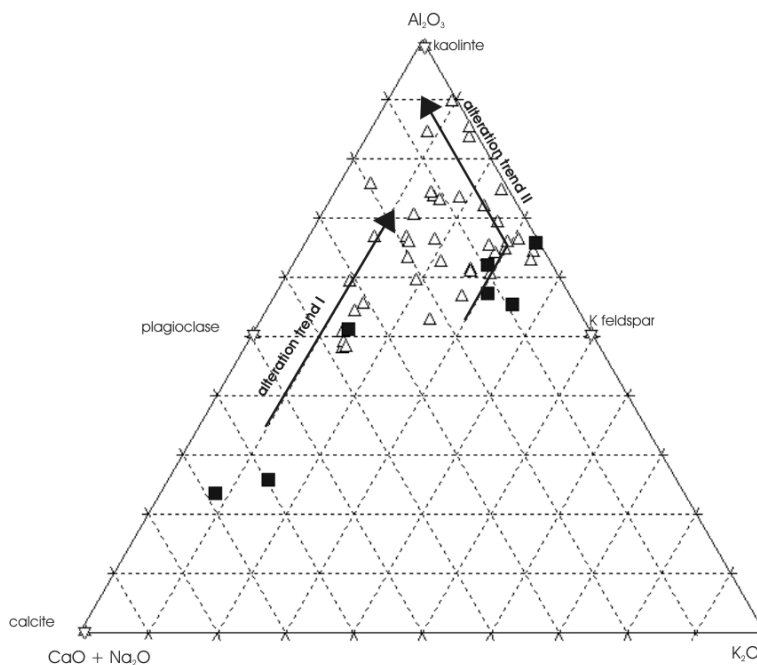


Fig. 72: Triangular $Na_2O + CaO - Al_2O_3 - K_2O$ plot (Nesbitt & Young 1989) showing two different alteration trends within the Skorpion metasediments. Alteration trend I results from the dissolution of calcite cement, whereas alteration trend II results from the dissolution of orthoclase and minor plagioclase. Triangle = Skorpion meta-arkoses, rectangle = meta-arkoses from the wider Skorpion area.

The quantitative loss of mobile elements, e.g. Ca, Na, and K during weathering and supergene alteration can be calculated by using the 'isocon'-diagram after Grant (1986). The fundamentals of this diagram have been described in Chapter 3.5.2.3.2 and are not repeated at this point.

The 'isocon' diagram for the Skorpion meta-arkoses is shown in Fig. 73. The least supergene altered metasediments are represented by meta-arkoses from the wider Skorpion area, whereas the highly altered metasediments are represented by the Skorpion meta-arkoses that are host to the non-sulphide ore body.

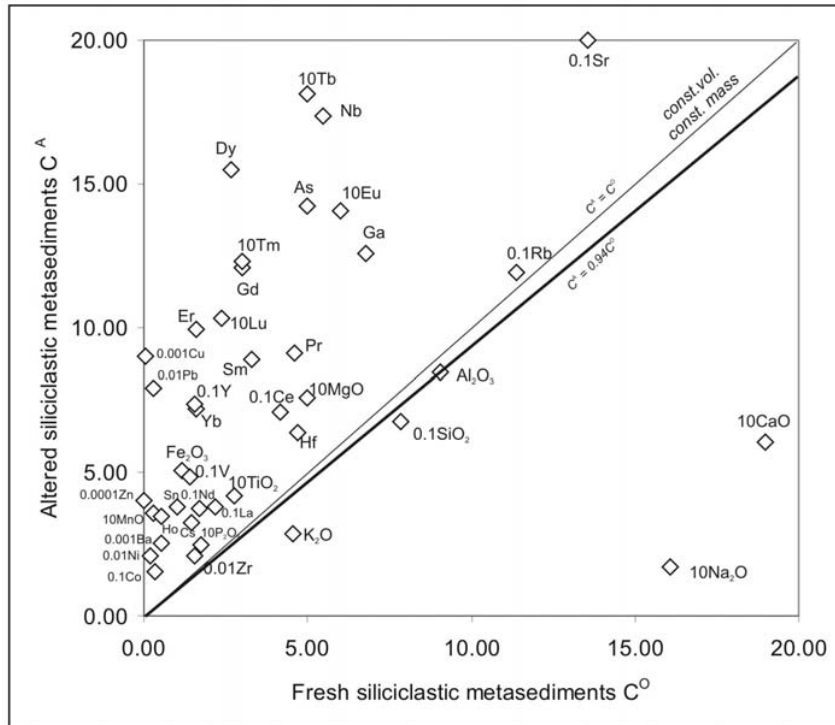


Fig. 73: Isocon diagram for average analyses of least altered siliciclastic metasediments from the wider Skorpion area ($n=6$) and supergene altered siliciclastic metasediments from the Skorpion deposit ($n=28$). Oxides are plotted in weight percent, elements in ppm. Data were plotted in a range from 0 to 20 wt % and 0 to 20 ppm. Components whose concentrations were not accommodated comfortably were scaled. Isocons are shown according to hypotheses of constant alumina, constant mass, and constant volume.

Tab. 7: Concentration changes in supergene altered siliciclastic metasediments corresponding to two model isocons. Calculation according to Grant (1986).

	SiO ₂	Al ₂ O ₃	Fe ₂ O ₃	MnO	MgO	CaO	Na ₂ O	K ₂ O	TiO ₂	P ₂ O ₅
$\Delta C_i/C_i^O$, if $C^A = C^O$	-0.14	-0.06	+3.35	+11.75	+0.52	-0.68	-0.89	-0.37	0.51	0.44
$\Delta C_i/C_i^O$, if $C^A = 0.936C^O$	-0.08	0	+3.65	+12.62	+0.62	-0.66	-0.89	-0.33	0.62	0.55

Generally, chemical elements can be divided into two groups, immobile and mobile, according to their behaviour during weathering. Elements that are immobile during weathering are Zr, Hf, Fe, Al, Th, Nb, Sc, and the REE. Very mobile are Ca, Na, P, K, Sr, Ba, Rb, Mg and Si (Middelburg et al. 1988). Indeed, the CIA has shown that the highly altered meta-arkoses are depleted in Na₂O, K₂O, and CaO. The isocon diagram gives quantitative evidence of the

mobility of these elements and shows that 89 mass % of Na_2O , 66 mass % of CaO and 33 mass % of K_2O were lost during the supergene alteration (Tab. 7). Petrographic studies have shown that the mobile elements must have released and dissolved mainly from leachable minerals such as feldspar, calcite, micas and apatite, since these minerals are only rarely preserved. Regarding the feldspars, orthoclase, which is more resistant to the weathering than plagioclase, is commonly only partly dissolved and looks even fresh in places. The lack of a positive correlation between of, K_2O with Al_2O_3 (Fig. 74) and Na_2O with Al_2O_3 (Fig. 75), respectively, also shows that feldspars have been widely dissolved, which is in agreement with the microscopic observations.

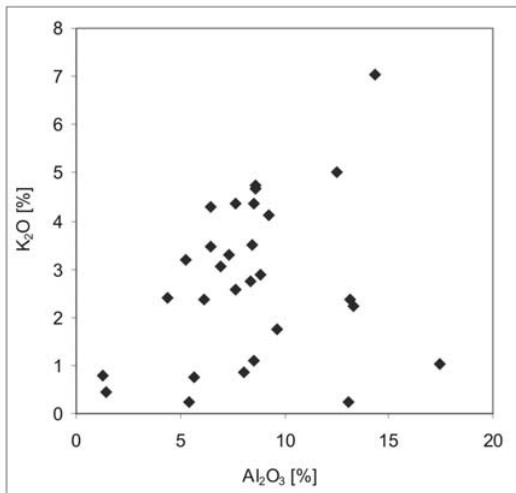


Fig. 74: The binary plot shows a very weak correlation of K_2O with Al_2O_3 , suggesting that K feldspars have been partly dissolved.

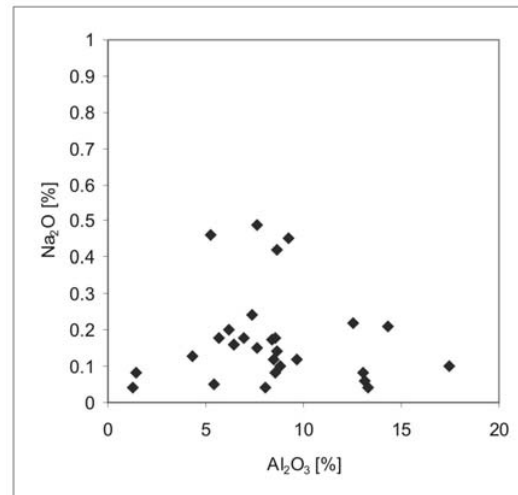


Fig. 75: The binary plot shows no correlation of Na_2O with Al_2O_3 , suggesting that Na feldspars have been almost completely dissolved.

Microscopic investigations have shown that the low CaO concentration within the highly altered meta-arkoses results from the dissolution of calcite cements. Calcite cement can only be seen in the least altered meta-arkoses in the vicinity of the Skorpion ore body, but has almost completely been dissolved from the meta-arkoses that host the ore body. Additionally, minor calcium has been released by the dissolution of detrital apatite from the metasediments.

Although Mg also belongs to the group of the mobile elements, MgO shows a mass gain of 62 mass %. The increase of MgO within the altered meta-arkoses can be best explained by the incorporation of Mg in the octahedral sites of the smectite lattice, as electron microprobe analyses have shown that sauconite contains between 0.33 and 0.85 % MgO averaging at 0.4 MgO . Additionally, MgO has been found as a minor constituent in smithsonite up to 0.14 %.

The general mobile-behaving elements phosphorus and barium (Middelburg et al. 1988) are also enriched in the supergene Skorpion altered meta-arkoses, thus indicating that some secondary precipitation of these elements must have occurred. Petrographic studies give evidence for phosphorous being released by the dissolution of apatite, and subsequently precipitated as secondary phosphate minerals or incorporated into the sauconite lattice. Barium has been most likely released from the dissolution of orthoclase, since SEM-EDX analyses have shown that orthoclase contains barium, averaging at 0.6 %. Additionally,

microscopic observations show that barium has been precipitated as secondary barite in intergranular pore space of both felsic metavolcanic and metasedimentary host rocks.

From the elements, named as immobile according to Middelburg et al. (1988), the following are concentrated in the highly altered meta-arkoses and are therefore considered to have behaved immobile during the supergene alteration: Fe, Hf, Nb, and REE, but also Mn and Ti. Especially, Mn and Fe are highly concentrated in the altered meta-arkoses, in which they occur as iron and manganese oxides and form extensive gossaneous zones. These gossaneous zones will be discussed separately.

Petrographic work has shown that Ti occurs mainly as titanite. It is generally not resident in clays, since there is no positive correlation between TiO_2 and Al_2O_3 , (Fig. 76). Electron microprobe analyses of sauconite confirmed that Ti is not incorporated in the clay mineral lattice. Therefore, it has to be presumed that the variable TiO_2/Al_2O_3 ratios depicted in Fig. 76 reflect a variable detrital (e.g. titanite) component (Conly et al. 2000).

Variations in REE and Y abundances in siliciclastic metasediments are not only dependent of the degree of weathering and alteration, but also strongly dependent on proportions of sand to clay in the original sediment (Condie 1991). LREE, middle REE, and Y occur preferentially in the fine-grained clay- and silt-sized fraction (Cullers et al. 1979), whereas HREE are dominantly in the sand-sized fraction (e.g. McLennan 1989, Condie 1991, Caggianelli et al. 1992). Thus, the strong positive correlation of sum REE's, which mainly includes LREE and middle REE, with Al_2O_3 in certain range of concentrations as depicted in Fig. 77, suggests that REE's were incorporated into clay minerals (Schandl et al. 2000), e.g. sauconite, which have formed by the weathering of mica and feldspar. However, at elevated absolute concentrations of REE's and Al_2O_3 no positive correlation can be found indicating the occurrence of individual REE minerals rather than REE-bearing clays. Indeed, SEM-EDX studies on highly supergene altered gossaneous metasediments have proven the occurrence of REE minerals like monazite and xenotime.

The isocon diagram also shows that the slope of the constant alumina isocon is about 0.94, corresponding to a volume increase of 6 % (Fig. 73). The increase of volume might well be the result of a simple hydration process, which is commonly observed in weathering profiles (Osterberg 1985, Middelburg et al. 1988). The formation of supergene clays (smectites), hydrosilicates and –carbonates at the Skorpion deposit, which are represented by the main ore minerals sauconite, hemimorphite, and hydrozincite, has most likely led to the increase of volume since all of these supergene minerals contain structural OH-groups, which not only significantly increase the amount of bound water in the host rocks but also the volume.

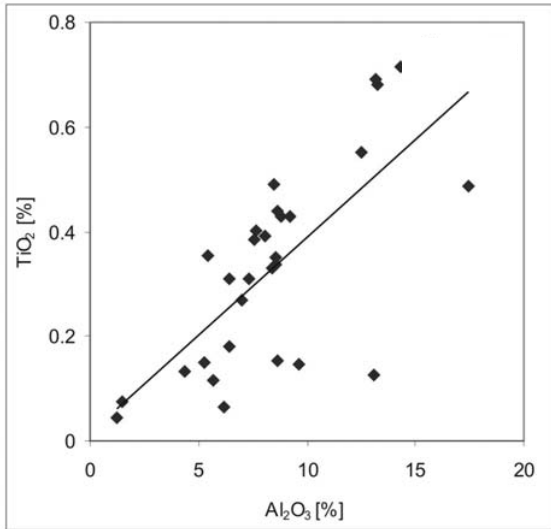


Fig. 76: Binary plot showing that there is no correlation between TiO_2 with Al_2O_3 suggesting that TiO_2 is mainly incorporated in a detrital mineral phase.

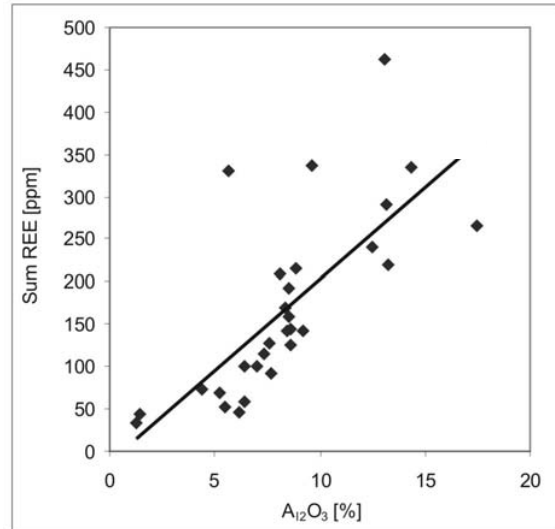


Fig. 77: The binary plot shows that there is a moderate positive correlation between Sum REE (La, Ce, Nd, Sm, Eu, Tb, Yb, and Lu) with Al_2O_3 in a certain range of concentrations, suggesting that these elements were preferentially incorporated into the clay fraction. A lack of correlation at higher concentrations points to the occurrence of REE minerals, e.g. monazite.

As the isocon diagram has shown (Fig. 73), both LREE and HREE are concentrated in the highly altered meta-arkoses indicating that they were enriched during supergene weathering. Bierlein (1995) demonstrated that primary REE distributions remained essentially unchanged, despite multiphase deformation and amphibolite grade metamorphism. Variable trends of preferential REE mobilisation are observed only where large amounts of fluid caused the rock to undergo strong retrogression and/or hydrothermal alteration. Therefore, it is generally agreed that pre-existing REE signatures remain unchanged during metamorphism (Leshner et al. 1986, Michard & Albarède 1986, Bau 1991, Bierlein 1995). However, REE's can well be mobilised or fractionated during advanced stages of weathering, but not during initial or moderate stages of weathering (Middelburg et al. 1988, Nesbitt 1979). This fractionation is caused by selective leaching of rocks composed of both stable and unstable minerals containing REE's (Middelburg et al. 1988). Once the REE's are in solution, an increase of pH can result in that the REE's come out of solution, precipitated as compounds, exchanged for H^+ on suitable clays or adsorbed on mineral surfaces. However, REE's are primarily recycled within the weathering profile rather than transported significant distances in solution (Nesbitt 1979).

The CIA values for the siliciclastic metasediments from the Skorpion deposit have been described above and indicate that the Skorpion meta-arkoses have undergone moderate to strong weathering. Thus, alternated REE patterns, which indicate an enrichment of REE's, can be expected.

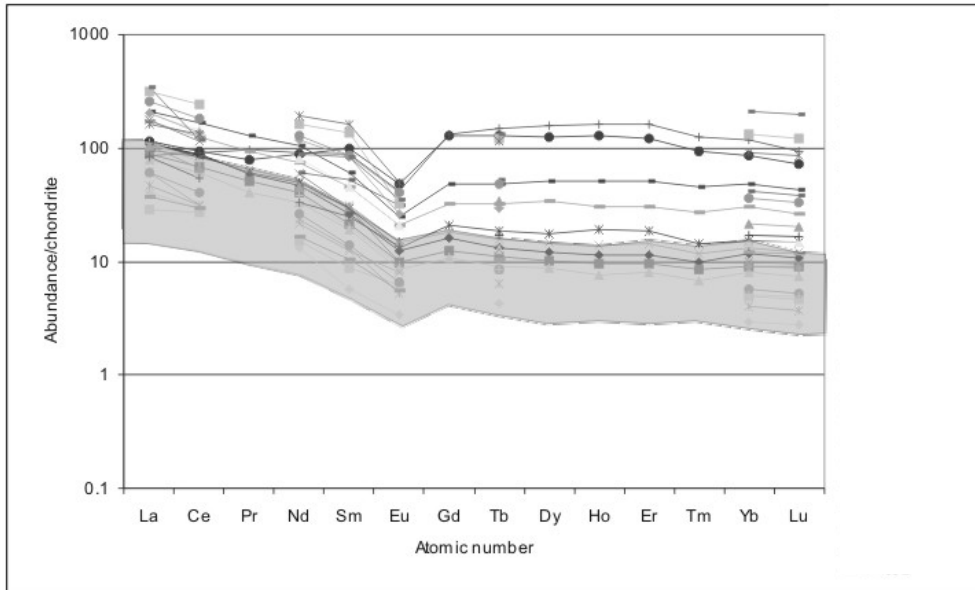


Fig. 78a: Chondrite-normalised REE plot of meta-arkoses that host the Skorpion ore body (normalised against the C1 concentrations of Boynton 1984) showing that REE's within the Skorpion meta-arkoses have partly been affected by weathering processes. Moderately weathered meta-arkoses show the same REE pattern as meta-arkose samples from the wider Skorpion area (grey outline), thus indicating that REE behaved inert towards moderate weathering. However, highly leached and gossaneous meta-arkoses from the Skorpion deposit, which have undergone extensive weathering, are enriched in both LREE and HREE.

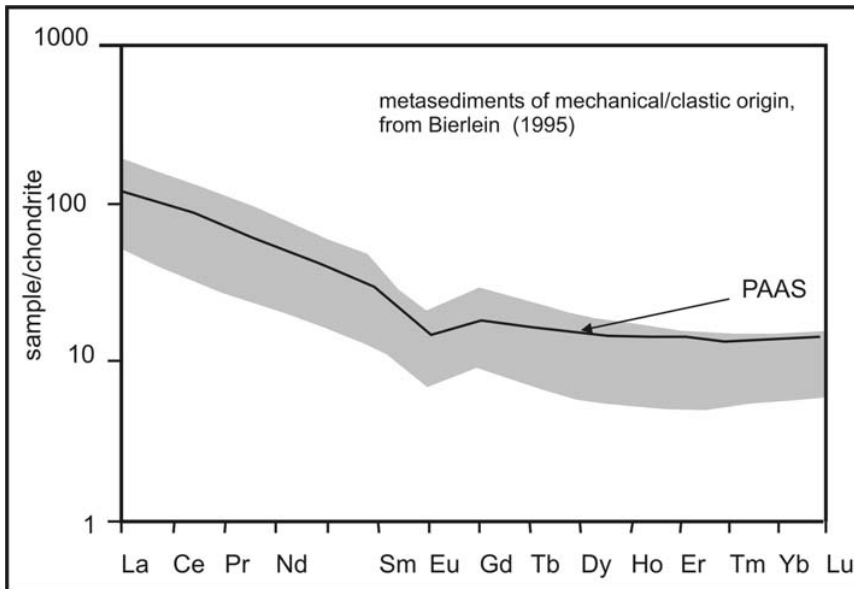


Fig. 78b: Chondrite-normalised REE patterns for Lower to Middle Proterozoic metasediments of mechanical/clastic origin from the Olary Block, Southern Australia, n = 5.

The REE distribution pattern of the Skorpion meta-arkoses shows a wide range in concentrations, which are commonly 10 to 100 times that of C1 chondrite in the moderately altered meta-arkoses and 20 to 200 times that of C1 chondrite in the highly altered meta-arkoses (Fig. 78a). Nesbitt (1979) has shown that REE's can be enriched up to a factor of two relative to parent rock in samples representing moderate to advanced stages of weathering and that HREE are preferentially enriched over LREE. Indeed, the highly altered meta-arkoses from the Skorpion deposit contain two times that of moderately altered meta-arkoses. Therefore, it

can be concluded that REE's were enriched residually in the Skorpion weathering profile, which is in agreement with a strong positive correlation of Sm and La as well as Yb and Y (Fig. 79). Residual enrichment of REE's in highly weathered metasediments in a supergene environment has also been reported by Leroy & Turpin (1988) and Gouveia et al. (1993).

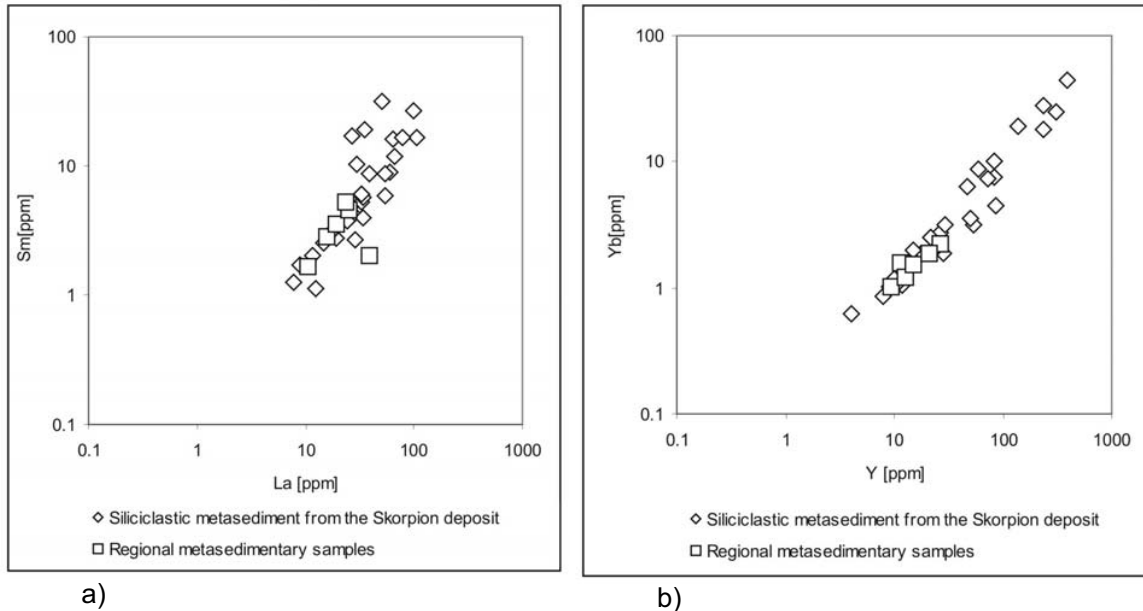


Fig. 79: Selected REE variations in meta-arkoses from the Skorpion deposit and from outcrops in the wider Skorpion area. A) La vs. Sm; b) Y vs. Yb. Their strong positive correlations represent their immobile behaviour. The absolute concentration, however, is higher within the highly altered meta-arkoses, which are host to the non-sulphide mineralisation, and thus indicate that they were residually enriched during the process of supergene weathering.

The REE distribution pattern within the moderately altered meta-arkoses is very similar to REE patterns of sediments elsewhere (Fig. 78b), which are interpreted to reflect the average continental crust (Taylor & McLennan 1985, Bierlein 1995).

Skorpion meta-arkoses are characterised by weak to moderate negative Eu anomalies with Eu/Eu^* averaging at 0.53 (range 0.39 – 0.62). Similar REE distribution patterns from siliciclastic metasediments of the Rosh Pinah deposit have recently reported by Gauert (pers. comm.). Non- to slightly altered meta-arkoses from the wider Skorpion area show very similar patterns with Eu/Eu^* averaging at 0.56 (range 0.52 – 0.65). However, the most leached and altered, gossaneous meta-arkoses from the Skorpion deposit show a more pronounced negative Eu anomaly compared to meta-arkoses within the wider Skorpion area averaging at 0.15 (range 0.13 – 0.18).

The negative Eu-anomalies, which are very typical for the Skorpion metasediments, are similarly found in most sedimentary rocks. Negative Eu-anomalies are interpreted to represent a feature of the upper continental crust (Bierlein 1995, Taylor & McLennan 1985). The ubiquitous negative Eu anomaly in sedimentary rocks worldwide is fairly constant at about 0.60 to 0.70 (Gromet et al. 1984).

Most post-Archean sedimentary rocks have fairly uniform REE patterns with $La_N/Yb_N < 15$ (MacLennan 1989), and thus, show only minor fractionation of REE's. Least altered meta-arkoses from the Skorpion area as well as moderately weathered meta-arkoses from the Skorpion deposit average at $La_N/Yb_N = 8.5$. In contrast, strongly weathered meta-arkoses

from the Skorpion deposit average only at $La_N/Yb_N = 3$, indicating that HREE's were preferentially enriched.

HREE patterns are typically flat in average metasediments worldwide with Gd_N/Yb_N rarely outside the range of 1.0 – 2.0 (MacLennan 1989). Least altered metasediments from the Skorpion area average at $Gd_N/Yb_N = 1.7$, their highly supergene altered equivalents from the Skorpion deposit display $Gd_N/Yb_N = 1.3$. The REE-ratios given above indicate that no substantial residual enrichment of REE minerals has taken place, as modest amount of zircon would result in $Gd_N/Yb_N < 1$, allanite in $La_N/Yb_N > 15$, and monazite in $Gd_N/Yb_N > 2$ (MacLennan 1989). However, traces of supergene monazite and xenotime have been found in highly altered gossaneous meta-arkoses from the Skorpion deposit and show that at least a small portion of the residually enriched REE's has formed secondary REE minerals.

As it has been documented above, the pre-existing REE signatures of sediments remain unchanged during metamorphism (Leshner et al. 1986, Michard & Albarède 1986, Bau 1991, Bierlein 1995). Thus and in addition to other generally immobile trace elements such as Zr, Ti, Th and Hf, REE's have proven to provide a powerful tool for the characterisation of provenances when applied to sedimentary rocks (McDaniel et al. 1994). Fig. 80 shows the La/Sc-Ti/Zr diagram of Bathia and Crook (1986) for meta-arkoses from the Skorpion deposit and their less altered equivalents from the wider Skorpion area. Samples generally plot within the 'passive continental margin' field (Fig. 80), which is in agreement with the Late Proterozoic setting within the Skorpion/Rosh Pinah area.

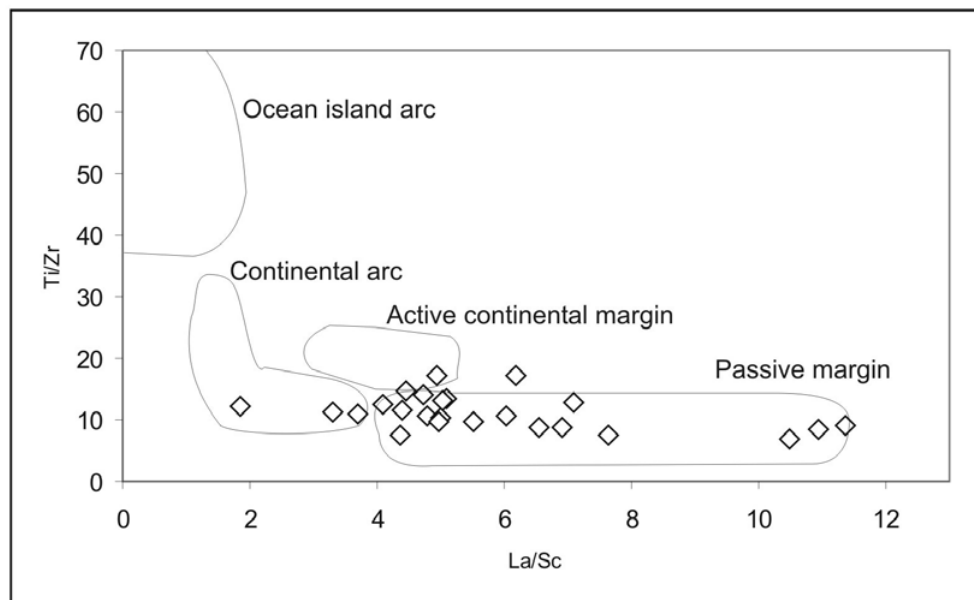


Fig. 80: La/Sc-Ti/Zr diagram of Bathia and Crook (1986). Late Proterozoic meta-arkoses plot within the "passive continental margin" field.

3.6.3 Covering Sediments

The blind non-sulphide ore body at Skorpion is covered by a transported barren regolith. The regolith profile consists of a surficial layer of wind blown sand above a massive calcrete (Fig. 81). Below this occurs a sequence of alluvial interlayered gravels and conglomerates, which are generally calcretised. A silcrete layer occurs locally at the base (Fig. 82). The sediments have been deposited onto a palaeo-erosional surface, which consisted of the host rocks of the Skorpion deposit. The erosional discordance is most likely an equivalent to the “Namib Unconformity Surface” (e.g. Paltridge & Maud 1987) and thus of an Early Tertiary age. The palaeo-surface was not a flat surface, since the exposed overburden profiles within the Skorpion area revealed both palaeo-highs and –lows.

The central, southern, and south-eastern part of the ore body is covered by 10 and 20 m thick alluvial sediments (Fig. 83 & 85, Fig. 159), whereas the western and north-western part of the ore body is covered by overburden material reaching only 2.5 m in maximum (Fig. 83 & 84, Fig. 159). The former represent palaeo-lows, whereas the latter represent palaeo-highs (Fig. 83).

The sedimentary facies of the transported regolith is apparently related to the palaeo-topography. Calcareous sands and minor gravels as well as a thin discontinuous ferrigenous silcrete (Fig. 82) occur above palaeo-highs. In contrast, decimeters to meters thick boulder beds have been deposited above the palaeo-lows. Thus, high-energy sediments have filled the palaeo-lows, whereas low-energy sediments have been deposited above palaeo-highs. The composition of boulders and gravels suggest an origin from a local source, as they consist mainly of Late Proterozoic metavolcanic and metasedimentary rocks, e.g. metarhyolite and marble. Palaeo-Proterozoic basement components such as granitic gneisses are rare.



Fig. 81: Uppermost part of the overburden profile showing some decimeters of recent wind-blown sand over calcretised gravels and sand.

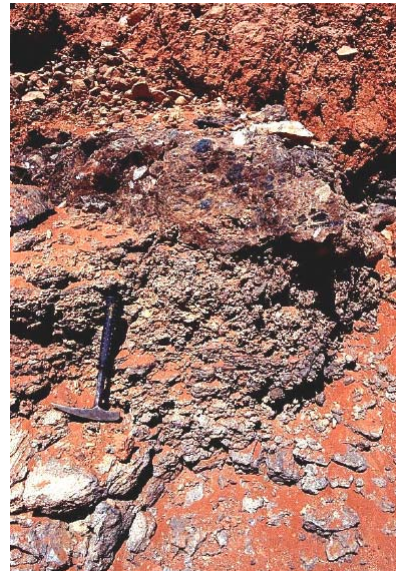


Fig. 82: Lowermost part of the overburden profile. A discontinuous silcrete layer rests locally on top of the Late Proterozoic host rocks.

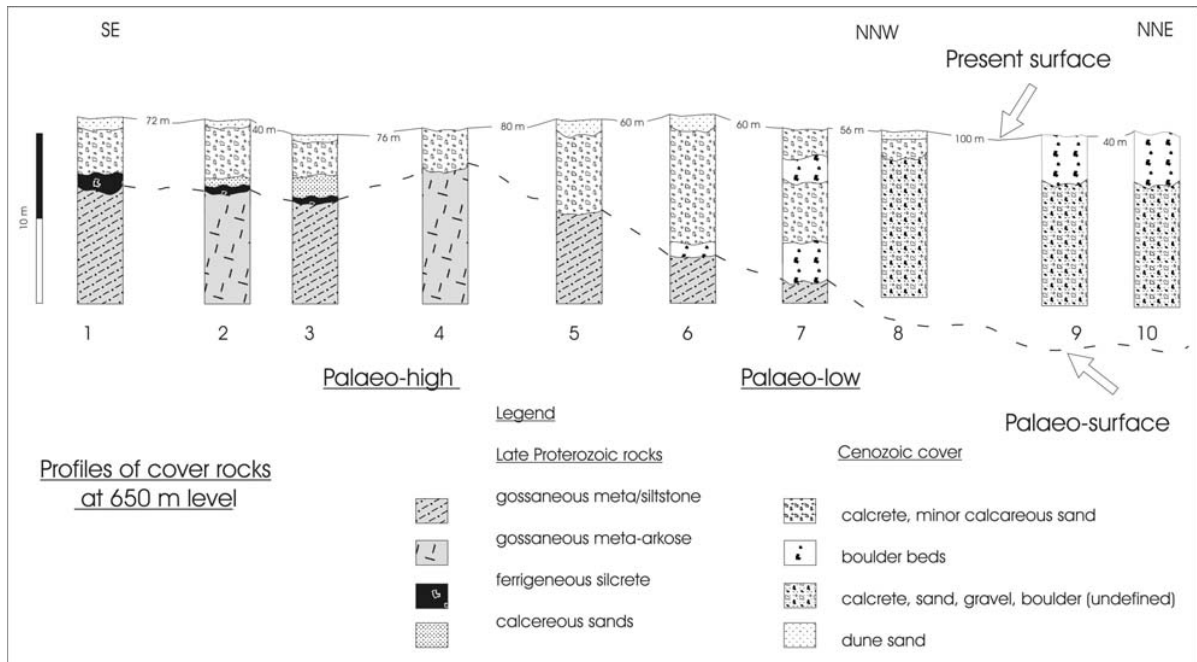


Fig. 83: The regolith profile along the western wall of the Skorpion open pit on the 650 m level shows the transition from a palaeo-high to a palaeo-low. At the position of the palaeo-high (profile 1 – 4), the overburden is relatively thin and composed of a discontinuous silcrete layer at the base and calcrete/calcareous sands on top. At the position of the palaeo-low the overburden is thicker and characterised by interlayered boulder beds and gravels and sand.



Fig. 84: Regolith profile (position 3 in Fig. 83) above a palaeo-high. The regolith lies unconformable on gossaneous meta-arkoses.



Fig. 85: Regolith profile (position 6 in Fig. 83) above a palaeo-low. The regolith lies unconformable on zinc-mineralised meta-arkoses.

3.7 Ore Minerals, Textures, and Styles of Mineralisation

3.7.1 Introduction

The aim of the following chapter is to describe the shape of the Skorpion ore body and both primary hypogene and secondary supergene ore paragenesis. The mineral chemistry, ore textures and styles of mineralisation are discussed for each ore mineral.

Both, the mixed sediment-/volcanic-hosted non-sulphide ore body and the remnants of volcanic-hosted sulphide mineralisation are known from abundant drill core and recently exposed non-sulphide mineralisation in the open pit. Remnants of a primary sulphide mineralisation are mainly preserved in the felsic metavolcanic rocks and their hyaloclastic equivalents, which structurally underlie the central portion of the supergene ore body at depth (Fig. 17). The felsic metavolcanic rocks are also exposed some hundreds meters west of the Skorpion open pit, displaying disseminated pyrite mineralisation or forming gossans. The most famous gossan, which is located west of the Skorpion ore body, is the so-called 'discovery outcrop'.

Within the footwall of the Skorpion non-sulphide zinc ore body disseminated to semi-massive primary pyrite-sphalerite mineralisation has been intersected at a depth of 250 m and 300 m, respectively, which features a 25-m-wide zone grading 0.6 % Zn and 0.35 % Cu (Corrans et al. 1993). Besides pyrite and sphalerite, the primary sulphide mineralisation comprises minor chalcopyrite, and traces of galena.

The sulphides form mm- to cm-thin sharp- to diffuse-defined bands mainly in the highly sheared felsic metavolcanic rocks ('sheared sericite schist (SSS)'). Pyrite also forms stringers in massive, partly brecciated felsic metavolcanic rocks ('quartz-sericite-schist (QSS)'). The sulphide banding parallels the penetrative foliation and the sulphide ore minerals within these bands generally show a granoblastic texture indicating that sulphides have been overprinted by metamorphism and undergone recrystallisation and metamorphic crystal growth (Franklin 1993). Partly, pyrite forms porphyroblasts in a sphalerite matrix. The sulphide grains, in particular pyrite, are commonly elongated and feature pressure shadows. The grain size of sulphides is highly variable and generally controlled by primary sulphide mineralogy and the extent of metamorphic recrystallisation. Thus, the sulphides pre-date the Pan-African metamorphic event and are of either syngenetic or early diagenetic origin. Apparently, pyrite behaved least ductile of the sulphides during the upper greenschist/lower amphibolite facies metamorphism, followed by sphalerite and galena, which is in agreement with Kalliokowski (1965).

For completeness it has to be mentioned that some minor primary sulphides have been found in metasiliciclastic rocks but also in marble in the northern extension of the Skorpion ore body about 1.5 km north of the Skorpion open pit, e.g. borehole SD104, at a depth between 550 m and 700 m in unaltered fresh equivalents of the Skorpion metasiliciclastic host rocks and marble, respectively. Grey metasandstones and meta-arkoses contain sphalerite, pyrite, pyrrhotite, galena and traces of chalcopyrite, which are found parallel to the foliation planes. The marble in the northern extension of the ore body contains some minor disseminated pyrite and sphalerite. In places, sulphides are hosted by quartz and/or calcite veins.

3.7.2 The Shape of the Supergene Ore Body

The post-deformational, post-metamorphic supergene oxidation of the primary Late Proterozoic sulphide deposit in a near-surface environment by low-temperature meteoric fluids led to the formation of the secondary supergene non-sulphide ore body at Skorpion. The non-sulphide ore body is broadly stratabound and hosted mainly by meta-arkoses, though supergene ore minerals have also been found in felsic metavolcanic rocks.

The non-sulphide ore body has a W-E extent of about 400 m, and an N-S extent of about 600 m (Fig. 86). Thus, the non-sulphide ore body strikes N-S, and follows the major structural direction within the Skorpion area. However, Fig. 86 also shows that the non-sulphide mineralisation cross-cuts the structural domains (Dirks 2004), and thus the anastomosing array of Mesozoic brittle-ductile shear zones, which correspond to the dextral wrench fault system defined by Borg et al. (2004).

The spatial relationship between the supergene ore body and the major fault system clearly indicates that the non-sulphide mineralisation post-dates both Pan-African and Jurassic/Cretaceous deformation events. Nevertheless, the major fault zones have provided open spaces for supergene fluids, which oxidised the Skorpion sulphide precursor, locally up to a depth of 800 m (Corrans et al. 1993). Therefore, it is not surprising that the highest supergene ore thicknesses, which reach up to 80 m, are found along the N-S striking deformation pattern (Fig. 86).

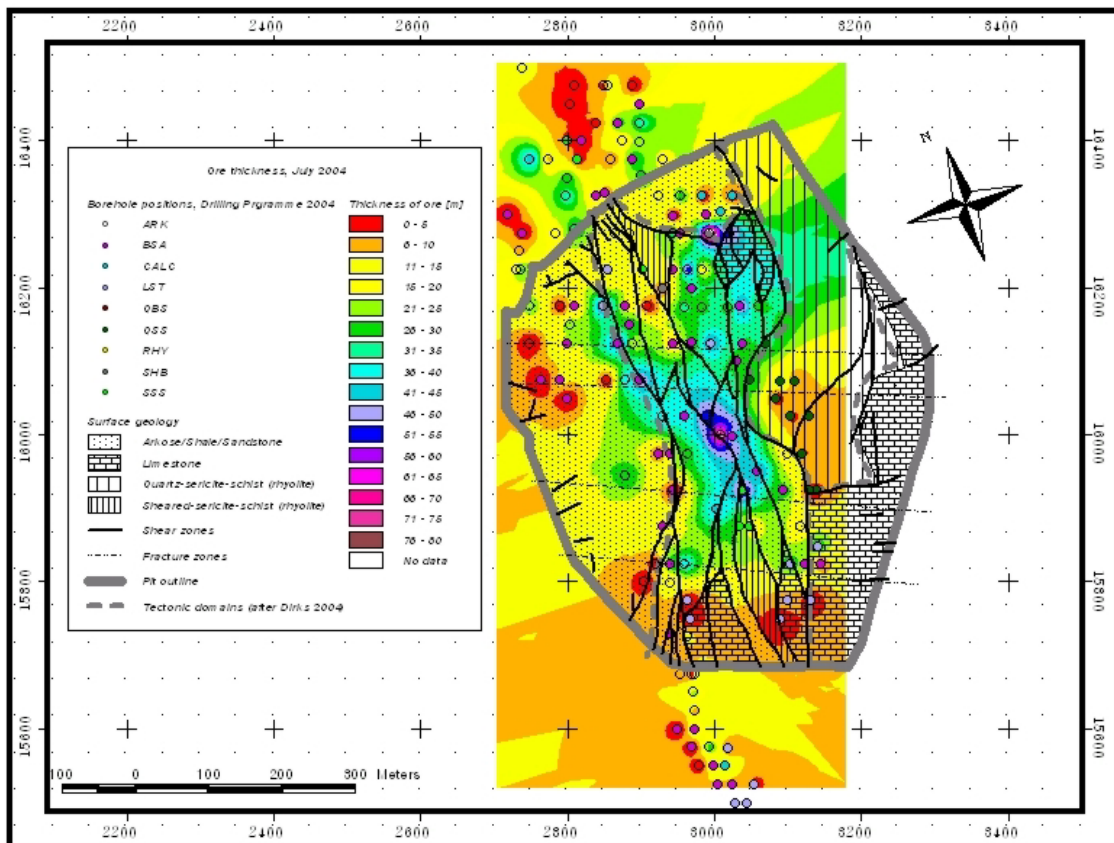


Fig. 86: Ore thickness (Zn > 5 %) in relation to the major geological and structural units, calculated from geochemical results obtained from Skorpion's infill drilling programme 2004. The map shows that the major portion of the ore body is hosted by meta-arkoses (mining term: arkose) and only minor by felsic metavolcanic rocks.

The supergene non-sulphide mineralisation, which includes carbonates, hydrosilicates, phosphates, and (hydro-)oxides, occurs transgressive to individual sedimentary layers as a large, irregular, and 'nebulous' mass. The minerals have either replaced primary sulphides or have grown in secondary pore space.

The contact of the non-sulphide ore body with the marble, which forms an antiform in the eastern and southern part of the Skorpion deposit (Fig. 17 & 86), is relatively sharp, with ore grades dropping to subeconomic and to background values over a short distance of less than 2 meters. The extent of the ore body away from the marble contact to the west and north is less well constrained. However, the western extent is defined by metal solubilities, which will be discussed in a separate chapter.

The supergene ore body is covered by a transported barren regolith that rests unconformable on top of the Skorpion ore body. The unconformity surface represents an erosional palaeo-surface, which will be discussed in detail in relation to the palaeo-morphological evolution of the Skorpion area later in this study.

However, at this point, it should be already mentioned that the palaeo-denudation process not only led to the formation of the palaeo-surface but also to the partial erosion of the uppermost part of the supergene mineralisation.

One may ask from that how much of the supergene ore body has been eroded. A rough estimate under certain conditions can be given in order to attempt to answer this question (Fig. 87). The most likely scenario indicates that a sulphide protore could have contained about 50 Mt @ 5 % Zn, and thus 2,500,000 t Zn. The present non-sulphide mineralisation contains only 2,400,000 t Zn. Therefore, it can be concluded that at least 5 % of the supergene zinc mineralisation must have been eroded. However, the initial Zn concentration of the sulphide protore prior to the oxidation is unknown, since the sulphides that presently occur in felsic metavolcanic rocks in the footwall of the supergene non-sulphide ore body show evidence of supergene sulphide enrichment. Initial Zn concentrations in the sulphide protore of less than 5 % would lead to a more significant imbalance between the tonnages of sulphide and non-sulphide mineralisation, and thus would increase the portion of the eroded supergene mineralisation.

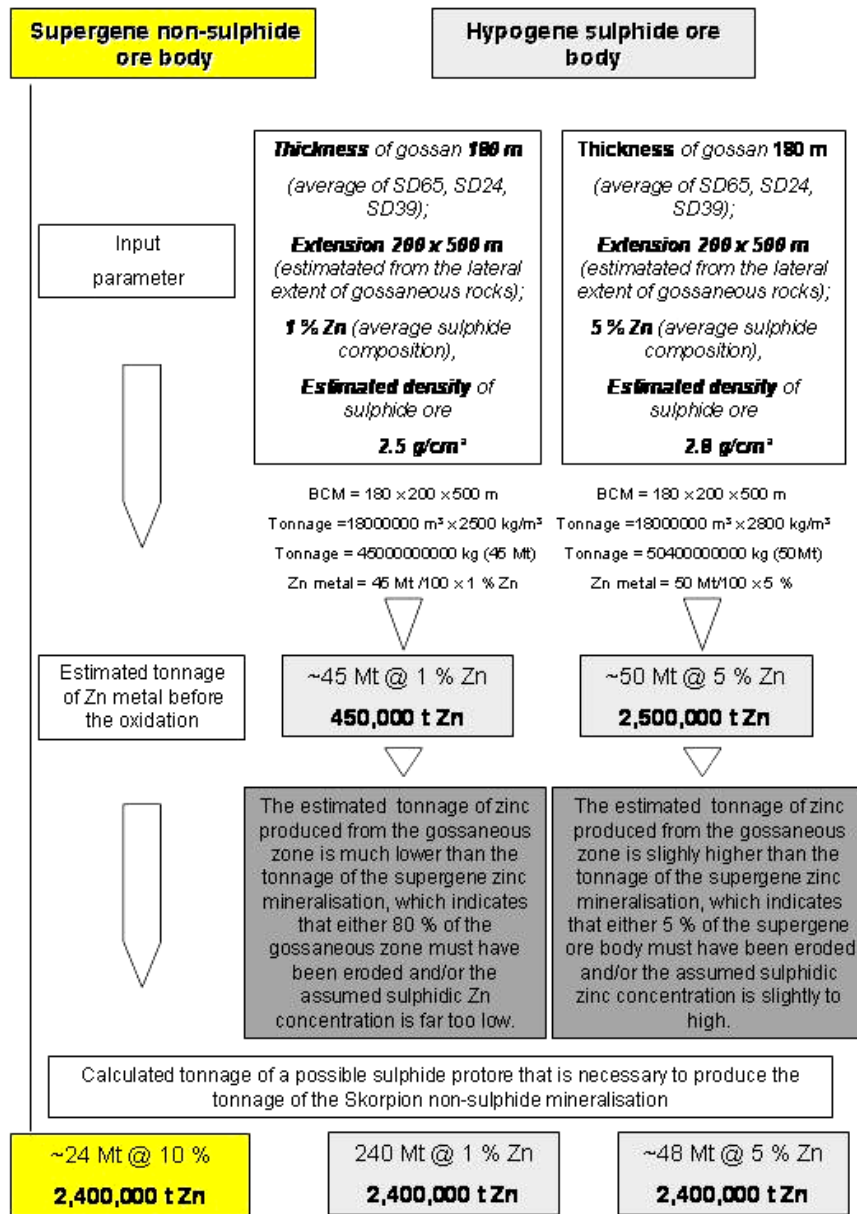


Fig. 87: Calculation of tonnages of a possible sulphide protore, which is based on the following assumptions regarding the hypogene sulphide mineralisation: i) Its lateral extent is equal to the lateral extent of the iron-rich gossaneous zone (Fig. 147). ii) Its thickness is equal to the average thickness of the gossaneous zone, which was calculated averaging the gossaneous zones of three boreholes from the northern, central and southern part of the gossaneous zone. iii) Its zinc concentration might have been between 1 and 5 %, but was rather higher than lower, since gossaneous zones still contain some hundreds to thousands ppm of zinc.

The following conclusions can be drawn: i) Regardless the primary zinc concentration of the sulphide protore, the sulphide protore must have been a world-class sulphide deposit with a tonnage that is above-average. ii) Case study two assuming a protore with a zinc concentration of 5 % seems to be the more likely scenario, since case study one would end up with unlikely high tonnage. Additionally, it is unlikely that 80 % of the gossaneous zone was eroded, while the supergene zinc mineralisation was preserved.

BMC = Bulk Cubic Meters.

3.7.3 Primary Hypogene Ore Minerals

Pyrite commonly occurs as medium-grained sub- to euhedral porphyroblasts. The porphyroblasts are generally surrounded by anhedral sphalerite and form diffuse- to sharp defined sulphide bands (Fig. 88). The porphyroblastic growth of pyrite is the result of thermal metamorphism, which causes sulphide aggregates to become coarser grained (Stanton 1972). Additionally, disseminated pyrite aggregates occur, which are commonly elongated and orientated along the penetrative foliation (Fig. 89).

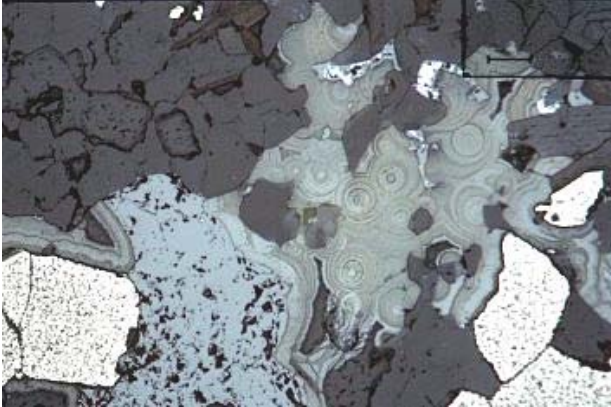


Fig. 88: Photomicrograph of a thin section showing diffuse banded sulphide ore with recrystallised pyrite porphyroblasts (light-yellow) in a sphalerite matrix (medium-grey) hosted by highly foliated felsic metavolcanic rock ('sheared-sericite-schist'). Colloform medium-grey sphalerite has a supergene origin and will be discussed below. Sample 2015, borehole SD20, depth 269.95 m, reflected light, scale bar 80 μm .

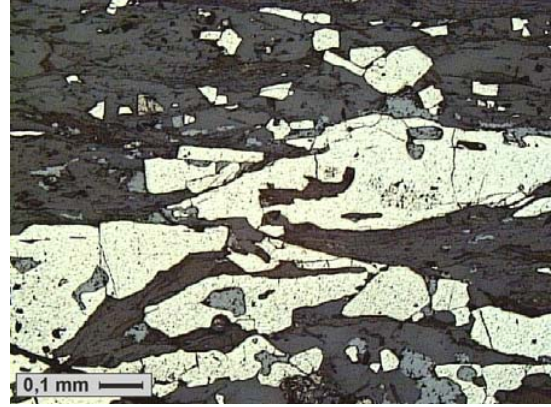


Fig. 89: Photomicrograph of a thin section showing elongated pyrite and sphalerite aggregates orientated parallel to the foliation planes in felsic metatuffite (quartz-biotite-schist). Sample 2042, borehole SD20, depth 349.95 m, reflected light.

Sphalerite forms medium-grained anhedral aggregates enclosing pyrite grains in mixed pyrite-sphalerite sulphide bands (Fig. 90 & 91). Electron microprobe analyses have shown that primary sphalerite contains significant amounts of Fe, ranging between 3 and 8 % (6.7 % Fe average). Traces of Mn (0.3 %) and Cd (0.17 %) have also been detected (Fig. 92). Intergrain boundary sites of sphalerite are predominately filled by chalcopyrite. Additionally, chalcopyrite disease textures in sphalerite occur in places, indicating that primary sphalerite must have formed and metamorph overprinted below 400°C (Guilbert & Park 1986). However, a more precise determination of the primary sphalerite formation temperatures by using the Ga/Ge-thermometer (Möller 1985) was not possible, since concentrations of these trace elements were below detection limit using electron microprobe technique.

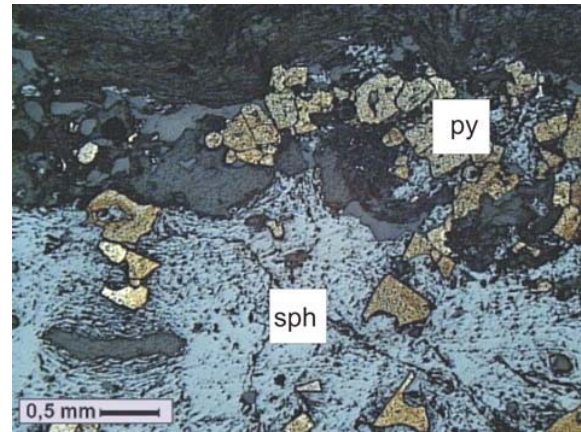
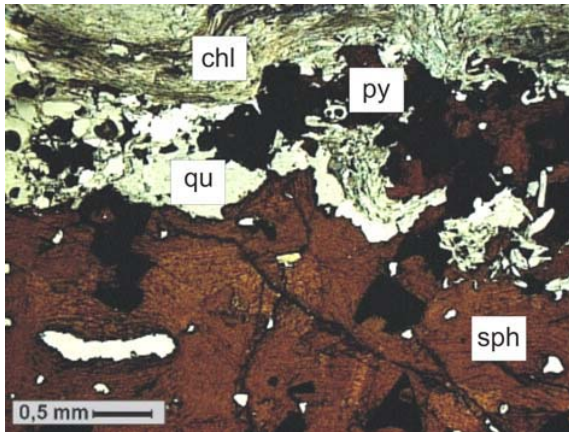


Fig. 90: Photomicrograph of a thin section showing diffuse-defined sphalerite bands with recrystallised pyrite porphyroblasts, hosted by highly foliated chloritised felsic metavolcanic rock ('sheared-sericite-schist'). Sample 2015, borehole SD20, depth 269.95 m, LLP.

Fig. 91: Same view as Fig. 90 under reflected light.

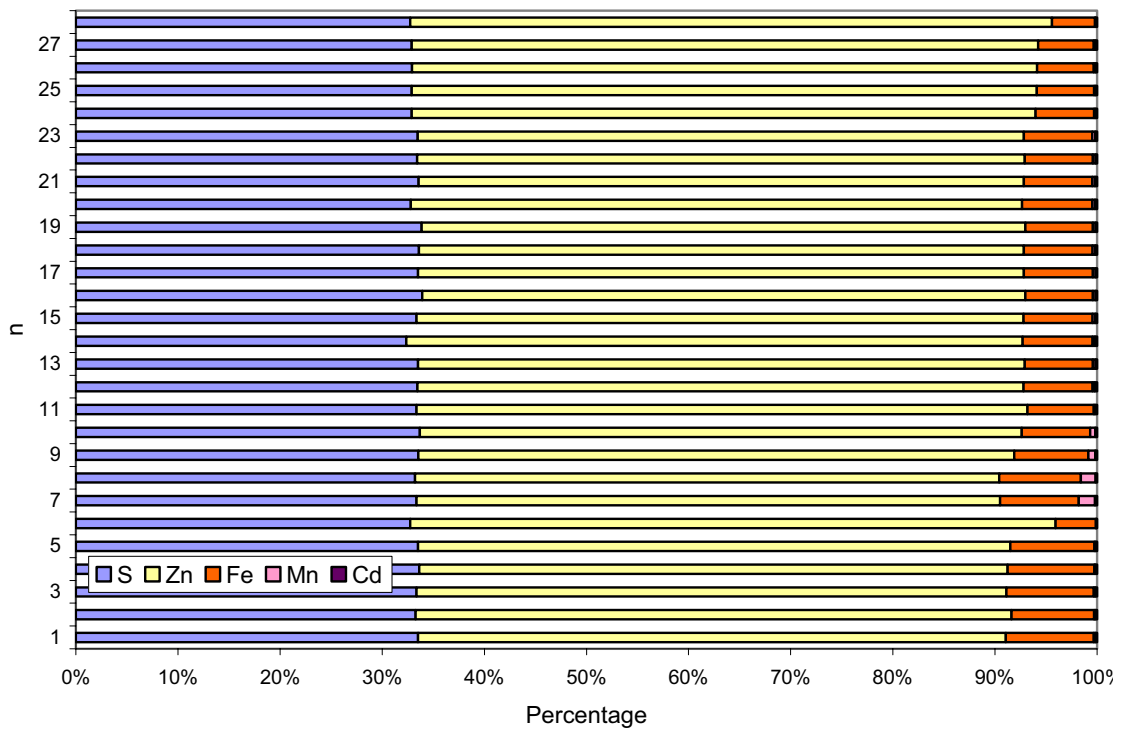


Fig. 92: Electron microprobe analyses of primary sphalerite from felsic metavolcanic rocks. 29 sphalerite aggregates from a total of 4 samples have been analysed for their geochemical composition.

Primary galena (Fig. 93 – 94) is very rare and can usually not be seen macroscopically in drill core. Primary galena occurs in association with sphalerite showing a granoblastic ore textures and has been found in samples of highly foliated felsic metavolcanic rocks ('sheared sericite schist') in the footwall of the non-sulphide ore body.

Electron microprobe analyses have shown that primary galena contains up to 0.73 % Ag, with an average content of 0.41 % Ag, and traces of Zn (0.43 %). Additionally, inclusions of native bismuth were found, which are generally typical for galena formed away from a feeder zone in a hydrothermal environment (Marcoux et al. 1996).

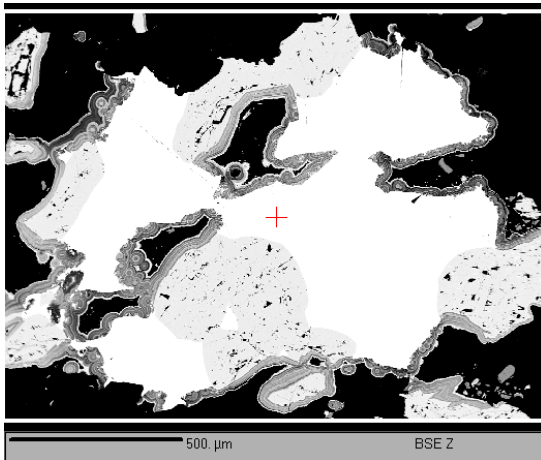


Fig. 93: BSE-photograph showing primary galena (white) and primary sphalerite (light-grey) in felsic volcanic metatuffite. Primary sulphides are overgrown by secondary colloform sphalerite (medium-grey). Sample 2015, borehole SD20, 269.85 m.

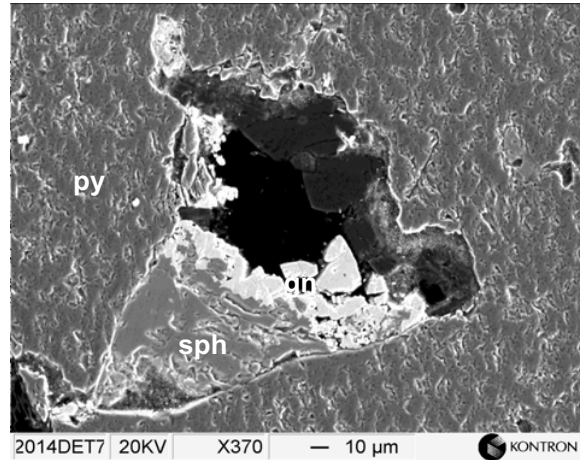


Fig. 94: SEM-picture showing sphalerite (sph)-galena (gn) inclusion in pyrite (py). Borehole SD20, sample 2014, depth 269.0 m.

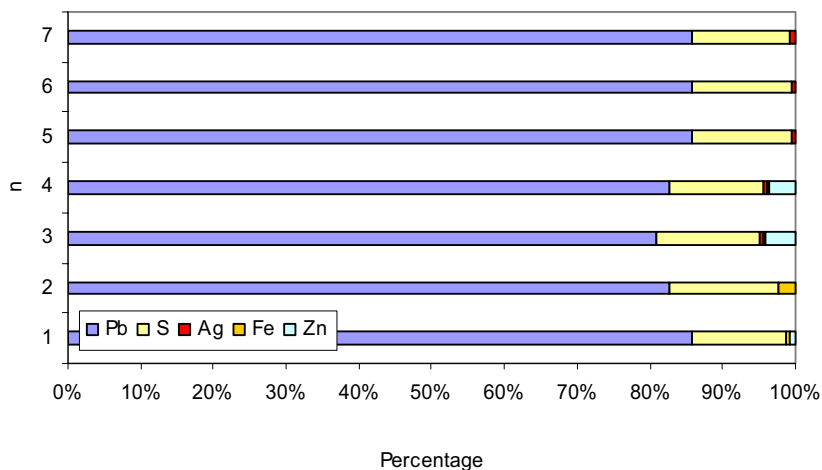
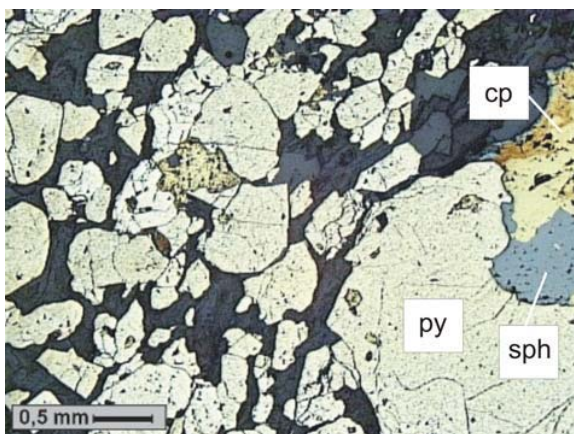


Fig. 95: Electron microprobe analyses of primary galena from highly foliated felsic metavolcanic rocks ('sheared sericite schist'). 7 galena aggregates from a total of 3 samples have been analysed for their geochemical composition.



Additionally, chalcopyrite occurs as a minor constituent of the primary sulphide paragenesis (Fig. 96). It forms anhedral aggregates, which are intergrown with sphalerite and pyrite displaying a granoblastic texture.

Fig. 96: Photomicrograph of a thin section showing stringer mineralisation of pyrite in felsic metarhyolite. Pyrite is partly intergrown with chalcopyrite and sphalerite. Borehole SD20, sample 2037, depth 345.05 m. Reflected light.

3.7.4 Secondary Supergene Ore Minerals

3.7.4.1 Supergene Sulphide Minerals

Secondary sphalerite is the most common supergene sulphide mineral. It occurs mainly as colloform masses (Fig. 88, 93 & 100) but also as crystalline aggregates in secondary pore space. Additionally, clay-like greenish-yellow zinc sulphide referred to as brunckite (Roedder 1968), has been found in secondary pore space (Fig. 97 & 98). Both, sphalerite and brunckite are depleted in Fe, Mn and Cd compared to primary sphalerite (Fig. 99).



Fig. 97: Photograph of drill core showing sulphide-mineralised felsic metavolcanic rock. Open voids are filled by supergene clay-like ZnS, so-called brunckite (arrow). Borehole SD20, sample 2028, depth 326.65 m.



Fig. 98: SEM-photograph showing colloform brunckite grown on quartz in felsic metavolcanic rock. Borehole SD20, sample 2028, depth 326.65 m.

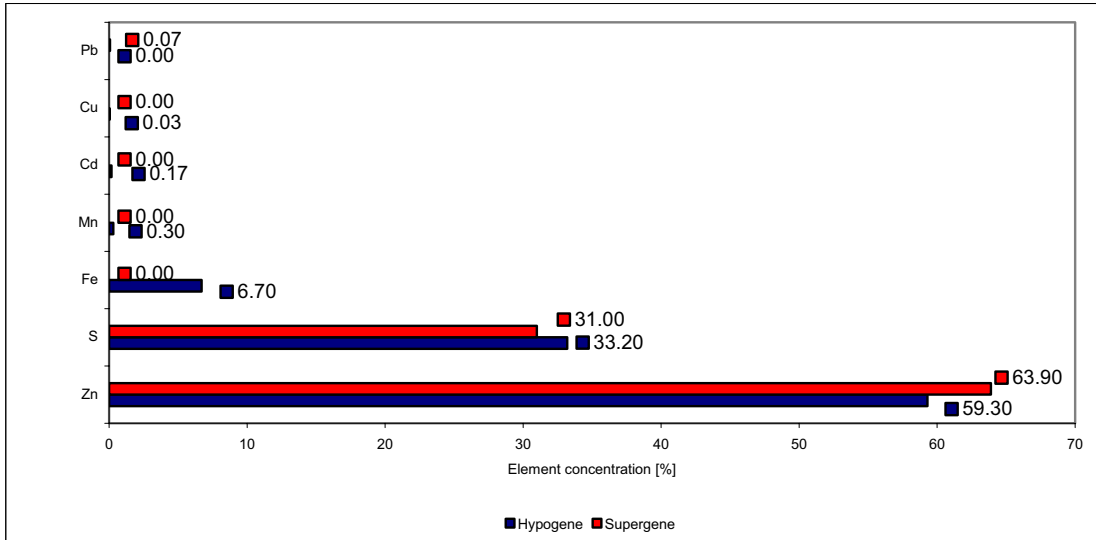


Fig. 99: Average composition from electron microprobe analyses of both hypogene and supergene sphalerite (hypogene sphalerite n = 27, supergene sphalerite n = 9).

Secondary galena (Fig. 100 & 101) has been found in secondary pore space as euhedral grains, but also as anhedral aggregates filling intergrain boundary sites of supergene sphalerite. Secondary galena is depleted of Ag compared to primary galena (Fig. 102). Supergene galena also forms cockade structures on chalcocite.

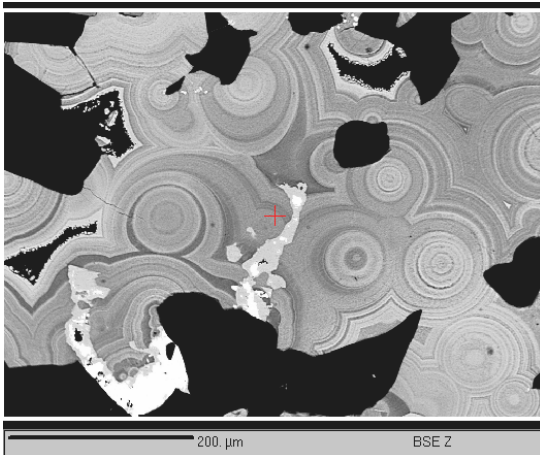


Fig. 100: Supergene galena filling intergrain boundary sites of supergene sphalerite. Felsic volcanic metatuffite. Borehole SD20, sample 2015, depth 269.95 m. BSE-photograph.

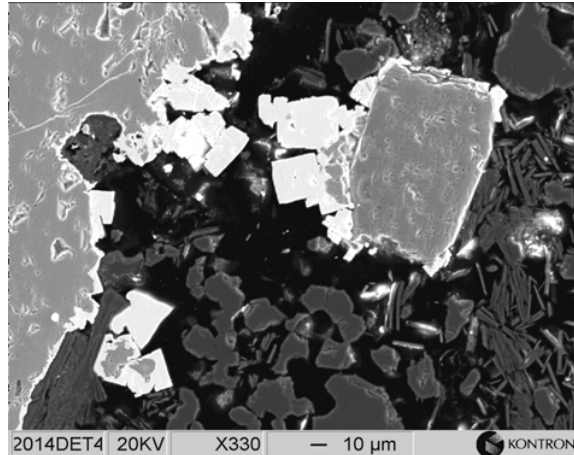


Fig. 101: SEM-photograph showing cubes of galena (white). Galena is grown unhindered in open pore space or replaces pyrite (light-grey). Borehole SD20, sample 2014, depth 268.8 m.

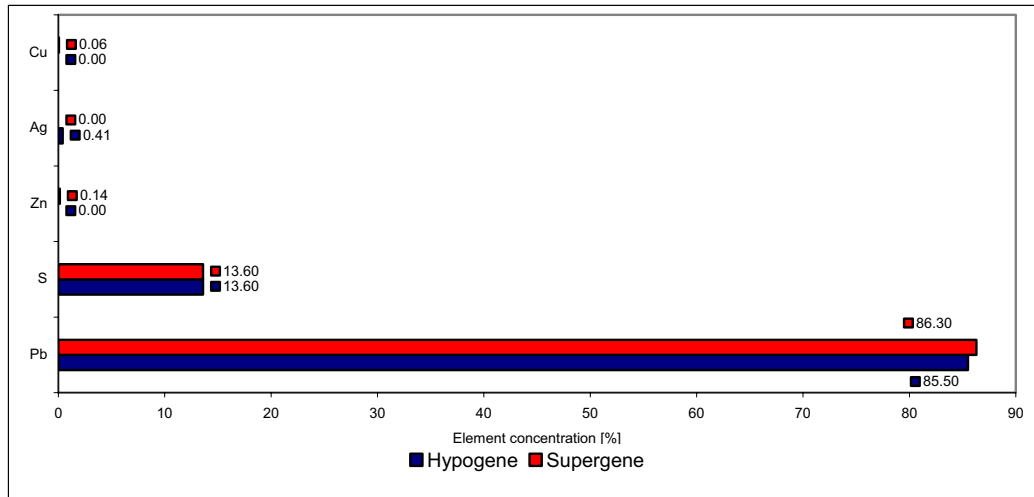


Fig. 102: Average composition from electron microprobe analyses of both hypogene and supergene galena (hypogene galena n = 7, supergene galena n = 8).

A common phenomenon observed on chalcopyrite within the supergene sulphide enrichment zone is its replacement by secondary chalcocite (Fig. 103).

Additionally, Cd, which has been released from primary sphalerite, has been partly incorporated in secondary greenockite (Fig. 103). Greenockite has been locally found in open pore space as euhedral crystals, but also replaces primary chalcopyrite (Fig. 103).

Supergene sulphates, which are very common in weathering profiles over a sulphide deposit (Scott 2001), are very rare at Skorpion and only occur in the form of supergene barite. Within the zone of supergene sulphide enrichment, barite displays pseudomorphs after primary euhedral pyrite. However, it has also been found as cements between detrital grains (Fig. 104).

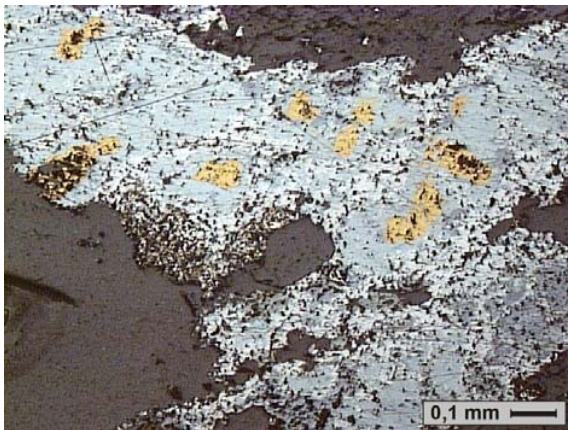


Fig. 103: Photomicrograph of a thin section showing remnants of primary chalcopyrite (yellow) in felsic metavolcanic rock. Chalcopyrite has almost completely been replaced by chalcocite (light-blue), galena (white) and greenockite (dark-blue). Borehole SD49, sample 4932, depth 314.84 m. Reflected light.

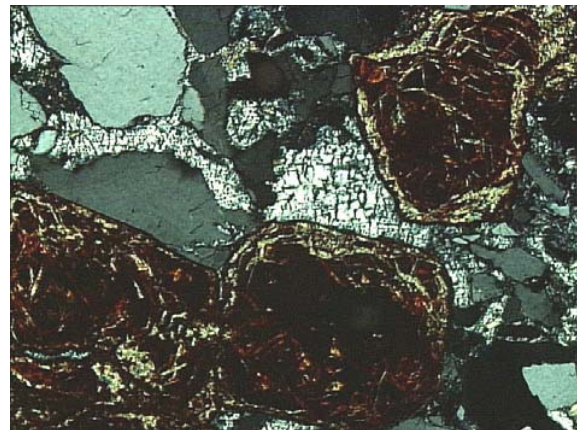


Fig. 104: Photomicrograph of a thin section showing supergene barite filling intergranular pore space in brecciated metasubarkose. Borehole SD65, sample 6506, depth 113.5 m. LLP, 1 cm = 0.1 mm.

3.7.4.2 Supergene Non-Sulphide Minerals

3.7.4.2.1 Sauconite

The predominant supergene non-sulphide zinc mineral is sauconite ($\text{ZnAl}[(\text{OH})_2 / \text{AlSi}_3\text{O}_{10}] (0.5 \text{ Ca, Na})_{0.3}(\text{H}_2\text{O})_4$), a zincian smectite (Borchardt 1989), which is hosted mainly by metasiliciclastic rocks. Macroscopically, sauconite mineralisation is highly inconspicuous and occurs as coatings of secondary intergranular spaces and as coatings of voids, which have formed due to the break-down or dissolution of detrital feldspar, mainly plagioclase, minor orthoclase and mica (Fig. 105). Additionally, sauconite has been found replacing other supergene zinc-bearing minerals of an earlier stage, namely hemimorphite and smithsonite (Fig. 106).

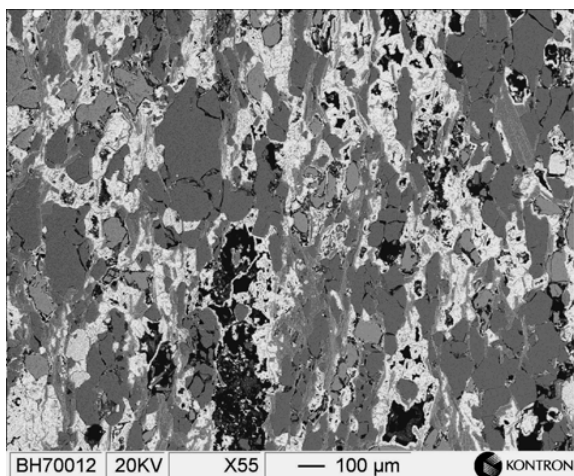


Fig. 105: SEM-photograph of metasubarkose. Sauconite (light grey coatings and fillings) occurs as impregnation in open pore space and has replaced feldspar and mica. Brecciated metasubarkose, borehole BH70, sample BH7001, depth 27.05 m.

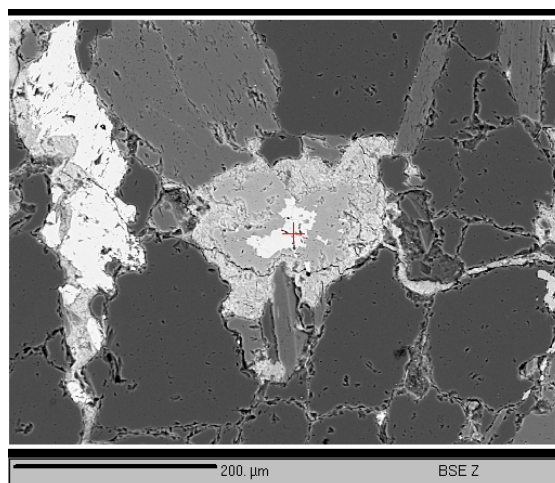


Fig. 106: BSE-photograph showing smithsonite (white) replacing apatite (light-grey). Smithsonite itself is partly replaced by sauconite (light-grey). Brecciated metasubarkose, borehole BH70, sample BH7007, depth 59.8 m.

Microprobe analyses have shown that sauconite displays a highly variable composition, which differs distinctly from the stoichiometric formula. Sauconite contains relatively high amounts of trace elements averaging at 3.3 % FeO, 2.9 % CaO, 1.4 % P_2O_5 , 0.5 % MgO, 0.4 % MnO, 0.2 % SO_2 , 0.2 % CuO, and 0.3 % PbO.

Unusual high amounts of Al_2O_3 , e.g. as seen in sample BH7014 (Fig. 107), are explained by Paquet et al. (1986) to be the result of advanced leaching and weathering of smectite. The progressive leaching mainly of Mg, Mn, and Zn as well as the contemporaneous enrichment in Al and Fe are accompanied by a transition from trioctahedral to dioctahedral smectite, as the former are not stable in an environment that undergoes strong weathering (Paquet et al. 1986, Borchardt 1989). The study of the CIA's of the Skorpion metasediments had shown that the degree of weathering varies between moderate and high. Therefore, a transition from trioctahedral to dioctahedral smectite can be expected in the highly weathered host rocks. The final stage of weathering is characterised by the decomposition of smectite and formation of kaolinite and oxi-hydroxides that can capture transition metals, released by the destruction of the smectitic crystal lattices (Paquet et al. 1986). Indeed, the local occurrence of kaolinite and goethite within the Skorpion host rocks testifies for the advanced stage of weathering in places.

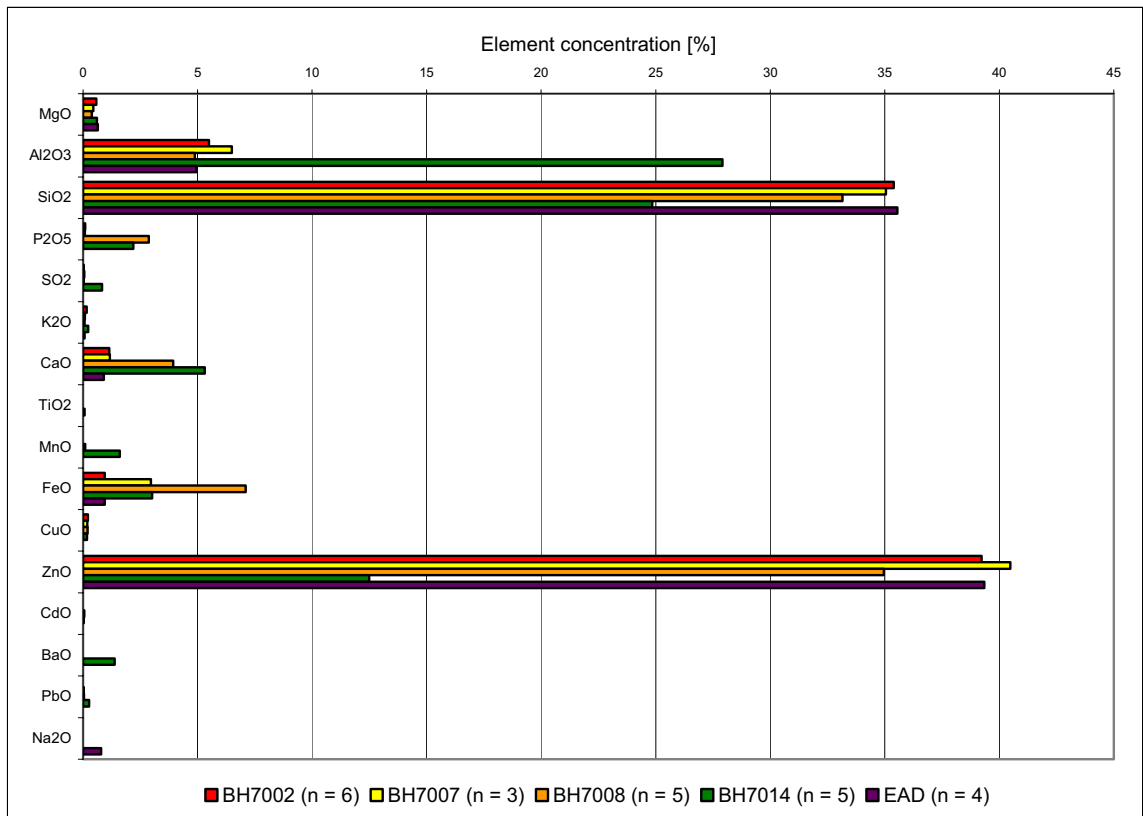


Fig. 107: Electron microprobe analyses of saucornite of samples from borehole BH70. Samples BH7002 (depth 35.5 m, meta-arkose), BH7007 (depth 59.8 m, meta-arkose), BH7008 (depth 65.4 m, meta-arkose), and BH7014 (depth 96.8 m, felsic meta-volcanic rock) were analysed during the present study. Composite sample EAD by courtesy of Anglo American (Theron et al. 2002, unpubl.).

3.7.4.2.2 Hemimorphite

The second most abundant non-sulphide ore mineral is hemimorphite, which is macroscopically generally unobtrusive (Fig. 31 & 32). Hemimorphite impregnates either intergranular pore space in metasedimentary rocks or replaces accretionary lapillis in metavolcaniclastic rocks (Fig. 108). Non-mineralised and least altered equivalents of the hemimorphite-mineralised accretionary lapillis are found in the vicinity of the Skorpion ore body (Fig. 109). Comparing the composition of the supergene altered and mineralised rocks and their least supergene altered barren equivalents, it becomes obvious that hemimorphite has replaced mainly calcite, which not only occurred as cement in metasediments, but also made up individual lapillis in the metavolcaniclastic rocks (Fig. 109). A minor constituent of the non-altered lapillis is biotite (Fig. 109), which obviously has been replaced by hemimorphite as well.

Additionally, hemimorphite is found as delicate euhedral crystals, which have grown unhindered in open spaces such as secondary pores, intergranular spaces or fractures (Fig. 110 & 111). In places, at least two generations – early and late stage hemimorphite – can be distinguished by texture. Late stage hemimorphite usually occurs as fracture fillings in hemimorphite-impregnated rocks. However, the different generations are composed chemically identically. Hemimorphite is ideally composed of 67.7 % ZnO, 24.9 % SiO₂, and 7.5 % H₂O with Ca, Mg, Fe, Ti, Al, and Cd as trace elements. Electron microprobe analyses of

hemimorphite from the Skorpion deposit display 66.5 % ZnO, 27.5 SiO₂, 0.3 % P₂O₅ and about 6 % H₂O, which shows that the composition of the Skorpion hemimorphite is close to the ideal composition. Locally, early hemimorphite is replaced by smithsonite or has been altered to sauconite.

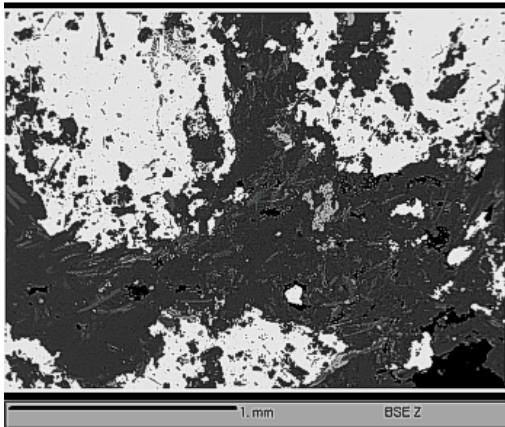


Fig. 108: SEM-picture of supergene altered and mineralised metatuffite. Accretionary lapillis (light-grey, diffuse oval aggregates) consist of hemimorphite. Borehole BH70, sample BH7015, depth 97.95 m.

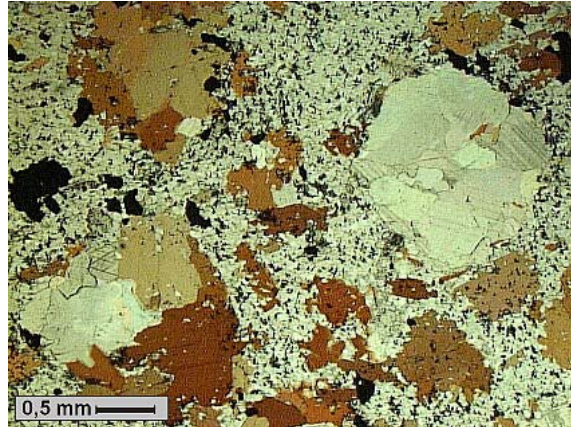


Fig. 109: Photomicrograph of a thin section showing accretionary lapillis consisting of calcite and biotite. They represent an unaltered equivalent to the sample depicted in Fig. 108. Borehole UTEM, sample UTEM 5, depth 145.71 m.

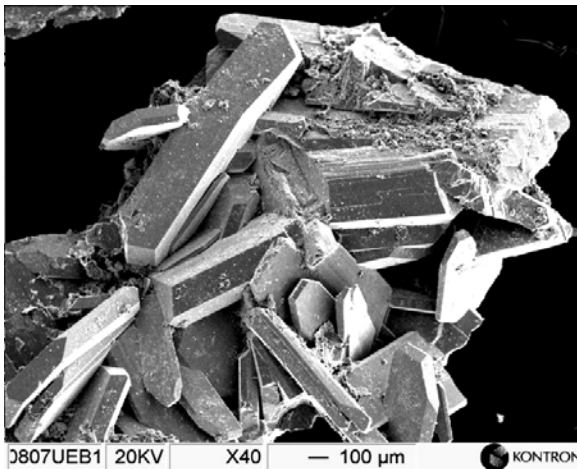


Fig. 110: SEM picture of euhedral hemimorphite crystals in open-fracture space. Borehole SD08, sample 0807, depth 69.45 m.

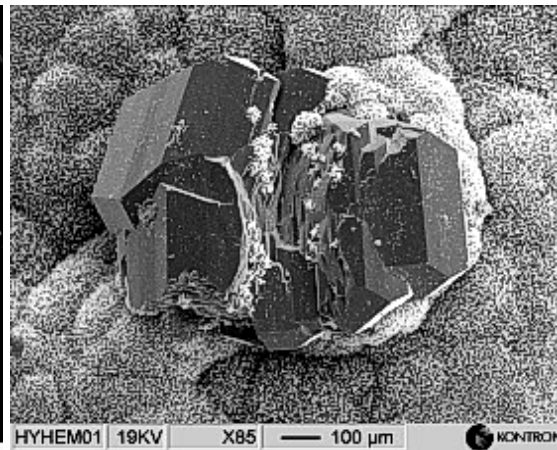


Fig. 111: SEM picture of collomorph hydrozincite in open-void space, overgrown by euhedral hemimorphite. Borehole BH70, sample BH7006, depth 61.9 m.

3.7.4.2.3 Smithsonite

Besides sauconite and hemimorphite, smithsonite (ZnCO₃) is one of the major ore minerals. It either impregnates inter- and intragranular pore space (Fig. 112) or occurs as delicate euhedral crystals, which have grown unhindered in open spaces such as secondary pores, intergranular spaces or fractures (Fig. 113). In places, smithsonite has also been replaced by sauconite (Fig. 106).

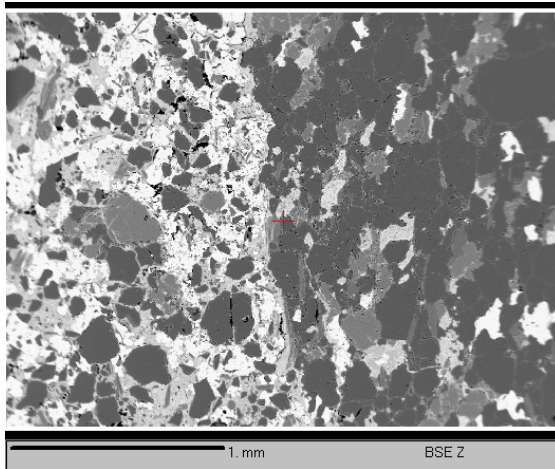


Fig. 112: SE-photograph of a thin section showing a brecciated metasubarkose (see drill core in Fig. 56). Smithsonite mineralisation occurs in both breccia clasts and matrix. Borehole BH70, sample BH7007, depth 59.8 m.

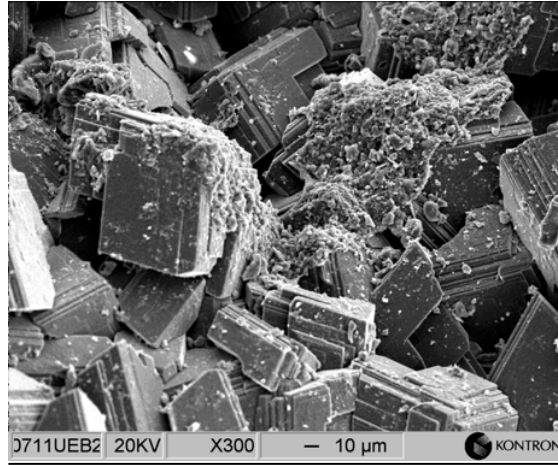


Fig. 113: SE-photograph showing euhedral smithsonite crystals in open pore space in siliclastic metasediment. Borehole SD07, sample 0711, depth 220.75 m.

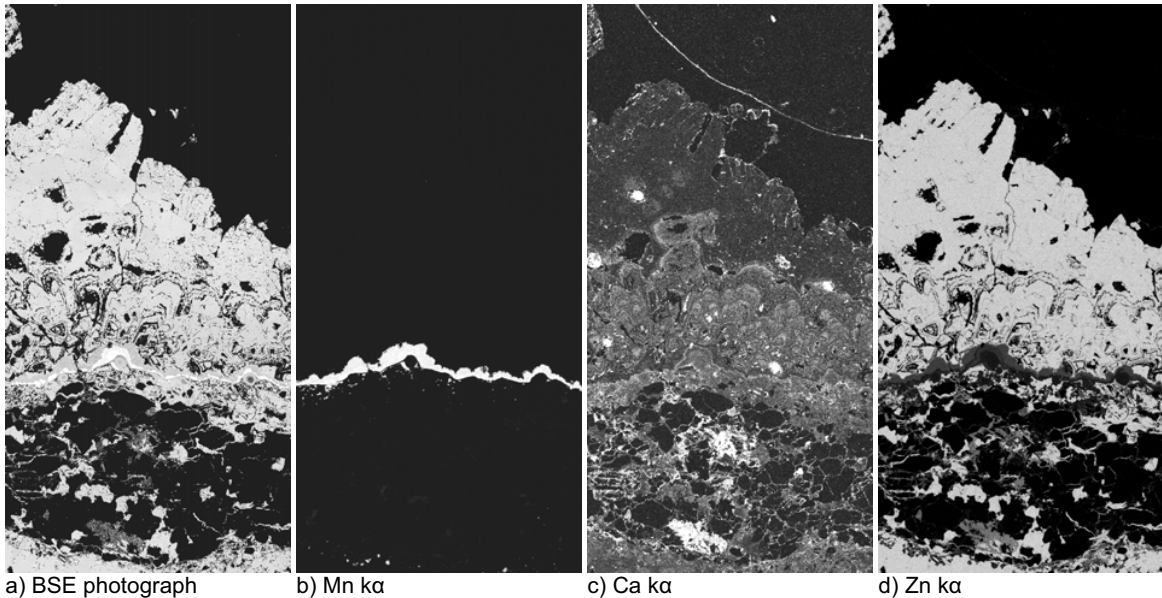


Fig. 114: Open space mineralisation of smithsonite, sample from the eastern pit area (640 m level). Different stages of smithsonite formation can be distinguished on basis of chemical composition analysed by electron microprobe techniques. Early-stage smithsonite (Fig. 114c), grown on zincian rhodochrosite (Fig. 114b), contains high amounts of MnO (2.9 %) and CaO (0.6 %). CaO and MnO have replaced Zn^{2+} in the smithsonite crystal lattice due to their similar ionic radii. Second-stage smithsonite contains only CaO (0.6 %). The third stage is characterised by the precipitation of pure zinc carbonate (Fig. 114d). The amount of Cd in the different generations of smithsonite is relatively constant averaging 0.2 % CdO. The different stages of smithsonite represent a nearly complete rhodochrosite-smithsonite ($MnCO_3$ - $ZnCO_3$) solid-solution series, whose growth stages are distinguishable by compositional changes. The occurrence of rhodochrosite-smithsonite series has also been reported by Böttcher et al. (1993) from the oxidised zone of the Broken Hill ore body, Australia.

Smithsonite from the Skorpion deposit is commonly impure and contains a high amount of trace elements averaging at 1377 ppm MgO, 4110 ppm CaO, 6564 ppm MnO, 532 ppm FeO, 1218 ppm CuO, 1531 ppm P₂O₅, and 1809 ppm CdO. The impurity of smithsonite is not uncommon and has also been reported from smithsonite of oxidised zones of base metal deposits worldwide, e.g. the supergene oxidised zone of the SHMS/VHMS Broken Hill ore body, Australia (Böttcher et al. 1993). At Skorpion, different stages of smithsonite are characterised by different concentrations of trace elements (Fig. 114).

Additionally, stable carbon and oxygen isotope studies on smithsonite have been carried out in order to elucidate the conditions of ore formation and the sources of the mineralising fluids. An accurate determination of isotope compositions and knowledge of the fractionation factors between minerals and water as a function of temperature are important for the correct interpretation of stable isotope data for carbonate minerals (Gilg et al. 2003a). Gilg established the phosphoric acid fractionation factors for smithsonite between 25 and 72°C (Gilg et al. 2003b). These factors are used to (re)calculate the isotope compositions of the studied smithsonite. Isotope compositions are expressed as delta values (δ) in per mil (‰) relative to V-SMOW (oxygen) and V-PDB (carbon).

Smithsonite samples from the Skorpion deposit show a very restricted range of $\delta^{18}\text{O}$ -values, with an average of 27.64 ‰ (range 27.32 – 28.13 ‰, n = 5). $\delta^{13}\text{C}$ -values vary between -3.99 and -8.01, averaging at -6.38 (Tab. 8). The comparison of the isotope composition of smithsonite from Skorpion with smithsonite from the oxidised zone of the SHMS/VHMS Broken Hill ore body, Australia ($\delta^{13}\text{C}_{\text{PDB}}$ -10.0 – -12.3, $\delta^{18}\text{O}_{\text{SMOW}}$ 26.5 – 28.1), but also of smithsonite from the oxidised zone of MVT-deposits of Sardinia (Gilg et al. 2001, Boni 2001) shows that they are very similar to each other (Fig. 115). This range of carbon isotope compositions points to a supergene origin of smithsonite (Boni 2001, Böttcher et al. 1993). In contrast, smithsonite of hypogene origin, e.g. early-stage smithsonite from the Anguran deposit, Iran (Gilg et al. 2003, Gilg & Boni 2004) is characterised by constant, but unusually heavy $\delta^{13}\text{C}$ values and variable $\delta^{18}\text{O}$ values, which points to a hydrothermal origin of smithsonite under variable thermal conditions (Gilg & Boni 2004).

Additionally, the $\delta^{18}\text{O}_{\text{SMOW}}$ values of smithsonite from the Skorpion deposit suggest a single, low-temperature meteoric fluid source and uniform formation temperatures (Boni et al. 2003). The low variability in the carbon isotope composition of smithsonite from the Skorpion deposit points to single isotopically uniform carbon source (Boni 2001). According to Boni (2001) and Böttcher et al. (1993) the isotopically light carbon component is generated by oxidation of organic matter under supergene low-temperature conditions, most likely in palaeo-soils. Therefore, it is reasonable to assume that the isotopically light carbon originated from the oxidation of organic matter as well. Thus, the carbon in smithsonite does not originate from carbon, bound to calcite in cements of the metasiliciclastic rocks or in marble. This hypothesis is supported by a markedly different isotopic composition of the marble, displaying $\delta^{13}\text{C}_{\text{PDB}}$ between 5.82 and 8.09, and $\delta^{18}\text{O}_{\text{SMOW}}$ between 17.70 and 19.48.

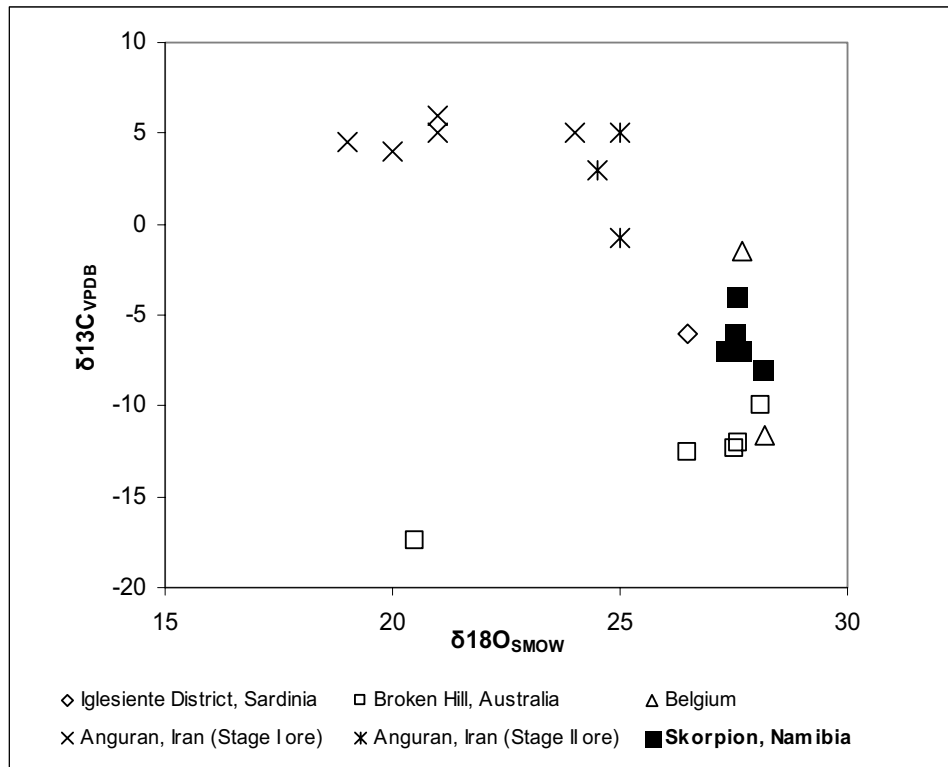


Fig. 115: Stable carbon and oxygen isotope composition of smithsonite from Skorpion deposit (n = 5) compared to smithsonite compositions from non-sulphide zinc deposits worldwide. Data from Boni (2001) [Sardinia], Böttcher et al. (1993) [Broken Hill], Gilg & Boni (2004) [Belgium, Iran].

Tab. 8: Carbon-, oxygen-isotope signature of smithsonite from the Skorpion deposit.

Sample no.	Borehole	Depth [m]	Mineral, rock type	$\delta^{13}\text{C}_{\text{VPDB}}$	$\delta^{18}\text{O}_{\text{VSMOW}}$
BH 7007	BH70	59.8	Smithsonite, metasiliciclastic unit	-6.03	27.53
0807	SD08	69.2	Smithsonite, metasiliciclastic unit	-3.99	27.58
8027	SD80	226.4	Smithsonite, metasiliciclastic unit	-8.01	28.13
0727	SD07	109.5	Smithsonite, metasiliciclastic unit	-6.93	27.64
0711	SD07	220.75	Smithsonite, metasiliciclastic unit	-6.92	27.32
0721	SD07	245.15	Calcite, marble	8.09	19.48
8001	SD80	171.84	Calcite, marble	5.82	17.70



Fig. 116: White colloform hydrozincite grown unhindered in open pore space. In this example, hydrozincite forms a coating on colloform goethite. Stockpile sample, Skorpion Mine.

3.7.4.2.4 Hydrozincite

Hydrozincite occurs within the uppermost portion of the non-sulphide ore body impregnating the highly to completely weathered host rocks or filling secondary open pore space as well as fractures (Fig. 116). Hydrozincite forms either microcrystalline masses or colloform crusts (Fig. 111).

3.7.4.2.5 Zn-bearing Phosphates

Several zinc-bearing phosphates were found within the non-sulphide ore body. The dominant phosphate is light-green tarbuttite ($Zn_2[OH/PO_4]$). At the time of the research, the major occurrence was located in the eastern part of the Skorpion open pit on the 645 m level. This tarbuttite occurrence is hosted by solution collapse breccias in metasediments. The tan-coloured metasedimentary breccia clasts are friable, weathered and mineralised by saucornite and/or smithsonite (Fig. 117). These breccia clasts are cemented mainly by tarbuttite. In places, tarbuttite has grown unhindered in open pore space and forms beautiful euhedral crystals (Fig. 118). Microscopic investigations have shown that minor scholzite ($CaZn[PO_4]_2 \cdot 2H_2O$) is intergrown with tarbuttite, though scholzite-dominated solution collapse breccias occur as well (Fig. 59). Microprobe analyses have revealed that both tarbuttite and scholzite contain traces of CdO averaging at 0.3 % and 0.1 %, respectively. The cadmium has most likely been released by the dissolution of primary sphalerite, as it is the only Cd-bearing hypogene sulphide mineral.

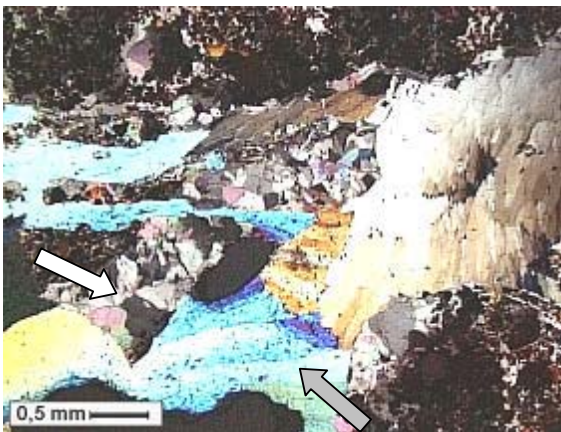


Fig. 117: Photomicrograph of a thin section showing early-stage smithsonite (white arrow) and late-stage tarbuttite (grey arrow) in solution collapse breccia. Sample SK0204, Skorpion open pit, 645 level m. XN.



Fig. 118: Solution collapse breccia with euhedral crystals of tarbuttite grown in open space. Skorpion open pit, 640 m level.

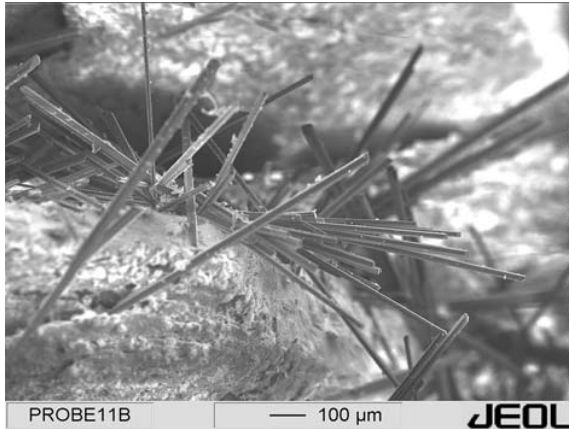


Fig. 119: SEM-photograph of individual needles of skorpionite grown on tarbutite.

In places, colourless needles up to 1 mm in length and up to 30 or 40 μm in width are grown on tarbutite (Fig. 119). These needles have been identified as a new mineral by Bernhardt et al. (submitted). They submitted the new mineral to the IMA under the name skorpionite ($\text{Ca}_3\text{Zn}_2(\text{PO}_4)_2\text{CO}_3(\text{OH})_2 \cdot \text{H}_2\text{O}$). Additionally, zincolebithenite, a Zn-dominant analogue of libethenite ($\text{CuZn}(\text{PO}_4)\text{OH}$) has been found in a sample from the Skorpion open pit by L. Krahn (pers. comm.).

3.7.4.2.6 Cu-bearing Minerals

The presence of primary chalcopyrite and its subsequent dissolution during weathering led to the formation of various secondary supergene copper minerals. Remnants of chalcopyrite are exclusively found in the felsic metavolcanic rocks, whereas, secondary copper minerals are found in both, metasedimentary (Fig. 120) and felsic metavolcanic rocks (Fig. 33 & 121). The major secondary copper mineral is malachite ($\text{Cu}_2(\text{CO}_3)(\text{OH})_2$), followed by atacamite ($\text{Cu}_2\text{Cl}(\text{OH})_3$) and chrysocolla ($\text{CuSiO}_3 \cdot n\text{H}_2\text{O}$).

Malachite occurs as impregnations (Fig. 122) but also as pseudomorphs after primary sulphides (Fig. 123) in both metasedimentary and felsic metavolcanic rocks, which indicates that it has formed by in-situ oxidation of primary chalcopyrite as well as by remobilisation of copper. Chrysocolla and atacamite are mainly found as impregnations, indicating that they have formed exclusively as a result of remobilised copper.



Fig. 120: Photograph of drill core showing malachite-stained brecciated meta-arkose. Borehole SD65, sample 6516, depth 127.54 m, length of drill core ~15 cm.

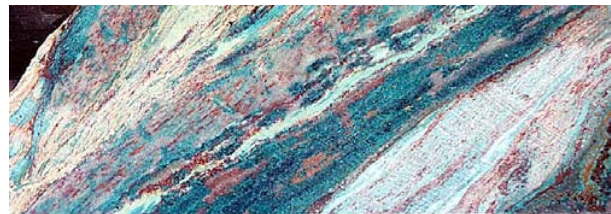


Fig. 121: Photograph of a drill core showing highly foliated felsic metavolcanic rock ('sheared sericite schist') mineralised by atacamite. Atacamite (green) forms discontinuous laminae parallel to the foliation planes. Borehole SD65, sample 6508, depth 111.25 m, length of drill core ~15 cm.



Fig. 122: Photomicrograph of a thin section showing malachite-impregnation in brecciated felsic metavolcanic rock. Malachite (green) is found mainly between individual mica layers. Pseudomorphs of goethite after pyrite can be seen as well. Borehole SD65, sample 6506, depth 113.5 m. LLP.

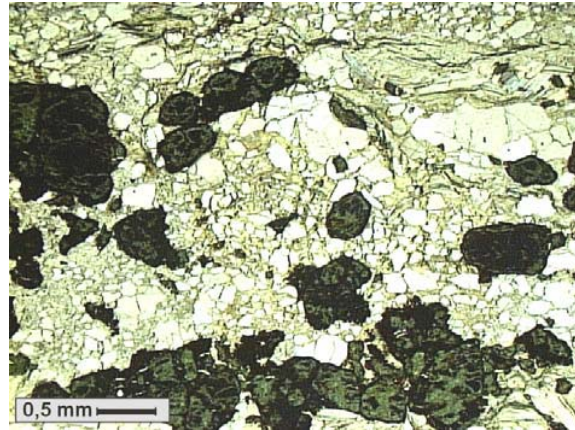


Fig. 123: Photomicrograph of a thin section showing malachite-impregnation in brecciated felsic metavolcanic rock. Malachite (green) replaces primary sulphide aggregates. Borehole SD65, sample 6506, depth 113.5 m. LLP.

3.7.4.2.7 Manganese Oxides



Fig. 124: Colloform chalcophanite, grown in open pore space on tarbuttite with hydrozincite veneer. Skorpion open pit, 645 m level.

Manganese oxides are readily recognised in hand-specimens by their distinctive dull black colour. Their finely banded or colloform texture is readily seen with a hand-lens but specific identification of manganese oxide minerals by optical means is difficult and thus, X-ray powder diffraction technique has been used. However, the results were often inconclusive and final identification required the use of SEM-EDX technique.

Manganese oxides occur as discrete masses, void and fracture fillings and discontinuous bands. Besides chalcophanite (Fig. 124), manganese has also been found in the form of hydroheteorolite ($Zn_2Mn_4O_8 \cdot H_2O$) and psilomelane. Hydro-

heteorolite as well as chalcophanite are spatially closely related to the supergene zinc mineralisation, whereas psilomelane is mainly associated with the gossaneous iron-rich portion of the Skorpion deposit.

3.7.4.2.8 Iron Hydroxides

Iron hydroxides have been found at the Skorpion deposit but also in gossans (Fig. 125 & 126) near the Skorpion deposit. The most famous gossan is the so-called 'discovery outcrop', some hundred meters west of the Skorpion non-sulphide zinc deposit (Fig. 125). The gossan is hosted by the same felsic metavolcanic rocks that are host to the primary sulphide mineralisation in the footwall of the Skorpion non-sulphide deposit. It contains

mainly hematite and barite, and is the most famous gossan within the Skorpion area since it led to the discovery of the Skorpion non-sulphide ore body.

In the vicinity of the 'discovery outcrop', felsic metavolcanic rocks are exposed as well, which also host a few massive, but small gossans. These gossans commonly contain goethite, quartz, and traces of barite and REE minerals (Fig. 127 & 128). Additionally, the felsic metavolcanic rocks contain abundant disseminated pseudomorphs of goethite after pyrite. In places, the felsic metavolcanic rocks are fractured and slightly brecciated; and fractures are filled by goethite (Fig. 126).



Fig. 125: 'Discovery outcrop' west of Skorpion mine (open pit in the background).

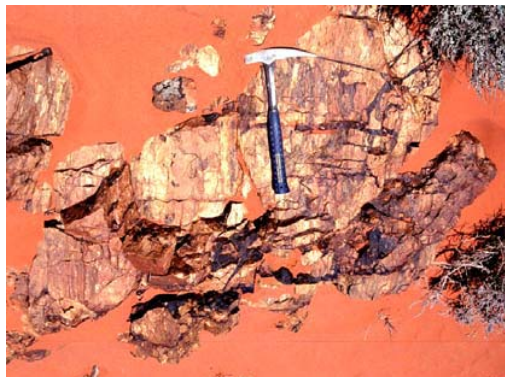


Fig. 126: Gossaneous, slightly brecciated felsic metavolcanic rock in the vicinity of the 'discovery outcrop', which is shown in Fig. 125.

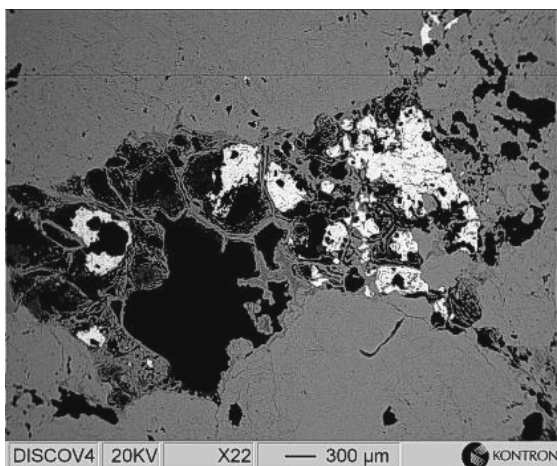


Fig. 127: BSE-photograph of a thin section showing a gossan sample from the 'discovery outcrop' west of Skorpion mine. Massive hematite features a cellular boxwork texture. Open spaces are filled by barite. Sample SK0217.

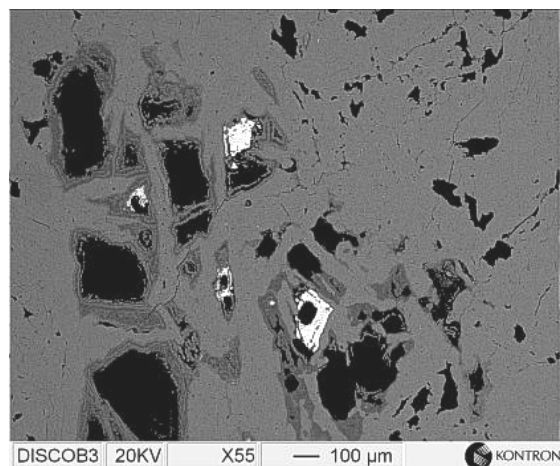


Fig. 128: Detail of Fig. 127 showing the porous cellular boxwork texture. Different grey tones of hematite are the result of different concentrations of trace elements. Microcrystalline hematite surrounding cellular boxwork texture averages at 4 % SiO₂, 1.7 % CuO, 0.8 % P₂O₅, 0.7 % CaO, and 0.6 % SO₂.

The gossan of the 'discovery outcrop' as well as gossaneous outcrops of felsic metavolcanic rocks in the vicinity of the Skorpion deposit show unequivocally that the Late Proterozoic felsic metavolcanic rocks were originally mineralised by base metal sulphides.

The geochemical composition of goethite-bearing gossans from felsic metavolcanic rocks west of the Skorpion deposit averages at 60.3 % Fe₂O₃, 0.4 % MnO, 0.4 % Ba, and 0.16 % S. Their base metal concentration, however, is very low and averages only at 1.4 % Zn. Cu

and Pb concentrations are commonly below detection limit using XRF technique. Hematite-bearing samples from the 'discovery outcrop' are even lower in base metals averaging only at 132 ppm Zn. Pb and Cu were not detected.

The low base metal content might indicate that they represent pyritic portions of the primary Late Proterozoic sulphide mineralisation, as gossans derived from massive Zn-Pb-Cu ore generally have higher amounts of base metals (Scott et al. 2001).

Additionally, there is a lot of evidence for a ferruginous oxidate zone as defined by Scott et al. (2001) consisting of various manganese oxides and goethite. The ferruginous oxidate zone is widely exposed in the Skorpion open pit along the western wall on the 645 m level (Fig. 129 & 130), but can also be seen in drill core in both metasedimentary and felsic metavolcanic rocks (Fig. 34). These gossaneous samples contain quartz, goethite, manganomelane, kaolinite, and minor muscovite. Their geochemical composition was determined using XRF-technique and averages at 7.1 % MnO, 32.3 % Fe₂O₃, 0.7 % Ba and 708 ppm S. Additionally, their base metal content averages at 0.4 % Pb, 1.2 % Zn, and 0.6 % Cu. SEM-EDX analyses have shown that the base metals are mainly incorporated into goethite (App. 2). These high base metal concentrations are indicative for gossans derived from the oxidation of a sulphidic Zn, Cu (Pb) mineralisation (Scott et al. 2001).

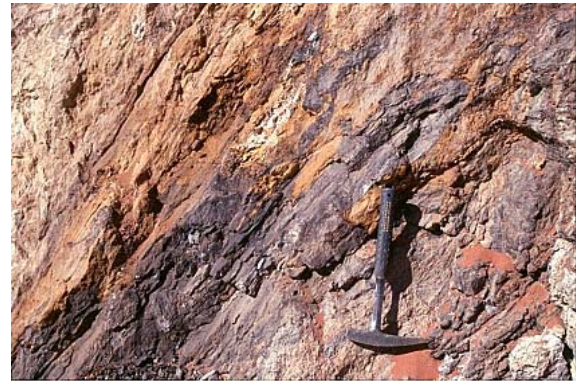


Fig. 129: Western wall of the Skorpion open pit, 640 m level. The photograph shows the uppermost of a gossan zone in metasediments and minor felsic metavolcanic rocks. The gossan consists mainly of semimassive to diffuse banded goethite and psilomelane.

Fig. 130: Detail of Fig. 129 showing semi-massive goethite and psilomelane.

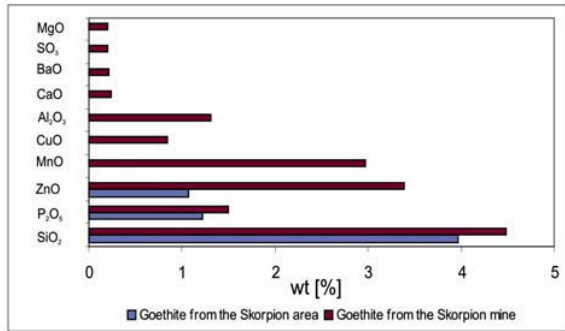


Fig. 131: Semiquantitative SEM-EDX analyses of goethite from the Skorpion mine and the wider Skorpion area showing that goethite from the Skorpion deposit is enriched mainly in base metals (Zn, Cu) but also Mn.

Iron oxide-dominated gossans from the Skorpion mine are composed of a micro- or cryptocrystalline matrix of goethite. SEM-EDX analyses of goethite have shown that it contains high amounts of base metal and other elements averaging at 3.4 % ZnO, 1.7 % CuO, 0.5 % CaO, 5.2 % MnO and 2 % P₂O₅ (Fig. 131). Additionally, pseudomorphs of goethite after pyrite from the high-grade zinc zone have been analysed by electron microprobe. Here, goethite also show high amounts of trace elements with 3.5 % ZnO, 0.4 % CuO, 1.2 % P₂O₅, 0.2 % MnO, 0.2 % MgO, 0.3 % CaO, 1.0 % Al₂O₃, 2.8 SiO₂, and 730 ppm CdO.

The manganese oxide-dominated gossaneous zones are composed of detrital material, mainly quartz, K-feldspar, and apatite, from which the latter two are partly dissolved. The detrital components are cemented by crypto- and microcrystalline minerals of Ba-poor, but Zn- and K-bearing members of the manganomelane group (cryptomelane) (Fig. 132 – 133). Remnants of minerals from an earlier stage of oxidation occur within the manganomelane masses, which are composed of Ba, Al-bearing phosphate, which is most likely gorceixite (Fig. 133).

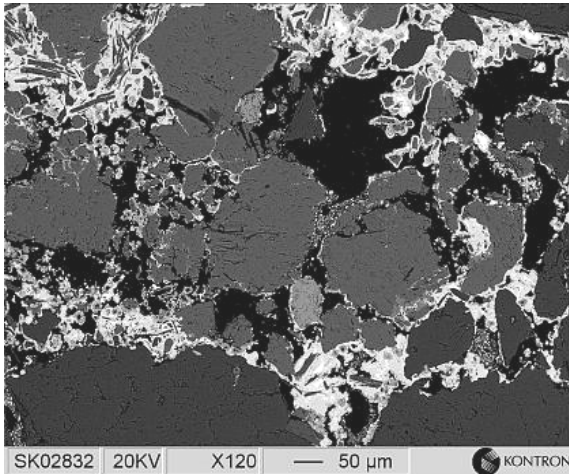


Fig. 132: BSE photograph of a manganiferous gossan with detrital quartz, orthoclase and apatite cemented mainly manganomelane. Manganomelane replaced a first stage of supergene mineralisation consisting of Ba-, Mn-, Zn-oxides and gorceixite. Sample SK0283, Skorpion mine, 645 m level.

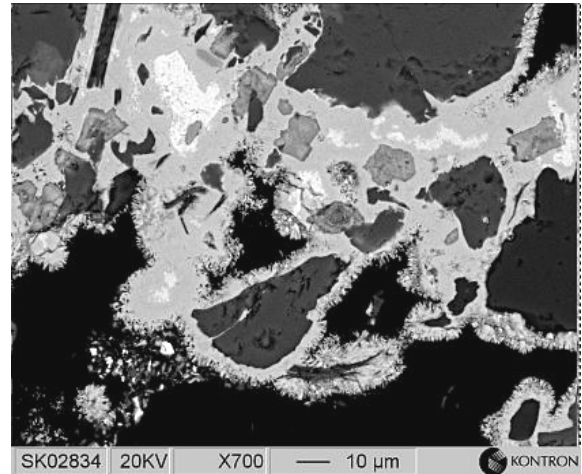


Fig. 133: Detail of Fig. 131: Manganomelane (light-grey) with remnants of gorceixite (medium-grey) and early-stage manganomelane (white) as well as detrital feldspar (dark-grey). BSE-photograph. Sample SK0283, Skorpion mine, 645 m level.

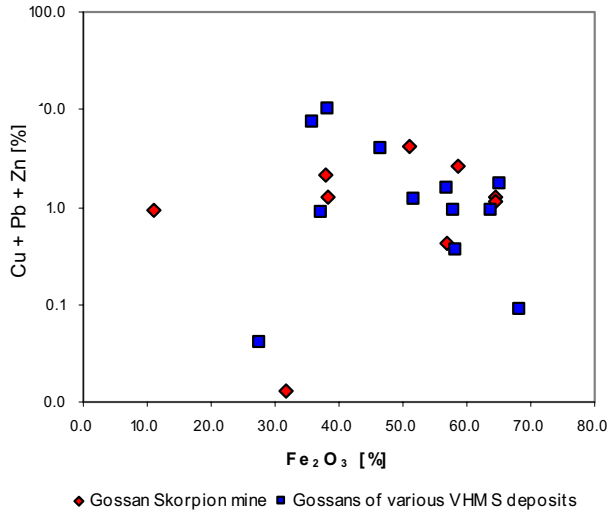


Fig. 134: Composition of gossaneous samples from the western wall of the Skorpion open pit compared to gossans of various VHMS deposits (data from various internet pages).

The distribution of base metals within the gossaneous samples from the Skorpion deposit is very similar to other base metal gossans worldwide (Fig. 134). Indeed, the deeper lying equivalent horizons of these gossaneous zones host primary sulphides. The average sulphide ore, determined from sulphide samples that entered into the present study contains 3.5 % Zn, 1.7 % Pb, and 0.1 % Cu. However, at this point it must be stressed that even the primary sulphides that are found at depth show evidence of a supergene overprint and are enriched in supergene sulphides.

However, a rough estimate comparing the average composition of the primary least altered sulphide paragenesis with the highly oxidised and altered gossaneous

samples from the Skorpion open pit shows that the highly altered gossaneous samples have lost about 35 mass % of their original Zn concentration, and 23 mass % of Pb as a result of their metal solubilities. Cd has not been detected in analysed samples of gossans, which most likely indicate that Zn was more strongly retained than Cd, which is in agreement with Scott et al. (2001), who presumed that Cd generally behaves more mobile than Zn during weathering. In contrast, Cu as a relatively immobile element has been retained during weathering, and is therefore enriched in the gossaneous samples.

3.8 Rock Weathering and the Formation of the Supergene Ore

3.8.1 Weathering and Profile Development

Supergene weathering takes place in near-surface or surface environments since minerals are only stable in the environment they formed under certain geochemical conditions. Especially, changes in pH/Eh conditions lead to the oxidation and the break-down of minerals and liberate products, which are in equilibrium with ambient surface/near-surface chemistry.

Thus, the supergene alteration of a primary mineral paragenesis leads to the development of a weathering profile including fresh parent rock, saprock, saprolite, and residual soil from the base to the top. Saprock is defined as a slightly altered parent rock, in which less than 20 % of the weatherable minerals are altered. More than 20 % of the weatherable minerals are altered within saprolite, though primary textures of the parent rock are still visible, even if the rock is partly disintegrated. In contrast, residual soils are completely disintegrated and weathered; the parent rock texture is not discernable anymore. Saprolite zones can easily reach a thickness of more than 100 m and are most likely to occur beneath remnants of relatively flat-surfaced upland areas (Gair et al. 1989).

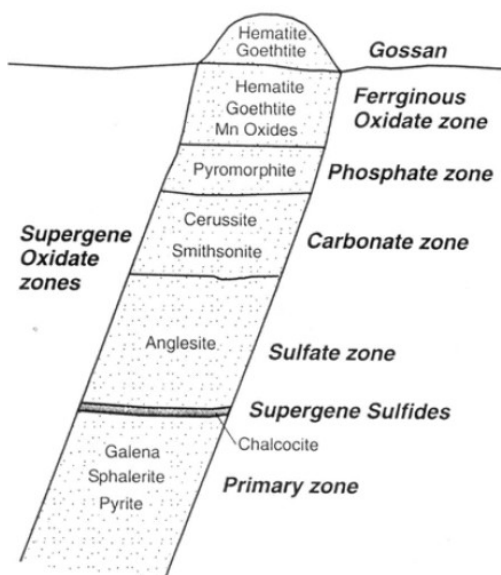


Fig. 135: Gossan profile above a volcanic Zn-Pb-Cu mineralisation, from Scott (2001).

The weathering includes not only the leaching of primary minerals such as feldspars, mica and calcite, but also the oxidation of ferrous iron minerals, e.g. pyrite. Additionally, weathering includes the precipitation of secondary minerals, such as clay minerals and a huge variety of other supergene base metal-bearing minerals. The weathering also results in the translocation of fine mineral particles, e.g. clay illuviation, because of the lateral and downward movement of water through the weathering profile (Gerrard 1994, Teeuw et al. 1994).

Summarizing it can be stated that the weathering profile developed from a primary sulphide deposit (Fig. 135) consists of saprolitic rocks containing a zone of supergene sulphides (in which the proportions of the metals are quite different from that in the primary ore) overlain by zones of secondary sulphate, carbonate and phosphate minerals of the supergene oxidised zone, before passing into the ferruginous

oxidate zone and finally into the exposed gossan, which may contain boxwork textures after the original sulphides. However, in cases there has not been enough time to develop a complete profile or erosion has partially stripped the upper Fe-oxide dominated portion of the profile, the weathering profile is incomplete (immature) with carbonate and phosphate minerals, especially malachite, being found in surficial material. These immature gossans contain more Cu, Pb and Zn than the mature gossans (Scott et al. 2001).

The process of chemical weathering of the Late Proterozoic rock sequence at Skorpion, and thus the formation of a thick saprolitic gossan profile, was controlled mainly by the availability of meteoric fluids, which percolated along suitable pathways, such as shear/fault zones on a

regional and macro-scale and inter-/intragranular pore space as well as micro fractures on a micro-scale. The relationship between permeability, fault zones, and deep oxidation supergene mineralisation has already been proven by Chavez (2000).

The thickness of the resulting saprolite/saprock profile, which hosts the non-sulphide ore body, averages at about 300 m, although zones of deeper weathering down to 800 m below surface, following fault zones and more susceptible rock types, can be observed as well (Corrans et al. 1993).

3.8.2 Parent Rock and Profile Development

The parent rocks, from which the Skorpion saprolite/saprock profile has developed, consist mainly of Late Proterozoic felsic metavolcanic as well as metasiliciclastic rocks. The main primary constituents of the parent rocks are quartz, mica (muscovite, minor biotite), feldspar (mainly orthoclase, minor plagioclase), calcite, and apatite.

The order, in which the main rock forming minerals are weathered in an open acidic environment, has been well established and mostly follows the sequence enumerated by Goldich (1938), namely:

plagioclase > biotite > orthoclase > muscovite > quartz,

classifying plagioclase as the most vulnerable, and quartz the most resistant mineral to chemical weathering.

3.8.2.1 Dissolution of Sulphides from Host Rocks

The dissolution of the main rock forming minerals has been initiated by acid meteoric fluids provided by the oxidation of pyrite, sphalerite, and minor chalcopyrite and galena, but also by the dissolution of calcite. The oxidation of primary sulphides within both felsic metavolcanic and metasiliciclastic host rocks produced sulphuric acid, insoluble iron hydroxides as well as Zn^{2+} , Pb^{2+} , and Cu^{2+} in solution.

The oxidation of the sulphides can be described as follows (Takahashi 1960):



Eh/pH diagrams (Fig. 136 – 138) infer that solutions, which are able to transport metals, must be acidic and oxidising. $\text{Fe}^{2+}_{(\text{aq})}$ and $\text{Fe}^{3+}_{(\text{aq})}$ can only be transported in aqueous solutions under strong acidic conditions ($\text{pH} < 4$). Furthermore, $\text{Fe}^{2+}_{(\text{aq})}$ requires highly oxidising ($\text{Eh} > 0.8$), whereas $\text{Fe}^{3+}_{(\text{aq})}$ requires moderate oxidising conditions ($\text{Eh} < 0.8$). In contrast to iron, Cu^{2+} and Zn^{2+} are also soluble under weakly acidic ($\text{pH} < 6$) and moderately oxidising conditions ($\text{Eh} < 0.8$).

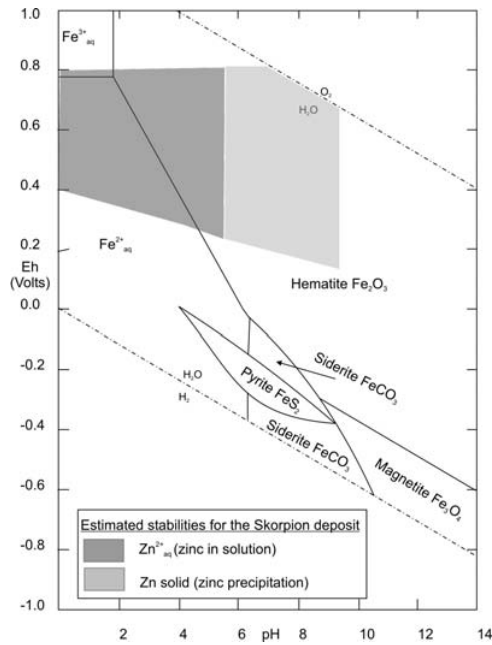


Fig. 136: Eh-pH diagram showing the stability fields of common iron minerals. Modified after Garrels & Christ (1990).

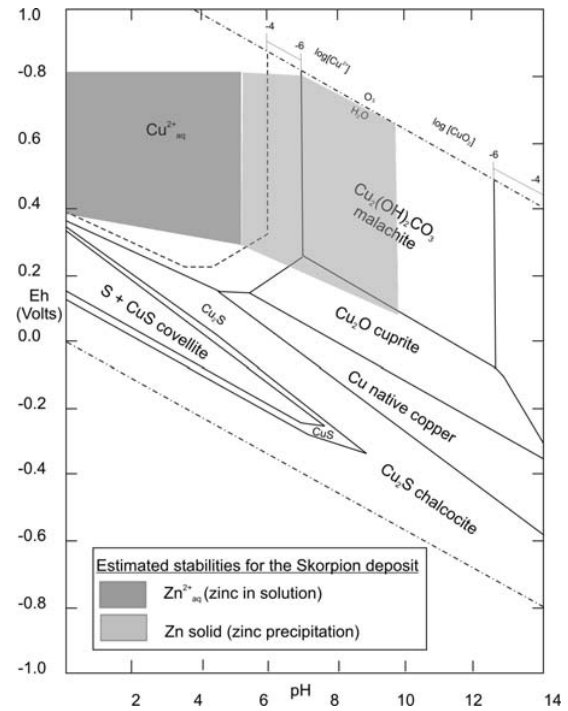


Fig. 137: Stability relations among some copper compounds in the system $\text{Cu-H}_2\text{O-O}_2\text{-S-CO}_2$ at 25°C and 1 atm total pressure. $P_{\text{CO}_2} = 10^{-3.5}$, total dissolved sulphur species = 10^{-1} . Modified after Garrels & Christ (1990).

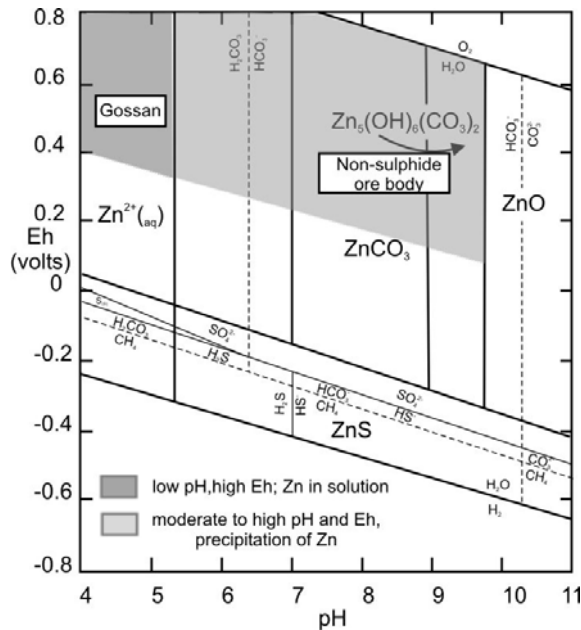
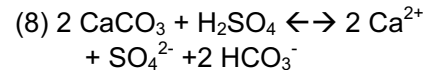


Fig. 138: Eh/pH stability reactions at 25°C and 1 atm of zinc compounds (heavy, solid lines). Activity of $Zn^{2+}_{aq} = 10^{-5.17}$. Thin solid and dashed lines represent the stability boundaries between the aqueous sulphur and carbon species, respectively. $\Sigma S = 10^{-2.27}$ and $\Sigma C = 10^{-1.48}$, respectively. Modified after Sangameshwar & Barnes (1983).

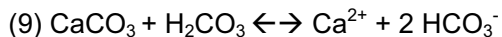
3.8.2.2 Dissolution of Calcite

The acidic metal-bearing solutions, which have been derived from the dissolution of primary sulphides, triggered the dissolution of calcite cements within the metasiliciclastic host rock by the sulphuric acid. The reaction equation can be written as follows:



Additionally, calcite weathering might have occurred by CO_2 in solution, produced by microorganisms and organic respiration and degradation. This process is likely to have occurred, as the influence of organic carbon on the weathering process has been proven by the carbon isotope signature of smithsonite (see chapter 3.7.4.2.3).

This dissolution process can be written as follows:



However, recent arid conditions within the Skorpion area exclude a high activity of microorganisms in the weathering profile. Therefore, it must be concluded that the dissolution of calcite represents a palaeo-weathering process. However, the timing details of the oxidation of primary mineral phases and precipitation of supergene mineral phases will be discussed separately.

The dissolution of calcite cements from the host rock led to a rapid decalcification, allowing the weathering front to penetrate more easily along suitable pathways such as secondary inter- and intragranular pore space within both metasiliciclastic and felsic metavolcanic host rocks. At this point, it should be stressed that the continuous dissolution of calcitic cements within the metasiliciclastic rocks resulted in a significant increase of secondary pore space, and thus in the development of a suitable host rock for the supergene ore body.

Summarizing it can be stated that two acids contributed to bedrock dissolution: i) strong sulphuric acid from sulphide oxidation and ii) weak carbonic acid from the dissolution of calcite. According to Hercod et al. (1998), the irreversible dissolution of sulphides is insensitive to seasonal changes in temperature, runoff, and organic activity and probably reflects the slow movement of a weathering front through an aquifer at depth. In contrast, temperature is the main factor controlling the process of calcite weathering from CO_2 in solution, as solute concentrations are highest in winter and spring, and lowest in summer when calcite solubility is least.

3.8.2.3 Dissolution of Feldspar

Strong sulphuric acid and weak carbonic acid, which were produced by the oxidation of sulphides and the dissolution of calcite, respectively, contributed to the formation of acidic supergene fluids. These acidic fluids migrated through the Late Proterozoic rock sequence along inter- and intragranular porosities, most likely preferentially following the foliation. The acidic supergene fluids were able to leach detrital silicate minerals, especially the feldspars within the Skorpion meta-arkoses (Fig. 139 – 142).

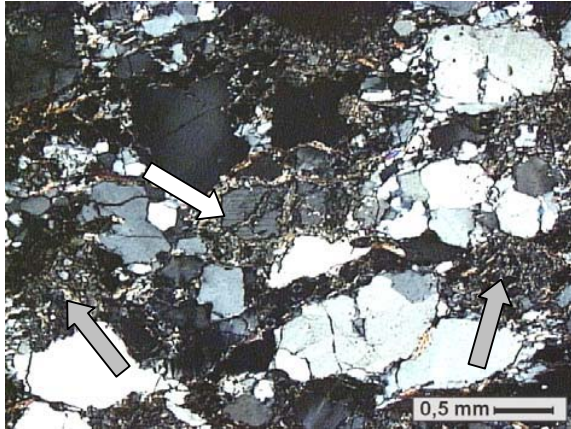


Fig. 139: Photomicrograph of a thin section showing a mineralised metasubarkose. The matrix takes up about 50 volume % and consists of sauconite. Remnants of plagioclase (arrow), which has partly been replaced by sauconite, are seen in the central part of the photograph. Completely replaced plagioclase can be seen as well (grey arrow) Sample 0318, borehole SD03, depth 27.5 m. XP.

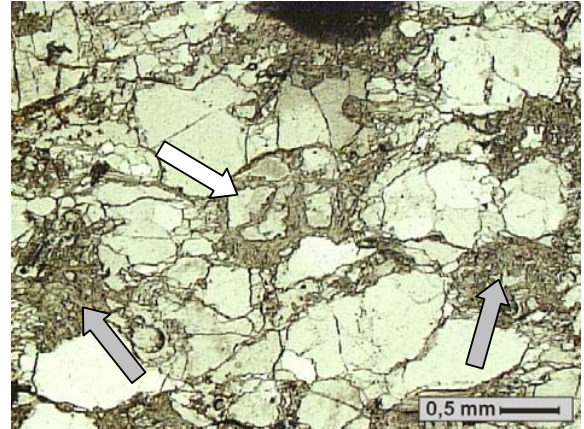


Fig. 140: Same frame as Fig. 139, but under LLP.

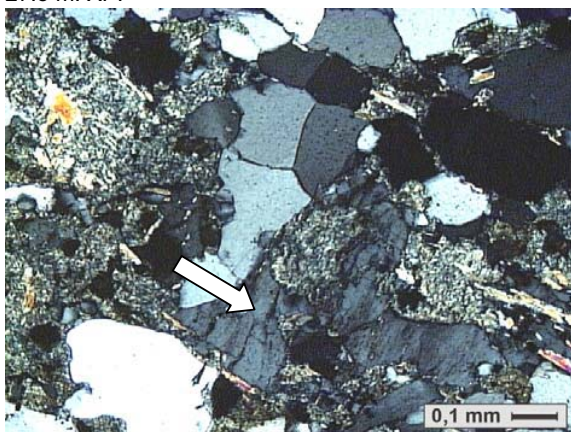


Fig. 141: Photomicrograph of a thin section showing sauconite-mineralised meta-arkose. Detrital orthoclase has partly been replaced by sauconite (arrow). Sample 4907, borehole SD49, depth 171.61 m. XP.

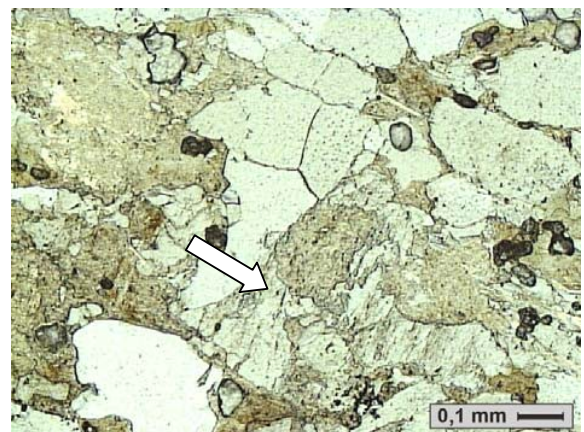


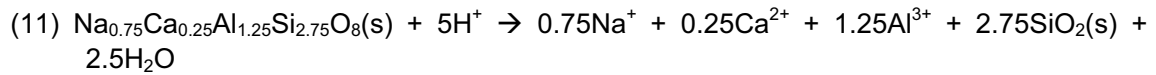
Fig. 142: Same frame as Fig. 141, but under LLP.

Generally, the acidic breakdown of feldspars can be extremely variable depending on thermodynamic conditions. Although kaolinite is the dominant clay mineral produced by the weathering of feldspars, other clay minerals can be produced as well (Gerrard 1994), e.g. gibbsite, montmorillonite, and smectite.

The feldspars within the metasiliciclastic host rocks of the Skorpion deposit are composed of orthoclase and plagioclase. Orthoclase features only initial stages of alteration such as the opening of grain boundaries, microfracturing, and the development of intragranular porosity (Fig. 141 – 142) as well as the formation of etch pits, and hairline cracks on mineral surfaces. The decomposition process (hydrolysis) of orthoclase can be written as follows:



By contrast, plagioclase is characterised by advanced mineral dissolution, the formation of inter- and intragranular pore space and the precipitation of secondary clay minerals that replace the primary phase (Fig. 139 – 140). The most common clay mineral is the Zn-bearing smectite (sauconite), which in fact forms a significant portion of the ore body. According to Gerrard (1994) the formation of smectite (sauconite) from plagioclase is favoured in relatively closed alkaline environments with the retention of alkaline earth and silica, hence the apparent relationship between sauconite and arid and semi-arid climates (Gerrard 1994). The relationship between climate and mineral formation will be discussed in a separate chapter. Additionally, kaolinite has been found locally (Fig. 71). The hydrolysis of plagioclase can be written as follows:



The hydrolysis equations of both orthoclase and plagioclase show that silica is a by-product of the decomposition process. The precipitation of silica led locally to secondary silification of the Late Proterozoic rocks (Fig. 143 – 144). Additionally, the limited dissolution of barium-bearing orthoclase (App. 2) has also released barium ions, which must have reacted to dissolved sulphur in the supergene fluid and precipitated as barite, and thus led to a secondary baritisation of Skorpion's host rocks (Fig. 37 & 104).

Additionally, it should be pointed out that the mineral-water reactions of the hydrolysis processes must have buffered the pH of the supergene fluids, since they produced two strong bases, namely NaOH and KOH (Sherman 2001). These bases contributed to the buffering/neutralisation of the acid meteoric fluid, which were migrating through the Skorpion meta-arkoses. Thus, the supergene fluids became less and less acidic during the progressive leaching of feldspars from the Late Proterozoic rocks. This neutralisation process played a significant role in the formation of the supergene non-sulphide zinc ore body, and is discussed separately in relation to mineral- and metal zonation patterns.



Fig. 143: Photograph of drill core showing slightly brecciated metasediment. Fractures are filled by quartz (white), because of secondary silification. Silica was released from the breakdown of feldspars. Borehole SD07, depth 105.15 m.



Fig. 144: Same photograph of drill core as Fig. 143. The light-orange reaction of the zinc indicator solution indicates a Zn concentration of about 5 %.

3.8.2.4 Dissolution of Mica

The Skorpion metasiliciclastic as well as metavolcaniclastic rocks contain micas, namely muscovite and minor biotite, which were also partly dissolved by the supergene acid fluids percolating through the rocks. Besides smectite (sauconite), this process has also formed two strong bases (KOH, NaOH), which buffered the pH of the supergene fluid (Sherman 2001).

The muscovite weathering can be written as follows:

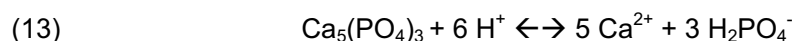


Though muscovite dominates within the original host rocks, smaller amounts of biotite occur as well, particularly within some of the felsic metavolcaniclastic rocks (mining term: quartz-biotite-schist). The weathering of biotite involves its alteration through vermiculite or mixed layer clay minerals to smectite and eventually kaolinite in temperate climates (Gerrard 1994, Sherman 2001).

3.8.2.5 Dissolution of Apatite

A minor constituent of the both metasiliciclastic and felsic metavolcanic rocks at the Skorpion deposit is apatite (Fig. 145 & 146). Dahanayake & Subasinghe (1989) have described the dissolution of apatite in a supergene environment. The dissolution of apatite (Fig. 146) released phosphorous that has been transported in the supergene fluid. The occurrence of various supergene zinc-bearing phosphates, e.g. tarbuttite and scholzite, shows that dissolved phosphorous was bounded onto zinc, which occurred in the solution as well.

The apatite dissolution process takes place in an acidic to neutral environment within a pH range from two to seven, and is characterised by increasing dissolution rates with decreasing pH (Valsami-Jones et al. 1998). The dissolution of apatite produces Ca in solution and contributes to the alkalinity of the meteoric fluid due to the release of OH⁻. The dissolution reaction can be written as follow:



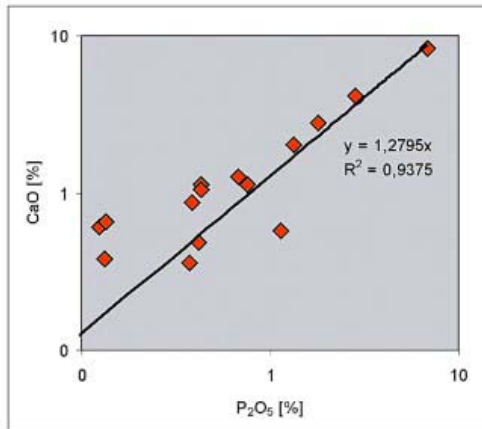


Fig. 145: Diagram showing CaO versus P₂O₅ of samples from borehole BH70 covering an interval of 100.4 m (depth 0 – 100.4 m). The positive linear trend indicates the occurrence of apatite throughout the lithological column including metasiliclastic and metavolcanic rocks.

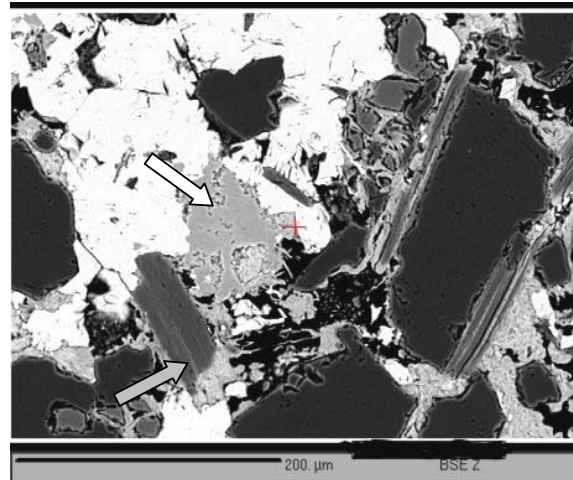


Fig. 146: BSE-photograph of a meta-arkose showing detrital quartz, mica (grey arrow) and apatite (white arrow). The two latter have partly been dissolved and replaced by sauconite. The matrix consists of smithsonite (white) and sauconite (light-grey). Borehole BH70, sample BH7007, depth 59.8 m.

3.8.2.6 Precipitation of Supergene Ore Minerals

3.8.2.6.1 Solubility of Metals

The previous chapter has shown that the oxidation of primary sulphides led to the release of base metals and, subsequently, to their transport in aqueous, initially acidic solutions. These metal-bearing fluids percolated through the rocks and were able to dissolve calcitic cements as well as some of the detrital siliclastic components from the Late Proterozoic metavolcanic and metasiliclastic host rocks. During this process, secondary inter- and intragranular pore space was formed, and as a result of this process, these rock units provided a suitable host to secondary supergene minerals, e.g. the non-sulphide ore minerals. The secondary supergene minerals impregnated the host rocks, replaced feldspars, micas, and calcite cements. Locally, extensive weathering of the host rocks led even to solution collapse and the formation of breccia-type ore (Fig. 58 & 59). However, it is important to note that not all non-sulphide mineralised breccias found at Skorpion have originated from solution collapse. In some of the breccias the non-sulphide mineralisation clearly post-dates the formation of the breccia. Those breccias are thought to have a tectonic origin and represent brittle-ductile shear zones (Fig. 56 & 57). For completeness, it should be mentioned that the tectonic breccias are usually well-mineralised, indicating that these breccia zones provided suitable permeabilities and porosities for the supergene zinc-bearing fluids.

Additional to the impregnation of the metasiliclastic and metavolcanic host rocks and the occurrence of breccia-type ore, there is also strong evidence of in-situ replacement of primary hypogene sulphides within felsic metavolcanic, -volcaniclastic as well as metasiliclastic host rocks by secondary supergene sulphides and non-sulphides in the form of laminated/banded supergene minerals.

The solubility of the relevant metals exerts the most significant control on the precipitation mechanism of secondary minerals at Skorpion. According to the values given in Tab. 9, hydroxides of iron and manganese, which were formed by the oxidation of sulphides, are

insoluble and as such would be expected to remain as precipitates in or very proximal to the source area and locally form pseudomorphs after primary sulphides.

Copper precipitates as a Cu-carbonate (malachite) under strong acidic and strongly oxidising conditions, as Cu-oxide or native metal under less oxidising conditions or as Cu-chloride under weak acidic conditions. Generally, copper is also relative immobile compared to lead and zinc, though its solubility is still higher than that of iron. Consequently, supergene copper-bearing minerals would be expected to replace primary sulphides directly, but also occur as impregnations in the immediate vicinity of the source rock.

Pb is more soluble but still forms insoluble supergene sulphides, carbonates, and sulphates in the immediate vicinity of the source rock. In contrast, zinc and cadmium are a highly mobile metals, and therefore, can easily be removed and transported away from the source rock, and thus would be expected to occur at a distance from the source rock, if thermodynamic and geochemical conditions enable a precipitation of secondary zinc-bearing minerals.

Tab. 9. Solubility or maximum concentrations of metals in equilibrium with common anions at 25°C. Columns 1-5 represent natural conditions in the oxidised zone. The S²⁻ concentration in the last column is typical of conditions at the base of the oxidised zone. Certain conditions have been set: (1) Eh is assumed to be in the oxidising range to prevent appreciable hydrolysis; (2) columns 3 and 4 assume slightly acidic conditions to prevent the precipitation of CuSO₄ and CuCl₂. From: <http://www.geology.csupomona.edu/drjessey/class/chemnote.htm>

	OH-	CO ₃ ²⁻	SO ₄ ²⁻	Cl ⁻	Eh	S ²⁻
Ca	10 ^{-4.3}	10 ^{-5.0}	>1	>1	10 ^{-1.3}	10 ^{-14.3}
Ag	>1	>1	>1	10 ^{-6.7}	10 ^{-8.5}	10 ^{-15.0}
Hg	10 ^{-6.8}	10 ^{-6.8}	10 ^{-3.9}	10 ^{-9.5}	10 ^{-16.3}	10 ^{-33.3}
Pb	>1	10 ^{-5.4}	10 ^{-5.8}	>1	>1	10 ^{-7.5}
Zn	0.2	10 ^{-3.3}	>1	>1	>1	10 ^{-4.7}
Cd	>1	10 ^{-6.0}	>1	>1	>1	10 ^{-7.0}
Sn	10 ^{-7.8}	10 ^{-7.8}	>1	>1	>1	10 ^{-5.9}
Ni	0.2	0.2	>1	>1	>1	10 ^{-6.6}
Co	>1	10 ^{-3.3}	>1	>1	>1	10 ^{-5.6}
Mn	10 ^{-6.0}	10 ^{-6.0}	>1	>1	>1	>1
Fe	10 ⁻¹³	10 ⁻¹³	>1	>1	>1	>1

3.8.2.6.2 Supergene Metal Zonation Pattern

The mobilisation and re-precipitation process of metals, with its solubility-controlled separation of iron, manganese and base metals, resulted in the formation of the markedly zinc-dominated non-sulphide ore body at Skorpion, which contains only minor concentrations of copper and no substantial amounts of lead. At Skorpion, two major iron-rich zones can be defined within the current pit outline (Fig. 147). The westernmost zone occurs within metavolcaniclastic and metasiliciclastic rocks, which belong mainly to the structural Domain I, defined by Dirks (2004), though it also crosses the domain boundary, which represents a Mesozoic brittle-ductile shear zone as part of a wrench fault system (Borg et al. 2004), and continues within Domain II. A second iron-rich zone is located within the northern part of the structural Domain II. Looking at the copper distribution at the same level of the open pit, it can be seen, that copper-rich zones are partly located east of the iron-rich zones, but in part also overlap with them (Fig. 148). Similar to the iron zones, the copper zone crosses one of the N-S trending fault zones. Zinc enrichment zones are clearly separated from iron-rich zones and the former are located significantly east of the latter ones (Fig. 149).

The more random distribution of manganese (Fig. 150) results from its different oxidation states. The occurrence of Mn^{2+} is generally related to a low pH/high Eh environment (Garrels & Christ 1990), and thus coincident with iron zones. On the other side, Mn^{3+} and Mn^{4+} are found in moderate pH/Eh environments (Garrels & Christ 1990) and thus, are associated with zinc enrichment zones.

Consequently, the supergene zinc ore body is characterised by a distinct lateral supergene metal zonation pattern. The lateral zonation displays an onion-like shape with a zinc-rich zone in the eastern and southeastern mining area and an iron-rich zone located mainly in the western pit area. A distinct copper rich zone and a subordinate lead enrichment zone occur between the (proximal) iron-/manganese-rich and the (distal) zinc-rich zones, with limited overlap between the individual zones. In contrast, a weak vertical metal zonation pattern is locally developed, but much less discernible.

Primarily controlled by metal solubilities, the lateral zonation pattern indicates a lateral migration direction of the metal-bearing fluids from NW/WNW to SE/ESE over a maximum distance of about 300 or 400 meters considering the lateral extent of the metal zonation pattern. The solution/precipitation process and, as a result, the formation of the supergene Skorpion ore body, post-dates the N-S-trending Mesozoic shear zones (domain boundaries), since the supergene metal zonation crosses the domain boundaries, and thus the shear zones (Fig. 151 & 152). However, the shear zone system has apparently partly affected the migration of the meteoric metal-bearing fluids, as the highest zinc concentrations (supergene ore body) follow the trend of the shear zone system (Fig. 86). A partly structural control of the mineralising event was first proposed by Corrans et al. (1993), assuming that faults, related to the break-up of Gondwana might have been responsible for the extreme deep oxidation and weathering of the Skorpion sulphide precursor, locally to more than 800 m depth. This is in agreement with the observations during the present metallogenic study that also suggests that the fault zones provided suitable permeabilities and ground preparation for oxidising/mineralising fluids, and thus controlled at least partly the supergene mineralising event. The development of the brittle-ductile wrench fault system resulted in the development of an abundance of dilatational joints and fractures, which drastically increased the reactive surface of the host rock (Borg et al. 2004). The enormous depth of oxidation is best explained by thermal convection of meteoric fluids below the groundwater table within the wrench fault system (Borg et al. 2004). Oxidation in such depths is impossible to explain by only lateral movement or vertical fluctuations of groundwater. However, away from the immediate fault zones, in the zone of groundwater closer to the ancient land surface, the lateral movement of groundwater led to the development of the pronounced lateral supergene metal zonation.

Assuming that the zinc-bearing supergene fluids moved from WNW to ESE, one might ask why the marble unit, which forms an antiform in the east and south, is not mineralised. The oxidation of primary sulphides in the western portion of the non-sulphide ore body, represented by the iron-rich zone, released sulphuric acid. The strong sulphuric acid together with weak carbonic acid, produced from the weathering calcite cements of the siliciclastic metasediments, contributed to the formation of highly acidic supergene fluids that were able to break down mainly feldspars, mica and minor apatite while migrating through the Skorpion siliciclastic metasediments and felsic metavolcanic host rocks. The mineral-water reactions buffered the pH of the supergene fluids. As it will be shown in detail in the next chapter, the majority of the non-sulphide zinc minerals requires slightly acidic to slightly alkaline conditions to precipitate. Therefore, conditions were favourable for the non-sulphide zinc minerals in an environment, where the breakdown of feldspar and mica occurred. Additionally, the breakdown of feldspar and mica provided secondary inter- and intragranular porosities, and thus suitable open space for non-sulphide mineralisation.

On the other side, the fluids not only became more alkaline through the progressive release of Na⁺, K⁺, and OH⁻, but also depleted in zinc, while migrating east towards the marble contact. Therefore, the supergene fluids were alkaline, when they hit the marble, and thus were unable to dissolve calcite of the marble, as calcite can only be dissolved under acidic conditions. As a result, the remaining zinc in solution precipitated along the marble contact.

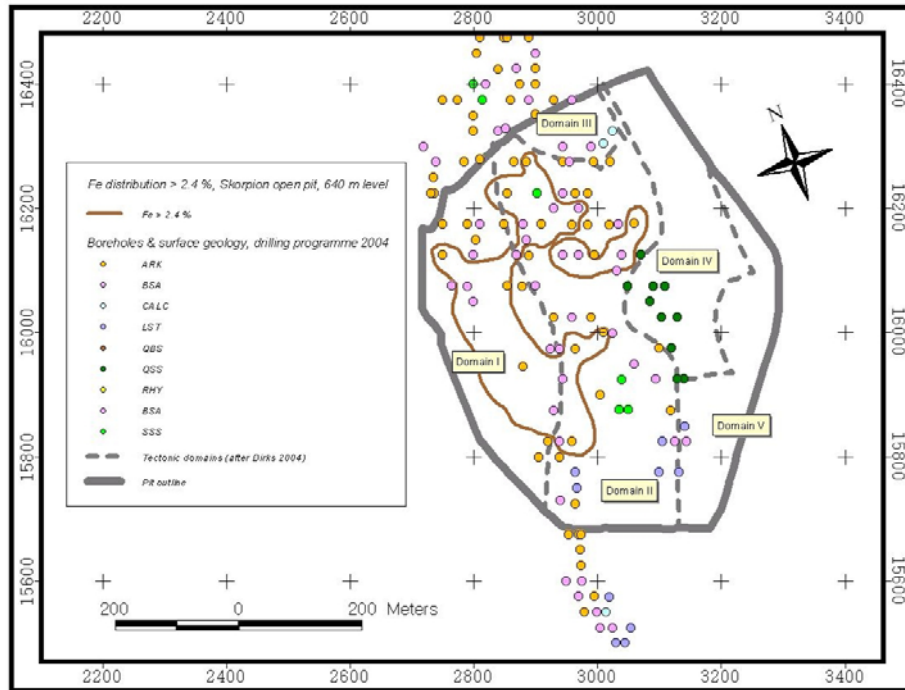


Fig. 147: Iron distribution (Fe > 2.4 %) at the Skorpion open pit, 640 m level. Two iron-rich zones occur, one in the north-western pit area, belonging to Domain I, and another one in the northern pit area belonging to Domain II. The distribution pattern shows that the iron-rich zones cross the domain boundaries, which are marked by N-S-trending brittle ductile shear zones.

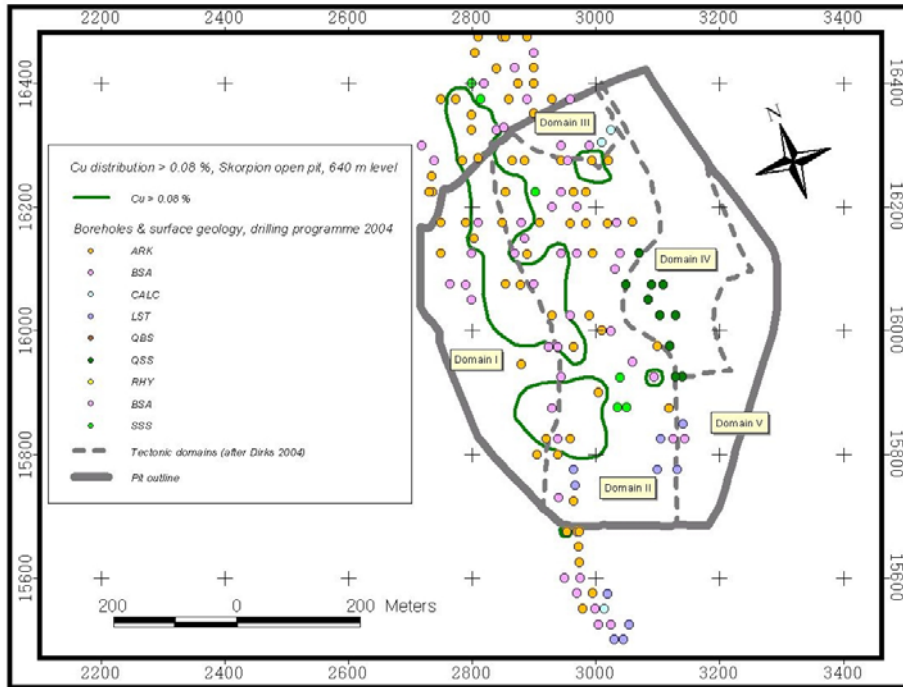


Fig. 148: Copper distribution (Cu > 0.08 %) at the Skorpion open pit, 640 m level. The distribution pattern shows that elevated copper concentrations following the trend of an N-S trending brittle shear zone (domain boundary), but they also cross this fault zone. Thus, copper enrichment occurs within both, Domains I and II, defined by Dirks (2004).

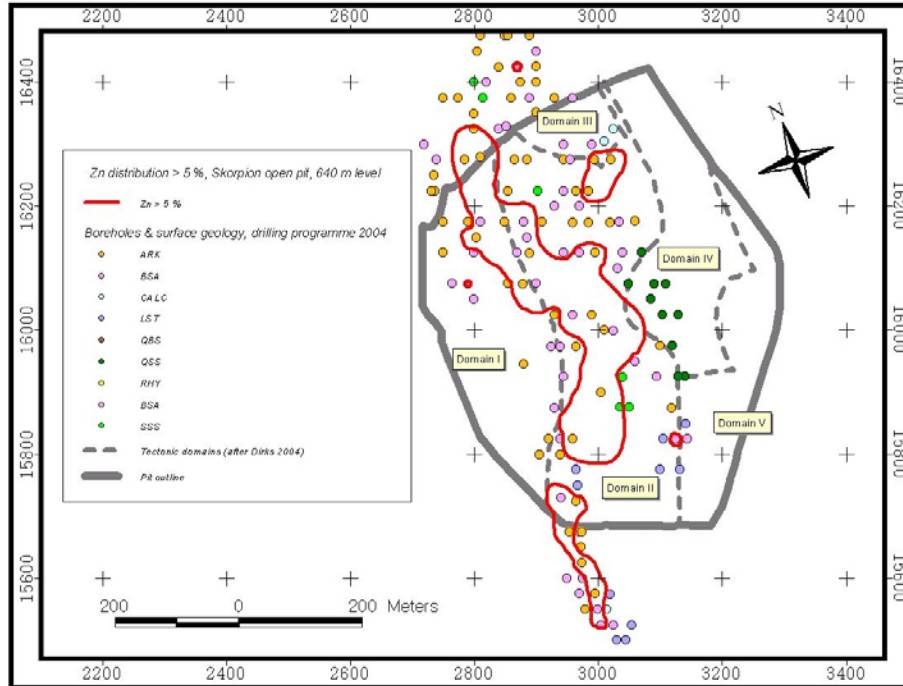


Fig. 149: Zinc distribution (Zn > 5 %) at the Skorpion open pit, 640 m level. The distribution pattern shows that the zinc enrichment zone follows the N-S trend of a brittle shear zone, which also represents a domain boundary. The main part of the non-sulphide zinc mineralisation occurs in Domain II. However, the zinc enrichment zone crosses the domain boundary in the north-western part of the Skorpion deposit.

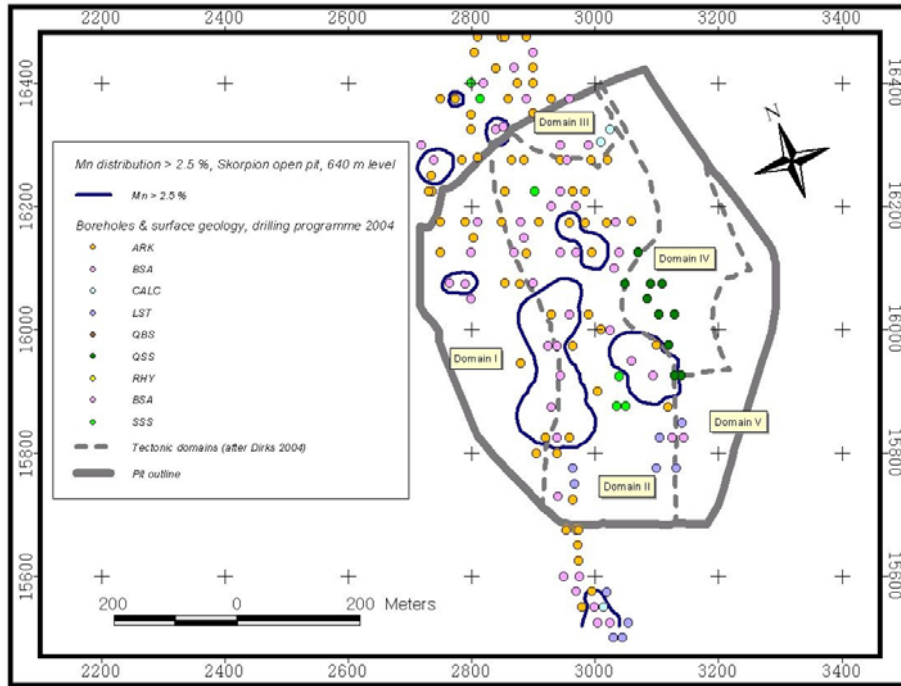


Fig. 150: Manganese distribution (Mn > 2.5 %) at the Skorpion open pit, 640 m level. The distribution pattern shows that zones of manganese enrichment are distributed over the entire pit area.

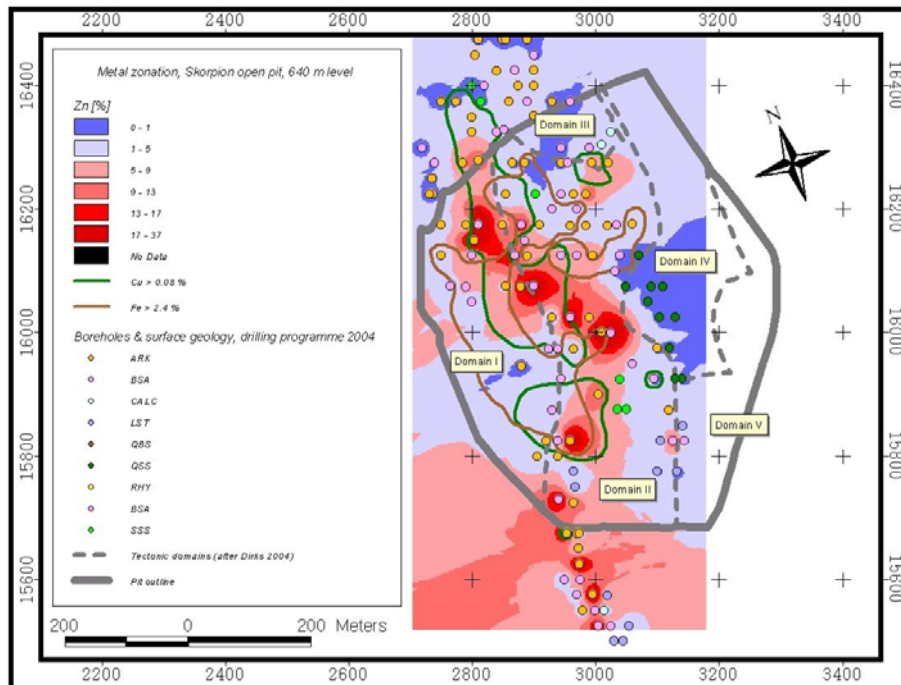


Fig. 151: Supergene metal zonation pattern the Skorpion open pit, 640 m level. The distribution pattern shows a lateral metal zonation. A major iron-rich zone on the west is separated from the zinc enrichment zone further to the east. A copper enrichment zone occurs in between and partly overlaps with the iron and zinc zone. The supergene metal zonation follows and crosses N-S trending brittle shear zones (domain boundaries defined by Dirks 2004), indicating that the mineralisation event post-dates the formation of the shear zones.

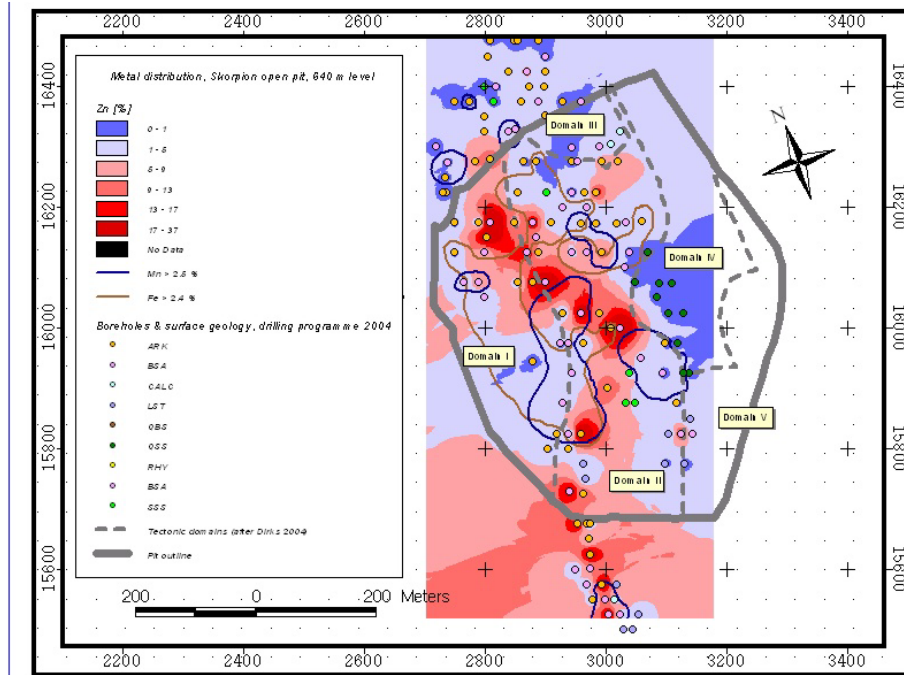


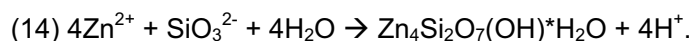
Fig. 152: Metal zonation pattern showing zinc concentrations as well as iron and manganese contours at the Skorpion open pit, 640 m level. The distribution pattern shows a lateral zonation pattern. An iron-rich zone in the west is separated from a zinc enrichment zone further to the east.

3.8.2.6.3 Supergene Mineral Zonation Pattern

The metal zonation pattern described above induced a supergene mineral zonation pattern as well. The dissolution of hypogene pyrite within the metasiliciclastic and metavolcanic host rocks provided sulphuric acid, which dissolved other primary sulphides such as sphalerite and minor chalcopyrite and galena.

The oxidation of pyrite also involved changes of both Eh and pH conditions. Solutions derived from this process were highly acidic and led to the formation of a high Eh/low pH mineral paragenesis (Scott 1986, Garrels & Christ 1990) with goethite, psilomelane and rare gorceixite in the western and north-western mining area. The metal-bearing fluids have been neutralised by mineral-water reactions, while they moved laterally to the east and southeast towards the marble antiform, due to the dissolution of detrital feldspar, mica, apatite and calcite cements. Thus, moderate Eh and pH conditions occurred in the central and eastern part of the deposit. These conditions were favourable for the precipitation of the supergene zinc-bearing minerals. In the following, the formation conditions for the major ore minerals including hemimorphite, smithsonite, sauconite, tarbuttite, and hydrozincite will be discussed in detail.

Dependent on the presence of SiO_3^{2-} , provided by the dissolution of feldspar and mica, HCO_3^- provided by organic carbon and the dissolution of calcite, and H_2PO_4^- , provided by the dissolution of apatite, different zinc-bearing minerals have been formed. Hemimorphite and smithsonite have been formed generally under neutral to weak alkaline oxidising conditions, although smithsonite has been preferentially formed under high CO_2 partial pressure and low concentrations of silicic acid (Ingwersen 1990, Takahashi 1960, Sangameshwar & Barnes 1983). The formation of hemimorphite under neutral to weak alkaline conditions can be written as follows:



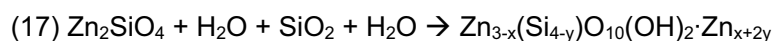
The formation of smithsonite under neutral to weak alkaline conditions can be written as follows:



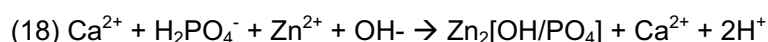
Smithsonite has also found as an alteration product of hemimorphite. The alteration of hemimorphite to smithsonite is mainly controlled by an increase of CO₂ partial pressure that triggers the alteration of hemimorphite (Ingwersen 1990). The alteration equation can be written as follows:



The formation of sauconite requires Eh-pH conditions similar to hemimorphite and smithsonite, although it is also stable under weak acid conditions, but with poorer crystallinity (Kloprogge et al. 1999, Roy and Mumpton 1956). It either represents an alteration product of detrital feldspar and mica or an alteration product of other non-sulphide zinc minerals, e.g. hemimorphite. The hemimorphite – sauconite alteration equation can be written as follows (Roy & Mumpton 1956):

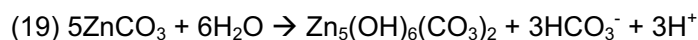


Peucker-Ehrenbrink et al. (2001) report the enrichment of phosphorous during the weathering. Indeed, the host rocks of the non-sulphide Skorpion deposit are enriched in phosphorous and are host to several supergene zinc-bearing phosphate minerals, e.g. tarbuttite. The formation of tarbuttite requires H₂PO₄⁻, which was provided by the dissolution of apatite from the Skorpion host rocks. The equation for the tarbuttite formation can be written as follows:



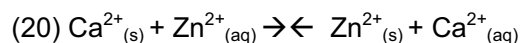
High concentration of H₂PO₄⁻ within the solution led to the formation of rare scholzite instead (Nriagu 1984, Ashley et al. 1997).

Hydrozincite, which has formed by the alteration of smithsonite, is the most stable mineral under surface conditions as it forms within a high alkaline environment as well as in a weakly acidic to neutral environment (Sangameshwar & Barnes 1983). The formation of hydrozincite can be written as follows:



At this point, it should also be stressed that zinc usually forms individual minerals as described above. However, there is some geochemical evidence of zinc being also adsorbed on calcite in the otherwise barren marble unit, which restricts the non-sulphide zinc ore body to the east and south. Whole rock analyses have shown that marble samples taken at or close to the contact to the non-sulphide ore body display some thousands ppm of zinc. Zachara (1988) has shown that zinc can be adsorbed on calcite via exchange with Ca²⁺ in a surface-adsorbed layer on calcite. The adsorption of Zn²⁺ occurs preferentially under alkaline conditions and high CO₂ partial pressure, when Ca²⁺ activities are lowest. Due to the buffering

effect of K^+ , Na^+ and OH^- , the supergene fluids were alkaline, when they hit the marble. Therefore, it is likely that adsorption of Zn^{2+} occurred at the Skorpion marble. Sites available for Zn^{2+} sorption are less than 10 % of Ca^{2+} sites on the calcite surface. Surface exchange of Zn^{2+} does not affect the solubility of calcite. The zinc adsorption, desorption, and isotopic exchange data are consistent with a reversible surface exchange or complexation reaction, which can be written as follows:



For completeness, it should be added that malachite forms under oxidising and alkaline conditions (Pollard et al. 1989) (Fig. 137). Chrysocolla and atacamite are formed under similar physicochemical conditions and are climatic indicators, as their occurrence is very common in oxidation zones of hot and arid climates (Woods & Garrels 1986, Cuarda & Rojas 2001). Atacamite is formed preferentially at pH 4 to 5 and moderate $CuCl_2^-$ concentrations (Pollard et al. 1989). The preservation of atacamite indicates a constant or increasing chloride concentration in the solution during its formation, as atacamite would have recrystallised to paratacamite under decreasing chloride concentrations (Cuarda & Rojas 2001).

Mn-bearing minerals are very common within the gossaneous profile of the Skorpion deposit. The divalent cation is only stable at low pH, whereas the additional oxidation states, 3^+ and 4^+ , are stable at high pH, oxidising conditions presumed (Garrels & Christ 1990). The main manganese minerals are psilomelane, cryptomelane, hydrohetaerolite and chalcophanite. The oxidation states of manganese within these minerals are: i) Mn^{2+} in psilomelane ($Ba, Mn^{2+})_3(O, OH)_6Mn_8O_{16}$; ii) Mn^{2+}, Mn^{4+} in cryptomelane: $K_{<2}(Mn^{4+}Mn^{2+})_8O_{16}$; iii) Mn^{3+} in hydrohetaerolite; and iv) Mn^{4+} in chalcophanite $ZnMn_3O_7 \cdot 3H_2O$. The apparent erratic distribution of manganese as it is depicted in a plan view in the previous chapter (Fig. 150) is not erratic looking at the distribution of manganese minerals and the predominant oxidation state of manganese within these zones. Psilomelane and cryptomelane are stable at a high redox potential regardless of the pH and are associated with the iron-rich gossaneous zones in the western part of the supergene ore body. Hydrohetaerolite and chalcophanite precipitate at low Eh and high pH and occur in the eastern zinc-rich portion of the Skorpion ore body.

To conclude, the supergene minerals and distribution thereof within the Skorpion non-sulphide zinc deposit represent a typical gossan profile containing a leached gossaneous zone, a supergene oxidate zone, and a zone of supergene sulphide enrichment zone (e.g. Scott 1987, Scott et al. 2001). Commonly, gossan profiles are vertically zoned (Scott 1987), if descendent meteoric fluids formed them with a leached gossaneous zone at the surface, a supergene enrichment zone at depth, and a supergene oxidate zone in between (Fig. 135).

However, the distribution of supergene minerals at the Skorpion deposit indicates that the gossaneous profile has rather laterally than vertically formed. The supergene lateral zonation pattern consists of a gossaneous zone in the western part of the deposit, e.g. western open pit wall at the 640 m level, containing mainly goethite and psilo- and cryptomelane. The gossaneous zone borders on a supergene oxidate zone, which follows to the east. The supergene oxidate zone hosts the non-sulphide mineralisation, mainly in the form of saucornite, smithsonite and hemimorphite. The supergene oxidate zone can be subdivided into a central and eastern portion, the former containing mainly saucornite, and the latter consisting mainly of smithsonite, hemimorphite, and minor tarbutite. This distribution pattern shows that Eh-pH conditions changed from high Eh/low pH to moderate Eh/pH towards east (Fig. 153).

Therefore, the formation of the supergene non-sulphide ore body from a hypogene sulphide ore body by predominantly vertically migrating meteoric fluids must be excluded. The remnants of a disseminated and stringer sulphide mineralisation within felsic metavolcanic rocks in the footwall of the non-sulphide ore body represent most likely a stratigraphic equivalent to

sulphide mineralisation, which was once exposed at the surface some hundred meters west of the supergene ore body. The former sulphide mineralisation is now completely oxidised and known as the most famous gossan in the Skorpion area, the so-called 'discovery outcrop'. Thus, it is reasonable to assume that the position of the 'discovery outcrop' marks the position of a significant portion of the Skorpion sulphide protore.

However, it cannot be excluded that minor vertical migration of supergene fluids occurred, which led to a redistribution of metals. The sulphide mineralisation in the footwall of the Skorpion non-sulphide zinc deposits features some characteristics, which are typical for a supergene overprint. Secondary supergene sphalerite as well as the clay-like colloform ZnS is found in felsic metavolcanic rocks. Primary sphalerite contains some percents of iron; the secondary zinc sulphides, however, are free of iron. The lack of iron within these secondary sulphides suggests that zinc was separated from iron, originally contained within iron-rich primary sphalerite. The zinc must have migrated in meteoric fluids from the protore, leaving the less soluble iron behind in the form of gossanous oxidised rocks, which locally occur at depth in the footwall of the Skorpion non-sulphide deposit. However, the well-developed lateral supergene metal zonation pattern clearly indicates that lateral-migrating fluids must have dominated. However, it has to be pointed out as well that the enormous depth of supergene mineralisation along the shear zones of the wrench fault system is best explained by thermal convection of meteoric fluids below the groundwater table, as oxidation in such depths is impossible to explain by only lateral movement or vertical fluctuations of groundwater (Borg et al. 2004).

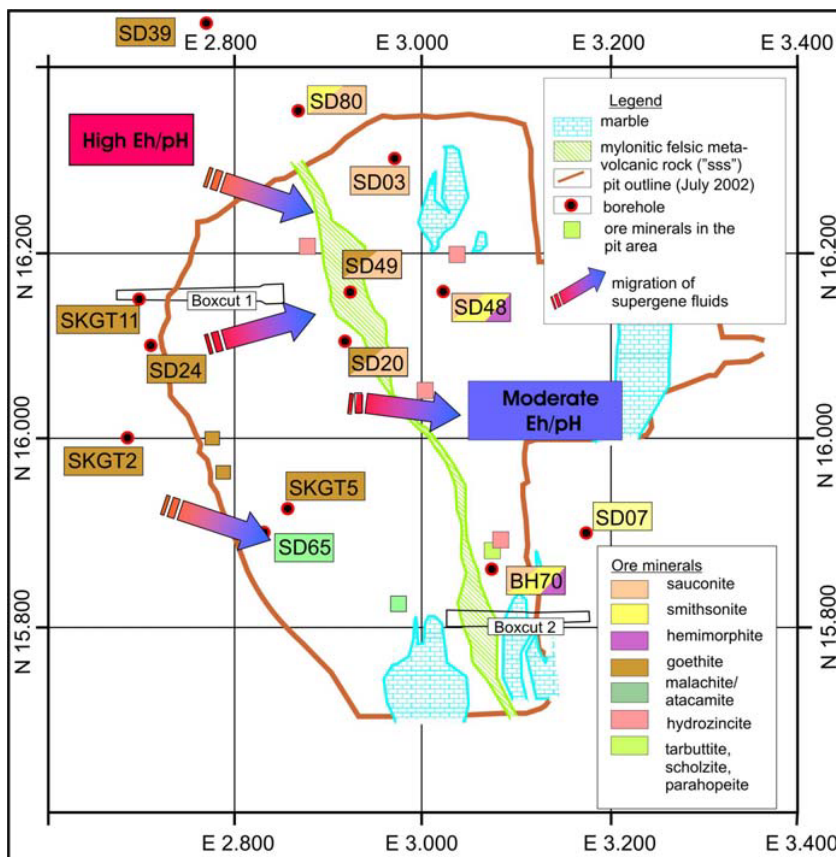


Fig. 153: Map of the Skorpion open pit as of July 2002, showing the position of boreholes, from which samples were taken for this study. The different colours point to the predominance of different ore minerals. The distribution of gossanous iron- and copper-rich zones in the western part and zinc-dominated central and eastern parts indicates a change of Eh/pH conditions from west to east.

3.9 Climate Regime and Development of the Weathering Profile

Climate is commonly the dominant factor influencing the weathering regime, as it controls both the rate and degree of mineral alteration. This climatic control can be viewed in terms of moisture delivery to the weathering profile and near-surface temperature conditions (Woodward et al. 1994). The volume of moisture percolating into the weathering profile (moisture throughput) regulates the intensity of weathering and leaching conditions, whilst temperature can influence the rate of chemical processes. Increased leaching may result in the removal of bases and build-up of iron oxides, while a rise in temperature will accelerate the rate of formation of a particular mineral. In contrast, in exceptionally arid environments, even the most mobile profile constituents, e.g. chlorides, can be retrained and the development of illuvial horizons is severely retarded or prevented. Therefore, the climate has a direct effect upon the type of weathering profile that is formed (Woodward et al. 1994).

A reconstruction of the palaeo-weathering environments can be attempted by using the clay minerals of weathered residues (Woodward et al. 1994, Sherman 2001). Swelling clays, such as montmorillonite and smectite but also chlorite, are associated with weathering under arid or semi-arid climates (Fig. 154). In contrast, kaolinite and halloysite would be expected to be the dominant clay mineral in deeply weathered zones under humid tropical conditions, though kaolinite can also be produced under a variety of conditions (e.g. Gerrard 1994, Woodward et al. 1994, Sherman 2001). Gibbsite, in appreciable amounts, probably indicates lateritic-type weathering, but small amounts are possible under a variety of conditions (Sherman 2001). Additionally, Woodward et al. (1994) pointed out that the mix of clay minerals may be more important than individual minerals and the absence of a clay mineral may be more significant than the presence of others.

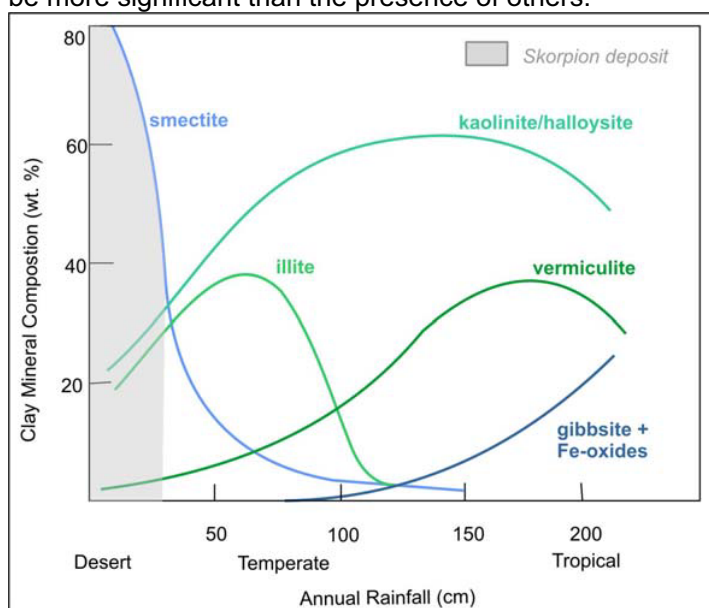


Fig. 154: Mineralogy of soil clay fraction in different climates, from Sherman (2001).

and clay minerals described above (Woodward et al. (1994), it must be concluded, that is has formed under semi-arid and arid rather than humid climatic conditions.

Additionally, the zinc carbonate smithsonite may act as a climatic indicator as well. Generally, hemimorphite is more stable than smithsonite under surface conditions assuming sufficiently high concentration of silica in the system (Ingwersen 1990). However, an increase

Mineralogical and geochemical studies have shown that the Skorpion ore body has formed by weathering. Since the ore body is covered by younger barren sediments, which are far less weathered than the host rocks of the Skorpion ore body, it has to be concluded that the weathering process that led to the formation of the ore body is a palaeo-weathering process. In order to elucidate the weathering history, clay minerals could be used as climatic indicators as discussed above.

The main ore mineral at Skorpion deposit is saunconite, a Zn-bearing smectite. Applying the relationship of climate

of CO₂ partial pressure, most likely resulting from an increase of microbiological activity as indicated by the carbon isotope signature of smithsonite, leads to the preferential formation of smithsonite. Since an increase of organic activity is related to a humid climate, there might be a relationship between humid climatic conditions and the formation of smithsonite. In contrast, the occurrence of the copper chloride atacamite as well as chrysocolla is indicative for oxidation zones of exceptional hot and arid climates (Woods & Garrels 1986, Cuarda & Rojas 2001), in which even the most mobile profile constituents, e.g. chlorides, can be retained.

Therefore, it is reasonable to assume that the Skorpion area has experienced marked changes of climate, most likely from humid-tropical to semi-arid and arid-hot, during the formation of the weathering profile and of the supergene ore body, respectively. Possible geological periods, when the environmental conditions were favourable for the formation of the supergene mineral paragenesis at Skorpion, are discussed in relation to morphological aspects in chapter 3.10.1 (Tab. 10).

3.10 Geomorphology and Development of the Weathering Profile

3.10.1 Regional Geomorphological Evolution

Weathering, and therefore the formation of supergene deposits, is closely related to geomorphology, since mechanical and chemical weathering liberates erodible and transportable debris that facilitate landscape denudation, and may produce distinct landforms.

Regionally, the geomorphological evolution of the southern Namib Desert as a distinct physiographic region began with the rifting of West Gondwanaland, an event that initiated the African erosion cycle (Partridge & Maud 1987, Gilchrist et al. 1994). The break-up of Gondwana and thus the opening of the South Atlantic Ocean from the south started at about 170 Ma (Tinker & de Witt 2004) to 130 Ma (Ward et al. 1983) ago with fully marine conditions established about 80 Ma ago (Ward et al. 1983). The opening of the Atlantic Ocean was accompanied by the formation of a narrow shallow coastal area, the future Namib Desert, between the South Atlantic Ocean to the west and the Great African Escarpment to the east.

Since the break-up of Gondwana, several hundred thousand km³ of sediment have been eroded episodically from the continent and most of this material is preserved offshore (Tinker & de Witt 2004), e.g. in the Orange Basin (Ward et al. 1983, Burke et al. 2004). The onshore evidence of erosion surfaces correlates with recent data on offshore sedimentation (e.g. Burke et al. 2004, Tinker & de Witt 2004), and reveals that a single cycle of erosion, interrupted by minor tectonic interludes, prevailed from the time of rifting to the early Miocene. Prominent offshore unconformities, testifying to the tectonic interludes, are notably at ca. 83 Ma (Santonian), ca. 30 Ma ('mid-Oligocene') and 14 Ma ('mid-Miocene') (Burke et al. 2004). Additionally, apatite fission track analyses give evidence for Mesozoic/Cenozoic uplift and erosion as well as the formation and evolution of the Great Escarpment (Raab et al. 2002). Cretaceous fission track outcrop ages indicate that since the Early Cretaceous there has been ~3 km of uplift and denudation (Raab et al. 2002). The lack of younger, Tertiary ages suggests that the major uplift had already occurred and had largely terminated by the end of the Cretaceous (Tinker & de Witt 2004). Most erosion and escarpment recession occurred during the earlier part of this interval under humid/ (sub-) tropical climatic conditions (Ward & Corbett 1990) and produced thick Late Jurassic and Cretaceous offshore sedimentary sequences (Raab et al. 2002). By Early Tertiary times (~65 Ma) an undulating plain with inselbergs, the so-called 'African Surface' (Partridge & Maud 1987) extended across most of southern Africa at elevations of 500 – 600 m above sea level.

The shelf sedimentation declined during the Tertiary and had virtually ceased in Oligocene, when interior planation had advanced to a stage where sediment supply to most rivers was minimal (Ward et al. 1983, Partridge & Maud 1987, Gilchrist et al. 1994). The decrease of denudation during the Early Tertiary is most likely related to arid climatic conditions, and therefore decreasing weathering rates, during the so-called Proto-Namib desert phase in Eocene and Oligocene times (53 – 23 Ma) (Pickford 2000).

Modest renewed uplift of 150 – 300 m in Miocene tilted the continent slightly to the west and initiated a new (Post-African I) landscape cycle (Partridge & Maud 1987). This was accompanied by renewed onshore erosion and offshore sedimentation, although at lower rates than during the Cretaceous. The climate became wetter in Lower to Middle Miocene (23 -14 Ma), documented by the deposition of fluvial sediments (Ward et al. 1983, Pickford 2000). A period of geomorphic stability at the end of Miocene resulted in widespread pedogenic calcrete formation, which may have occurred in a semi-arid climate with summer rainfall. The calcretes were deposited either around 6 Ma ago according to Ward et al. (1983) or around 14 – 11 Ma ago according to Pickford (2000). The full development of the Benguela Current coming from Antarctica and its associated cold upwelling system in Late Miocene accentuated the arid to semi-arid conditions in the Namib during Late Tertiary. Thus, the Benguela Current has contributed to the character of the current desert ecosystem (Ward et al. 1983). The Post-African I landscape cycle was terminated near the end of Pliocene, and its relative short duration resulted in imperfect planation in most areas to levels of no more than 100 – 300 m below the African surface (Partridge & Maud 1987).

The subsequent Post-African II cycle (Partridge & Maud 1987) at the end of the Pliocene is characterised by deep incision of the coastal hinterland and down cutting along major rivers of the interior. Earlier surfaces were severely deformed and dissected. Planation was limited to a few areas close to the coast. The resulting sedimentation is evident mainly in offshore deltas of major rivers (Partridge & Maud 1987). The main Namib Sand Sea probably dates from the Pliocene and was apparently maintained through the Pleistocene to the present day, possibly with minor expansion and contraction of its boundaries (Ward et al. 1983).

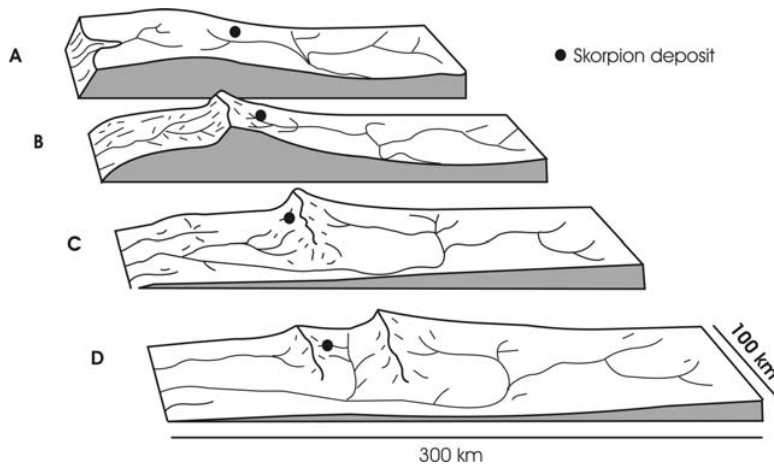


Fig. 155: Conceptual block model of landscape evolution for the rifted continental margin of Southern Namibia, showing the basic evolution of the morphology and of drainage patterns. (A - Synrift stage, Late Jurassic and Cretaceous; B - Some time after rifting in the Late Cretaceous/Lower Tertiary; C - Breaching of the marginal upwarp by a major river system in the Tertiary; D - Recent development of a 'stepped' landscape due to the exposure of substrate layers resistant to denudation. The black circle shows the approximate position of the Skorpion deposit. Modified after Gilchrist et al. 1994).

inland drainage divide and adjusting to the new base level of the coast. The initial location of the present escarpment was probably controlled by a major inland drainage divide separating low-gradient interior drainage from the higher-gradient river systems flowing to the newly formed South Atlantic margin (Cockburn et al. 2000). At present, the major, N-S-striking escarpment is well defined with a relief of about 1000 m. It is located between 100 and 170 km inland of the present coastline (Fig. 156) separating a gently inclined coastal plain with a regional slope of 0.3° from an interior plateau with a mean elevation of about 1800 m. The escarpment is generally coincident with a major drainage divide. The coastal plain is locally dissected by ephemeral channels, the Kuiseb, Swakop and Orange systems, sourced from the escarpment zone. Given the age of rifting and the present position of the escarpment, the conventional models require a mean escarpment retreat rate of about 1 km Ma^{-1} for the Namibian margin (Cockburn et al. 2000, Weber & Raab 2002).

The rifting and successive uplift during Late Mesozoic and Cenozoic times had major implications for the subsequent landscape evolution through its interaction with, and modification of, antecedent drainage patterns (Fig. 155).

The endurance of the Great Escarpment up to the Present as a major topographic feature (Fig. 156) is a function of the high elevations consequent upon the central position of southern Africa in Gondwanaland prior to this event.

The initial escarpment, which had formed at the coast at the time of break-up, was degraded by river systems flowing from an

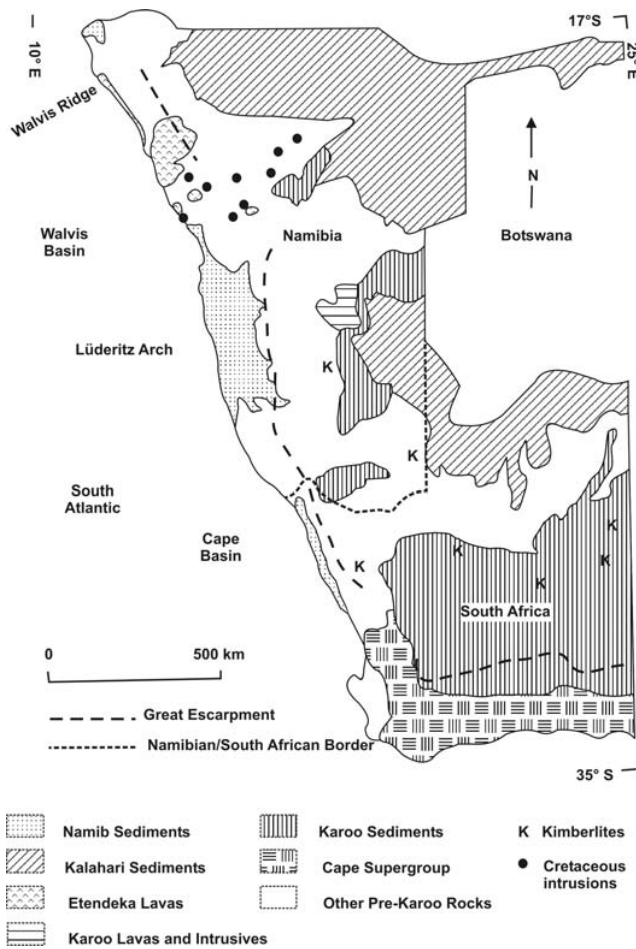


Fig. 156: Simplified map of the surficial geology for Namibia and South Africa. The dashed line marks the present position of the Great Escarpment. After Gilchrist et al. (1994).

retreat of the Great Escarpment were presumably promoted by the high local relief, generated by rifting and the establishment of lower base levels along the new continental margin. However, from the end of the Eocene to the Present much lower denudation rates have prevailed, apparently in response to the eventual adjustment to the base levels established at the time of break-up (e.g. Gilchrist et al. 1994). The major Mesozoic and Cenozoic events and climatic conditions are summarised in Tab. 10.

However, thermochronological and cosmogenic isotope data are incompatible with a simple escarpment retreat model, since they show that denudation rates ocean ward of the present escarpment position have been very low ($< 20 \text{ m Ma}^{-1}$) since the end of the Eocene, and the estimated rate of escarpment retreat has been only about 10 m Ma^{-1} (Cockburn et al. 2000). The difference of two orders of magnitude between the hypothetical retreat rate of about 1 km Ma^{-1} and the estimated real rates of escarpment retreat of about 10 m Ma^{-1} strongly suggests that the landscape has not evolved simply through progressive inland migration of a major escarpment from the coast. The highest rates of denudation and retreat of escarpment are most likely linked to the initial phase of rifting in the Late Mesozoic, when relatively rapid denudation occurred mainly in the coastal zone. The rapid denudation and therefore also the

Tab. 10: The Mesozoic/Cenozoic evolution of Namibia's passive continental margin with reference to the Skorpion deposit (after Ward et al. 1983, Partridge & Maud 1987, Pickford 2000, Ségalen et al. 2004, Gilchrist et al. 1994, Burke et al. 2004, Tinker & de Witt 2004).

	Ma [to]	Major Geological Events	Climate (e.g. Ségalen et al. 2004)	Skorpion Ore body	Sedimentation	
					Uplift/Erosion	Stable Land-surface
Quaternary	0	Deep incision of the coastal hinterland and down cutting along major rivers of the interior, formation of the main Namib Sand Sea probably from Pliocene and maintained through Pleistocene to the present day (e.g. Ward et al. 1983)	Arid	Recent red sand		
Pliocene	1.6	Thin Pliocene series due to progressive aridification of the Namib towards present day conditions including significant Aeolian erosion which limited the preservation of the dune systems	Arid	Deposition of the uppermost red sand cover, formation of normal fault zones that cross-cut the Miocene boulder beds and calcrete		
	Late	10 – 7 Ma full establishment of the cool-water upwelling system of the Benguela Current, persistence of the Namib desert phase since Late Miocene (e.g. Ward et al. 1983); pedogenic calcrete formation between 4 and 6 Ma (Ward et al. 1983); meteorite impact (Roter Kamm)	Semi-arid to arid	Calcrete formation		
Middle	11	Pedogenic calcretes (Partridge & Maud 1987)	Semi-humid			
Early	14	Moderate uplift of 150 – 300 m (~ 18 Ma); at 14 Ma offshore unconformity (Burke et al. 2004); pluvial phase in Early to Middle Miocene; Karfen-kliff fluvial phase, deep incision of the Proto-Orange River and fluvial terrace deposits	Semi-humid, tropical/ sub-tropical	Modification of the Palaeogene land surface, erosion and partial loss of the upper part of the Skorpion weathering profile including the uppermost part of the supergene ore body; deposition of boulder beds and fluvial sands		

3.10.2 Geomorphological Evolution and Development of the Weathering Profile at the Skorpion Deposit

Prior to the beginning of the break-up of Gondwana in the Late Jurassic, the Skorpion sulphide precursor must have been located at least 3 km below the ancient land surface, otherwise it would have been eroded completely during the Post-Gondwana erosional phase (Partridge & Maud 1987, Gilchrist et al. 1994) in the Lower Cretaceous. Rapid uplift and surface denudation within the Skorpion area dominated in Cretaceous times and were accompanied by the retreat of the Great Escarpment. The Great Escarpment was most likely located about 65 km east of the present coast line at this time, assuming retreat rates given by Cockburn et al. (2000) and Weber & Raab (2002).

Since the Skorpion deposit is located about 80 km east of the present coastline, it is reasonable to assume that the escarpment had not retreated completely from the Skorpion area by the end of Cretaceous. Nevertheless, humid/subtropical climatic conditions, which prevailed during Late Cretaceous (Ségalen et al. 2004), could have initiated the oxidation of the hypogene sulphide Skorpion precursor within the already dissected landscape. Furthermore, persistent tectonic activity and thus the formation of the N-S-trending wrench fault system (Borg et al. 2004) have caused the opening of dilational joints. These joints could have served as pumping device (McCaig 1988) sucking water from nearby areas that then could have travelled along the fault conduits and led to the deep oxidation of the Skorpion sulphide precursor. Additionally, convection of meteoric fluids way below the groundwater table (Borg et al. 2004) could have contributed as well. However, in the near-surface and surface environment the oxidation of primary sulphides was predominantly driven by vertical fluctuations of groundwater as a humid climate is related to high water tables and a predominantly vertical movement of groundwater (Mitchell 2002). These conditions were favourable for the development of a preliminary vertical supergene metal and mineral zonation pattern of the Skorpion deposit.

The Late Cretaceous offshore unconformity around 83 Ma (Burke et al. 2004) points to a phase of geomorphological stability without or with only minor uplift and low surface denudation, all that could have led to a further deepening of the weathering profile and oxidation at Skorpion.

Minor uplift took place during the Early Tertiary, however, erosion and surface denudation was low due to the progressive adjustment to base level (Gilchrist et al. 1994) and the climatic change from humid to semi-arid/arid (Ségalen et al. 2004). The escarpment within the Skorpion area had probably completely retreated by that time (Late Palaeocene/Early Eocene) and an erosional surface had developed on the Late Proterozoic Gariep sequence, which might be a correlative to the 'Namib unconformity surface' (Partridge & Maud 1987, Ward et al. 1983).

The lack of major Palaeocene offshore sediments (Burke et al. 2004, Partridge & Maud 1987) could well be indicative for a stable land surface during the Palaeogene with only minor surface denudation. Therefore, it is most likely that the weathering profile at Skorpion has deepened during that time. The supergene mineralising processes must have been controlled mainly by climatic changes and fluctuations of the groundwater-table, since this was a time characterised by low tectonic activity, geomorphic stability, and low rates of erosion (e.g. Partridge & Maud 1987, Raab et al. 2002, Cockburn et al. 2000).

The (semi-) arid climate through in Eocene and Oligocene times (Ward et al. 1983, Ward & Corbett 1990) was most likely accompanied by a decrease in the through-flow of meteoric fluids and lower water tables, which led to predominantly lateral groundwater movements (Mitchell 2002). Therefore, the initial vertical supergene metal zonation pattern of the

Skorpion deposit has most probably been overprinted by a lateral mineral and metal zonation pattern. Since sauconite is known to represent arid climatic conditions (Sherman 2001), it is likely that it has formed within that period.

Renewed uplift during the Early Miocene (Burke et al. 2004), as part of the Post-African I cycle (Partridge & Maud 1987), and associated surface denudation modified the Early Tertiary palaeo-surface, which was composed of weathered Late Proterozoic rocks that have already hosted the supergene non-sulphide zinc deposit at that time. The Early Miocene surface denudation led to the partial removal of the Late Cretaceous/Early Tertiary weathering profile, which had evolved over a time period of about 50 Ma. The denudation also resulted in the truncation of the Skorpion weathering profile, which corresponds to the erosion of the uppermost part of the supergene ore body (Fig. 157). The supergene mineralisation that is now exposed in the open pit area shows that especially the uppermost central and southern portion of the supergene ore body must have been eroded. Rough calculations, which were presented in one of the previous chapters, have shown that at least 5 % of the supergene ore body were removed by denudation processes.

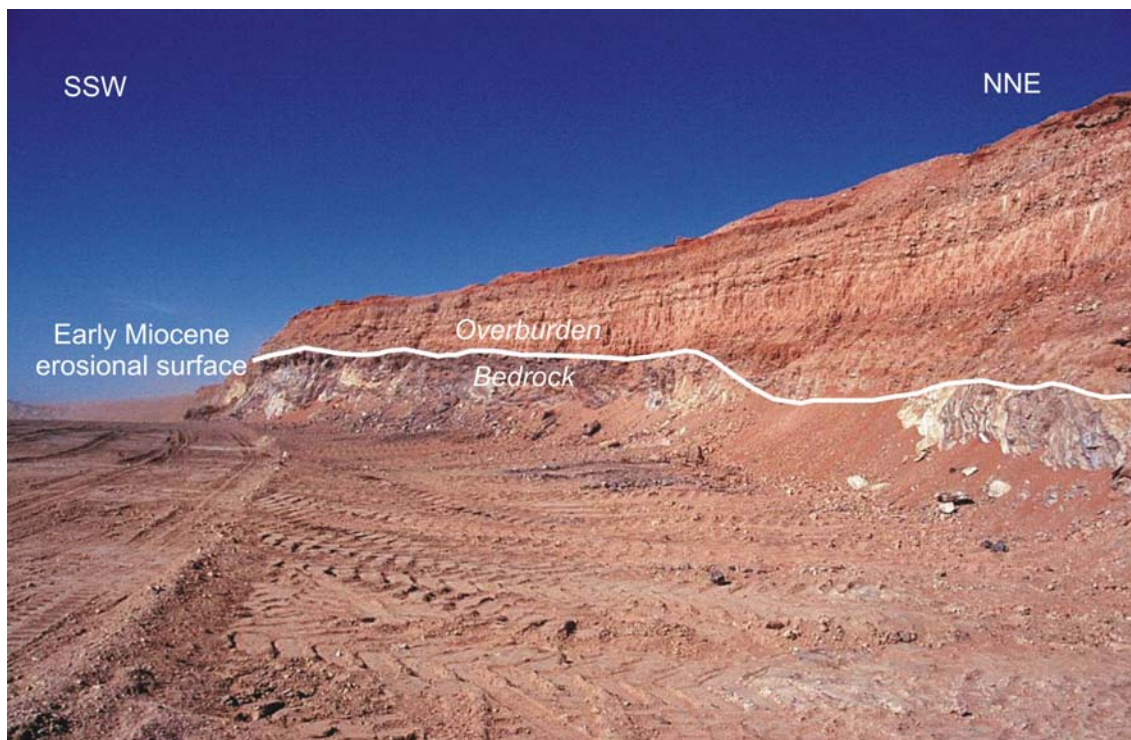


Fig. 157: Undulating Early Miocene erosional surface representing an altered Early Tertiary land surface. The erosional surface separates bedrock from overburden. The palaeo-high in the background is covered by 1 – 3 m thick overburden, whereas the palaeo-low in the foreground is covered by 10 to 15 m thick overburden.

Despite the Miocene denudation, the distribution of metals and minerals within the supergene ore body indicates that the morphology of the pre-existing Early Tertiary land surface ('Namib unconformity surface') has been widely preserved. The Palaeogene surface must have been geomorphologic stable during the Early Tertiary (Palaeocene), as the supergene metal and mineral zonation patterns give evidence for a relationship between palaeo-morphology and ore-forming processes. If lateral movement of groundwater occurs along a morphological/hydrological gradient, soluble products of weathering like mobile metals in solution but also clays in suspension (clay illuviation) migrate laterally along that gradient, parallel to the morphological slope (Teeuw et al. 1994). Therefore, an enrichment of

mobile metals and clay minerals as well as alkaline cations can be observed at the position of topographic depressions in the lower parts of the landscape. Such alkaline environment favours the formation of certain minerals such as smectites in the lower positions (Righi & Mennier 1995), which is in agreement with the occurrence of sauconite (Zn-bearing smectite) in the palaeo-topographic depressions. The relationship mineralogy – palaeo-morphology is discussed in detail below.

The erosional Pre-Miocene palaeo-relief features a low WSW-ENE-trending morphological gradient within the Skorpion area (Fig. 157 – 160). The western part represents a palaeo-high, whereas the eastern part displays a palaeo-low.

The lateral supergene metal zonation pattern is closely related to these palaeo-morphological features. The highest enrichment of supergene (most soluble) zinc minerals occurs at the position of palaeo-lows; the highest enrichment of (least soluble) supergene iron, copper, manganese, and minor lead minerals is located at the position of palaeo-highs instead. This geochemical-morphological relationship indicates that the transport of dissolved metals but also clays in suspension e.g. sauconite, took place predominantly laterally by meteoric fluids following the palaeo-morphological and palaeo-hydrological gradient from northwest to southeast, partly through the Mesozoic N-S-trending fault zones, which provided excellent permeabilities.

The supergene mineral distribution pattern shows that Eh-pH conditions changed from high Eh/low pH to moderate Eh/pH towards east (Fig. 153), and thus the acidity of supergene fluids changed from acidic to weakly/moderate alkaline while percolating through the Late Proterozoic rocks from palaeo-highs towards palaeo-lows. The fluids were weak to moderate alkaline, when they hit the marble in the east, and thus unable to dissolve calcite. This fact explains why the marble is less weathered and thus less permeable than the metasiliciclastic and metavolcanic units. The marble also represents a hydrological barrier as its impermeability hindered the supergene fluids from migrating further to the east.

Summarizing, it can be stated that the distinct supergene lateral metal zonation pattern points to the predominance of lateral moving meteoric fluids, which migrated along a geomorphological/hydrological gradient, similar to that described by Righi & Mennier (1995) for other areas, rather than descending fluids, which would have formed a distinct vertical metal zonation pattern (Scott 1987). Additionally, the predominance of lateral moving fluids implies semi-arid climatic conditions (Mitchell 2002), which prevailed within the Skorpion area in the Early Tertiary. Therefore, it is reasonable to assume that the main stage of oxidation took place in Early Tertiary.

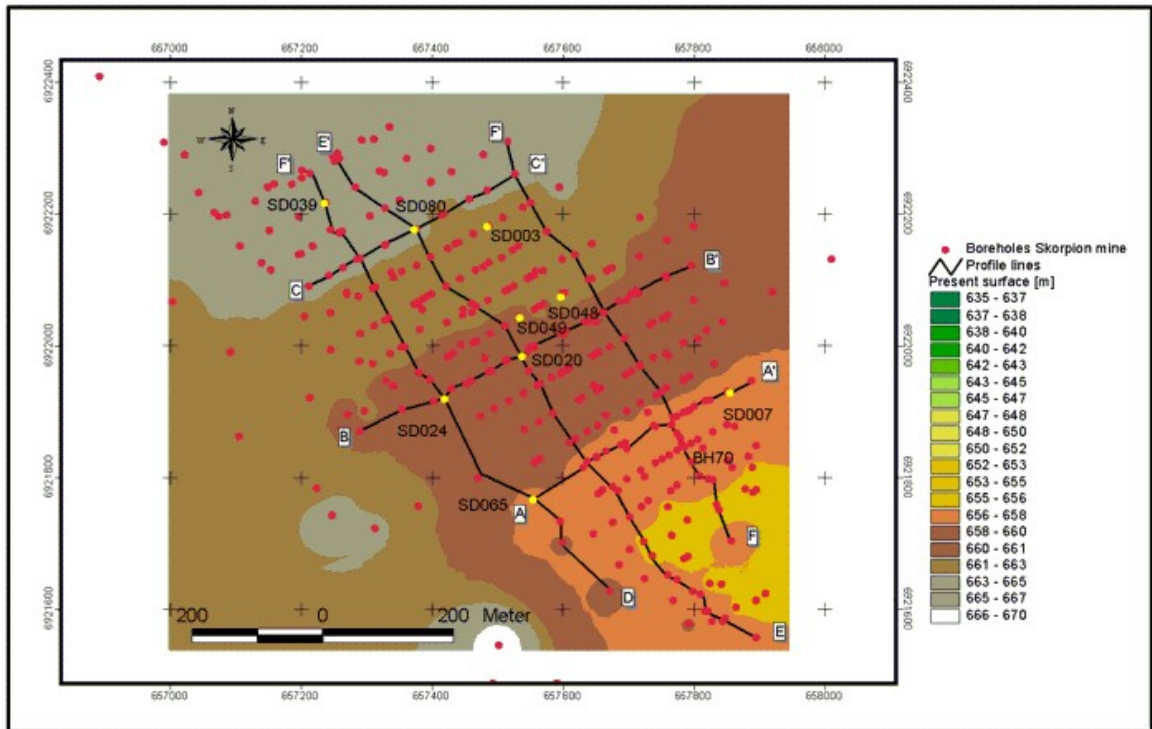


Fig. 158: The surface of the pre-mining area has been relatively flat, dipping slightly to SE, and formed a wide valley trending NW-SE with a shallow geomorphological gradient along its axis of about 1°. The geomorphological gradient of the south-western and north-eastern valley sides is slightly higher, up to 2.5°. Boreholes depicted as yellow circles have been sampled for the present study.

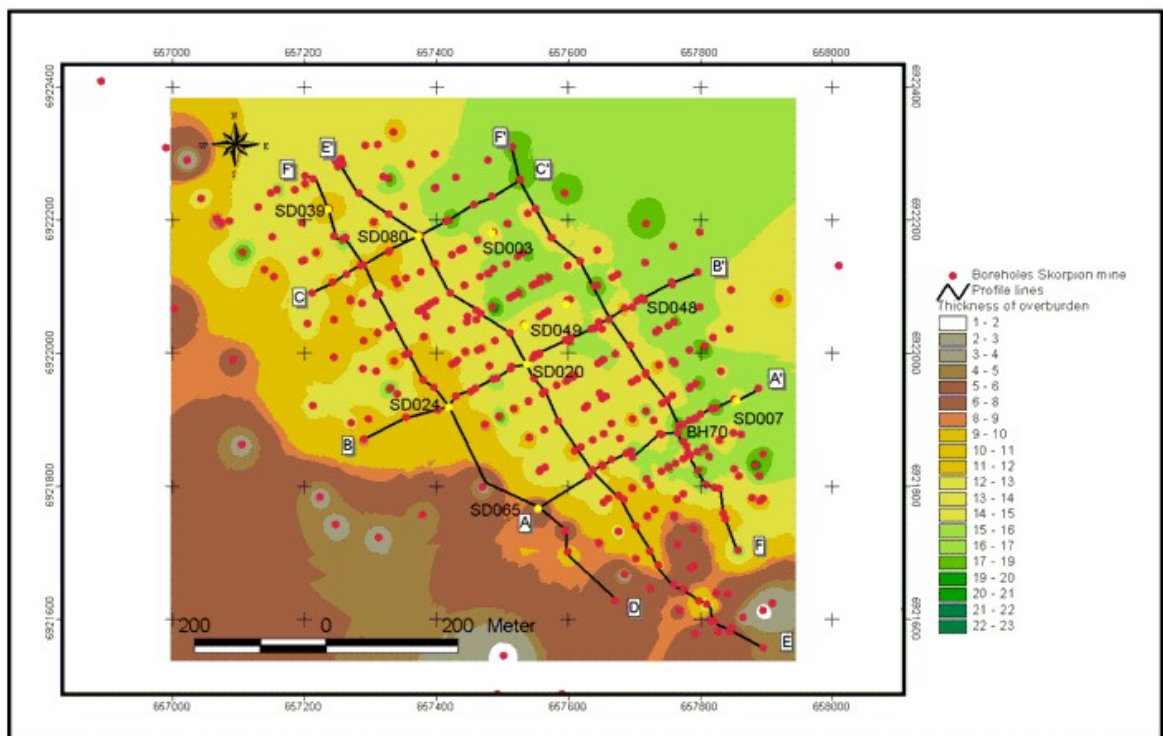


Fig. 159: Thickness of the Miocene alluvial/colluvial/aeolian overburden, covering the Skorpion deposit. The thickness of the overburden ranges between 5 and 10 m in the western part of the area, whereas the overburden in the eastern and south-eastern part reaches between 15 and 20 m.

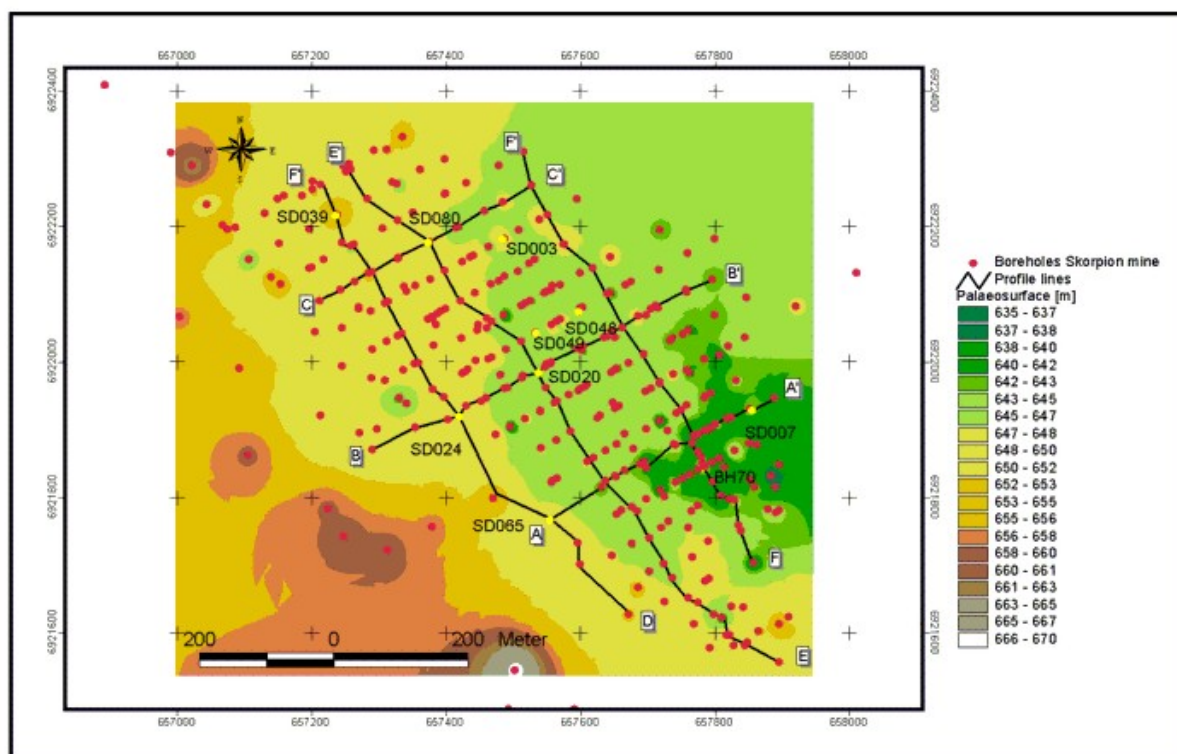


Fig. 160: Early Miocene erosional palaeo-surface, calculated from the difference between the pre-mining elevation (Fig. 158) and the thickness of overburden (Fig. 159), shows palaeo-highs in the west, southwest, and northwest and palaeo-lows in the east and southeast. The WSW-ENE-trending geomorphological gradient ranges between 2.5° in the northern part and 4.5° in the southern part. Boreholes depicted as yellow circles have been sampled for the present study.

A renewed humid climate and modest erosion rates during the Miocene resulted in the alteration of the Early Tertiary palaeo-surface and in deposition of alluvial sediments on to it. The debris being most likely transported along-valley filled the valley in the rugged terrain, both from the adjacent valley slopes and from the continually eroding escarpment in the east. The sediments are probably correlatives of the widespread Miocene fluvial sediments (Ward et al. 1983) within the Namib Desert.

The thickness of the barren alluvial sediments (overburden) that cover the ore body varies showing a coincidence with the palaeo-morphological features. The thickness of the overburden ranges between 5 and 10 m in the western part of the Skorpion deposit, whereas the overburden reaches between 15 and 20 m in the eastern and southeastern part (Fig. 159). Areas with a thin alluvial/colluvial cover represent palaeo-highs, whereas areas with a thick overburden represent palaeo-lows. The morphology of the erosional palaeo-surface has also influenced the sediment facies of the overburden material. Low-energy sediments like calcareous sands and minor gravels have been deposited above palaeo-highs instead of high-energy thick boulder beds, which have been deposited above palaeo-lows.



Fig. 161: Karst cave in marble. Unconsolidated orange-brown sand and silt in blue-grey marble. Skorpion open pit, eastern pit wall.

Additionally, the occurrence of a karst cave (Borg et al. 2004) within the marble gives evidence for karstification within the Skorpion area. This karst cave might be a correlative of karst holes/caves known from northern Namibia (Otavi Mountain Land, Kaokoland), from which fossiliferous karst fillings have been dated at a Middle Miocene age ($13 \pm 1 \text{ Ma}^{-1}$; Pickford et al. 1994). The karst cave at Skorpion, of which the top is about 2 m below the present surface, is filled with poorly consolidated silt and fine-grained sand, which might have deposited during the fluvial phase in Early/Middle Miocene.

The well-developed calcrete horizons seen at the top of the Skorpion valley-infill

sequence might be correlated to the major phase of pedogenic calcrete formation in either Middle (Pickford 2000) or Late (Ward et al. 1983) Miocene times. The calcrete horizon is covered by red dune sand, which forms the uppermost part of the transported regolith profile and has most likely been deposited since latest Pliocene, after Namib Desert conditions were established (Ward et al 1983, Ward & Corbett 1990).

The described relationship between the geomorphological evolution and the development of the weathering profile at the Skorpion deposit has shown that the weathering profile has formed by: lowering of the landscape, subsequent deepening, thinning and truncation of the weathering profile, and finally its burial (Tab. 11). This behaviour is in agreement with the development of weathering profiles over long periods elsewhere (Thomas 1989, Thomas 1994).

Tab. 11: The behaviour of weathering profiles over long periods (modified after Thomas 1989, from Thomas 1994) with reference to the evolution of the Skorpion supergene ore body.

Profile behaviour	Denudation balance ^a	Geomorphic outcome (Thomas 1994)	Geomorphic outcome at the Skorpion deposit	Supergene processes at the Skorpion deposit
Lowering	Balanced WP : SD (vertical lowering)	Mantled etch surfaces, Fe ₂ O ₃ accumulation	Development of ferrigenous silcrete; remnants thereof are found resting on gossanous Late Proterozoic metasiliciclastic and metavolcanic rocks in the western part of the ore body	Initial oxidation of the Skorpion sulphide precursor in a near-surface environment in Late Cretaceous; Initial formation of the supergene non-sulphide ore body and a preliminary vertical metal zonation pattern as a result of humid climatic conditions

Deepening	WP > SD (stable land surface)	Weathered land- surfaces	Formation of the Palaeogene land surface with ferrigenous silcrete resting on Late Proterozoic rocks	Progressive weathering and oxidation of the Skorpion sulphide precursor in a surface environment in the Lower Tertiary; Formation of a lateral metal zonation pattern as a result of arid to semi-arid climatic conditions
Thinning	SD > WP (resistant rock at depth)	Rock exposure, etch surfaces	Modification of the Palaeogene land surface due to Miocene uplift and thus, erosion of the uppermost part of the supergene non-sulphide ore body. This process resulted in a weathered land surface with a palaeo-high in the present western mining area and a palaeo-low in the eastern mining area. The non-sulphide ore body became thinned due to the occurrence of Late Proterozoic marble at depth, which is more weathering-resistant compared to metavolcanic and metasiliciclastic rocks. Finally, fresh to slightly weathered marble was exposed at the eastern contact to the non-sulphide ore body. During this period a west-east-trending geomorphological/ hydromorphological gradient has developed.	Modification of the mineral paragenesis, e.g. formation of saucnite from hemimorphite and/or smithsonite, formation of hydrozincite from smithsonite)
Truncation	SD >> WP (lateral erosion)	Slope pediments, rock exposure	Progressive surface erosion and thus, formation of the erosional surface, which truncates the ore body and separates it from the overburden material	Progressive erosion of the uppermost part of the weathering profile (supergene non-sulphide ore body) in Early Miocene; Modification of the mineral paragenesis (see above)
Collapse	SD and WP minimal (hydromorphic pedogenesis)	White sand and breakdown of kaolinite clays, depression	There is no evidence of hydromorphic pedogenesis like widespread leaching of Al^{3+} , Fe^{2+} , and SiO_2 or breakdown of kaolinite. Geochemical work carried out during this study has shown that kaolinite and goethite are stable within the present environment.	Modification of the mineral paragenesis (see above)
Burial	SD and WP = 0 (sedimentation)	Sedimentary Cover	Deposition of Miocene boulder beds, calcrete, and Pliocene dune sands	Preservation of the non-sulphide ore body

^a WP indicates rate of weathering penetration, SD rate of surface denudation.

4 Conclusions

Corrans et al. (1993) assumed a supergene origin for the Skorpion non-sulphide ores, however, without further detailed investigations of the metallogenesis. Therefore, the present metallogenic study has been undertaken in order to investigate the origin of the non-sulphide ore body in detail. The deformed and foliated nature of the remnants of the primary pyrite-sphalerite-chalcopyrite mineralisation (Fig. 162) hosted mainly by felsic metavolcanic and metavolcaniclastic rocks at Skorpion gives evidence for the pre-metamorphic origin of the sulphides. The sulphide paragenesis and its ore textures are highly suggestive of a syn- to early post-volcanic origin of the sulphides. No primary sulphides were found within the metasiliciclastic rocks. However, the widespread occurrence of semi-massive gossans as well as disseminated pseudomorphs of goethite after pyrite indicate that the metasiliciclastic rocks must have been host to a portion of the Skorpion sulphide precursor.

While the primary sulphides are hosted mainly by the felsic metavolcanic rocks, the major portion of the non-sulphide mineralisation is hosted by metasiliciclastic rocks, which indicates that wall rock replacement (Heyl & Bozion 1960) must have taken place as the predominant ore-forming process (Fig. 162). Sulphuric acid, formed from the oxidation of primary sulphides, has caused the development secondary porosity and permeability by the selective dissolution of calcite cements, feldspars and minor mica of metasiliciclastic rocks, as well as intercalated lenses of marble. Supergene non-sulphide minerals, namely sauconite, hemimorphite, smithsonite, and minor tarbuttite, were precipitated as euhedral or subhedral crystals in secondary intra- and intergranular pore space (Fig. 162). Progressive dissolution of either remaining calcite cements, feldspars or even the alteration of supergene zinc minerals, e.g. alteration from hemimorphite to sauconite, resulted in limited solution collapse of metasiliciclastic rocks and thus in the formation of solution collapse breccias, which provided open space for late-stage non-sulphide mineralisation, e.g. tarbuttite-cemented hemimorphite-impregnated solution collapse breccia.

In addition to wall rock replacement, there is a lot of evidence for in-situ oxidation/-replacement in both, felsic metavolcanic and metasiliciclastic rocks (Fig. 162). Banded primary sulphides, e.g. sphalerite, pyrite, and minor chalcopyrite, hosted by felsic metavolcanic rocks have been replaced by supergene colloform spalerite, chalcocite, greenockite, hematite and malachite. Additionally, abundant Fe- and Mn-hydroxide staining within the metasiliciclastic rocks suggests an origin of these mineral phases from pre-existing primary Fe- and Zn-sulphides. Other forms of alteration associated with the formation of the non-sulphide ores include silicification from the breakdown and minor baritisation with barium liberated by the breakdown of the feldspar during ore formation.

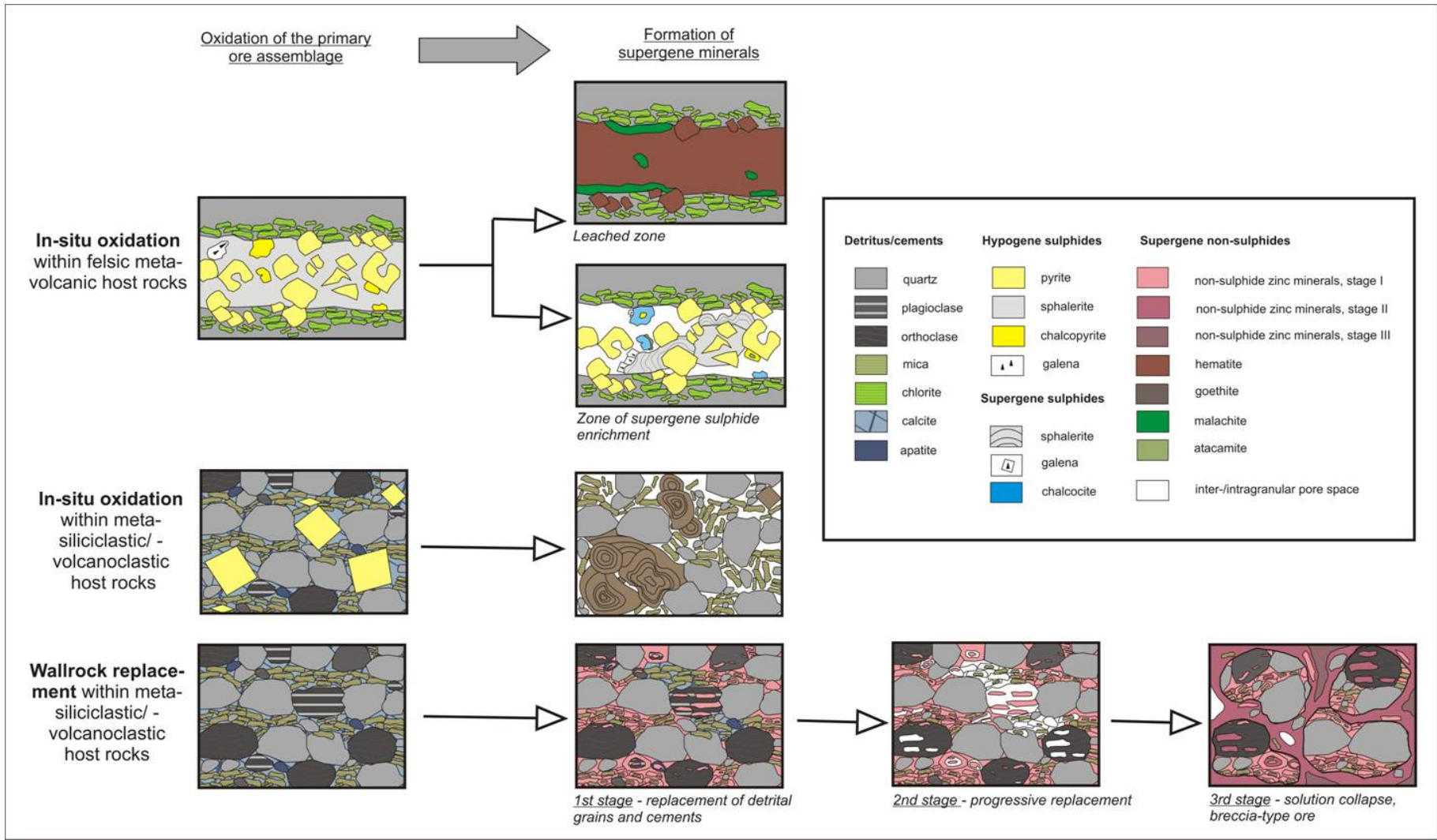


Fig. 162: Supergene ore-forming processes that have taken place at the Skorpion deposit including wall-rock replacement and in-situ oxidation.

This metallogenic study has also shown that the mobilization - re-precipitation process also included the spatial separation of iron and base metals due to differences in solubility and mobility. The different metal solubilities resulted in the formation of a distinct supergene lateral metal and mineral zonation pattern away from the sulphide protore, containing a western mixed Fe-oxihydroxide/Mn-hydroxide zone, a marked Cu zone, a weakly developed Pb zone and a main eastern Zn ore zone.

This supergene metal and mineral distribution pattern indicates that Eh-pH conditions of the supergene fluids have changed from high Eh/low pH to moderate Eh/pH migrating towards east, and thus the acidity of supergene fluids changed from acidic to weakly/moderate alkaline, while they were migrating through the Late Proterozoic host rocks following palaeo-geomorphological features.

The supergene fluids were buffered by the dissolution of calcite cements, feldspar and mica, and thus were neutralised, while moving eastward towards the marble. As a result, the supergene fluids were not reactive enough to dissolve the calcite and mineralise the marble, preventing the formation of a marble-hosted replacement deposit, similar to carbonate-hosted smithsonite deposits in Sardinia (e.g. Boni et al. 2003).

In the course of the study, it turned out as well that the N-S trending major brittle fault system within the metasiliciclastic and felsic metavolcanic rocks played a significant role regarding the depth of the oxidation within the Skorpion area. The brittle-ductile fault system, which is interpreted as the upper, western to central part of a positive flower structure (Borg et al. 2005), has formed at a shallow crustal level, possibly related to the Gondwana break-up or to later, continuing faulting during the opening of the Atlantic ocean (Borg et al. 2005). The faulting has caused intensive dilatational fracturing, which allowed oxygenated surface water to penetrate deeply by fluid convection. This deep penetration of surface water allowed the deep oxidation, which formed the root zone of the present supergene ore body at Skorpion ore body. However, the distinct lateral supergene metal zonation, which is developed at the present mining level, reaches across the fault zone, indicating that the supergene mineralising event post-dates the major fault system. The pronounced lateral W-E (WNW-ESE-)-trending supergene metal zonation has formed along a palaeo-hydrogeological/-morphological gradient following suitable intra- and intergranular porosities within the metasiliciclastic and minor felsic metavolcanic rocks.

Whole rock geochemistry on the Skorpion host rocks has shown that both metasiliciclastic and felsic metavolcanic rocks, show a markedly higher degree of weathering than their equivalents within the Skorpion area. The metasiliciclastic rocks display moderate to high Chemical Alteration Indices (CIA, Nesbitt & Young (1982)), which are associated with a depletion of mobile major elements, such as K, Na, and Ca. Additionally, trace element distribution patterns including REE's have changed their concentration within the highest supergene altered metasiliciclastic rocks.

The mass balance calculation for the felsic metavolcanic rocks using the isocon diagram after Grant (1986) has shown that the effects of an early (Late Proterozoic) hydrothermal alteration and a late (Tertiary) supergene alteration interfere, and thus the gain and losses of elements, e.g. Mg, K, or Ca cannot always be classified beyond doubt as the result of either supergene or hydrothermal alteration. In contrast to the metasiliciclastic rocks, the felsic metavolcanic rocks do not feature any changes in trace element and REE composition, indicating that the felsic metavolcanic rocks are generally less weathered.

A general conclusion that can be drawn from comparing metasiliciclastic and felsic metavolcanic rocks is that the former were more vulnerable to supergene weathering processes since they contained plagioclase and calcite (cement), which were not stable during the weathering, whereas the latter were mainly composed of quartz, K feldspar and mica, and thus contained mineral phases, which were more stable.

Additionally, supergene ore textures have indicated that fracturing and faulting also played a significant role during the formation of the supergene ore body. Cenozoic faulting as well as fracturing during physical weathering increased porosities and permeabilities, and hence provide suitable host properties for mineralisation (Chávez 2000). The intensity of fracturing and faulting has been observed to be highest in the metasiliciclastic rocks, less in the felsic metavolcanic rocks and markedly less in the marble. In particular, tectonic breccias within the siliciclastic but also within the felsic metavolcanic unit are mineralised by supergene mineralisation.

The supergene ore textures (Fig. 162) as well as supergene metal- and mineral zonation pattern (Fig. 151 & 153) indicate that the supergene mineralising event post-dates the brittle-ductile fault system that has developed in late Jurassic/Cretaceous. From the palaeomorphological evolution of the Skorpion area as well as from stability conditions of the supergene ore minerals it must be concluded that the oxidation of the primary hypogene mineralisation and thus formation of the supergene non-sulphide zinc mineralisation was initiated in Cretaceous times under humid and subtropical climatic conditions and continued in Palaeogene times under mainly semi-arid conditions. Continued uplift and erosion led to the removal of a minor portion of the original supergene ore body; before it became covered and protected underneath alluvial sediments of early Miocene age (Pickford 2000). By this time, the supergene ore forming processes had ceased, due to the development of the hyper-arid climate of the Namib Desert.

Summarising it can be stated that the non-sulphide ores at Skorpion are non-deformed and represent a low-T, low-p assemblage and thus post-date the Pan-African metamorphism. Thus, a pre-metamorphic origin of the Skorpion non-sulphide ores, perhaps similar to the anhydrous metamorphosed ores of the Franklin and Sterling Hill deposits in New Jersey (Johnson 2001; Metsger 2001), must be excluded. The low-T, low-p assemblage also indicates that a hydrothermal origin of the Skorpion non-sulphide ores, similar to the willemite occurrences of Beltana, Australia (Groves et al. 2003, Hitzman et al. 2003) or Vazante, Brasil (Monteiro et al. 1999, Hitzman et al. 2003), must be excluded. Therefore, the Skorpion non-sulphide zinc deposit is classified unequivocally as to be an example of a supergene deposit, which has formed by weathering in a surface/near-surface environment. The supergene ore-forming processes described above indicate that the Skorpion deposit is classified most appropriately as a hybrid between a wall rock deposit and a direct-replacement deposit as defined by Heyl and Bozion (1960).

This present metallogenic study is based mainly on drill core and minor surface samples from the Skorpion open pit and the wider Skorpion area. However, on-going mining operations at the Skorpion zinc mine expose new ore textures and structures almost every day. Consequently, there is a high potential for future metallogenic but also structural research.

The study of palaeo-climatic conditions and the palaeo-morphological evolution of the Skorpion area have revealed that the supergene ore body must have formed in Early Tertiary times. However, isotopic Rb/Sr dating of sauconite, which has been carried out in order to confirm this hypothesis, was unsuccessful and the results have not entered the study. However, isotopic age determination of certain secondary minerals, e.g. Ar/Ar dating of K-bearing Mn oxides could be a subject of future research as it could help to elucidate the timing of the supergene mineralising events in more detail.

Supergene ore bodies generally contain a large variety of secondary ore minerals. The likelihood of finding new minerals that have not described before is high, as the discovered occurrence of skorpionite shows. Therefore, eyes should be kept open, when new portions of the supergene ore body are excavated.

References

- Alchin, D. (1993): The structural and stratigraphic setting of the Rosh Pinah Pb-Zn deposit within the Gariep trough. Unpublished MSc thesis. University of Stellenbosch, South Africa. 189 pp.
- Alchin, D.J., Frimmel, H.E. & Jacobs, L.E. (2005): Stratigraphic setting of the metalliferous Rosh Pinah Formation and the Spitzkop and Koivib Suites in the Pan-African Gariep Belt, southwestern Namibia. *South African Journal of Geology*, 108, 19 – 34.
- Alchin, D.J. & Moore, J.M. (2005): A review of the Pan-African, Neoproterozoic Rosh Pinah Zn-Pb deposit, southwestern Africa. *South African Journal of Geology*, 108, 71 – 86.
- Allen, R.L., Lundström, I., Ripa, M., Simeonov, A. & Christofferson, H. (1996): Facies Analysis of a 1.9 Ga, continental margin, back-arc, felsic caldera province with diverse Zn-Pb-Ag-(Cu-Au) sulfide and Fe oxide deposits, Bergslagen Region, Sweden. *Economic Geology*, 91, 979 – 1008.
- Ashley, P.M., Lottermoser, B. G. & Scott, K.N. (1997): Supergene iron phosphate minerals in Proterozoic ironstones from the Olary Block, South Australia. *Neues Jahrbuch Mineralogische Mitteilungen*, 7, 309 – 327.
- Barresi, T. & Dostal, J. (2005): Geochemistry and Petrography of Upper Hazelton Group Volcanics: VHMS-Favourable Stratigraphy in the Iskut River and Telegraph Creek Map Areas, Northwestern British Columbia. *British Columbia Geological Survey. Geological Fieldwork 2004, Paper 2005 – 1.*
- Barrett, T.L., Cattalani, S. & MacLean, W.H. (1993): Volcanic litho-geochemistry and alteration at the Delbridge massive sulfide deposit, Noranda, Quebec. *Journal of Geochemical Exploration*, 48, 135 – 173.
- Bathia, M. & Crook, K. (1986): Trace element characteristics of graywackes and tectonic setting discrimination of sedimentary basins. *Contrib. Mineral. Petrol.*, 92, 181 – 193.
- Bau, M. (1991): Rare-earth element mobility during hydrothermal and metamorphic fluid-rock interaction and the significance of the oxidation state of europium. *Chemical Geology*, 93, 219 – 230.
- Bernhardt, H.J., Effenberger, H., Krause, W. & Medenbach, O. (submitted): Check-list for new mineral proposals 2003 – Skorpionite. Submitted to the International Mineral Association. 13 p.
- Bierlein, F.P. (1995): Rare-earth element geochemistry of clastic and chemical metasedimentary rocks associated with hydrothermal sulphide mineralization in the Olary Block, South Australia. *Chemical Geology*, 122, 77 – 98.
- Böttcher, M.E., Gehlken, P.L., Birch, Usdoswki, E. & Hoefs, J. (1993): The rhodochrosite – smithsonite solid-solution series from Broken Hill (NSW), Australia: Geochemical and infrared spectroscopic investigations. *Neues Jahrbuch Mineralogische Mitteilungen*, 8, 352 – 362.
- Boland, M.B., Kelly, J.G. & Schaffalitzky, C. (2003): The Shaimerden supergene zinc deposit, Kazakhstan: a preliminary examination. *Economic Geology*, 98, 787 – 795.
- Boni, M., Aversa, G., Balassone, G. & Gilg, A.H. (2001): A new (“old”) type of Zn-ore resource: The “Calamine” of SW-Sardinia (Italy). *GSA Annual Meeting*, Nov 5 –8, Boston.
- Boni, M., Gilg, H.A., Aversa, G. & Balassone, G. (2003): The “calamine” of SW Sardinia: Geology, mineralogy and stable isotope geochemistry of supergene Zn mineralisation. *Economic Geology*, 98, 731 – 748.
- Boni, M. & Large, D. (2003): Non-sulfide zinc mineralisation in Europe: An Overview. *Economic Geology*, 98, 4, 715 – 729.

- Borchardt, G. (1989): Smectites. - In: Dixon, J.B. & Weed, S.B. (eds.): Minerals in Soil Environments. SSSAJ Special Publication 1, 675 – 727.
- Borg, G. (2000): Regional Controls on sediment-hosted Pb-Zn (Ba-Cu) occurrences within the Pan-African Orogenic Belts of Namibia. Communications Geological Survey of Namibia, 12, 211-220.
- Borg, G. (2001): Memorandum: Regional geometry and setting of the Skorpion basin. Unpubl. Company Report, 4 pp.
- Borg, G. & Armstrong, R. (2002): Isotopic SHRIMP age dating of zircons from igneous basement and rhyolitic cover rocks at Skorpion, southern Namibia: IAGOD Symposium and Geocongress 2002, 11th quadrennial: Extended abstract volume on CD-ROM, Windhoek, Geological Survey of Namibia.
- Borg, G., Kärner, K., Buxton, M., Armstrong, R. & van der Merwe, S. (2003): Geology of the Skorpion supergene zinc deposit, Southern Namibia. Economic Geology, 98, 749 – 771.
- Borg, G., Kärner, K. & Klein, E. (2005): Structural control on the localisation and deep oxidation of the Skorpion supergene zinc deposit, Namibia. Abstract Volume, 8th Biennial SGA Meeting, Beijing, August 18 – 21, 2005.
- Borg, G., Klein, E., Kärner, K., Botha, R. & Harney, D. (2004): Lithology, structure, and deep weathering characteristics of the supergene Skorpion zinc ore body. Geoscience Africa 2004, Abstract Volume 1, University of the Witwatersrand, Johannesburg, South Africa, 71 – 72.
- Boynton, W.V. (1984): Geochemistry of rare earth elements: Meteorite studies. – In: Henderson (ed.): Element Geochemistry. Rare earth. 63 – 114.
- Burke, K., Webb, S.J. & Gunnell, Y. (2004): Possible causes and timing of Africa's elevation changes. Geoscience Africa 2004, Abstract Volume 1, University of the Witwatersrand, Johannesburg, South Africa, p. 93.
- Buxton, M.W.N., van der Merwe, S.W. & Moyes, A.B. (2000): The Tectonostratigraphical Evolution of the Gariiep Belt, Namibia. PowerPoint Presentation, Anglo American, Exploration & Acquisitions Division (unpubl.).
- Caggianelli, A., Fiore, S., Mongelli, G. & Salvemini, A. (1992): REE distribution in the clay fraction of pelites from the southern Apennines, Italy. Chemical Geology, 99, 253 – 263.
- Cas, R.A.F. & Wright, J.V. (1987): Volcanic successions: Modern and ancient. A geological approach to processes, products and successions. London, Allen and Unwin, 518 p.
- Chávez, W.X. (2000): Supergene oxidation of copper deposits: Zoning and distribution of copper oxide minerals. SEG Newsletter, 41, 10 - 21.
- Christelis, G. & Struckmeier, W. (2001): Groundwater in Namibia – an explanation to the hydrogeological map. 127 pp.
- Cockburn, H.A.P., Brown, R.W., Summerfield, M.A. & Seidl, M.A. (2000): Quantifying passive margin denudation and landscape development using a combined fission-track thermochronology and cosmogenic isotope analysis approach. Earth and Planetary Science Letters, 179, 429 – 435.
- Condie, K.C. (1991): Another look at rare earth elements in shales. Geochimica et Cosmochimica Acta, 55, 2527 – 2531.
- Conly, A.G., Goodfellow, W.D., Taylor, R.P. & Lydon, J.W. (2000): Geology, geochemistry, and sulphur isotope geochemistry of the hanging wall sulphide zones and their related hydrothermal alteration, Sullivan Zn-Pb-Ag deposit.– In: Lydon, J.W., Höy, T., Slack, J.F. & Knapp, M.E. (eds.): The geological environment of the Sullivan deposit, British Columbia. Geological Association of Canada, Mineral Deposits Division, Special Publication No. 1, 541 – 573.

- Cooke, D.R., Bull, S.W., Donovan, S. & Rogers, J.R. (1998): K-metasomatism and base metal depletion in volcanic rocks from the McArthur Basin, Northern Territory – Implications for base metal mineralization. *Economic Geology*, 93, 1237 – 1263.
- Corrans, R.D., Gewald, H., Whyte, R.M. & Land, B.N. (1993): The Skorpion SZ secondary zinc deposit – South western Namibia. Abstracts: Conference on mining investment in Namibia, 17 – 19 March 1993, Windhoek, Namibia. 46 – 56.
- Cuadra C., P. & Rojas S., G. (2001): Oxide mineralization at the Radomiro Tomic Porphyry Copper Deposit, Northern Chile. *Economic Geology*, 96, 387 – 400.
- Cullers, R.L., Chaudhuri, S., Kilbane, N. & Koch, R. (1979): Rare earths in size fractions and sedimentary rocks of Pennsylvanian-Permian age from the mid-continent of the U.S.A. *Geochimica Cosmochimica Acta*, 43, 1285 – 1302.
- Dahanayake, K. & Subasinghe, S.M.N.D. (1989): Secondary phosphate mineralization in a karstic environment in central Sri Lanka. *Mineralium Deposita*, 24, 169 – 175.
- Daliran, F. & Borg, G. (2003): A preliminary appraisal of the non-sulphide zinc deposit of Angouran, North-West Iran.
- Davies, C.J. & Coward, M.P. (1982): The structural evolution of the Gariep arc in southern Namibia. *Precambrian Research*, 17, 173 – 198.
- Dirks, P.H.G.M. (2004): A structural geological framework for the Skorpion Zn deposit; implications for pit design. Unpublished Company Report. 17 pp.
- Eastoe, C.J., Solomon, M. & Walshe, J.L. (1987): District-scale alteration associated with massive sulfide deposits in the Mount Read Volcanics, western Tasmania. *Economic Geology*, 82, 5, 1239 – 1258.
- Ewart, A. (1979): A review of the mineralogy and chemistry of Tertiary - Recent dacitic, latitic, rhyolitic and related salic volcanic rocks. – In: Barker, F. (ed.): *Trondhjemites, dacites and related rocks*. Amsterdam, Elsevier. 13 – 121.
- Floyd, P.A. & Winchester, J.A. (1978): Identification and discrimination of altered and metamorphosed volcanic rocks using immobile elements. *Chemical Geology*, 21, 291 – 306.
- Fölling, P.G., Frimmel, H.E. & Zartmann, R.E. (1998): Chemostratigraphical correlation and Pb-Pb dating of metasedimentary sequences in the Gariep Belt: evidence for the two diamictites. 10th International Gondwana Conference, Cape Town. *Journal of African Earth Sciences*, 27, 1A, 76 – 77.
- Fölling, P.G., Frimmel, H.E. & Zartmann, R.E. (2000): Chemostratigraphical correlation and Pb-Pb dating of metasedimentary sequences in the Gariep Belt: evidence for different diamictites. *Journal of African Earth Sciences, Gondwana 10: Event Stratigraphy of Gondwana (Abstracts)*, 76 – 77.
- Franklin, J.M. (1993): Volcanic-associated massive sulphide deposits. – In: Kirkham, R.V., Sinclair, W.D., Thorpe, R.I. & Duke, J.M. (eds.): *Mineral deposit modelling*. Geological Association of Canada, Spec. Paper, 40, 315 – 334.
- Frimmel, H.E. (2000a): New U-Pb zircon ages for the Kuboos pluton in the Pan-African Gariep belt, South Africa: Cambrian mantle plume or far field collision effect?
- Frimmel, H.E. (2000b): The Pan African Gariep belt in southwestern Namibia and western South Africa. *Geological Survey of Namibia Communications*, 12, 197 – 209.
- Frimmel, H.E., Fölling, P.G. & Eriksson, P. (2002): Neoproterozoic tectonic and climatic evolution recorded in the Gariep Belt, Namibia and South Africa. *Basin Research*, 14, 55 – 67.
- Frimmel, H.E. & Frank, W. (1998): Neoproterozoic tectono-thermal evolution of the Gariep belt and its basement, Namibia and South Africa. *Precambrian Research*, 90, 1 – 28.

- Frimmel, H.E., Hartnady, C.J.H., & Koller, F. (1996a): Geochemistry and tectonic setting of magmatic units in the Pan-African Gariep belt, Namibia. *Chemical Geology*, 130, 101 – 121.
- Frimmel, H.E., Jonasson, I.R. & Mubita, P. (2004): An Eburnean base metal source for sediment-hosted zinc-lead deposits in Neoproterozoic units of Namibia: Lead isotopic and geochemical evidence. *Mineralium Deposita*. 39, 328 – 343.
- Frimmel, H.E., Klötzli, U.S. & Siegfried, P.R. (1996b): New Pb-Pb single zircon age constraints on the timing of Neoproterozoic glaciation and continental break-up in Namibia. *Journal of Geology*, 104, 459 – 469.
- Frimmel, H., Koller, F., Watkins, R.T. & Faure, K. (1995): Tectonic history of mafic and ultramafic rocks in the Gariep Belt. Abstracts Centennial Geocongress, Geological Society South Africa, 226 – 229.
- Frimmel, H.E. & Lane, K. (2005): Geochemistry of carbonate beds in the Neoproterozoic Rosh Pinah Formation, Namibia: Implications on depositional setting and hydrothermal ore formation. *South African Journal of Geology*, 108, 5 – 18.
- FrondeL, C. & Bam, J.L. (1974): Structure and mineralogy of the Franklin Zinc-Iron-Manganese deposit, New Jersey. *Economic Geology*, 69, 2, 157 – 180.
- Garrels, R.M. & Christ, C.L. (1990): Solutions, minerals, and equilibria. Lones and Bartlett Publishers, Boston, 450 pp.
- Gair, J.E., D'Agostino, J.P., Loferski, P.J. & Whitlow, J.W. (1989): Saprolite deposits. – In: Mineral Resources of the Charlotte 1° X 2° Quadrangle, North Carolina and South Carolina. U.S. Geological Survey Professional Paper 1462, 73 – 81.
- GermS, G.J.B. & Gresse, P.G. (1991): The foreland basin of the Damara and Gariep orogens in Namaqualand and southern Namibia; stratigraphic correlations and basin dynamics. *South African Journal of Geology*. 94, 159 – 169.
- Gerrard, A.J. (1994): Weathering of granitic rocks: Environment and clay mineral formation. – In: Robinson, D.A. & Williams, R.B.G. (eds.): Rock weathering and landform evolution. John Wiley & Sons, p. 3 – 20.
- Gilchrist, A.R., Kooi, H. & Beaumont, C. (1994): Post-Gondwana geomorphic evolution of southwestern Africa: Implications for the controls on landscape development from observations and numerical experiments. *Journal of Geophysical Research*, 99, B6, 12211 – 12228.
- Gilg, H.A., Allen, C., Balassone, G., Boni, M. & Moore, F. (2003a): The 3-stage evolution of the Angouran Zn “oxide”-sulfide deposit, Iran. – In: Eliopoulos et al. (eds.): Mineral Exploration and Sustainable Development. Proceedings of 7th Biennial SGA Meeting. 11 -13 Aug 2003, Athens, Greece, 77 – 80 (extended abstract).
- Gilg, H.A., Aversa, G. and Boni, M. (2001): A stable isotope study of smithsonite with application to Pb-Zn deposits of SW Sardinia. *Journal of Conference Abstracts (Proc. EUG XI, Strasbourg, 8-12.4. 2001)*, 6, 1, 592.
- Gilg, H.A. & Boni, M. (2004): Stable isotope compositions of Zn- and Pb-carbonates: their role in exploration of non-sulfide ores. – In: Predictive mineral discovery under cover. Proceedings of SEG 2004 meeting in Perth, Australia.
- Gilg, H.A., Struck, U., Vennemann, T. & Boni, M. (2003b): Phosphoric acid fractionation factors for smithsonite and cerussite between 25 and 72 °C. *Geochimica et Cosmochimica Acta*, 67, 4049 – 4055.
- Goldich, S.S. (1938): A study of rock weathering. *Journal of Geology*, 46, 17 – 58.
- Gouveia, M.A., Prudêncio, M.I., Figueiredo, M.O., Pereira, L.C.J., Waerenborgh, J.C., Margado, I., Pena, T. & Lopes, A. (1993): Behaviour of REE and other trace and major elements during weathering of granitic rocks, Évora, Portugal. *Chemical Geology*, 107, 293 – 296.

- Grant, J. A. (1986): The isocon diagram – a simple solution to ‘Gresens’ equation for metasomatic alteration. *Economic Geology*, 81, 1976 – 1982.
- Grauch, R.I. (1991): Rare earth elements in metamorphic rocks. – In: Lipin, B.R. & McKay, G.A. (eds.): *Geochemistry and mineralogy of rare earth elements. Reviews in Mineralogy*. 147 – 167.
- Gresse, P.G. (1994): Strain partitioning in the southern Gariep arc as reflected by sheath folds and stretching directions. *South African Journal of Geology*, 97, 52 – 61.
- Gromet, L.P., Dymek, R.F., Haskin, L.A. & Korotev, R.L. (1984): The ‘North American shale composite’: Its compilation, major and trace element characteristics. *Geochimica Cosmochimica Acta*, 48, 2469 – 2482.
- Groves, I.M., Carman, C.E. & Dunlap, W.J. (2003): Geology of the Beltana willemite deposit, Flinders Ranges, South Australia. *Economic Geology*, 98, 4, 797 – 818.
- Guilbert, J.M. & Park, C.F. (1986): *The geology of ore deposits*. 985 p.
- Hartmann, K., Kart, K. & Townshend, P. (2000): Skorpion Zinc Project – Geological site report on pre-feasibility deposit drilling, condemnation drilling and bulk-sampling. Volume 1. Unpublished company report.
- Hartnady, C.J.H. & von Veh, M.W. (1990): Tectonostratigraphic and structural history of the Late Proterozoic – Early Palaeozoic Gariep belt, Cape Province, South Africa. *Geocongress '90, Geological Society of South Africa, Cape Town, Guidebook, P01, 1 - 49*.
- Hercod, D.J., Brady, P.V. & Gregory, R.T. (1998): Catchment-scale coupling between pyrite oxidation and calcite weathering. *Chemical Geology*, 151, 259 – 276.
- Herron, M.M. (1988): Geochemical classification of terrigenous sands and shales from core or log data. *Journal of Sedimentary Petrology*, 58, 820 – 829.
- Heyl, A.V. & Bozior, C.N. (1960): Varieties of supergene zinc deposits in the United States. – In: *Short Papers in the Geological Sciences: U.S. Geological Survey, 400-B, B2 – B5*.
- Hirayama, K. (1986): Geological study on the Anguran mine, northwestern part of Iran. *Geological Survey of Japan, Report 226, 25 pp*.
- Hitzman, M. W. (2001): Zinc oxide and zinc silicate deposits – a new look. *GSA Annual Meeting, Nov 5 –8, Boston*.
- Hitzman, M.W., Reynolds, N.A., Sangster, D.F., Allen, C.R. & Carman, C.E. (2003): Classification, genesis, and exploration guides for nonsulfide zinc deposits. *Economic Geology*. 98, 685 – 714.
- Hughes, C.J. (1973): Spilites, keratophyres and the igneous spectrum. *Geological Magazine*, 6, 513 – 527.
- Ingwersen, G. (1990): Die sekundären Mineralbildungen der Pb-Zn-Cu-Lagerstätte Tsumeb, Namibia (Physikalisch-chemische Modelle). *Diss. Institut für Mineralogie und Kristallchemie, Universität Stuttgart. 232 p*.
- Jasper, M.J.U., Stanistreet, I.G. & Charlesworth, E.G. (2000): Neoproterozoic inversion tectonics, half-graben depositories and glacial controversies, Gariep fold-thrust belt, southern Namibia. *Geological Survey of Namibia Communications, 12, 187 – 196*.
- Johnson, C.A. (2001): Geochemical constraints on the origin of the Sterling Hill and Franklin zinc deposits, and the Furnace Magnetite Bed, Northwestern New Jersey: *Economic Geology, Guidebook Series, v. 35, p. 89-97*.
- Johnson, C.A. & Skinner, B.J. (2003): Geochemistry of the Furnace Magnetite Bed, Franklin, New Jersey, and the relationship between stratiform iron oxide ores and stratiform zinc-oxide-silicate ores in the New Jersey Highlands. *Economic Geology*. 98, 837 – 854.

- Kärner, K. (2003a): Mineralogical and geochemical observations on the non-sulphide zinc deposit Shaimerden, Northern Kazakhstan. – In: Eliopoulos, D., Allen, C., Baker, T., Barriga, F., Beaudoin, G., Bernados, B., Boni, M., Borg, G., Bouchot, V., Brown, A., Christidis, G., Damigos, D., Economou-Eliopoulos, M., Eilu, P., Garuti, G., Gervilla, F., Gize, A., Goldfarb, R., Groves, D., Hedenquist, J., Heinrich, C., Johnson, K., Kaliambakos, D., Kelly, K., Kiliyas, S., Malitch, K., Markey, R., Merkle, R., Menegaki, M., Molnar, F., Mouchez, P., Mposkos, E., Naden, J., Papavassiliou, C., Pava, J., Petersen, S., Pushkarev, E., Scott, P., Spry, P., Stamatakis, S., Stein, H., Thompson, J., Varsami-Jones, E., Weihed, P. & Zaccarini, F. (eds.): Mineral Exploration and Sustainable Development. Proceedings of 7th Biennial SGA Meeting. 11 -13 Aug 2003, Athens, Greece, 85 – 88.
- Kärner, K. (2003b): Geochemistry of the 'sheared sericite schist' ('sss') at the Skorpion mine, Namibia. Unpubl. Company Report, 6 p.
- Kalliokowski, J. (1965): Metamorphic features in North American massive sulphide deposits. *Economic Geology*, 60, 485 – 505.
- Kamona, F. & Friedrich, G. (1994): Die Blei-Zink-Lagerstätte Kabwe in Zentral Sambia. *Erzmetall*, 47, 1, 34 – 44.
- Kaufmann, A.J., Hayes, J.M., Knoll, A.H. & Germs, G.J.B. (1991): Isotopic compositions of carbonates and organic carbon from upper Proterozoic successions in Namibia: Stratigraphic variation and the effects of diagenesis and metamorphism. *Precambrian Research*, 49, 301 – 327.
- Klein, E. (2005): Geochemical Investigation of the Sheared Sericite Schist and Geology of the Skorpion Area, Skorpion, Southern Namibia. Unpubl. Combined Mapping- and Laboratory Thesis. Martin-Luther-University Halle-Wittenberg, 86 p.
- Kloprogge, J. T., Komarneni, S. & Amonette, J.E. (1999): Synthesis of smectite clay minerals: A critical review. *Clay and Clay Minerals*, 47, 529 – 554.
- Kortman, C. (1972): The Geology of the Zambia Broken Hill mine, Kabwe. *Geologie en Mijnbouw*, 51, 3, 347 – 356.
- Kranidiotis, P. & MacLean, W.H. (1987): Systematics of chlorite alteration at the Phelps Dodge massive sulphide deposit, Matagami, Quebec. *Economic Geology*, 82, 1898 – 1911.
- Large, D. (2001): The Geology of Non-Sulphide Zinc Deposits – An Overview. *Erzmetall*, 54, 264–274.
- LeMaitre, R.W., Bateman, P., Dudek, A., Keller, J., Lameyre, J., LeBas, M.J., Sabine, P.A., Schmid, R., Sorensen, H., Streckeisen, A., Woodley, A.R. & Zanettin, B. (1989): A classification of igneous rocks and glossary of terms. Blackwell Scientific Publications Oxford, England, 193 pp.
- Lentz, D.R. (1996): Trace element systematics of felsic volcanic rocks associated with massive sulphide deposits in the Bathurst Mining camp: Petrogenetic, tectonic and chemostratigraphic implications for VMS exploration. – In: Wyman, D.A. (ed.): Trace element geochemistry of volcanic rocks. Applications for massive sulphide exploration. Geological Association of Canada, Short Course Notes, 12, 359 – 402.
- Leroy, J. & Turpin, L. (1988): REE, Th, and U behaviour during hydrothermal and supergene processes in a granitic environment. *Chemical Geology*, 68, 239 – 251.
- Leshner, C.M., Gibson, H.L. & Campbell, I.H. (1986): Composition-volume changes during hydrothermal alteration of andesite at Buttercup Hill, Noranda District, Québec. *Geochimica et Cosmochimica Acta*, 50, 2693 – 2705.
- Levell, B.K. (1980): A late Precambrian tidal shelf deposit, the Lower Sanjford Formation, Finnmark, North Norway. *Sedimentology*, 27, 153 – 166.

- MacLean, W.H. (1988): Rare earth element mobility at constant inter-REE ratios in the alteration zone at the Phelps Dodge massive sulfide deposit, Matagami, Quebec. *Mineralium Deposita*, 23, 231 – 238.
- Marcoux, E., Moelo, Y. & Leistel, J.M. (1996): Bismuth and cobalt minerals as indicators of stringer zones to massive sulphide deposits, Iberian Pyrite Belt. *Mineralium Deposita*, 31, 1 – 26.
- McCaig, A.M. (1988): Deep fluid circulation in fault zones. *Geology*, 16, 10, 867 – 870.
- McDaniel, D.K., Hemming, S.R., McLennan, S.M. & Hanson, G.N. (1994): Petrographic, geochemical, and isotopic constraints on the provenance of the early Proterozoic Chelmsford Formation, Sudbury Basin, Ontario. *Journal of Sedimentary Research*, 64, 362 – 372.
- McLennan, S.M. (1989): Rare earth elements in sedimentary rocks: Influence of provenance and sedimentary processes. – In: Lipin, B.R. & McKay, G.A. (eds.): *Geochemistry and mineralogy of rare earth elements. Reviews in Mineralogy*. 169 – 200.
- McMillan, M.D. (1968): The geology of the Witputs-Sendelingsdrift area. *Precambrian Research Unit, University of Cape Town Bulletin*, 4, 177 p.
- Metsger, R.W. (2001): Evolution of the Sterling Hill zinc deposit, Ogdensburg, Sussex County, New Jersey. *Economic Geology, Guidebook Series*, 35, 75-87.
- Michard, A. & Albarède, F. (1986): The REE content of some hydrothermal fluids. *Chemical Geology*, 55, 51 – 60.
- Middelburg, J.J., van der Weijden, C. & Woittiez, J.R.W. (1988): Chemical processes affecting the mobility of major, minor and trace elements during weathering of granitic rocks. *Chemical Geology*, 68, 253 – 273.
- Mining Journal (2000): Anglo American builds Skorpion. December, 2000.
- Mitchell, A.C. (2002): Geochemical evolution of regoliths over the Hannibals disseminated nickel-sulfide deposit and the dispersional response of ore-associated elements. <http://www.geol.uwa.edu.au/geology/postgrad/amitchell/amitchell.html> (downloaded on 25.09.2002).
- Möller, P. (1985): Development and application of the Ga/Ge-geothermometer for sphalerite from sediment-hosted deposits. *Monograph Series on Mineral Deposits*, 25, 15 – 30.
- Monteiro, L.V.S., Bettencourt, J.S., Spiro, B., Graca, R. & de Oliveira, T.F. (1999): The Vazante zinc mine, Minas Gerais, Brazil; constraints in willemite mineralisation and fluid evolution. – In: Sangster, A.L. & Zentilli, M. (eds.): *Latin American mineral deposits. Exploration and Mining Geology*, 8, 1 – 2, 21 – 42.
- Muller, D.W. (1972): The geology of the Beltana willemite deposit. *Economic Geology*, 67, 1146 – 1167.
- Nesbitt, H.W. (1979): Mobility and fractionation of rare earth elements during weathering of a granodiorite. *Nature*, 279, 206 - 210.
- Nesbitt, H.W. & Young, G.M. (1982): Early Proterozoic climates and plate motions inferred from major element chemistry of lutites. *Nature*, 299, 715 – 717.
- Nesbitt, H.W. & Young, G.M. (1989): Formation and diagenesis of weathering profiles. *Journal of Geology*, 97, 129 – 147.
- Nesbitt, H.W., Young, G.M., McLennan, S.M. & Keays, R.R. (1996): Effects of chemical weathering and sorting on the petrogenesis of siliciclastic sediments, with implications for provenance studies. *Journal of Geology*, 104, 525 – 542.
- Nriagu, J.O. (1984): Formation and stability of base metal phosphates in soil and sediments. – In: Nriagu, J.O. & Moore, P.B. (eds.): *Phosphate Minerals*. 319 – 329.
- Onstott, T.C., Hargraves, R.B., Joubert, P. & Reid, D.L. (1986): Constraints on the tectonic evolution of the Namaqua province. I: Palaeomagnetic and $^{41}\text{Ar}/^{39}\text{Ar}$ results of the

- Richtersveld subprovince: *Geological Society of South Africa Transactions*, 89, 117 – 142.
- Osterberg, S.A. (1985): Stratigraphy and hydrothermal alteration of Archean volcanic rocks at the Headway-Coulee massive sulfide prospect, Northern Onaman area, Northwestern Ontario. 154 p. University of Minnesota Duluth, M.S. Thesis, (unpubl.).
- Paquet, H., Colin, F., Duplay, J., Nahon, D. & Millot, G. (1986): Ni, Mn, Zn, Cr-smectites, early and effective traps for transition elements in supergene ore deposits. – In: Rodriguez-Clemente & Tardy, Y. (eds.): *Proceedings of the International Meeting “Geochemistry of the earth surface and processes of mineral formation”*, Granada (Spain), 16 – 22 March 1986, 221 – 229.
- Partridge, T.C. & Maud, R.R. (1987): Geomorphic evolution of southern Africa since the Mesozoic. *South African Journal of Geology*, 90, 179 – 208.
- Pearce, J.A. (1996): A user's guide to basalt discrimination diagrams. *Geological Association of Canada, Short Course Notes*, 12, 79 – 113.
- Pearce, J. A., Harris, N. B. W. & Tindle, A. G. (1984): Trace element discrimination diagrams for the tectonic interpretation of granitic rocks. *Journal of Petrology*, 25, 956 – 983.
- Pearce, J. A., & Norry, M. J. (1979): Petrogenetic implications of Ti, Zr, Y, and Nb variations in volcanic rocks. *Contributions to Mineralogy and Petrology*, 69, 33 – 47.
- Pettijohn, F.J., Potter, P.E. & Siever, R. (1972): *Sand and Sandstones*. Springer Verlag, New York. 553 p.
- Peucker-Ehrenbrink, B., Jaffe, L. & Petsch, S. (2001): Towards Quantifying Trace and Nutrient Element Release Rates during Black Shale Weathering. *EUG XI*, 108.
- Philips, D., Kiviets, G.B., Biddulph, M.G. & Madav, M.K. (2000): Cenozoic Volcanism. – In: Partridge, T.C. & Maud, R.R. (eds.): *The Cenozoic of Southern Africa*. Oxford University Press. U.K. 182 – 197.
- Pickford, M. (2000): Neogene and Quaternary vertebrate biochronology of the Sperrgebiet and Otavi Mountainland, Namibia. *Geological Survey of Namibia Communications*, 12, 359 – 365.
- Pickford, M., Mein, P. & Senut, B. (1994): Fossiliferous Neogene karst fillings in Angola, Botswana and Namibia. *Suid-Afrikaanse Tydskrif vir Wetenskap*, 90, 227 – 230.
- Pollard, A.M., Thomas, R.G. & Williams, P.A. (1989): Synthesis and stabilities of the basic copper (II) chlorides atacamite, paratacamite and bottallackite. *Mineralogical Magazine*, 53, 557 – 563.
- Porada, H. (1989): The Damara-Ribeira Orogen of the Pan-African-Brasiliano Cycle in Namibia (South West Africa and Brazil) as interpreted in terms of continental collision: *Tectonophysics*, 57, 237 – 265.
- Raab, M.J., Weber, K. & Brown, R.W. (2002): Quantifying denudation rates with vertical relief fission track profiles in Namibia. *AdG – Forschung und Entwicklungszusammenarbeit in Afrika*. Göttingen, 28. – 29. Juni.
- Reid, D.L., Ransome, I.G.D., Onstott, T.C. & Adams, C.J. (1991): Time of emplacement and metamorphism of late Precambrian mafic dikes associated with the Pan-African Gariep orogeny, southern Africa: Implications for the age of the Nama Group. *Journal of African Earth Sciences*, 13, 531 – 541.
- Righi, D. & Mennier, R. (1995): Origin of clays by rock weathering and soil formation. – In: Velde, B. (ed.): *Origin and mineralogy of Clays – Clays and the environment*. 43 – 161.
- Robertson, J.M. & Condie, K.C. (1989): Geology and geochemistry of Early Proterozoic volcanic and subvolcanic rocks of the Pecos greenstone belt, Sangre de Cristo Mountains, New Mexico. – In: Grambling, J.A. & Tewksbury, B.J. (eds.): *Proterozoic geology of the southern Rocky Mountains*. *Geol. Soc. Amer. Spec. Paper* 235, Boulder, Colorado, 119 – 146.

- Roedder, E. (1968): The noncolloidal origin of „colloform“ textures in sphalerite ores. *Economic Geology*, 63, 451 – 471.
- Rollinson, H. (1993): Using geochemical data: evaluation, presentation, interpretation, 362 p.
- Rougvie, J.R. & Sorensen, S.S. (2002): Cathodoluminescence record of K-metasomatism in ash-flow tuffs: Grain-scale mechanisms and large-scale geochemical implications. *Geology*, 30, 4, 307 – 310.
- Roy, D.M. & Mumpton, F.A. (1956): Stability of minerals in the system ZnO – SiO₂-H₂O. *Economic Geology*, 51, 432 – 443.
- SACS (South African Committee for Stratigraphy) (1980): Stratigraphy of South Africa: Handbook Geological Survey of South Africa, 8, 690 p.
- Sangameshwar, S.R. & Barnes, H.L. (1983): Supergene processes in zinc-lead-silver sulfide ores in carbonates. *Economic Geology*, 78; 7, 1379 - 1397.
- Schaffalitzky, C. & Boland, M.B. (2001): The Shaimerden Zinc Oxide Deposit, Kazakhstan. GSA Annual Meeting, Nov 5 – 8, Boston.
- Schandl, E.S., Gorton, M.P. & Lydon, J.W. (2000): Trace and rare earth element study of metasedimentary rocks associated with the Sullivan sedex deposit, British Columbia: Implications for element mobility and sediment provenance. – In: Lydon, J.W., Höy, T., Slack, J.F. & Knapp, M.E. (eds.): The geological environment of the Sullivan deposit, British Columbia. Geological Association of Canada, Mineral Deposits Division, Special Publication No. 1, 202 – 217.
- Scott, K.M. (1987): The mineralogical distribution of pathfinder elements in gossans derived from dolomitic shale-hosted Pb-Zn deposits, Northwest Queensland, Australia. *Chemical Geology*, 64, 295 – 306.
- Scott, K.M. (1986): Elemental partitioning into Mn- and Fe-oxides derived from dolomitic shale-hosted Pb-Zn deposits, Northwest Queensland, Australia. *Chemical Geology*, 57, 395 – 414.
- Scott, K.M., Ashley, P.M. & Lawie, D.C. (2001): The geochemistry, mineralogy and maturity of gossans derived from volcanogenic Zn-Pb-Cu deposits of the eastern Lachlan Fold Belt, NSW, Australia. *Journal of Geochemical Exploration*, 72, 169 – 191.
- Ségalen, L., Renard, M., Lee-Thorp, J.A., Senut, B. & Pickford, M. (2004): Palaeoclimate and palaeoenvironment reconstruction of the Namib Desert during the Neogene. *Geoscience Africa 2004. Abstract Volume 2*, University of the Witwatersrand, Johannesburg, South Africa, 586.
- Sherman, D.M. (2001): Weathering Reactions and Soil-Groundwater Chemistry. *Environmental Geochemistry*, University of Bristol, Unpubl. Lecture Notes 2001/2002. 11 p.
- Slack, J.F. & Höy, T. (2000): Geochemistry and provenance of clastic metasedimentary rocks of the Aldridge and Fort Steele Formations, Purcell Supergroup, southeastern British Columbia. – In: Lydon, J.W., Höy, T., Slack, J.F. & Knapp, M.E. (eds.): The geological environment of the Sullivan deposit, British Columbia. Geological Association of Canada, Mineral Deposits Division, Special Publication, 1, 180 – 201.
- Söhnge, P.G. and De Villiers, J. (1947): Résumé of the geology of the Richtersveld and the eastern Sperrgebiet: *Transactions Geological Society South Africa*, 49, 263-276.
- Stanisreet, I.G., Kukla, P.A. & Henry, G. (1991): Sedimentary basinal response to a late Precambrian Wilson cycle: The Damara orogen and Nama foreland, Namibia. *Journal of African Earth Sciences*, 13, 141 – 156.
- Stanton, R.L. (1972): *Ore petrology*. McGraw-Hill, New York, 713 p.
- Sun, S.S. & McDonough, W.F. (1995): Composition of the Earth. *Chemical Geology*. 120, 223 – 253.

- Taboada, T. & Garcia, C. (1999): Smectite formation produced by weathering in a coarse granite saprolite in Galicia (NW Spain). *Catena* 35, 281 – 290.
- Takahashi, T. (1960): Supergene alteration of zinc and lead deposits in limestone. *Economic Geology*, 55, 6, 1083 – 1115.
- Tankard, A. J., Jackson, M. P. A., Eriksson, K. A., Hobday, D. K., Hunter, D. R. & Minter, W. E. L. (1982): *Crustal Evolution of Southern Africa*: Springer, Berlin, p. 314-328.
- Taylor, S.R. & McLennan, S.M. (1985): *The continental crust: Its composition and evolution*. Blackwell, Oxford, 312 p.
- Teeuw, R.M., Thomas, M.F. & Thorp, M.B. (1994): Regolith and landscape development in the Koidu Basin of Sierra Leone. – In: Robinson, D.A. & Williams, R.B.G. (eds.): *Rock weathering and landform evolution*. John Wiley & Sons, 303– 320.
- Theron, S., Dobbe, R., Gnoinski, G. & Boshoff, F. (2002): Suitability of sauconite, from the Skorpion Zn-oxide orebody, for Ar-Ar (K-Ar) age dating. Anglo American Corporation, Exploration Acquisition Division, Petrology Unit, Unpublished Company Report, 5 p.
- Thomas, M.F. (1989): The role of etch processes in landform development II. Etching and the formation of relief. *Zeitschrift für Geomorphologie, Supplementband NF33*, 257 – 274.
- Thomas, M.F. (1994): Ages and geomorphic relationships of saprolite mantles. – In: Robinson, D.A. & Williams, R.B.G. (eds.): *Rock weathering and landform evolution*. John Wiley & Sons, p. 287 – 301.
- Tinker, J.H. & de Witt, M.J. (2004): Balancing erosion and deposition on and around Southern Africa since Gondwana breakup. *Geoscience Africa 2004*, 634 – 635.
- Tiwary, A. & Deb, M. (1997): Geochemistry of hydrothermal alteration at the Deri massive sulphide deposit, Sirohi district, Rajasthan, NW India. *Journal of Geochemical Exploration*, 59, 99 – 121.
- Trompette, R. (1994): *Geology of western Gondwana (2000 - 500 Ma). Pan-African-Brasiliano aggregation of South America and Africa*: Balkema, Rotterdam, 350 p.
- Valsami-Jones, E., Ragnarsdottir, K.V., Putnis, A., Bosbach, D., Kemp, A.J., Cressey, G. (1998): The dissolution of apatite in the presence of aqueous metal cations at pH 2 – 7. *Chemical Geology*, 151, 215 – 233.
- Van Vuuren, C.J.J. (1986): Regional setting and structure of the Rosh Pinah zinc-lead deposit, South West Africa/Namibia. – In: Anhaeusser, C.R. & Maske, S. (eds.): *Mineral Deposits of Southern Africa*. Geological Society of South Africa, 1593 – 1607.
- Velde, B. (1984): *Clay Minerals. Developments in Sedimentology*, 40. 428 p.
- Viola, G., Andreoli, M., Ben-Avraham, Z., Stengel, I. & Reshef, M. (2005): Offshore mud volcanoes and onland faulting in southwestern Africa: neotectonic implications and constraints on the regional stress field. *Earth and Planetary Science Letters*.
- von Veh, M.W. (1993): The stratigraphy and structural evolution of the Late Proterozoic Gariiep belt in the Sendelingsdrif-Annisfontein area, Northwestern Cape Province. *Precambrian Research Unit, University of Cape Town Bulletin*, 38, 174 p.
- Ward, J.D. & Corbett, I. (1990): Towards an age for the Namib. – In: Seely, M.K. (ed.): *Namib ecology: 25 years of Namib research*, Transvaal Museum Monograph, 7, 17 –26.
- Ward, J.D., Seely, M.K. & Lancaster, N. (1983): On the antiquity of the Namib. *South African Journal of Science*. 79, 175 – 183.
- Weber, K. & Raab, M. (2002): Tektonomorphologische Entwicklung Namibias. AdG – Forschung und Entwicklungszusammenarbeit in Afrika. Göttingen 28. – 29. Juni.
- Woods, T.L. & Garrels, R.M. (1986): Use of copper minerals as environmental indicators: *Applied Geochemistry*, 1, 181 – 187.
- Woodward, J.C., Macklin, M.G. & Lewin, J. (1994): Pedogenic weathering and relative-age dating of Quaternary alluvial sediments in the Pindus Mountains of northwest Greece. –

- In: Robinson, D.A. & Williams, R.B.G. (eds.): Rock weathering and landform evolution. John Wiley & Sons, p. 259 – 283.
- Yamamoto, M., Kase, K. Carvalho, T. & Mitsuno, C. (1993): Ore mineralogy and sulfur isotopes of the volcanogenic massive sulfide deposits in the Iberian Pyrite Belt. Resource Geology Special Issue, 15, 67 – 80.
- Zachara, J.M., Kittrick, J.A. & Harsh, J.B. (1988): The mechanism of Zn^{2+} adsorption on calcite. Geochimica et Cosmochimica Acta, 52, 2281 – 2291.

Appendix 1

Sample Data			Analytical Data								
Sample ID	From [m]	To [m]	TS	XRD	SEM-EDX	XRF	ICP-MS	MP	SI	Depth [m]	Lithology
										86	BSA
										87	SSS
BH7010	87.15	87.25	x	x		x				88	SSS
										89	SSS
BH7011	89.1	89.25	x	x	x	x				90	SSS
										91	SSS
										92	SSS
										93	SSS
										94	SSS
										95	SSS
										96	SSS
BH7014	96.8	97	x	x		x		x		97	SSS
BH7015	97.8	97.95	x	x	x	x	x			98	SSS
BH7012	98.2	98.4	x	x		x	x			99	ARK
BH7013	99.25	99.5	x	x		x				100.4	ARK

Sample Data			Analytical Data					
Sample ID	From [m]	To [m]	TS	XRD	XRF	ICP-MS	Depth [m]	Lithology
							178	LST
							179	LST
315	179.2	179.3		x	x		180	LST
316	179.55	179.65					181	LST
							182	LST
							183	LST
							184	LST
							185	LST
							185.55	LST

Sample Data			Analytical Data						
Sample ID	From [m]	To [m]	TS	XRD	XRF	ICP-MS	SI	Depth [m]	Lithology
								194	LST
								195	LST
								196	LST
								197	LST
								198	LST
								199	LST
								200	ARK
								201	LST
								202	ARK
								203	LST
								204	LST
								205	LST
								206	LST
								207	LST
								208	LST
								209	LST
								210	LST
701	210.1	210.2	x					211	LST
702	212.25	212.35	x					212	LST
703	212.45	212.72						213	ARK
704	213	212.18	x					214	ARK
705	213.45	213.8	x		x			215	ARK
706	214.7	214.9			x	x		216	ARK
707	215.75	215.9		x	x			217	ARK
708	216.7	216.87		x	x			218	ARK
709	216.9	217.1						219	ARK
710	220.05	220.2		x	x			220	ARK
711	220.75	220.95		x				221	ARK
								222	ARK
								223	ARK
712	223.65	223.85		x	x			224	ARK
713	224.6	224.75		x	x			225	ARK
								226	ARK
714	226.45	226.57		x	x			227	ARK
								228	ARK
								229	ARK
715	229.85	230.05		x	x			230	ARK
								231	ARK
								232	ARK
								233	ARK
716	233	233.15	x					234	ARK
								235	ARK
								236	ARK
								237	ARK
717	237.36	237.63	x					238	ARK
								239	ARK
718	239.55	239.78		x	x			240	ARK
719	240	240.1		x	x			241	LST
								242	LST
720	242.6	242.65	x					243	LST

Sample Data			Analytical Data						
Sample ID	From [m]	To [m]	TS	XRD	XRF	ICP-MS	SI	Depth [m]	Lithology
								244	LST
								245	LST
721	245.15	245.3		x		x		246	LST
								247	LST
								248	LST
								249	LST
								250	LST
								251	LST
								252	LST
								253	LST
								254	LST
								255	LST
								256	LST
								257	LST
								258	LST
								259	LST
								260	LST
								260.55	LST

Sample Data			Analytical Data				
Sample ID	From [m]	To [m]	XRD	XRF	ICP-MS	Depth [m]	Lithology
						178	LST
						179	LST
						180.5	LST

Sample Data			Analytical Data								
Sample ID	From [m]	To [m]	TS	XRD	XRF	SEM-EDX	MP	ICP-MS	SI	Depth [m]	Lithology
										224	ARK
										225	ARK
										226	ARK
2004	226.9	227	x							227	ARK
										228	ARK
										229	ARK
										230	ARK
										231	ARK
										232	ARK
										233	ARK
										234	ARK
										235	ARK
										236	ARK
										237	ARK
										238	ARK
										239	ARK
										240	ARK
										241	ARK
										242	ARK
2005	242.55	242.65								243	ARK
2006	243.24	243.49								244	ARK
										245	ARK
2007	245.1	245.25								246	ARK
										247	ARK
2066	247.1	247.25			x					248	ARK
										249	ARK
										250	ARK
										251	QSS
2067	251.2	251.35			x					252	QSS
										253	SHB
2008	253.08	253.2								254	SHB
										255	SHB
										256	SHB
2009	257.85	257.88		x				x		257	SHB
2010	258.45	258.52	x							258	SHB
2012	259.14	259.2								259	SHB
2011	259.8	259.9	x							260	QSS
2013	260.45	260.55								261	SHB
										262	SHB
										263	QSS
										264	QSS
										265	QSS
										266	QSS
										267	QSS
										268	QSS
2014	268.8	269	x			x				269	QSS

Sample Data			Analytical Data								
Sample ID	From [m]	To [m]	TS	XRD	XRF	SEM-EDX	MP	ICP-MS	SI	Depth [m]	Lithology
2015	269.85	269.95	x			x	x			270	QSS
										271	QSS
										272	QSS
										273	QSS
										274	QSS
										275	QSS
										276	QSS
										277	QSS
										278	QSB
										279	QSB
										280	QSB
										281	QSB
										282	QSB
										283	QSB
2017	283.8	283.88								284	QSB
2016	284.28	284.4								285	QSB
2068	285	285.15			x					286	QSB
										287	QSB
2018	287.93	288	x	x				x	x	288	QSB
										289	QSB
										290	QSB
										291	QSB
										292	QSB
2020	292	292.14								293	QSB
										294	QSB
										295	QSB
2021	295.62	295.65								296	QSB
2022	295.75	295.82								297	QSB
										298	QSB
										299	QSB
										300	QSB
										301	QSB
										302	QSB
2019	302.43	302.5								303	QSB
										304	QSB
										305	QSB
										306	QSB
										307	QSB
										308	QSB
										309	QSB
										310	QSB
										311	QSB
										312	QSB
										313	QSB
										314	QSB
										315	QSB

Sample Data			Analytical Data								
Sample ID	From [m]	To [m]	TS	XRD	XRF	SEM-EDX	MP	ICP-MS	SI	Depth [m]	Lithology
										362	QSB
										363	RHY
										364	RHY
										364.95	RHY

Sample Data			Analytical Data				
Sample ID	From [m]	To [m]	XRD	XRF	ICP-MS	Depth [m]	Lithology
						94	ARK
						95	ARK
						96	ARK
						97	ARK
						98	ARK
						99	ARK
						100	ARK
						101	ARK
						102	ARK
						103	ARK
						104	ARK
						105	ARK
						106	ARK
						107	ARK
						108	ARK
						109	ARK
						110	ARK
						111	ARK
						112	ARK
						113	ARK
						114	ARK
						115	ARK
						116	ARK
						117	ARK
						118	ARK
						119	ARK
						120	ARK
						121	ARK
						122	ARK
						123	ARK
						124	ARK
						125	ARK
						126	ARK
						127	ARK
						128	ARK
						129	ARK
						130	ARK
						131	ARK
						132	ARK
						133	ARK
						134	ARK
						135	ARK
						136	ARK
						137	ARK
						138	ARK
						139	ARK
						140	ARK
						141	ARK
						142	ARK
2406	142.3	142.45				143	QSS

Sample Data			Analytical Data				
Sample ID	From [m]	To [m]	XRD	XRF	ICP-MS	Depth [m]	Lithology
						244	QSS
						245	QSS
						245.5	QSS

Sample Data			Analytical Data						
Sample ID	From [m]	To [m]	TS	XRD	SEM-EDX	XRF	ICP-MS	Depth [m]	Lithology
								270	ARK
								271	ARK
								272	ARK
								273	ARK
								274	ARK
								275	ARK
								276	ARK
								277	ARK
								278	ARK
								278.59	ARK

Borehole SD48								
E N		3020 16150		Inclination Azimuth		- 70° 270°		Elevation 662 m
Sample Data			Analytical Data					
Sample ID	From [m]	To [m]	XRD	XRF	ICP-MS	Depth [m]	Lithology	
						1		OVB
						2		OVB
						3		OVB
						4		OVB
						5		OVB
						6		OVB
						7		OVB
						8		OVB
						9		OVB
						10		OVB
						11		OVB
						12		OVB
						13		OVB
						14		OVB
						15		OVB
						16		ARK
						17		ARK
						18		ARK
						19		ARK
4817	20	20.1				20		ARK
						21		CL
						22		CL
						23		CL
						24		CL
						25		CL
						26		CL
4818	26.75	26.9	x	x		27		ARK
						28		ARK
						29		ARK
4819	29.45	29.55	x	x		30		ARK
						31		ARK
						32		ARK
						33		ARK
						34		ARK
4825	34.85	35	x	x		35		ARK
						36		ARK
						37		ARK
						38		ARK
						39		ARK
						40		ARK
						41		ARK
						42		ARK
						43		ARK

Sample Data			Analytical Data				
Sample ID	From [m]	To [m]	XRD	XRF	ICP-MS	Depth [m]	Lithology
						294	LST
						295	LST
						296.2	LST

Sample Data			Analytical Data							
Sample ID	From [m]	To [m]	TS	XRD	SEM-EDX	XRF	MP	ICP-MS	Depth [m]	Lithology
									270	BSA
									271	
									272	
									273	
									274	
									275	
									276	
									277	
4923	277.82	277.95							278	
									279	
4924	279.9	280							280	
									281	
									282	
									283	
									284	
									285	
									286	
									287	
									288	
									289	
4927	289.58	289.73							290	
									291	
									292	
									293	
4968	294	294.15				x			294	
									295	
									296	
4928	296.37	296.47	x		x				297	
									298	
									299	
									300	
									301	
									302	
									303	
									304	
4929	305.52	305.57							305	
4925	306	306	x						306	
4926	306.06	306.15							307	
4930	307.37	307.52	x						308	
4931	308.28	308.36	x						309	
4955	309.84	309.9							310	
4956	312.18	312.23	x						311	
4957	312.78	312.85		x				x	312	
4958	312.95	313	x						313	
4959	313.93	313.98							314	
4932	314.65	314.84							315	

Sample Data			Analytical Data						
Sample ID	From [m]	To [m]	TS	SEM-EDX	XRD	XRF	ICP-MS	Depth [m]	Lithology
								244	LST
								245	LST
								246	LST
								247	LST
								248	LST
								249	LST
								250	LST
								251	LST
								252	LST
								253	LST
								254	LST
								255	LST
								256	LST
								256.8	LST

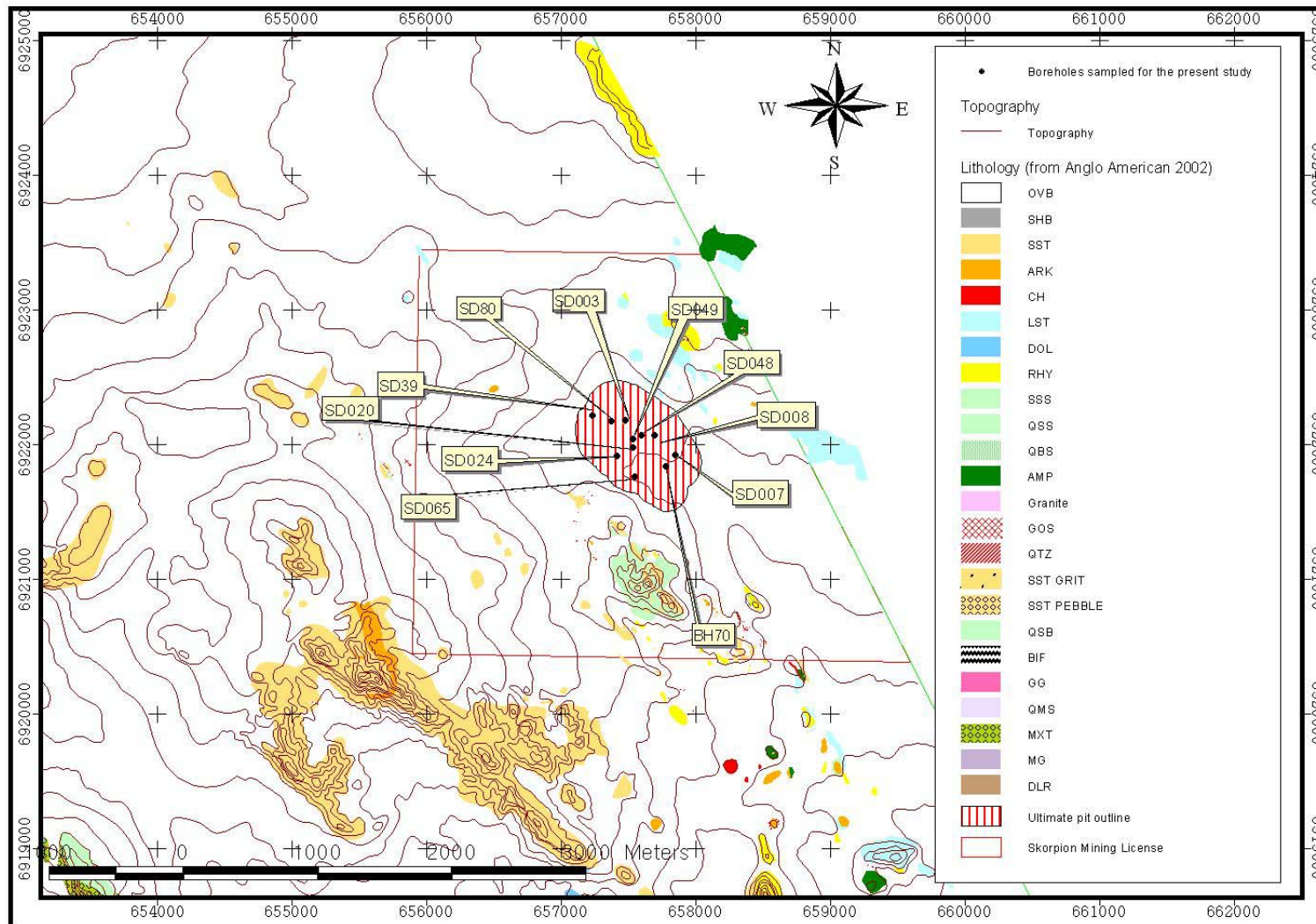
Sample Data			Analytical Data					
Sample ID	From [m]	To [m]	TS	XRD	XRF	SEM-EDX	Depth [m]	Lithology
							132	LST
							133	LST
							134	LST
							135	LST
							136	LST
							137	LST
							138	LST
							139	LST
							140	LST
							141	LST
							142	LST
							143	LST
							144	LST
							145	LST
							146	LST
							147	LST
							148	LST
							149	LST
							150	LST
							151	LST
							152	LST
							153	LST
							154	LST
							155	LST
							156	LST
							157	LST
							158	LST
							159	LST
							160	LST
							161	LST
							162	LST
							163	LST
							164	LST
							165	LST
							166	LST
							167	LST
							168	LST
8003	168.3	168.47					169	LST
							170	LST
8004	170.63	170.7					171	LST
8001	171.84	172.25	x	x	x		172	LST
8005	172.91	173					173	LST
8006	173.43	173.58					174	LST
8007	174.35	174.47					175	LST
8009	175.1	175.25					176	LST
8008	176.45	176.57					177	LST

Sample Data			Analytical Data					
Sample ID	From [m]	To [m]	TS	XRD	XRF	SEM-EDX	Depth [m]	Lithology
							224	ARK
							225	ARK
8026	225.65	225.9					226	ARK
8027	226.4	226.6	x	x	x	x	227	ARK
							228	ARK
							229	ARK
8028	229.85	230					230	ARK
							231	ARK
							232	ARK
							233	ARK
							234	ARK
							235	ARK
							236	ARK
							237	ARK
							238	ARK
							239	ARK
							240	ARK
							241	ARK
							242	ARK
							243	QSS
							244	QSS
							245	ARK
							246	ARK
							247	ARK
							248	ARK
							249	ARK
							250	ARK
							251	ARK
							252	ARK
							253	ARK
							254	ARK
							255	ARK
							256	ARK
							257	ARK
							257.9	ARK

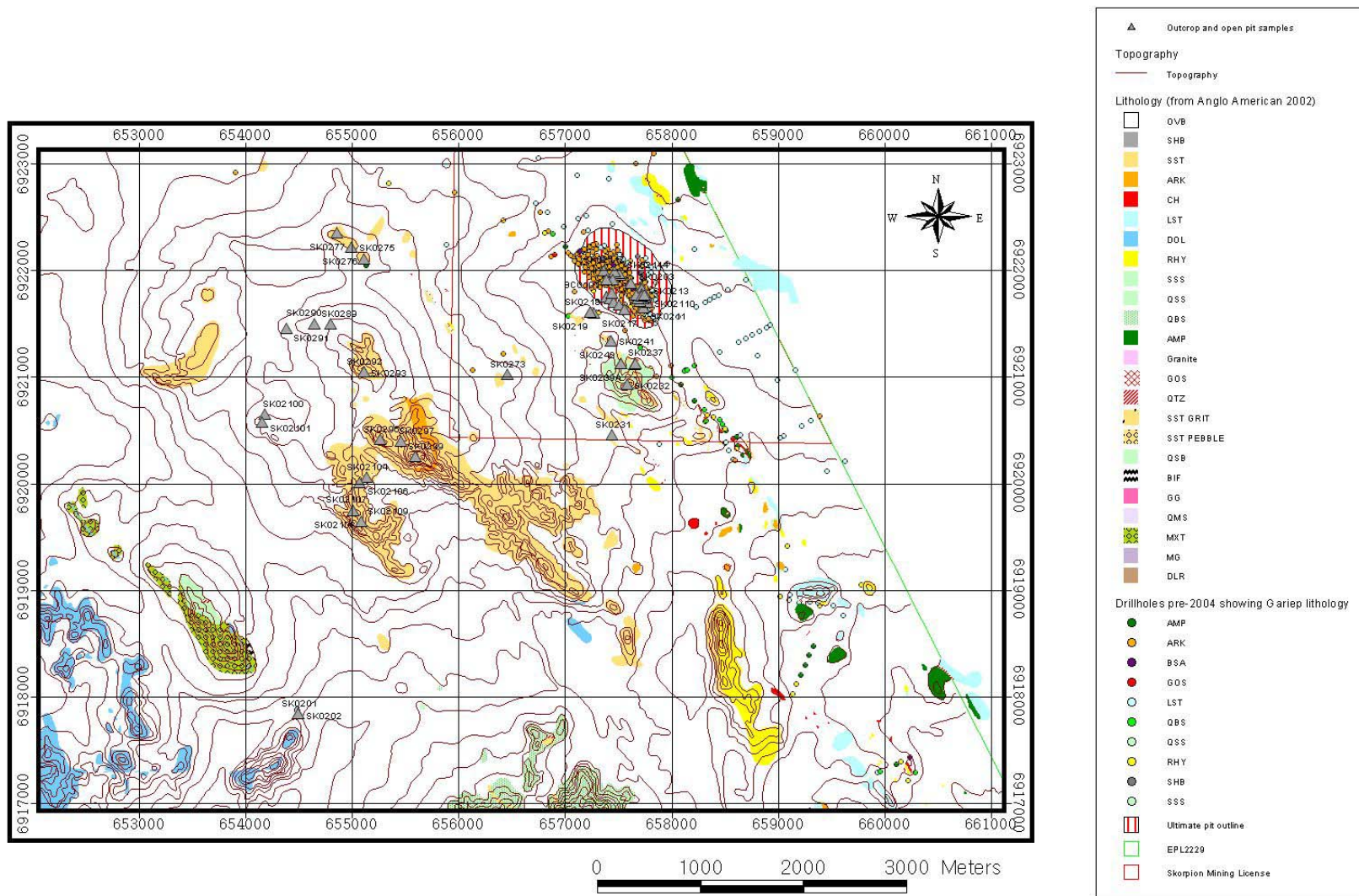
Legend

	Mining Term		Metamorphic Classification
	OVB	Overburden	
	ARK	Arkose	Psammitic siliciclastic metasediments, e.g. meta-arkose
	LST	Limestone	Marble
	BSA	Banded shale and arkose	Semipelitic siliciclastic metasediments
	SSS	Sheared sericite schist	Felsic metavolcanic rocks
	QSS	Quartz sericite schist	Felsic metavolcanic rocks
	RHY	Rhyolithe	Felsic metavolcanic rocks
	QBS	Quartz biotite schist	Felsic metavolcanic rocks
	CL	<i>Core Loss</i>	

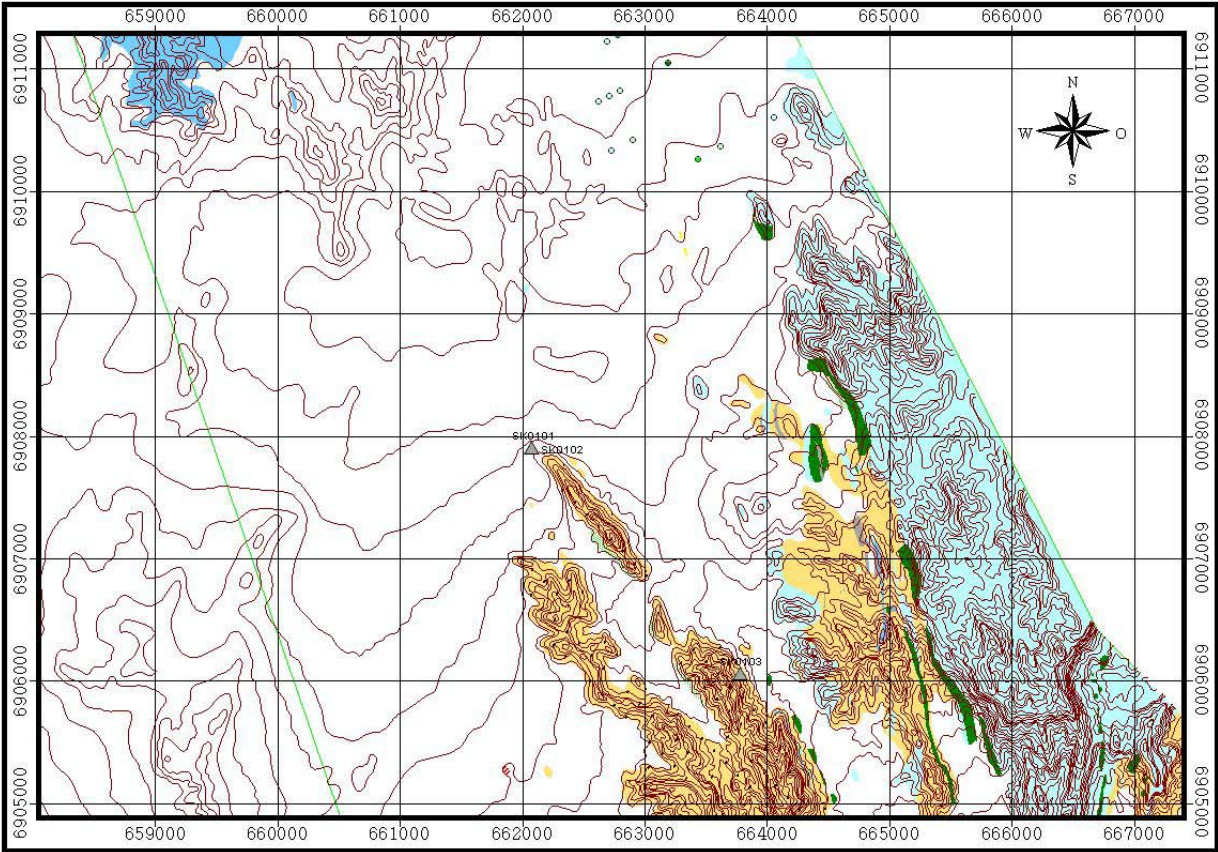
Location of Boreholes



Location of Open Pit and Outcrop Samples – Northern Part

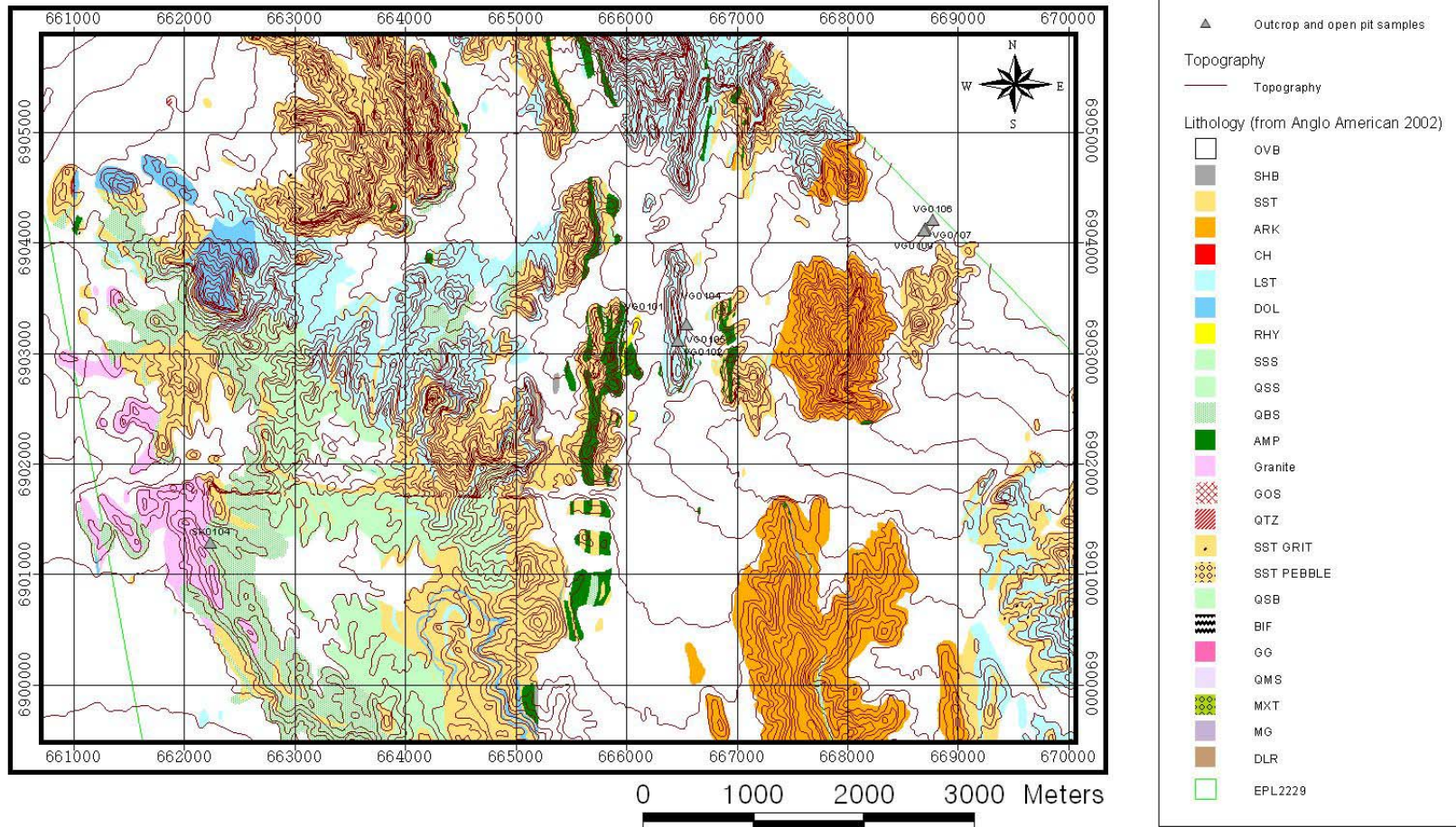


Location of Open Pit and Outcrop Samples – Central Part



- ▲ Outcrop and open pit samples
- Topography
 - Topography
- Lithology (from Anglo American 2002)
 - OVB
 - SHB
 - SST
 - ARK
 - CH
 - LST
 - DOL
 - RHY
 - SSS
 - QSS
 - QBS
 - AMP
 - Granite
 - GOS
 - QTZ
 - SST GRIT
 - SST PEBBLE
 - QSB
 - BIF
 - GG
 - QMS
 - MKT
 - MG
 - DLR
- Drillholes pre-2004 showing G ariep lithology
 - AMP
 - ARK
 - BSA
 - GOS
 - LST
 - QBS
 - QSS
 - RHY
 - SHB
 - SSS
- ▭ Ultimate pit outline
- ▭ EPL2229
- ▭ Skorpion Mining License

Location of Open Pit and Outcrop Samples – Southern Part



Appendix 2

Sample Number geochemical analyses (CPM)

Sample ID	Location	Depth from [m]	Depth to [m]	Lithology (Mining term)	UTM		Local Mine Grid	
					E	N	E	N
0301	SD03	66.5	66.65	ARK	657485	6922181	2973	16300
0305	SD03	82.9	83.05	ARK	657485	6922181	2973	16300
0307	SD03	98.75	99	ARK	657485	6922181	2973	16300
0311	SD03	151	151.15	ARK	657485	6922181	2973	16300
0313	SD03	170.4	170.55	SSS	657485	6922181	2973	16300
0314	SD03	166.4	166.5	SSS	657485	6922181	2973	16300
0315	SD03	179.2	179.3	LST	657485	6922181	2973	16300
0317	SD03	154.5	154.65	SSS	657485	6922181	2973	16300
0318	SD03	77.5	77.6	ARK	657485	6922181	2973	16300
0319	SD03	74.8	74.9	ARK	657485	6922181	2973	16300
0705	SD07	213.45	213.8	ARK	657855	6921927	3175	15900
0706	SD07	214.7	214.9	ARK	657855	6921927	3175	15900
0707	SD07	215.75	215.9	ARK	657855	6921927	3175	15900
0708	SD07	216.7	216.87	ARK	657855	6921927	3175	15900
0710	SD07	220.05	220.2	ARK	657855	6921927	3175	15900
0712	SD07	223.65	223.85	ARK	657855	6921927	3175	15900
0713	SD07	224.6	224.75	ARK	657855	6921927	3175	15900
0714	SD07	226.45	226.57	ARK	657855	6921927	3175	15900
0715	SD07	229.85	230.05	ARK	657855	6921927	3175	15900
0718	SD07	239.55	239.78	ARK	657855	6921927	3175	15900
0719	SD07	240	240.1	ARK	657855	6921927	3175	15900
0721	SD07	245.15	245.3	LST	657855	6921927	3175	15900
0722	SD07	64	64.1	LST	657855	6921927	3175	15900
0726	SD07	102.5	102.6	ARK	657855	6921927	3175	15900
0727	SD07	109.5	109.6	ARK	657855	6921927	3175	15900
0734	SD07	156	156.2	ARK	657855	6921927	3175	15900
0803	SD08	63	63.1	ARK	657697	6922069	3105	16100
0807	SD08	69.2	69.45	ARK	657697	6922069	3105	16100
0809	SD08	105.85	106	ARK	657697	6922069	3105	16100
0811	SD08	108	108.1	ARK	657697	6922069	3105	16100
2009	SD20	257.85	257.88	SHB	657539	6921983	2925	16100
2018	SD20	287.93	288	QSB	657539	6921983	2925	16100
2024	SD20	328.8	328.94	RHY	657539	6921983	2925	16100
2052	SD20	30	30.15	ARK	657539	6921983	2925	16100
2065	SD20	112.2	112.35	BSA	657539	6921983	2925	16100
2066	SD20	247.1	247.25	ARK, GOS	657539	6921983	2925	16100
2067	SD20	251.2	251.35	QSS, GOS	657539	6921983	2925	16100
2068	SD20	285	285.15	QSB, GOS	657539	6921983	2925	16100
2404	SD24	39.85	40	ARK	657420	6921918	2790	16100
2409	SD24	159.1	159.3	QSS	657420	6921918	2790	16100
2410	SD24	170	170.2	ARK	657420	6921918	2790	16100
2413	SD24	177.95	178.05	QSS	657420	6921918	2790	16100
2418	SD24	207.6	207.75	QSS	657420	6921918	2790	16100
3901	SD39	70.3	70.5	ARK	657236	6922217	2772	16450
3902	SD39	52.6	52.75	ARK	657236	6922217	2772	16450
3905	SD39	68.7	68.9	ARK	657236	6922217	2772	16450
3906	SD39	76.55	76.65	LST	657236	6922217	2772	16450
3909	SD39	117.53	117.63	LST	657236	6922217	2772	16450
3915	SD39	181	181.1	LST	657236	6922217	2772	16450
3916	SD39	184.2	184.3	ARK	657236	6922217	2772	16450
3917	SD39	186.9	187.1	ARK	657236	6922217	2772	16450
3918	SD39	231.1	231.25	ARK, GOS	657236	6922217	2772	16450
3919	SD39	229.8	229.9	ARK	657236	6922217	2772	16450
3922	SD39	196.9	197	QSS	657236	6922217	2772	16450
4801	SD48	96	96.11	LST	657598	6922073	3020	16150
4802	SD48	105.44	105.5	ARK	657598	6922073	3020	16150
4805	SD48	116.45	116.53	LST	657598	6922073	3020	16150
4806	SD48	116.66	116.8	LST	657598	6922073	3020	16150
4807	SD48	123.85	124	LST	657598	6922073	3020	16150

Sample Number geochemical analyses (CPM)

Sample ID	Location	Depth from [m]	Depth to [m]	Lithology (Mining term)	UTM		Local Mine Grid	
					E	N	E	N
4809	SD48	136.81	136.85	LST	657598	6922073	3020	16150
4810	SD48	138.63	138.77	LST	657598	6922073	3020	16150
4812	SD48	147.35	147.45	SSS	657598	6922073	3020	16150
4814	SD48	165.8	165.92	LST	657598	6922073	3020	16150
4815	SD48	171.88	172.03	LST	657598	6922073	3020	16150
4816A	SD48	182	182.2	LST	657598	6922073	3020	16150
4816B	SD48	182	182.2	LST	657598	6922073	3020	16150
4818	SD48	26.75	26.9	ARK	657598	6922073	3020	16150
4819	SD48	29.45	29.55	ARK	657598	6922073	3020	16150
4820	SD48	46.35	46.5	ARK	657598	6922073	3020	16150
4821	SD48	52.23	52.3	ARK, GOS	657598	6922073	3020	16150
4822	SD48	64.4	64.7	ARK	657598	6922073	3020	16150
4823	SD48	65.1	65.25	ARK	657598	6922073	3020	16150
4825	SD48	34.85	35	ARK	657598	6922073	3020	16150
4826	SD48	47.35	47.55	ARK	657598	6922073	3020	16150
4910	SD49	186	186.18	ARK	657535	6922042	2950	16153
4915	SD49	220.4	220.57	ARK	657535	6922042	2950	16153
4920	SD49	250.26	250.44	ARK	657535	6922042	2950	16153
4952	SD49	220.8	220.85	ARK	657535	6922042	2950	16153
4957	SD49	312.78	312.85	QSS	657535	6922042	2950	16153
4968	SD49	294	294.15	ARK, GOS	657535	6922042	2950	16153
4969	SD49	252	252.15	ARK, GOS	657535	6922042	2950	16153
6506	SD65	113.2	113.5	SSS	657555	6921764	2835	15900
6512	SD65	117.8	117.9	SSS	657555	6921764	2835	15900
6518	SD65	183.3	183.4	BSA	657555	6921764	2835	15900
6519	SD65	184.55	184.65	ARK	657555	6921764	2835	15900
6521	SD65	185	185.2	ARK	657555	6921764	2835	15900
6522	SD65	186.25	186.4	LST	657555	6921764	2835	15900
8001	SD80	171.84	172.25	LST	657374	6922177	2873	16350
8011	SD80	180.69	180.85	ARK	657374	6922177	2873	16350
8013	SD80	184.65	184.78	ARK	657374	6922177	2873	16350
8014	SD80	184.9	185.04	ARK	657374	6922177	2873	16350
8016	SD80	189.35	189.5	BSA	657374	6922177	2873	16350
8022	SD80	201.65	201.85	ARK	657374	6922177	2873	16350
8024	SD80	217.4	217.55	ARK, GOS	657374	6922177	2873	16350
8025	SD80	219.4	219.55	ARK, GOS	657374	6922177	2873	16350
8027	SD80	226.4	226.6	ARK	657374	6922177	2873	16350
BH7001	BH70	26.09	27.05	ARK	657780	6921842	3070	15861
BH7002	BH70	35.5	35.7	ARK	657780	6921842	3070	15861
BH7003	BH70	32.25	32.5	ARK	657780	6921842	3070	15861
BH7004	BH70	41.5	41.3	ARK	657780	6921842	3070	15861
BH7005	BH70	37.9	38.1	ARK	657780	6921842	3070	15861
BH7006	BH70	61.65	61.9	ARK	657780	6921842	3070	15861
BH7007	BH70	59.8	59.9	ARK	657780	6921842	3070	15861
BH7008	BH70	65.4	65.5	ARK	657780	6921842	3070	15861
BH7009	BH70	72.65	72.8	ARK	657780	6921842	3070	15861
BH7010	BH70	87.15	87.25	SSS	657780	6921842	3070	15861
BH7011	BH70	89.1	89.25	SSS	657780	6921842	3070	15861
BH7012	BH70	98.2	98.4	ARK	657780	6921842	3070	15861
BH7013	BH70	99.25	99.5	ARK	657780	6921842	3070	15861
BH7014	BH70	96.8	97	SSS	657780	6921842	3070	15861
BH7015	BH70	97.8	97.95	SSS	657780	6921842	3070	15861
BH7016	BH70	21	21.1	ARK	657780	6921842	3070	15861
BH7017	BH70	43.5	43.6	ARK	657780	6921842	3070	15861
BNS 1	SD20	13.3	31	ARK	657539	6921983	2925	16100
BNS 2	SD20	31	49.65	ARK	657539	6921983	2925	16100
BNS 3	SD20	49.65	56.55	LST	657539	6921983	2925	16100
BNS 4	SD20	56.55	76.45	ARK	657539	6921983	2925	16100
BNS 5	SD20	76.45	94	LST	657539	6921983	2925	16100

Sample Number geochemical analyses (CPM)

Sample ID	Location	Depth from [m]	Depth to [m]	Lithology (Mining term)	UTM		Local Mine Grid	
					E	N	E	N
BNS 6	SD20	94	111.27	LST	657539	6921983	2925	16100
BNS 7	SD20	111.27	125	BSA	657539	6921983	2925	16100
BNS 8	SD20	125	153	ARK	657539	6921983	2925	16100
BNS 9	SD20	153	171	ARK	657539	6921983	2925	16100
BNS 10	SD20	171	201	ARK	657539	6921983	2925	16100
BNS 11	SD20	201	225	ARK	657539	6921983	2925	16100
BNS 12	SD20	225	254	ARK	657539	6921983	2925	16100
BNS 13	SD20	254	260	SHB	657539	6921983	2925	16100
BNS 14	SD20	260	277	QSS	657539	6921983	2925	16100
BNS 15	SD20	277	281	QSB	657539	6921983	2925	16100
BNS 16	SD20	281	304	QSB	657539	6921983	2925	16100
BNS 17	SD20	304	327	QSB	657539	6921983	2925	16100
BNS 18	SD20	327	347	RHY	657539	6921983	2925	16100
BNS 19	SD20	347	363	QBS	657539	6921983	2925	16100
SK0101	outcrop			ARK	662084	6907908		
SK0102	outcrop			ARK	662084	6907908		
SK0103	outcrop			ARK	663787	6906061		
SK0104	outcrop			ARK	657764	6921902		
SK0111	outcrop			ARK	670008	6892337		
SK0114	outcrop			ARK	665838	6898466		
SK0201	outcrop			RHY	654434	6917773		
SK0202	outcrop			RHY	654434	6917773		
SK0203	open pit	645 m level		ARK	657764	6921902		
SK0204	open pit	645 m level		ARK	657764	6921902		
SK0205	open pit	645 m level		ARK	657784	6921853		
SK0207	open pit	645 m level		ARK	657770	6921773		
SK0208	open pit	645 m level		ARK	657657	6921943		
SK02100	outcrop			ARK	654106	6920675		
SK02101	outcrop			SS	654083	6920594		
SK02104	outcrop			GOS	655095	6920063		
SK02106	outcrop			ARK	655027	6920013		
SK02107	outcrop			ARK	654968	6919745		
SK02108	outcrop			ARK	654968	6919745		
SK02109	outcrop			ARK	655047	6919636		
SK0211	open pit	645 m level		ARK	657777	6921704		
SK02110	open pit	645 m level		SSS	657810	6921762		
SK02110	open pit	645 m level		SSS	657810	6921762		
SK02113	open pit	645 m level		SSS	657760	6921892		
SK02113	open pit	645 m level		SSS	657760	6921892		
SK02114	open pit	645 m level		ARK	657555	6922022		
SK02116	open pit	645 m level		SSS	657545	6922040		
SK02116	open pit	645 m level		SSS	657545	6922040		
SK02117	open pit	645 m level		SSS	657394	6922067		
SK02117	open pit	645 m level		SSS	657394	6922067		
SK02118	open pit	645 m level		ARK	657499	6922061		
SK02119	open pit	645 m level		ARK	657479	6921981		
SK0212	open pit	645 m level		SSS	657782	6921792		
SK0213	open pit	645 m level		BSA	657798	6921817		
SK0213B	open pit	645 m level		BSA	657798	6921817		
SK0214	open pit	645 m level		BSA	657730	6921817		
SK0215	open pit	645 m level		BSA	657730	6921817		
SK0216A	open pit	645 m level		SSS	657761	6921841		
SK0216B	open pit	645 m level		SSS	657761	6921841		
SK0217	outcrop			GOS	657299	6921655		
SK0218	outcrop			BARITE	657260	6921664		
SK0219	outcrop			BARITE	657260	6921664		
SK0231	outcrop			RHY	657477	6920472		
SK0232	outcrop			RHY	657619	6920965		
SK0235	outcrop			SSS	657695	6921154		

Sample Number geochemical analyses (CPB)

Sample ID	Location	Depth from [m]	Depth to [m]	Lithology (Mining term)	UTM		Local Mine Grid	
					E	N	E	N
SK0235	open pit	645 m level		SSS	657695	6921154		
SK0236	outcrop			SSS	657694	6921157		
SK0236	open pit	645 m level		SSS	657694	6921157		
SK0237	outcrop			GOS	657702	6921169		
SK0239A	outcrop			GOS	657558	6921170		
SK0239B	outcrop			GOS	657558	6921170		
SK0241	outcrop			ARK	657466	6921382		
SK0242	outcrop			ARK	657466	6921382		
SK0246	open pit	645 m level		ARK, GOS	657740	6921766		
SK0247	open pit	645 m level		ARK, GOS	657723	6921794		
SK0249	open pit	645 m level		ARK	657707	6921830		
SK0251	open pit	645 m level		LST	657421	6921814		
SK0253	open pit	645 m level		LST	657421	6921814		
SK0254	open pit	645 m level		LST	657421	6921814		
SK0256	open pit	645 m level		GOS	657458	6921794		
SK0257	open pit	645 m level		ARK	657458	6921794		
SK0258	open pit	645 m level		ARK	657458	6921794		
SK0259	open pit	645 m level		GOS	657458	6921794		
SK0260	open pit	645 m level		GOS	657490	6921764		
SK0265	open pit	645 m level		ARK	657540	6921735		
SK0267	open pit	645 m level		GOS	657599	6921687		
SK0268	open pit	645 m level		ARK	657599	6921687		
SK0269	open pit	645 m level		GOS	657599	6921687		
SK0273	outcrop			ARK	656458	6921061		
SK0275	outcrop			ARK	655066	6922181		
SK0276	outcrop			ARK	654948	6922295		
SK0277	outcrop			ARK	654804	6922436		
SK0279	open pit	645 m level		BSA	657765	6921821		
SK0283	open pit	645 m level		ARK	657785	6921827		
SK0287	open pit	645 m level		ARK, GOS	657475	6921844		
SK0289	outcrop			ARK	654749	6921550		
SK0290	outcrop			RHY	654589	6921551		
SK0291	outcrop			ARK	654315	6921505		
SK0292	outcrop			RHY	655068	6921087		
SK0293	outcrop			RHY	655068	6921087		
SK0296	outcrop			ARK	655231	6920432		
SK0297	outcrop			ARK	655425	6920412		
SK0299	outcrop			ARK	655564	6920265		
VG0101	outcrop			LST	666470	6903120		
VG0101	outcrop			LST	666470	6903120		
VG0102	outcrop			LST	666470	6903120		
VG0104	outcrop			ARK	666549	6903270		
VG0104	outcrop			LST	666549	6903270		
VG0105	outcrop			LST	666549	6903270		
VG0105	outcrop			LST	666549	6903270		
VG0106	outcrop			ARK	668776	6904210		
VG0106	outcrop			ARK	668776	6904210		
VG0107	outcrop			LST	668705	6904133		
VG0107	outcrop			LST	668705	6904133		
VG0109	outcrop			LST	668696	6904116		
VG0109	outcrop			LST	668696	6904116		

CP hole rockanalyses

Sample ID	Location	Lithology	E	N	SiO ₂ [%]	Al ₂ O ₃ [%]	Fe ₂ O ₃ [%]	MgO [%]	CaO [%]	Na ₂ O [%]	K ₂ O [%]	TiO ₂ [%]	P ₂ O ₅ [%]	MnO [%]	Total S [%]	LOI [%]	SUM [%]	Cr [ppm]	Ba [ppm]
BNS 1	SD20	ARK	657539	6921983	59.32	9.21	2.64	0.87	0.63	0.45	4.13	0.43	0.24	0.28	0.13	6.2	84.53	41.1	1339
BNS 2	SD20	ARK	657539	6921983	67.63	7.35	2.24	1.22	0.28	0.24	3.31	0.31	0.18	0.31	0.02	4.2	87.29	27.4	1215
BNS 3	SD20	LST	657539	6921983	51.77	6.04	1.42	1.23	19.09	0.3	3.17	0.29	0.14	0.1	0.01	14.3	97.86	13.7	772
BNS 4	SD20	ARK	657539	6921983	67.26	6.97	1.7	1.1	1.26	0.18	3.05	0.27	0.15	0.09	0.03	5	87.06	20.5	1250
BNS 5	SD20	LST	657539	6921983	21.73	3.38	0.94	0.36	41.35	0.14	1.55	0.16	0.11	0.06	0.01	30.4	100.19	13.7	678
BNS 6	SD20	LST	657539	6921983	22.66	3.88	1.16	0.48	40.16	0.09	1.71	0.22	0.13	0.07	0.01	29	99.57	20.5	824
BNS 7	SD20	BSA	657539	6921983	59.87	8.44	3.18	1.65	0.89	0.12	3.51	0.49	0.37	0.46	0.03	6.2	85.21	41.1	1203
BNS 8	SD20	ARK	657539	6921983	65.34	8.61	7.28	0.37	0.23	0.14	4.74	0.44	0.25	2.06	0.05	4.2	93.71	27.4	2576
BNS 9	SD20	ARK	657539	6921983	70.62	8.82	7.85	0.43	0.05	0.1	2.88	0.43	0.18	0.89	0.03	3.4	95.68	27.4	1500
BNS 10	SD20	ARK	657539	6921983	50.89	8.07	27.99	0.33	0.05	0.04	0.86	0.39	0.42	0.22	0.11	7.4	96.77	20.5	3340
BNS 11	SD20	ARK	657539	6921983	68.52	13.15	5.06	0.79	0.15	0.06	2.38	0.69	0.13	0.01	0.08	5.4	96.42	47.9	2181
BNS 12	SD20	ARK	657539	6921983	69.85	13.27	3.63	0.59	0.03	0.04	2.23	0.68	0.16	0.22	0.18	4.7	95.58	47.9	8061
BNS 13	SD20	SHB	657539	6921983	71.39	9.88	2.28	0.72	0.01	0.05	2.65	0.45	0.02	0.01	1.87	4.2	93.53	27.4	4491
BNS 14	SD20	QSS	657539	6921983	73.66	9.62	3.06	0.57	0.02	0.04	1.96	0.46	0.07	0.01	2.71	4.1	96.28	6.8	5770
BNS 15	SD20	QSB	657539	6921983	70.62	8.98	5.36	0.35	0.02	0.02	1.09	0.21	0.06	0.03	4.95	5.5	97.19	34.2	10099
BNS 16	SD20	QSB	657539	6921983	54.26	13.04	12.29	2.95	0.07	0.09	4.51	3.68	0.04	0.33	4.99	5.9	102.15	6.8	4125
BNS 17	SD20	QSB	657539	6921983	52.8	12.35	13.57	4.44	0.25	0.08	5.05	3.53	0.15	0.38	4.47	4.7	101.77	6.8	4125
BNS 18	SD20	RHY	657539	6921983	66.4	8.41	8.42	0.58	0.05	0.14	5.45	0.37	0.05	0.03	7.29	5.2	102.39	6.8	5995
BNS 19	SD20	QBS	657539	6921983	51.18	12.52	15.58	2.82	0.46	0.11	5.21	3.29	0.36	0.17	6.64	5.9	104.24	6.8	5695
BH 7001	BH70	ARK	657780	6921842	57.32	7.65	2.02	0.75	0.73	0.49	2.57	0.403	0.37	0.057	0.023	8.310	80.69	42.9	750
BH 7012	BH70	ARK	657780	6921842	62.24	6.17	0.54	0.30	0.65	0.20	2.38	0.063	0.07	0.095	0.011	8.350	81.07	22.9	547
BH 7015	BH70	SSS	657780	6921842	66.22	1.45	1.08	0.19	0.38	0.08	0.45	0.075	0.31	0.092	0.013	4.250	74.59	115.0	114
0706	SD07	ARK	657855	6921927	22.31	2.72	1.12	0.75	1.69	0.09	0.57	0.147	0.87	0.087	0.018	23.440	53.81	31.9	119
0721	SD07	LST	657855	6921927	3.41	1.05	0.39	0.48	52.70	0.12	0.42	0.047	0.06	0.022	0.175	41.050	99.92	8.7	187
0722	SD07	LST	657855	6921927	3.82	1.07	0.59	0.09	52.93	0.04	0.55	0.052	0.06	0.022	0.053	40.850	100.13	11.0	86
0726	SD07	ARK	657855	6921927	49.57	12.52	4.03	1.68	1.58	0.22	5.02	0.553	0.48	0.003	0.016	9.700	85.37	75.1	823
0727	SD07	ARK	657855	6921927	9.53	1.74	0.74	0.58	5.03	0.06	0.54	0.089	3.44	0.048	0.016	27.070	48.88	19.8	132
0803	SD08	ARK	657697	6922069	83.14	6.45	1.01	2.34	0.13	0.16	4.30	0.182	0.05	0.124	0.012	1.510	99.41	43.4	773
0807	SD08	ARK	657697	6922069	76.03	1.24	1.05	2.22	2.83	0.04	0.78	0.043	2.02	0.072	0.011	5.080	91.42	352.0	49
0809	SD08	ARK	657697	6922069	80.23	4.35	0.62	0.82	0.37	0.13	2.40	0.132	0.08	0.021	0.013	3.990	93.16	46.0	374
0811	SD08	ARK	657697	6922069	78.69	5.24	0.76	0.76	5.49	0.46	3.19	0.151	0.08	0.021	0.026	4.950	99.82	199.0	734
2009	SD20	SHB	657539	6921983	66.40	9.64	4.34	0.90	nd	0.06	3.11	0.519	0.02	0.015	5.328	5.820	96.15	91.8	2963
2018	SD20	QSB	657539	6921983	53.05	11.93	16.06	3.40	0.05	0.08	4.93	2.895	0.04	0.231	5.734	6.030	104.43	31.6	2885
2024	SD20	RHY	657539	6921983	54.77	6.10	22.09	0.33	0.15	0.00	3.06	0.216	0.02	0.028	14.450	12.060	113.27	112.0	4044
2052	SD20	ARK	657539	6921983	70.26	8.62	1.05	0.31	0.20	0.42	4.66	0.154	0.09	0.011	0.022	4.580	90.38	8.8	1090
2404	SD24	ARK	657420	6921918	77.27	8.53	1.48	0.44	0.04	0.18	4.35	0.349	0.08	3.692	0.012	2.810	99.23	48.7	2767
2409	SD24	QSS	657420	6921918	57.27	5.45	29.90	0.05	0.16	0.05	0.25	0.353	0.11	0.075	0.163	4.980	98.81	63.0	5392
2410	SD24	ARK	657420	6921918	70.28	17.43	0.77	0.23	0.02	0.10	1.04	0.487	0.24	0.006	0.632	8.040	99.27	51.1	7243
2418	SD24	QSS	657420	6921918	76.25	13.06	3.93	0.02	0.06	0.08	0.25	0.127	0.30	0.003	0.229	5.910	100.22	8.8	1208

Sample ID	Location	Lithology	E	N	SiO ₂ [%]	Al ₂ O ₃ [%]	Fe ₂ O ₃ [%]	MgO [%]	CaO [%]	Na ₂ O [%]	K ₂ O [%]	TiO ₂ [%]	P ₂ O ₅ [%]	MnO [%]	Total S [%]	LOI [%]	SUM [%]	Cr [ppm]	Ba [ppm]
4910	SD49	ARK	657535	6922042	83.06	7.61	1.79	0.10	0.06	0.15	4.37	0.385	0.09	0.004	0.020	1.200	98.84	109.0	1949
4915	SD49	ARK	657535	6922042	85.10	8.54	0.97	0.33	0.04	0.08	1.11	0.338	0.06	0.002	0.050	2.830	99.45	24.8	1555
4920	SD49	ARK	657535	6922042	7.88	0.86	74.47	0.03	0.10	0.04	0.03	0.014	0.91	0.120	0.057	12.170	96.68	33.3	1433
4957	SD49	QSS	657535	6922042	63.27	11.00	7.29	0.19	0.02	0.06	0.72	0.092	0.06	0.016	6.958	8.460	98.14	nd	13327
6506	SD65	SSS	657555	6921764	61.42	9.65	3.06	0.37	0.08	0.12	1.74	0.147	0.04	0.007	0.038	10.150	86.82	30.0	2056
6518	SD65	BSA	657555	6921764	68.03	14.32	1.77	2.05	0.18	0.21	7.03	0.714	0.07	0.004	0.014	4.830	99.22	90.8	2429
6519	SD65	ARK	657555	6921764	20.54	3.72	20.18	0.82	0.72	nd	1.42	0.204	0.46	19.690	0.014	14.740	82.51	26.6	590
6521	SD65	ARK	657555	6921764	55.08	6.44	11.50	0.98	0.85	0.16	3.46	0.309	0.43	1.285	0.025	8.790	89.31	39.5	1445
6522	SD65	LST	657555	6921764	6.01	1.53	0.68	0.62	50.67	0.05	0.87	0.076	0.04	0.386	0.145	39.120	100.20	10.6	420
6512	SD65	SSS	657555	6921764	66.53	5.64	1.90	0.17	0.03	0.18	0.75	0.115	0.14	0.021	0.084	8.360	83.92	27.2	16289
SK0111	outcrop	ARK	670008	6892337	na	na	na	na	na	na	na	na	na	na	na	na	na	20.4	561
BH 7007	BH70	ARK	657780	6921842	na	na	na	na	na	na	na	na	na	na	na	na	na	na	634
SK 0114	outcrop	ARK	665838	6898466	na	na	na	na	na	na	na	na	na	na	na	na	na	28.5	697
VG0104	outcrop	LST	666549	6903270	na	na	na	na	na	na	na	na	na	na	na	na	na	na	114
VG0106	outcrop	ARK	668776	6904210	na	na	na	na	na	na	na	na	na	na	na	na	na	27.5	303
VG0105	outcrop	LST	666549	6903270	na	na	na	na	na	na	na	na	na	na	na	na	na	na	32
VG0101	outcrop	LST	666470	6903120	na	na	na	na	na	na	na	na	na	na	na	na	na	na	60
VG0109	outcrop	LST	668696	6904116	na	na	na	na	na	na	na	na	na	na	na	na	na	na	567
SK0104	outcrop	ARK	657764	6921902	na	na	na	na	na	na	na	na	na	na	na	na	na	22.3	23200
VG0107	outcrop	LST	668705	6904133	na	na	na	na	na	na	na	na	na	na	na	na	na	32.6	2880
SK0101	outcrop	ARK	662084	6907908	na	na	na	na	na	na	na	na	na	na	na	na	na	na	464
SK0102	outcrop	ARK	662084	6907908	na	na	na	na	na	na	na	na	na	na	na	na	na	na	325
SK02110	open pit	SSS	657810	6921762	69.12	8.53	10.36	0.3	0.35	0.16	7.21	0.09	0.09	nd	0.26	3.5	99.97	nd	918
SK02113	open pit	SSS	657760	6921892	78.92	11.56	0.78	1.26	0.14	0.08	3.77	0.07	nd	nd	0.01	2.8	99.39	nd	235
SK02116	open pit	SSS	657545	6922040	91.46	4.42	0.44	0.72	0.02	0.06	1.52	0.06	0.02	nd	0.01	0.9	99.63	nd	1228
SK02117	open pit	SSS	657394	6922067	85.97	7.22	0.54	1.12	0.02	0.1	2.47	0.05	0.01	nd	0.01	1.7	99.21	nd	1751
SK0235	open pit	SSS	657695	6921154	76.55	9.67	3.4	0.17	0.08	0.16	7.85	0.12	0.03	nd	0.05	1	99.08	nd	4396
SK0236	open pit	SSS	657694	6921157	80.72	9.65	0.49	0.06	0.04	0.16	8.05	0.12	nd	nd	0.01	0.3	99.60	nd	3469

nd - not detected

na - not analysed

CPM hole rockanalyses

Sample ID	Location	Lithology	E	N	Ni [ppm]	Sc [ppm]	Co [ppm]	Cs [ppm]	Ga [ppm]	Hf [ppm]	Nb [ppm]	Rb [ppm]	Sn [ppm]	Sr [ppm]	Ta [ppm]	Th [ppm]	Tl [ppm]	U [ppm]	V [ppm]	W [ppm]
BNS 1	SD20	ARK	657539	6921983	94	7	7.1	3.6	11.9	4.6	15.2	198.9	3	213.7	2	14.9	0.7	3.3	53	5
BNS 2	SD20	ARK	657539	6921983	84	4	6.7	4.3	8.8	5.3	11	156.7	2	208.9	1.3	12.8	1.2	1.5	35	5
BNS 3	SD20	LST	657539	6921983	20	4	3.8	5.1	6.7	4.9	9.5	147.1	3	305.9	1.2	9.9	0.6	1.1	28	2
BNS 4	SD20	ARK	657539	6921983	62	4	5.5	5.8	8.2	3.8	11.3	156.7	6	255.5	1.7	10.4	0.7	1.4	24	3
BNS 5	SD20	LST	657539	6921983	20	2	2.6	2.2	3.1	1.8	5.2	74	2	425.9	0.6	4.9	0.5	0.6	20	1
BNS 6	SD20	LST	657539	6921983	20	4	3	2.5	4.1	2.7	6.8	85.6	2	464.2	0.7	5.5	0.4	0.9	25	2
BNS 7	SD20	BSA	657539	6921983	92	8	6.9	6	11.3	6	16.2	192.6	3	386.5	1.7	13.6	1.6	3.2	50	5
BNS 8	SD20	ARK	657539	6921983	53	7	10.8	2.3	10.6	6.4	15.4	177.8	3	351.3	1.8	16.4	2.5	4.1	39	10
BNS 9	SD20	ARK	657539	6921983	27	7	15.2	2.2	12.5	5	14.2	136.5	3	130.1	1.8	13.4	1.6	4	46	7
BNS 10	SD20	ARK	657539	6921983	24	8	12.9	0.8	10.2	5.3	12.8	50.5	3	25.8	1.6	11.3	0.8	11.9	39	11
BNS 11	SD20	ARK	657539	6921983	20	13	2	3.5	19.4	8	24.7	153.9	4	66	3.3	21.8	1.1	3.1	76	9
BNS 12	SD20	ARK	657539	6921983	20	12	2.6	0.9	20.1	7.8	35.5	76.2	7	55.2	3.5	23.2	1.2	3.4	91	11
BNS 13	SD20	SHB	657539	6921983	23	9	9.5	0.3	16.4	5.6	30.2	72	5	17.4	2.5	18.2	0.8	3.2	68	4
BNS 14	SD20	QSS	657539	6921983	29	8	10.2	0.2	18.4	6.6	53.6	50.9	9	13	4.3	14.4	0.5	3.7	66	6
BNS 15	SD20	QSB	657539	6921983	30	8	7.3	0.3	11.6	5.7	45.3	31.8	7	21.1	3.4	16.8	1.1	3.3	61	4
BNS 16	SD20	QSB	657539	6921983	26	49	45.3	0.5	27.5	6.4	25.5	91.8	3	30.2	1.9	3.7	1.1	1.3	441	13
BNS 17	SD20	QSB	657539	6921983	33	45	41.1	0.8	25.9	6.3	24.1	120.1	3	39.7	1.9	3.2	1.1	1.1	417	11
BNS 18	SD20	RHY	657539	6921983	20	5	9.4	0.2	16.8	13.1	74.3	116.5	7	75.8	5.7	16.4	3	4.3	47	3
BNS 19	SD20	QBS	657539	6921983	28	42	57.4	0.9	25.2	10.3	41.4	122.8	4	28.3	3.1	5.6	4.8	2	430	10
BH 7001	BH70	ARK	657780	6921842	195	6.5	12.6	2	na	9.5	na	116	na	170	1.4	18.1	na	1.7	36	13
BH 7012	BH70	ARK	657780	6921842	309	1.1	33.7	nd	na	0.8	na	83	na	157	1.1	4.8	na	1.2	8	438
BH 7015	BH70	SSS	657780	6921842	530	2	23.6	nd	na	1.2	na	nd	na	26	nd	2.1	na	1.4	14	405
0706	SD07	ARK	657855	6921927	234	3.6	11.7	nd	na	2.4	na	nd	na	122	0.8	6.1	na	2.5	16	56
0721	SD07	LST	657855	6921927	12	1	1.1	0.5	na	0.6	na	20	na	1213	nd	1.6	na	0.6	7	3
0722	SD07	LST	657855	6921927	12	1.3	1	0.5	na	0.6	na	21	na	181	nd	1.7	na	0.2	8	1
0726	SD07	ARK	657855	6921927	253	12.3	5.9	8.1	na	5.6	na	226	na	842	1.7	19.5	na	1.4	76	8
0727	SD07	ARK	657855	6921927	218	3.8	3.8	3	na	1.2	na	49	na	128	0.5	2	na	1.8	15	nd
0803	SD08	ARK	657697	6922069	121	2.9	2.9	9.8	na	3.2	na	189	na	247	0.5	5.3	na	0.9	17	36
0807	SD08	ARK	657697	6922069	1525	1.4	11.1	11.3	na	0.3	na	105	na	24	nd	1.3	na	1.2	8	502
0809	SD08	ARK	657697	6922069	251	1.8	2.8	5	na	2.8	na	95	na	133	0.4	6.4	na	0.4	8	49
0811	SD08	ARK	657697	6922069	933	2.2	3	4.5	na	3.1	na	124	na	177	0.4	7.8	na	0.8	14	285
2009	SD20	SHB	657539	6921983	77	11.2	24.5	nd	na	6.1	na	88	na	9	1.5	12.3	na	2.4	133	13
2018	SD20	QSB	657539	6921983	117	42.3	47.2	0.6	na	6.5	na	118	na	12	1.4	3.3	na	1	429	40
2024	SD20	RHY	657539	6921983	380	4.3	30.3	nd	na	2.9	na	80	na	44	2.6	14.3	na	2	141	139
2052	SD20	ARK	657539	6921983	85	1.5	3.9	2.8	na	2.1	na	174	na	195	1.4	14.2	na	1.5	13	5
2404	SD24	ARK	657420	6921918	115	6	134	4.5	na	6.8	na	190	na	408	1.6	17	na	3.1	30	26
2409	SD24	QSS	657420	6921918	121	6.2	7.3	0.6	na	3.5	na	21	na	17	0.7	6.7	na	1.6	36	120
2410	SD24	ARK	657420	6921918	91	9	2.5	1	na	7.1	na	50	na	308	2.5	18.4	na	1.2	42	39
2418	SD24	QSS	657420	6921918	49	0.7	1.9	nd	na	37.3	na	nd	na	469	11.1	19.8	na	3.3	-5	15

Sample ID	Location	Lithology	E	N	Ni [ppm]	Sc [ppm]	Co [ppm]	Cs [ppm]	Ga [ppm]	Hf [ppm]	Nb [ppm]	Rb [ppm]	Sn [ppm]	Sr [ppm]	Ta [ppm]	Th [ppm]	Tl [ppm]	U [ppm]	V [ppm]	W [ppm]
4910	SD49	ARK	657535	6922042	429	5	1.8	1.7	na	8.2	na	158	na	93	2	20.8	na	3.5	32	123
4915	SD49	ARK	657535	6922042	20	5	11.4	1.3	na	5.7	na	71	na	24	2.1	18.7	na	0.7	26	6
4920	SD49	ARK	657535	6922042	177	8.8	7.3	nd	na	nd	na	nd	na	18	nd	2.6	na	10.1	6	299
4957	SD49	QSS	657535	6922042	39	5	7	nd	na	11.1	na	17	na	15	7.1	44.7	na	11.4	13	11
6506	SD65	SSS	657555	6921764	171	1.6	5.4	0.4	na	8.4	na	50	na	25	6.4	26.1	na	7.7	38	40
6518	SD65	BSA	657555	6921764	64	12.8	5.7	8.5	na	6.8	na	260	na	481	2.1	23.4	na	2.5	92	12
6519	SD65	ARK	657555	6921764	171	6.3	131	nd	na	1.5	na	38	na	142	0.6	4.4	na	14.2	82	8
6521	SD65	ARK	657555	6921764	154	6.9	58.5	3	na	4.5	na	108	na	272	0.3	8.6	na	6.1	35	14
6522	SD65	LST	657555	6921764	8	1.4	2.5	0.8	na	0.8	na	33	na	1293	nd	2.3	na	1	10	1
6512	SD65	SSS	657555	6921764	116	2.1	5.4	nd	na	9.4	na	20	na	21	6.2	31.5	na	4.4	6	31
SK0111	outcrop	ARK	670008	6892337	nd	na	47	2.1	4	4.3	4	120	nd	85	0.9	8.9	1.5	1.1	14	751
BH 7007	BH70	ARK	657780	6921842	46	na	15	3.5	4	4.3	3	90	nd	106	0.4	5.6	0.6	0.7	9	63
SK 0114	outcrop	ARK	665838	6898466	nd	na	31	1.5	8	4.4	6	128	nd	84	0.9	12.6	0.8	1.9	20	397
VG0104	outcrop	LST	666549	6903270	nd	na	nd	nd	4	2.2	7	nd	nd	1120	0.6	3.8	nd	1.0	19	20
VG0106	outcrop	ARK	668776	6904210	nd	na	35	0.7	7	5.5	7	58	nd	109	1.0	10.4	0.3	1.4	13	539
VG0105	outcrop	LST	666549	6903270	nd	na	nd	nd	1	0.4	nd	5	nd	1010	0.1	1.4	nd	0.7	12	36
VG0101	outcrop	LST	666470	6903120	nd	na	nd	nd	nd	0.5	nd	5	nd	840	nd	0.7	nd	0.3	6	29
VG0109	outcrop	LST	668696	6904116	nd	na	5	1.7	8	7.7	7	84	nd	840	0.8	11.7	0.3	2.1	26	64
SK0104	outcrop	ARK	657764	6921902	nd	na	24	1.6	12	7.9	10	212	nd	491	1.4	38.0	1.2	2.9	12	294
VG0107	outcrop	LST	668705	6904133	nd	na	10	2.2	9	6.0	7	105	nd	1250	0.8	10.8	0.7	1.7	28	136
SK0101	outcrop	ARK	662084	6907908	nd	na	26	1.7	5	3.4	3	102	nd	26	0.6	5.9	0.6	0.9	13	277
SK0102	outcrop	ARK	662084	6907908	nd	na	45	1.2	4	2.7	3	63	nd	20	0.6	4.4	0.4	0.5	13	565
SK02110	open pit	SSS	657810	6921762	13.3	1	41.3	0.4	25.7	26.7	110.5	168.8	4	136	7	19	1.5	3.7	76	599.6
SK02113	open pit	SSS	657760	6921892	0.2	2	14.8	3.7	27.2	11.5	63.1	258	15	23	7.3	31.3	0.9	2.9	10	184.2
SK02116	open pit	SSS	657545	6922040	0.8	1	57	2.6	10.2	3.7	30.2	76.2	7	8	2.7	12.1	1.6	1.1	9	865.7
SK02117	open pit	SSS	657394	6922067	0.6	1	31	4	16.1	6.5	24.1	122.2	10	11.9	2.5	21.4	2.5	1.1	8	507
SK0235	open pit	SSS	657695	6921154	3	1	25.9	0.4	27.4	42.6	135.6	154.4	3	76.9	8.5	14.9	1.1	3.1	10	334.5
SK0236	open pit	SSS	657694	6921157	0.6	nd	18.8	0.3	23.5	43.1	130.9	171.3	4	34.1	8.7	19.4	1.3	5.2	8	365.1

nd - not detected

na - not analysed

CP hole rock analyses

Sample ID	Location	Lithology	E	N	Zr [ppm]	Y [ppm]	La [ppm]	Ce [ppm]	Pr [ppm]	Nd [ppm]	Sm [ppm]	Eu [ppm]	Gd [ppm]	Tb [ppm]	Dy [ppm]	Ho [ppm]	Er [ppm]	Tm [ppm]	Yb [ppm]	Lu [ppm]
BNS 1	SD20	ARK	657539	6921983	184.1	21.8	33.1	70.5	7.1	28.3	5.2	0.91	4.17	0.62	3.86	0.82	2.38	0.32	2.48	0.35
BNS 2	SD20	ARK	657539	6921983	215.7	18	27.6	55.6	6.29	24.2	4.2	0.73	3.25	0.52	3.29	0.69	2.04	0.28	1.87	0.29
BNS 3	SD20	LST	657539	6921983	216.1	18.3	21	42.9	4.92	19.4	3.6	0.66	2.87	0.47	2.91	0.61	1.87	0.25	1.87	0.27
BNS 4	SD20	ARK	657539	6921983	151.6	15.1	24.1	49.1	5	19.8	3.7	0.63	2.77	0.43	2.83	0.55	1.68	0.22	1.68	0.24
BNS 5	SD20	LST	657539	6921983	77.4	10	12.2	24.1	2.83	11.3	2	0.39	1.8	0.27	1.7	0.35	1.07	0.13	0.95	0.14
BNS 6	SD20	LST	657539	6921983	110.1	12.3	13.7	28.6	3.08	13	2.5	0.45	2.19	0.32	2	0.44	1.24	0.17	1.22	0.19
BNS 7	SD20	BSA	657539	6921983	235.2	26.4	32.7	67.8	7.86	30.3	6.1	1.09	4.71	0.74	4.71	0.99	2.99	0.38	2.73	0.39
BNS 8	SD20	ARK	657539	6921983	247.3	54.3	33.5	70.4	7.48	29.9	5.7	0.97	5.36	0.88	5.67	1.38	3.96	0.46	3.17	0.47
BNS 9	SD20	ARK	657539	6921983	190.6	235.7	35.7	76.6	9.68	53	19.1	3.5	33.43	6.12	40.68	9.15	25.5	3.01	18.16	2.3
BNS 10	SD20	ARK	657539	6921983	207.5	305.5	26.5	72.8	11.61	54.6	17.2	3.06	34.21	7.09	51.07	11.64	33.66	4.1	24.77	3.06
BNS 11	SD20	ARK	657539	6921983	317.1	83.9	65.4	136.6	15.74	62.4	11.7	1.82	12.36	2.29	16.57	3.67	10.88	1.46	10.2	1.38
BNS 12	SD20	ARK	657539	6921983	278.7	46.7	53.6	102	11.36	45.1	8.8	1.52	8.37	1.52	10.83	2.21	6.41	0.87	6.38	0.85
BNS 13	SD20	SHB	657539	6921983	186.2	61.6	21.3	49.7	6.15	28.1	7.3	0.75	8.22	1.47	10.38	2.28	6.85	0.95	6.83	0.91
BNS 14	SD20	QSS	657539	6921983	150.3	78.7	12.3	26.1	2.85	12.4	3.7	0.33	6.11	1.33	10.92	2.64	8.86	1.26	9.26	1.35
BNS 15	SD20	QSB	657539	6921983	131.9	64.9	20.2	43	4.76	19.6	5.4	0.93	6.5	1.44	10.65	2.52	7.74	1.09	8.17	1.15
BNS 16	SD20	QSB	657539	6921983	257.5	105	29.4	79.8	11.65	60.5	18.2	4.12	18.85	3.19	20.59	4.24	12.05	1.52	10.54	1.38
BNS 17	SD20	QSB	657539	6921983	242.6	101.4	20.8	51.4	6.79	35.1	10.4	3.03	14.31	2.46	16.17	3.63	10.27	1.25	8.19	1.12
BNS 18	SD20	RHY	657539	6921983	381.8	109.2	29.6	73.3	8.99	38.8	11.9	1.12	13.89	2.7	19	4.2	12.71	1.72	12.07	1.65
BNS 19	SD20	QBS	657539	6921983	384	75.6	22.2	57.2	7.52	34	9.2	2.61	10.39	1.81	12.63	2.81	8.62	1.14	8.07	1.15
BH 7001	BH70	ARK	657780	6921842	322	15	28.4	40	na	17	2.67	0.5	na	0.4	na	na	na	na	1.97	0.3
BH 7012	BH70	ARK	657780	6921842	42	4	12.5	24	na	8	1.11	0.25	na	0.2	na	na	na	na	0.62	0.09
BH 7015	BH70	SSS	657780	6921842	39	9	8.8	22	na	9	1.72	0.46	na	0.4	na	na	na	na	1.03	0.15
0706	SD07	ARK	657855	6921927	69	14	20.2	35	na	19	3.16	0.64	na	0.4	na	na	na	na	1.33	0.21
0721	SD07	LST	657855	6921927	27	5	5.7	11	na	5	0.91	0.19	na	0.2	na	na	na	na	0.39	0.06
0722	SD07	LST	657855	6921927	30	6	8.5	16	na	6	1.2	0.25	na	0.2	na	na	na	na	0.63	0.09
0726	SD07	ARK	657855	6921927	194	29	60.9	118	na	48	8.84	1.55	na	0.6	na	na	na	na	3.13	0.47
0727	SD07	ARK	657855	6921927	39	22	18.9	25	na	13	2.42	0.6	na	0.8	na	na	na	na	2.1	0.31
0803	SD08	ARK	657697	6922069	105	8	14.5	25	na	14	2.54	0.38	na	0.3	na	na	na	na	0.85	0.12
0807	SD08	ARK	657697	6922069	27	11	7.7	16	na	6	1.24	0.27	na	0.2	na	na	na	na	1.1	0.16
0809	SD08	ARK	657697	6922069	115	10	18.9	33	na	16	2.75	0.48	na	0.4	na	na	na	na	1.18	0.17
0811	SD08	ARK	657697	6922069	121	12	16.8	31	na	15	3	0.52	na	0.4	na	na	na	na	1.45	0.21
2009	SD20	SHB	657539	6921983	217	40	23.2	45	na	20	5.4	0.56	na	0.9	na	na	na	na	4.19	0.62
2018	SD20	QSB	657539	6921983	216	54	18	49	na	35	11.4	2.29	na	1.9	na	na	na	na	7.67	1.15
2024	SD20	RHY	657539	6921983	131	29	15.8	35	na	16	4.47	0.61	na	0.8	na	na	na	na	3.96	0.6
2052	SD20	ARK	657539	6921983	77	12	34.5	61	na	23	3.93	0.69	na	0.4	na	na	na	na	1.06	0.16
2404	SD24	ARK	657420	6921918	216	60	29.8	68	na	36	10.3	2.3	na	2.5	na	na	na	na	8.82	1.25
2409	SD24	QSS	657420	6921918	174	22	11.5	24	na	10	2.02	0.41	na	0.5	na	na	na	na	2.54	0.38
2410	SD24	ARK	657420	6921918	226	28	63.7	109	na	71	16.2	1.94	na	1.4	na	na	na	na	1.9	0.28
2418	SD24	QSS	657420	6921918	911	235	98.3	199	na	98	26.4	2.4	na	5.7	na	na	na	na	27.6	3.93

Sample ID	Location	Lithology	E	N	Zr [ppm]	Y [ppm]	La [ppm]	Ce [ppm]	Pr [ppm]	Nd [ppm]	Sm [ppm]	Eu [ppm]	Gd [ppm]	Tb [ppm]	Dy [ppm]	Ho [ppm]	Er [ppm]	Tm [ppm]	Yb [ppm]	Lu [ppm]
4910	SD49	ARK	657535	6922042	264	87	32.8	53	na	27	5.96	1.08	na	1.6	na	na	na	na	4.48	0.66
4915	SD49	ARK	657535	6922042	239	24	54.7	94	na	35	5.82	0.73	na	0.6	na	na	na	na	2.06	0.31
4920	SD49	ARK	657535	6922042	15	44	2.2	6	na	5	3.69	0.74	na	1	na	na	na	na	6.15	0.91
4957	SD49	QSS	657535	6922042	168	133	13.9	40	na	19	8.35	0.72	na	2.5	na	na	na	na	18.2	2.6
6506	SD65	SSS	657555	6921764	131	138	50.8	107	na	117	31.7	3.65	na	5.4	na	na	na	na	19	2.8
6518	SD65	BSA	657555	6921764	249	84	79.1	147	na	77	16.8	3.02	na	2.3	na	na	na	na	7.54	1.08
6519	SD65	ARK	657555	6921764	56	124	29.1	102	na	44	12.5	2.99	na	2.7	na	na	na	na	6.76	0.99
6521	SD65	ARK	657555	6921764	171	50	25.6	44	na	20	4.87	1	na	0.8	na	na	na	na	3.54	0.53
6522	SD65	LST	657555	6921764	34	6	7.7	14	na	6	1.08	0.23	na	0.2	na	na	na	na	0.48	0.07
6512	SD65	SSS	657555	6921764	152	388	106	96	na	53	16.5	2.56	na	6.3	na	na	na	na	44.2	6.46
SK0111	outcrop	ARK	670008	6892337	157	13	18.9	38.7	4.51	17.6	3.5	0.57	3.0	0.4	2.3	0.5	1.3	0.21	1.2	0.18
BH 7007	BH70	ARK	657780	6921842	157	16	11.6	19.8	2.66	10.1	2.2	0.37	2.2	0.4	2.2	0.5	1.6	0.27	1.7	0.25
SK 0114	outcrop	ARK	665838	6898466	165	15	24.8	51.6	5.80	22.7	4.5	0.76	3.8	0.5	2.9	0.5	1.6	0.24	1.5	0.23
VG0104	outcrop	LST	666549	6903270	74	19	21.8	45.1	5.10	20.8	4.0	0.68	3.7	0.6	3.5	0.7	2.0	0.31	2.0	0.28
VG0106	outcrop	ARK	668776	6904210	206	21	23.7	49.3	6.00	24.5	5.2	0.98	4.6	0.7	3.8	0.8	2.1	0.31	1.9	0.28
VG0105	outcrop	LST	666549	6903270	14	6	4.9	10.6	1.15	4.7	1.0	0.21	1.1	0.2	1.0	0.2	0.6	0.09	0.5	0.08
VG0101	outcrop	LST	666470	6903120	29	3	3.3	6.1	0.66	2.5	0.5	0.12	0.6	nd	0.4	nd	0.2	nd	0.3	nd
VG0109	outcrop	LST	668696	6904116	285	27	25.8	53.5	6.47	26.4	5.3	0.92	5.0	0.8	4.7	1.0	2.9	0.44	2.8	0.42
SK0104	outcrop	ARK	657764	6921902	173	12	38.7	64.8	5.47	15.0	2.0	0.23	1.7	0.2	1.5	0.3	1.1	0.22	1.6	0.28
VG0107	outcrop	LST	668705	6904133	231	25	37.0	72.6	8.36	32.0	6.2	1.10	5.2	0.8	4.4	0.9	2.5	0.38	2.4	0.35
SK0101	outcrop	ARK	662084	6907908	126	26	15.5	27.1	3.53	13.9	2.8	0.63	3.1	0.6	4.0	0.9	2.5	0.38	2.2	0.32
SK0102	outcrop	ARK	662084	6907908	99	9	10.6	17.9	2.26	8.7	1.6	0.34	1.8	0.3	1.6	0.4	1.0	0.16	1.0	0.14
SK02110	open pit	SSS	657810	6921762	766.2	190.9	48.8	102.4	12.56	48	13.1	1.61	16.69	3.68	24.86	5.93	19.94	3.22	21.8	3.1
SK02113	open pit	SSS	657760	6921892	176.9	54.7	21.9	55.5	7.21	29.3	9.2	0.16	9.86	1.86	10.61	2.12	6.16	1	7.39	1.21
SK02116	open pit	SSS	657545	6922040	63	34.3	7.7	20.3	2.99	13.4	4.6	nd	4.43	0.92	5.42	1.15	3.7	0.6	4.24	0.67
SK02117	open pit	SSS	657394	6922067	82.4	54.6	11.4	27.3	4.04	15.9	4.7	0.06	5.04	1.05	7.27	1.71	5.58	0.95	6.44	1
SK0235	open pit	SSS	657695	6921154	1304.5	149.1	4.6	21.2	2.75	16.7	9.3	1.49	12.91	3.14	20.96	4.93	16.54	2.82	19.72	3.12
SK0236	open pit	SSS	657694	6921157	1294.5	158.6	5.8	33	2.41	12.1	7.8	1.31	12.16	3.4	25.09	5.77	19.39	3.33	22.47	3.37

nd - not detected

na - not analysed

CPM hole rockanalyses

Sample ID	Location	Lithology	E	N	Mo [ppm]	Cu [ppm]	Pb [ppm]	Zn [ppm]	As [ppm]	Cd [ppm]	Sb [ppm]	Bi [ppm]	Se [ppm]	Au [ppb]	Br [ppm]	Hg [ppm]	Ag [ppm]	Be [ppm]	Ge [ppm]	In [ppm]
BNS 1	SD20	ARK	657539	6921983	1.1	1002	27	>99999	11	22.5	1	1	2.5	8.7	na	0.1	0.3	8.8	0.2	0.09
BNS 2	SD20	ARK	657539	6921983	0.9	612	28	84489	7	70.4	2	1	0.8	9.6	na	0.1	0.6	3.7	0.1	0.02
BNS 3	SD20	LST	657539	6921983	1.1	33	15	4677	6	180.7	1	1	0.3	3.5	na	1.3	1.2	1.1	0.1	0.02
BNS 4	SD20	ARK	657539	6921983	1.1	245	22	87322	7	32.4	1	1	2.4	0.2	na	0.0	0.5	1.6	0.3	0.02
BNS 5	SD20	LST	657539	6921983	1.2	3	3	4441	4	85.8	1	1	0.4	0.6	na	0.5	0.7	0.8	0.1	0.02
BNS 6	SD20	LST	657539	6921983	1	49	21	8320	6	133.2	2	1	0.7	0.2	na	0.5	1.0	0.9	0.1	0.04
BNS 7	SD20	BSA	657539	6921983	1.2	1333	54	>99999	11	99.4	1	1	6.9	0.2	na	0.0	0.4	4.2	0.1	0.04
BNS 8	SD20	ARK	657539	6921983	2.2	7665	866	21458	21	52.4	5	1	2.9	2.9	na	0.4	1.5	16.4	0.1	0.04
BNS 9	SD20	ARK	657539	6921983	1.2	4329	495	4725	25	11.4	4	1	2.6	5.7	na	0.1	2.2	9	0.2	0.07
BNS 10	SD20	ARK	657539	6921983	4.1	6484	2588	9062	27	16.3	5	1	7	13.4	na	0.1	1.9	15.3	0.2	0.03
BNS 11	SD20	ARK	657539	6921983	2.4	1557	1603	1794	22	4.4	4	1	2.7	3.1	na	0.1	14.1	4.2	0.1	0.07
BNS 12	SD20	ARK	657539	6921983	12.7	3127	3595	562	26	2.4	4	1	8.3	26.4	na	0.4	10.2	1.2	0.1	0.1
BNS 13	SD20	SHB	657539	6921983	9.9	441	32008	5236	3	1229.6	3	1	5.4	0.2	na	0.5	0.8	0.8	0.2	0.25
BNS 14	SD20	QSS	657539	6921983	8.8	230	14004	4365	4	498.5	1	1	2.8	3.4	na	0.0	0.6	0.1	0.2	0.16
BNS 15	SD20	QSB	657539	6921983	12.8	499	21385	11085	4	4385.6	4	1	1.3	11.6	na	0.3	3.6	0.3	0.1	0.53
BNS 16	SD20	QSB	657539	6921983	1.5	508	681	6289	4	144.8	4	4	0.4	9.7	na	0.0	0.8	0.4	0.1	0.13
BNS 17	SD20	QSB	657539	6921983	0.6	376	205	7086	5	8.5	2	3	0.4	14.7	na	0.0	1.1	0.9	0.2	0.11
BNS 18	SD20	RHY	657539	6921983	11.9	829	839	13241	6	26.3	4	19	1.5	10.9	na	0.2	2.2	0.4	0.1	0.37
BNS 19	SD20	QBS	657539	6921983	2.6	742	30	1864	7	3.8	3	10	1.5	13.5	na	0.0	0.6	0.5	0.1	0.09
BH 7001	BH70	ARK	657780	6921842	nd	600	44	>99999	6	109	0.7	nd	nd	nd	2.5	nd	0.4	5	na	na
BH 7012	BH70	ARK	657780	6921842	nd	122	25	>99999	3	22.4	0.3	nd	nd	nd	nd	nd	nd	4	na	na
BH 7015	BH70	SSS	657780	6921842	nd	56	27	>99999	7	24.5	0.4	nd	3.3	nd	nd	nd	nd	11	na	na
0706	SD07	ARK	657855	6921927	nd	676	32	>99999	11	1017	0.4	nd	6.5	nd	nd	nd	nd	3	na	na
0721	SD07	LST	657855	6921927	nd	42	nd	204	3	0.9	0.2	nd	0.6	nd	nd	nd	nd	nd	na	na
0722	SD07	LST	657855	6921927	nd	7	nd	2709	3	56.2	0.1	nd	na	na						
0726	SD07	ARK	657855	6921927	3	138	25	>99999	10	10.4	0.4	nd	nd	nd	nd	nd	nd	4	na	na
0727	SD07	ARK	657855	6921927	nd	423	34	>99999	10	1003	0.3	nd	nd	nd	nd	nd	nd	5	na	na
0803	SD08	ARK	657697	6922069	nd	29	6	2833	3	4.8	0.3	nd	nd	11	0.8	nd	0.9	2	na	na
0807	SD08	ARK	657697	6922069	3	20	14	67240	6	560	0.4	nd	nd	nd	nd	nd	nd	7	na	na
0809	SD08	ARK	657697	6922069	nd	79	20	74359	3	3.1	0.3	nd	1.5	nd	nd	nd	0.3	2	na	na
0811	SD08	ARK	657697	6922069	nd	19	6	3297	3	104	0.6	nd	nd	nd	nd	nd	0.9	1	na	na
2009	SD20	SHB	657539	6921983	15	1012	48412	26549	16	4395	1.6	nd	3.4	4	nd	nd	2.1	nd	na	na
2018	SD20	QSB	657539	6921983	nd	139	114	2098	35	4.5	0.7	nd	nd	8	nd	nd	1.5	2	na	na
2024	SD20	RHY	657539	6921983	60	275	90	72902	144	267	3.8	nd	2.5	45	nd	nd	2.4	1	na	na
2052	SD20	ARK	657539	6921983	2	647	36	94302	3	16.7	0.8	nd	nd	nd	nd	nd	2.1	3	na	na
2404	SD24	ARK	657420	6921918	nd	373	39	9348	5	41.8	0.4	nd	nd	nd	nd	nd	4.4	4	na	na
2409	SD24	QSS	657420	6921918	4	1312	3730	2242	73	9.4	1.9	nd	nd	28	1.2	nd	1.4	2	na	na
2410	SD24	ARK	657420	6921918	nd	26	3445	457	11	nd	1.9	nd	nd	8	nd	nd	0.6	2	na	na
2418	SD24	QSS	657420	6921918	nd	334	226	1154	14	3.7	0.3	nd	3.1	nd	nd	nd	2.5	2	na	na

Sample ID	Location	Lithology	E	N	Mo [ppm]	Cu [ppm]	Pb [ppm]	Zn [ppm]	As [ppm]	Cd [ppm]	Sb [ppm]	Bi [ppm]	Se [ppm]	Au [ppb]	Br [ppm]	Hg [ppm]	Ag [ppm]	Be [ppm]	Ge [ppm]	In [ppm]
4910	SD49	ARK	657535	6922042	3	1160	111	1355	22	1.7	1.5	nd	1.4	nd	nd	nd	6.0	3	na	na
4915	SD49	ARK	657535	6922042	2	90	316	324	16	1.1	0.8	nd	33.7	10	nd	nd	4.4	2	na	na
4920	SD49	ARK	657535	6922042	9	2102	1106	24546	468	70.7	61.6	nd	4	5	nd	nd	5.7	60	na	na
4957	SD49	QSS	657535	6922042	9	2753	20827	36348	13	3151	1.6	nd	nd	5	nd	nd	4.6	1	na	na
6506	SD65	SSS	657555	6921764	7	111116	818	3769	5	15.7	1.9	nd	nd	11	nd	2	126	3	na	na
6518	SD65	BSA	657555	6921764	nd	49	260	9961	5	2.8	0.8	nd	12.5	11	nd	nd	0.4	3	na	na
6519	SD65	ARK	657555	6921764	23	294	4254	>99999	26	830	1.4	nd	nd	nd	nd	nd	nd	14	na	na
6521	SD65	ARK	657555	6921764	5	113	1543	86220	17	172	1.4	nd	nd	8	nd	nd	0.6	7	na	na
6522	SD65	LST	657555	6921764	nd	12	101	713	2	106	0.4	nd	0.7	nd	nd	2	1.8	nd	na	na
6512	SD65	SSS	657555	6921764	nd	118030	2890	729	9	4.1	2.8	nd	1	nd	nd	nd	5.9	nd	na	na
SK0111	outcrop	ARK	670008	6892337	nd	nd	19	nd	nd	na	nd	nd	na	na	na	na	nd	na	1	na
BH 7007	BH70	ARK	657780	6921842	nd	353	9	>99999	nd	na	nd	nd	na	na	na	na	nd	na	nd	na
SK 0114	outcrop	ARK	665838	6898466	nd	nd	62	58	nd	na	nd	nd	na	na	na	na	nd	na	1	na
VG0104	outcrop	LST	666549	6903270	nd	46	7	nd	nd	na	nd	nd	na	na	na	na	nd	na	nd	na
VG0106	outcrop	ARK	668776	6904210	nd	nd	15	nd	nd	na	nd	nd	na	na	na	na	nd	na	nd	na
VG0105	outcrop	LST	666549	6903270	nd	29	nd	69	nd	na	nd	nd	na	na	na	na	nd	na	nd	na
VG0101	outcrop	LST	666470	6903120	nd	29	nd	nd	nd	na	0.5	nd	na	na	na	na	nd	na	nd	na
VG0109	outcrop	LST	668696	6904116	nd	12	8	nd	nd	na	nd	nd	na	na	na	na	nd	na	nd	na
SK0104	outcrop	ARK	657764	6921902	3	307	43	nd	nd	na	nd	nd	na	na	na	na	nd	na	1	na
VG0107	outcrop	LST	668705	6904133	nd	nd	25	nd	nd	na	nd	nd	na	na	na	na	nd	na	nd	na
SK0101	outcrop	ARK	662084	6907908	nd	nd	19	nd	nd	na	nd	nd	na	na	na	na	nd	na	1	na
SK0102	outcrop	ARK	662084	6907908	nd	nd	9	nd	nd	na	nd	nd	na	na	na	na	nd	na	nd	na
SK02110	open pit	SSS	657810	6921762	5.1	15.6	175.5	339	17	0.2	1.2	0.5	na	na	na	na	1.4	na	na	na
SK02113	open pit	SSS	657760	6921892	0.3	6.7	24.1	67	3	0.1	nd	0.1	na	na	na	na	nd	na	na	na
SK02116	open pit	SSS	657545	6922040	0.1	54.8	9.8	568	3	0.9	0.2	0.1	na	na	na	na	1.1	na	na	na
SK02117	open pit	SSS	657394	6922067	0.2	57.3	6.4	370	4	0.6	0.3	nd	na	na	na	na	0.9	na	na	na
SK0235	open pit	SSS	657695	6921154	1.5	27.4	169.2	155	5	0.3	1.6	0.3	na	na	na	na	nd	na	na	na
SK0236	open pit	SSS	657694	6921157	0.4	5.7	61.1	37	3	0.7	0.2	0.2	na	na	na	na	nd	na	na	na

nd - not detected

na - not analysed

XRF whole rock analyses

Sample ID	Location	Lithology	E	N	SiO ₂ [%]	Al ₂ O ₃ [%]	Fe ₂ O ₃ [%]	MgO [%]	CaO [%]	Na ₂ O [%]	K ₂ O [%]	TiO ₂ [%]	P ₂ O ₅ [%]	MnO [%]	ZnO [%]	S [%]	Cl [%]	LOI [%]	Total [%]
0301	SD03	ARK	657485	6922181	71.30	11.10	3.43	1.13	1.98	0.67	6.11	0.358	0.133	0.156	0.663	0.035	0.061	2.400	99.522
0305	SD03	ARK	657485	6922181	54.30	22.80	2.50	2.11	0.66	0.61	3.80	0.865	0.635	0.034	1.238	0.012	0.037	9.660	99.255
0307	SD03	ARK	657485	6922181	63.80	17.10	4.15	2.35	0.23	0.33	6.75	0.944	0.142	0.052	0.429	0.012	0.032	3.050	99.373
0311	SD03	ARK	657485	6922181	45.80	11.70	8.74	1.15	1.36	2.01	2.02	0.501	0.363	0.599	16.209	0.015	0.041	9.150	99.659
0313	SD03	SSS	657485	6922181	57.90	18.30	2.60	2.41	0.53	nd	5.68	0.389	0.104	0.120	6.637	0.018	0.042	4.960	99.687
0314	SD03	SSS	657485	6922181	45.20	12.70	3.82	2.93	1.12	nd	2.39	0.441	0.164	0.142	21.251	0.006	0.019	9.540	99.722
0315	SD03	LST	657485	6922181	32.90	16.10	7.98	1.89	16.70	0.41	3.57	0.644	0.543	0.098	0.568	0.010	0.032	18.070	99.510
0317	SD03	SSS	657485	6922181	53.90	16.70	4.07	2.31	0.70	1.00	4.59	0.348	0.181	0.043	9.296	0.006	0.020	6.560	99.726
0318	SD03	ARK	657485	6922181	67.20	15.80	1.65	1.67	0.75	0.80	5.58	0.591	0.175	0.117	1.229	0.010	0.036	4.040	99.652
0319	SD03	ARK	657485	6922181	52.40	13.00	3.52	1.57	1.38	1.95	4.46	0.518	0.429	0.214	12.853	0.009	0.036	7.440	99.779
3901	SD39	ARK	657236	6922217	62.40	13.60	2.45	4.71	0.55	2.54	3.85	0.344	0.202	0.795	4.535	0.011	0.038	3.450	99.474
3902	SD39	ARK	657236	6922217	73.20	12.80	1.72	0.68	0.31	0.96	5.71	0.279	0.151	0.376	1.046	0.006	0.029	2.030	99.296
3905	SD39	ARK	657236	6922217	52.60	13.10	2.07	1.78	8.15	2.16	3.88	0.406	0.129	0.689	6.045	0.009	0.052	8.260	99.330
3906	SD39	LST	657236	6922217	48.70	8.52	2.24	1.02	22.20	0.37	4.03	0.381	0.112	0.125	0.199	0.006	0.049	11.700	99.656
3909	SD39	LST	657236	6922217	39.60	8.38	2.11	4.79	24.50	nd	4.39	0.163	0.058	0.249	0.599	0.004	0.020	14.680	99.543
3915	SD39	LST	657236	6922217	20.10	6.81	3.81	1.83	35.50	nd	3.37	0.433	0.253	0.663	0.743	0.011	0.049	25.800	99.372
3916	SD39	ARK	657236	6922217	70.20	8.54	4.06	0.85	0.76	nd	3.94	0.399	0.441	0.966	5.202	0.013	0.039	3.240	98.644
3917	SD39	ARK	657236	6922217	55.10	14.20	4.00	0.96	0.65	0.57	6.66	0.774	0.353	0.152	4.257	0.017	0.049	6.110	93.853
3918	SD39	ARK, GOS	657236	6922217	31.70	22.20	13.70	0.78	0.18	nd	2.60	0.644	0.676	11.800	2.535	0.013	0.014	10.610	97.454
3919	SD39	ARK	657236	6922217	78.20	12.70	2.54	0.00	0.05	nd	2.48	0.437	0.166	0.017	0.027	0.068	0.041	2.430	99.152
3922	SD39	QSS	657236	6922217	61.90	12.80	2.33	10.50	0.11	nd	4.24	0.479	0.072	0.354	2.092	0.007	0.034	3.520	98.440
8001	SD80	LST	657374	6922177	8.80	2.27	0.75	1.63	49.10	0.38	0.97	0.164	0.059	0.086	0.030	0.101	0.016	35.270	99.621
8011	SD80	ARK	657374	6922177	62.00	12.90	2.18	0.99	0.78	1.33	6.38	0.596	0.000	0.025	8.310	0.017	0.027	3.800	99.333
8013	SD80	ARK	657374	6922177	59.60	10.10	1.63	0.60	1.00	1.83	4.89	0.397	0.102	nd	13.617	0.008	0.022	5.540	99.334
8014	SD80	ARK	657374	6922177	55.80	8.61	1.59	0.59	1.38	2.31	4.04	0.360	0.127	0.018	17.517	0.010	0.025	6.870	99.246
8016	SD80	BSA	657374	6922177	52.70	6.94	1.55	0.62	1.29	2.46	3.10	0.374	0.210	2.050	20.627	0.024	0.029	7.160	99.131
8022	SD80	ARK	657374	6922177	68.10	12.90	3.24	2.45	0.29	0.62	7.16	0.525	0.204	0.323	1.549	0.011	0.028	2.040	99.441
8024	SD80	ARK, GOS	657374	6922177	60.50	13.90	8.16	4.66	0.15	0.46	4.42	0.627	0.386	0.486	1.574	0.013	0.032	2.890	98.258
8025	SD80	ARK, GOS	657374	6922177	66.10	9.82	2.19	9.90	0.11	0.47	5.96	0.342	0.075	0.535	1.726	0.014	0.044	1.820	99.115
8027	SD80	ARK	657374	6922177	45.30	8.18	6.00	1.26	0.22	nd	4.35	0.152	nd	0.966	21.254	0.011	0.021	11.320	99.030
BH7001	BH70	ARK	657780	6921842	48.80	11.10	2.27	1.26	0.87	2.31	3.00	0.581	0.385	0.042	20.751	0.014	0.089	8.310	99.783
BH7002	BH70	ARK	657780	6921842	45.50	6.99	0.98	1.96	2.02	nd	1.61	0.153	1.330	0.557	31.224	0.020	0.067	7.310	99.720
BH7003	BH70	ARK	657780	6921842	35.10	7.38	1.87	1.94	4.13	nd	1.82	0.337	2.850	0.320	34.073	0.023	0.057	9.742	99.642
BH7004	BH70	ARK	657780	6921842	48.30	9.64	2.31	2.06	1.14	2.01	2.50	0.356	0.428	0.288	22.538	0.016	0.051	8.183	99.820
BH7005	BH70	ARK	657780	6921842	38.40	11.60	3.94	2.72	1.26	nd	2.98	0.557	0.676	0.163	26.755	0.015	0.058	10.450	99.574
BH7006	BH70	ARK	657780	6921842	35.60	6.62	2.29	0.93	1.05	nd	1.35	0.192	0.433	0.288	33.136	0.005	0.034	17.860	99.785
BH7008	BH70	ARK	657780	6921842	47.10	5.55	3.07	4.35	1.13	nd	2.40	0.130	0.765	0.322	22.669	nd	0.034	12.110	99.630

XRF whole rock analyses

Sample ID	Location	Lithology	E	N	SiO ₂ [%]	Al ₂ O ₃ [%]	Fe ₂ O ₃ [%]	MgO [%]	CaO [%]	Na ₂ O [%]	K ₂ O [%]	TiO ₂ [%]	P ₂ O ₅ [%]	MnO [%]	ZnO [%]	S [%]	Cl [%]	LOI [%]	Total [%]
BH7009	BH70	ARK	657780	6921842	69.40	6.67	1.20	3.34	0.38	nd	3.94	0.194	0.132	0.025	9.734	nd	0.022	4.700	99.737
BH7010	BH70	SSS	657780	6921842	53.10	17.40	2.16	2.32	0.60	1.08	5.12	0.350	0.125	0.017	10.987	nd	0.021	6.500	99.782
BH7011	BH70	SSS	657780	6921842	52.50	16.90	1.68	1.93	0.65	1.22	4.60	0.320	0.135	0.108	13.466	0.004	0.024	6.287	99.825
BH7012	BH70	ARK	657780	6921842	55.60	8.63	0.82	0.58	1.08	nd	2.72	0.064	0.082	0.136	26.035	0.008	0.019	3.970	99.747
BH7013	BH70	ARK	657780	6921842	27.20	3.72	3.82	0.39	8.36	nd	0.63	0.102	6.860	0.227	40.704	0.015	0.025	7.791	99.842
BH7014	BH70	SSS	657780	6921842	43.90	1.94	0.46	0.22	0.36	nd	0.36	0.046	0.374	0.224	45.915	0.245	0.021	5.978	100.045
BH7015	BH70	SSS	657780	6921842	63.00	2.45	1.40	0.38	0.48	nd	0.60	0.087	0.419	0.119	27.188	0.015	0.017	3.730	99.883
BH7016	BH70	ARK	657780	6921842	27.90	6.75	1.86	0.57	0.58	nd	0.69	0.244	1.140	0.254	49.822	0.019	0.118	9.770	99.712
BH7017	BH70	ARK	657780	6921842	34.30	9.73	3.29	1.22	2.80	nd	2.09	0.428	1.790	0.995	31.712	0.009	0.053	11.170	99.588
4801	SD48	LST	657598	6922073	22.60	1.00	1.65	3.83	58.30	nd	0.75	0.075	0.064	0.069	0.243	0.005	0.016	10.990	99.585
4802	SD48	ARK	657598	6922073	38.70	6.18	2.29	1.44	1.44	nd	1.22	0.205	0.142	0.060	44.492	0.006	0.027	3.474	99.675
4805	SD48	LST	657598	6922073	15.00	3.64	2.30	1.00	45.30	nd	1.38	0.227	0.060	0.156	9.327	0.006	0.023	20.920	99.339
4806	SD48	LST	657598	6922073	23.60	5.45	1.76	1.64	49.70	0.97	2.52	0.363	0.091	0.056	0.076	0.217	0.015	12.330	98.785
4807	SD48	LST	657598	6922073	20.90	4.31	1.71	1.37	41.90	0.73	2.32	0.282	0.056	0.074	0.057	0.208	0.016	25.000	98.929
4809	SD48	LST	657598	6922073	26.60	7.62	2.34	1.17	35.40	0.50	3.19	0.461	0.144	0.084	0.752	0.429	0.013	20.740	99.447
4810	SD48	LST	657598	6922073	41.00	14.50	9.26	2.48	18.10	nd	5.42	0.753	0.169	0.066	0.222	nd	0.014	7.356	99.339
4812	SD48	SSS	657598	6922073	40.30	19.50	2.45	3.68	0.13	1.28	6.46	0.121	nd	0.013	0.731	0.447	0.012	24.610	99.732
4814	SD48	LST	657598	6922073	34.20	8.96	1.21	1.70	18.90	1.08	2.35	0.247	0.065	0.125	0.004	0.166	0.016	24.610	93.633
4815	SD48	LST	657598	6922073	41.50	13.50	3.34	2.23	21.90	1.01	5.32	0.675	0.126	0.104	0.994	0.582	0.029	8.198	99.508
4816A	SD48	LST	657598	6922073	45.70	7.98	1.81	3.59	24.60	1.86	4.28	0.321	0.080	0.134	0.566	0.304	0.009	8.440	99.674
4816B	SD48	LST	657598	6922073	5.97	1.86	1.25	2.08	49.50	nd	0.72	0.150	0.034	0.259	0.010	0.121	0.012	37.410	99.380
4818	SD48	ARK	657598	6922073	38.50	12.50	5.67	3.48	0.86	nd	4.00	0.743	0.252	0.023	19.212	0.016	0.117	14.130	99.501
4819	SD48	ARK	657598	6922073	48.30	15.40	7.23	1.34	0.74	nd	5.06	0.879	0.400	0.012	13.497	0.021	0.177	6.267	99.321
4820	SD48	ARK	657598	6922073	47.50	10.60	2.50	1.33	0.70	nd	4.05	0.521	0.124	0.116	20.718	0.006	0.035	6.267	94.467
4821	SD48	ARK, GOS	657598	6922073	37.60	11.20	6.01	0.99	0.97	nd	4.03	0.670	0.346	0.065	29.345	0.014	0.062	8.000	99.304
4822	SD48	ARK	657598	6922073	39.50	2.85	1.46	0.41	1.00	nd	0.40	0.097	0.388	0.025	34.890	0.004	0.020	18.760	99.808
4823	SD48	ARK	657598	6922073	37.40	4.76	1.61	1.33	0.75	nd	0.91	0.166	0.156	0.145	48.200	0.014	0.027	4.467	99.941
4825	SD48	ARK	657598	6922073	13.90	3.54	1.84	2.17	1.82	nd	0.58	0.127	0.249	0.608	44.702	0.006	0.037	29.700	99.281
4826	SD48	ARK	657598	6922073	51.50	13.20	3.01	1.51	0.56	nd	5.95	0.560	0.200	0.052	11.454	0.011	0.029	11.510	99.547
0705	SD07	ARK	657855	6921927	27.40	4.68	1.36	0.85	1.17	nd	0.59	0.239	0.228	0.114	31.604	0.063	0.022	23.350	91.670
0706	SD07	ARK	657855	6921927	27.20	5.07	1.48	1.19	2.13	nd	0.76	0.189	1.180	0.095	39.462	0.007	0.020	21.000	99.785
0707	SD07	ARK	657855	6921927	15.50	4.39	0.95	0.90	2.49	nd	1.18	0.149	1.628	0.055	36.185	0.006	0.018	27.330	90.782
0708	SD07	ARK	657855	6921927	28.60	3.48	0.90	0.77	0.84	nd	0.44	0.159	0.199	0.116	31.995	0.006	0.029	24.230	91.764
0710	SD07	ARK	657855	6921927	30.90	6.27	3.47	1.78	4.75	nd	1.78	0.412	2.729	0.045	24.583	0.014	0.025	16.130	92.888
0712	SD07	ARK	657855	6921927	25.30	7.27	2.18	1.37	4.39	nd	1.74	0.301	3.088	0.055	26.815	0.009	0.028	20.590	93.136
0713	SD07	ARK	657855	6921927	31.80	7.87	2.49	1.34	5.65	nd	2.00	0.373	3.747	0.028	23.079	0.010	0.027	15.560	93.975
0714	SD07	ARK	657855	6921927	39.50	12.90	4.60	2.90	4.64	nd	4.23	0.673	2.555	0.022	14.417	0.012	0.030	9.630	96.109

XRF whole rock analyses

Sample ID	Location	Lithology	E	N	SiO ₂ [%]	Al ₂ O ₃ [%]	Fe ₂ O ₃ [%]	MgO [%]	CaO [%]	Na ₂ O [%]	K ₂ O [%]	TiO ₂ [%]	P ₂ O ₅ [%]	MnO [%]	ZnO [%]	S [%]	Cl [%]	LOI [%]	Total [%]
0715	SD07	ARK	657855	6921927	36.10	8.57	4.47	2.12	6.58	nd	2.63	0.530	3.698	0.021	18.997	0.012	0.023	11.100	94.851
0718	SD07	ARK	657855	6921927	65.60	5.55	4.26	0.80	0.85	nd	1.22	0.211	0.162	0.322	11.353	0.008	0.031	6.590	96.948
0719	SD07	ARK	657855	6921927	74.10	4.40	3.34	0.65	4.05	nd	1.60	0.165	3.112	0.372	3.192	0.009	0.022	3.760	98.775
0726	SD07	ARK	657855	6921927	42.20	14.10	4.22	2.44	1.65	1.75	4.43	0.481	0.370	nd	13.945	nd	0.025	14.000	99.610
0727	SD07	ARK	657855	6921927	16.70	4.11	0.92	1.25	5.89	nd	0.79	0.119	4.510	0.058	39.530	0.007	0.017	26.000	99.909
0734	SD07	ARK	657855	6921927	41.00	8.42	3.40	2.33	2.34	nd	2.37	0.370	0.670	nd	20.852	0.007	0.022	12.800	94.581
2065	SD20	BSA	657539	6921983	43.20	10.90	4.94	0.94	2.27	nd	4.23	0.659	0.869	nd	15.341	0.014	0.026	12.170	95.565
2067	SD20	QSS, GOS	657539	6921983	16.00	3.78	65.20	0.16	0.06	nd	0.26	0.046	0.659	0.074	1.936	0.025	0.013	10.720	98.932
2068	SD20	QSB, GOS	657539	6921983	15.60	8.51	54.20	0.56	0.08	nd	1.14	0.274	0.596	0.057	1.826	0.151	0.028	13.980	97.002
2066	SD20	ARK, GOS	657539	6921983	48.90	13.30	27.60	0.71	0.06	nd	1.85	0.263	0.338	0.071	0.794	0.027	0.015	5.440	99.369
2052	SD20	ARK	657539	6921983	61.10	10.40	1.84	0.64	0.38	2.40	4.98	0.220	0.113	0.022	15.124	0.014	0.054	2.500	99.789
4969	SD49	ARK, GOS	657535	6922042	9.67	0.75	73.90	0.00	0.14	nd	0.02	nd	0.786	0.144	3.096	0.060	0.014	11.000	99.575
4968	SD49	ARK, GOS	657535	6922042	35.20	14.40	32.50	0.99	0.10	nd	2.65	0.594	0.471	0.014	0.475	0.366	0.016	8.980	96.760
4952	SD49	ARK	657535	6922042	59.70	25.40	1.82	1.16	0.05	0.28	4.05	0.922	0.204	nd	0.077	0.015	0.038	5.580	99.289
4910	SD49	ARK	657535	6922042	76.20	11.30	2.94	0.15	0.12	0.18	6.46	0.531	0.179	0.010	0.153	0.013	0.028	1.090	99.360
2413	SD24	QSS	657420	6921918	61.30	21.80	3.16	0.00	0.03	0.28	1.15	0.271	0.066	nd	2.796	1.758	0.030	6.800	99.433
6519	SD65	ARK, GOS	657555	6921764	20.60	5.59	21.90	1.07	0.67	nd	1.52	0.221	0.340	10.400	22.984	0.017	0.023	14.000	99.335
SK0101	outcrop	ARK	662084	6907908	84.10	8.81	0.93	0.51	0.08	nd	4.51	0.207	0.060	0.022	0.004	0.011	0.032	0.612	99.887
SK0102	outcrop	ARK	662084	6907908	87.10	5.53	0.68	0.36	0.83	nd	2.55	0.149	0.470	nd	0.590	0.375	0.032	1.130	99.797
SK0103	outcrop	ARK	663787	6906061	54.60	17.40	7.98	3.94	4.06	3.90	4.23	0.804	0.264	0.171	nd	0.010	0.020	1.870	99.248
SK0104	outcrop	ARK	662242	6901289	70.50	13.60	0.92	0.14	0.33	1.54	8.96	0.107	0.000	0.035	0.659	0.256	0.024	0.620	97.688
SK0111	outcrop	ARK	670008	6892337	85.40	7.28	0.46	0.11	0.10	1.10	4.64	0.257	0.067	0.011	nd	0.024	0.019	0.340	99.801
SK0114	outcrop	ARK	665838	6898466	78.20	9.90	1.80	0.70	0.45	1.61	5.35	0.376	0.181	0.039	0.007	0.086	0.050	0.860	99.609
VG0101	outcrop	LST	666470	6903120	1.45	0.38	0.56	1.68	53.00	nd	0.10	0.025	0.042	0.023	nd	0.015	0.016	42.620	99.910
VG0102	outcrop	ARK	666470	6903120	69.80	8.09	1.35	0.44	8.70	2.62	3.12	0.436	0.211	0.033	nd	0.066	0.017	4.740	99.619
VG0104	outcrop	LST	666549	6903270	7.03	2.30	2.43	0.89	48.60	1.40	0.03	0.163	0.049	0.193	nd	0.018	0.014	36.630	99.746
VG0105	outcrop	LST	666549	6903270	2.72	0.90	0.50	0.63	53.10	0.35	0.10	0.060	0.029	0.020	0.016	0.012	0.013	41.430	99.889
VG0106	outcrop	ARK	668776	6904210	73.50	10.30	2.01	1.11	2.67	4.39	2.72	0.396	0.215	0.057	0.533	0.327	0.020	1.450	99.698
VG0107	outcrop	LST	668705	6904133	51.70	8.73	2.11	1.20	18.40	1.72	4.93	0.507	0.189	0.060	0.004	0.036	0.021	9.670	99.277
VG0109	outcrop	LST	668696	6904116	51.40	8.29	1.46	0.81	21.70	2.47	2.80	0.557	0.299	0.052	nd	0.013	0.019	9.840	99.705
SK0201	outcrop	RHY	654434	6917773	42.90	0.35	44.20	0.12	0.31	nd	0.08	0.013	1.151	0.250	0.059	0.017	0.013	8.507	97.970
SK0202	outcrop	RHY	654434	6917773	91.20	0.42	6.35	0.00	0.17	nd	0.09	0.016	0.145	0.052	0.165	0.007	0.012	1.070	99.688
SK0203	open pit	ARK	657764	6921902	19.60	4.13	0.92	0.62	9.74	nd	0.41	0.179	0.246	0.057	37.797	0.110	0.081	15.960	89.860
SK0204	open pit	ARK	657764	6921902	17.50	2.12	0.57	0.52	6.69	nd	0.36	0.091	6.453	3.570	40.701	0.228	0.064	9.390	88.261
SK0205	open pit	ARK	657784	6921853	80.50	10.40	0.57	0.35	0.20	4.42	1.39	0.282	0.071	0.009	0.093	0.070	0.019	1.010	99.377
SK0207	open pit	ARK	657770	6921773	65.30	13.50	1.41	1.31	0.39	2.18	5.05	0.295	0.095	0.055	4.993	0.058	0.074	3.480	98.188
SK0208	open pit	ARK	657657	6921943	8.05	2.59	0.74	0.65	2.46	nd	0.32	0.081	0.427	0.197	44.385	0.060	0.180	28.640	88.786

XRF whole rock analyses

Sample ID	Location	Lithology	E	N	SiO ₂ [%]	Al ₂ O ₃ [%]	Fe ₂ O ₃ [%]	MgO [%]	CaO [%]	Na ₂ O [%]	K ₂ O [%]	TiO ₂ [%]	P ₂ O ₅ [%]	MnO [%]	ZnO [%]	S [%]	Cl [%]	LOI [%]	Total [%]
SK02100	outcrop	ARK	654106	6920675	88.50	5.55	0.71	0.19	0.32	nd	2.06	0.117	0.060	0.027	nd	0.110	0.103	1.326	99.067
SK02101	outcrop	ARK	654083	6920594	87.00	8.21	0.34	0.32	0.03	nd	2.46	0.229	0.102	nd	0.005	0.005	0.073	0.867	99.650
SK02104	outcrop	GOS	655095	6920063	60.60	2.62	31.60	0.28	0.18	nd	0.47	0.124	0.298	0.021	0.395	0.112	0.027	2.450	99.177
SK02106	outcrop	ARK	655027	6920013	88.90	6.99	0.68	0.29	0.22	nd	0.64	0.117	nd	nd	0.212	0.109	0.149	1.485	99.786
SK02107	outcrop	ARK	654968	6919745	87.10	6.67	1.61	0.57	0.20	nd	0.72	0.175	0.112	nd	nd	0.084	0.067	2.040	99.344
SK02108	outcrop	ARK	654968	6919745	90.30	6.49	0.13	0.26	0.04	nd	0.57	0.164	0.083	nd	nd	0.009	0.105	1.544	99.694
SK02109	outcrop	ARK	655047	6919636	69.90	14.50	0.49	nd	0.06	0.32	13.20	0.157	0.393	nd	0.008	0.017	0.163	0.433	99.636
SK0211	open pit	ARK	657777	6921704	47.00	6.63	1.10	1.98	23.20	1.07	4.09	0.133	0.080	0.067	0.170	0.035	0.021	14.010	99.586
SK02110	open pit	SSS	657810	6921762	64.40	11.80	9.83	0.32	0.11	0.25	9.05	0.120	0.115	nd	0.638	0.332	0.019	2.480	99.462
SK02113	open pit	SSS	657760	6921892	73.10	16.20	1.30	1.72	0.02	nd	5.35	0.105	0.045	nd	0.012	0.006	0.099	1.870	99.823
SK02114	open pit	ARK	657555	6922022	35.30	8.36	5.35	1.83	4.91	nd	2.28	0.396	3.340	0.724	27.232	0.031	0.118	9.900	99.771
SK02116	open pit	SSS	657545	6922040	88.20	6.19	0.65	1.16	0.04	nd	2.20	0.069	0.038	0.010	0.076	0.005	0.132	0.953	99.724
SK02117	open pit	SSS	657394	6922067	83.70	8.89	0.64	1.27	0.03	0.20	2.97	0.066	nd	nd	0.052	0.005	0.121	1.625	99.572
SK02118	open pit	ARK	657499	6922061	64.80	17.50	3.55	1.74	0.10	0.43	6.80	0.912	0.127	0.654	0.138	0.020	0.142	2.641	99.551
SK02119	open pit	ARK	657479	6921981	17.70	3.20	64.30	0.16	0.10	nd	0.52	0.074	1.400	0.215	0.778	0.054	0.056	10.840	99.392
SK0212	open pit	SSS	657782	6921792	83.60	8.43	0.71	1.00	0.70	nd	2.89	0.060	0.034	0.012	0.170	0.011	0.038	2.100	99.759
SK0213	open pit	BSA	657798	6921817	21.30	6.33	2.37	1.41	8.86	nd	0.88	0.300	0.782	1.670	32.379	0.100	0.105	14.160	90.643
SK0213B	open pit	BSA	657798	6921817	18.50	4.11	1.15	1.58	6.29	nd	0.67	0.159	3.796	6.450	35.089	0.255	0.128	10.300	88.477
SK0214	open pit	BSA	657730	6921817	39.70	11.20	3.05	1.73	3.63	nd	3.19	0.441	0.247	0.027	16.576	1.617	0.118	11.610	93.135
SK0215	open pit	BSA	657730	6921817	53.60	16.30	4.96	1.79	0.69	nd	6.21	0.536	0.371	0.019	6.897	0.020	0.084	6.240	97.717
SK0216A	open pit	SSS	657761	6921841	87.90	6.06	1.12	0.75	0.26	nd	2.08	0.089	nd	0.041	0.054	0.019	0.020	1.200	99.600
SK0216B	open pit	SSS	657761	6921841	85.00	7.95	0.98	1.35	0.04	nd	2.59	0.096	nd	0.015	0.103	0.010	0.021	1.550	99.703
SK0218	outcrop	BAR	657260	6921664	33.80	0.36	5.52	0.10	0.25	0.50	0.03	nd	0.314	0.212	0.044	8.582	0.010	1.320	51.035
SK0217	outcrop	GOS	657299	6921655	2.54	1.91	91.20	0.12	0.70	nd	0.01	0.031	0.539	0.082	0.019	0.245	0.015	1.520	98.937
SK0219	outcrop	BAR	657260	6921664	14.80	0.86	4.48	nd	0.25	0.68	nd	nd	0.728	0.477	0.140	10.447	0.012	1.380	34.258
SK0231	outcrop	RHY	657477	6920472	84.80	9.49	0.93	0.77	0.18	nd	2.01	0.273	0.129	0.012	0.023	0.030	0.025	1.195	99.860
SK0232	outcrop	RHY	657619	6920965	89.00	6.35	0.32	nd	0.06	nd	0.84	0.146	1.590	nd	n	0.091	0.133	1.010	99.537
SK0235	outcrop	SSS	657695	6921154	73.00	11.70	2.78	0.15	0.09	0.25	10.10	0.144	0.052	0.025	0.015	0.023	0.071	0.710	99.117
SK0236	outcrop	SSS	657694	6921157	76.80	11.00	0.43	0.00	0.09	0.27	10.20	0.168	0.041	0.000	0.004	0.005	0.036	0.227	99.269
SK0237	outcrop	GOS	657702	6921169	14.60	2.02	64.30	0.29	0.57	nd	1.07	0.029	1.320	0.194	1.748	0.254	0.112	11.796	98.305
SK0239A	outcrop	GOS	657558	6921170	80.70	10.40	1.67	0.52	0.03	nd	1.63	0.229	0.110	0.012	0.005	0.012	0.032	4.450	99.803
SK0239B	outcrop	GOS	657558	6921170	23.40	9.17	56.20	1.06	0.11	nd	2.12	0.396	1.030	0.634	0.351	0.069	0.029	4.450	99.018
SK0241	outcrop	ARK	657466	6921382	88.60	6.74	0.40	0.17	0.07	nd	0.40	0.139	1.230	0.010	0.006	0.037	0.153	1.680	99.636
SK0242	outcrop	ARK	657466	6921382	88.70	7.27	0.55	0.23	0.16	nd	0.54	0.147	0.197	0.068	0.009	0.015	0.110	1.590	99.586
SK0246	open pit	ARK, GOS	657740	6921766	48.70	24.40	7.07	0.36	0.39	0.56	0.97	0.784	0.454	5.420	0.259	0.036	0.233	8.534	98.164
SK0247	open pit	ARK, GOS	657723	6921794	32.90	15.60	2.13	0.58	0.26	0.36	1.59	0.434	0.374	28.500	1.243	0.043	0.187	9.870	94.067
SK0249	open pit	ARK	657707	6921830	71.00	19.50	1.76	0.81	0.04	0.51	1.94	0.416	0.065	0.069	0.047	0.032	0.255	3.245	99.694

XRF whole rock analyses

Sample ID	Location	Lithology	E	N	SiO ₂ [%]	Al ₂ O ₃ [%]	Fe ₂ O ₃ [%]	MgO [%]	CaO [%]	Na ₂ O [%]	K ₂ O [%]	TiO ₂ [%]	P ₂ O ₅ [%]	MnO [%]	ZnO [%]	S [%]	Cl [%]	LOI [%]	Total [%]
SK0251	open pit	LST	657421	6921814	43.10	9.97	3.79	1.54	18.80	0.55	0.99	0.378	0.151	5.170	0.125	0.065	0.279	13.490	98.401
SK0253	open pit	LST	657421	6921814	46.80	7.10	3.50	2.41	15.70	1.59	1.73	0.436	nd	0.089	0.010	0.036	0.338	19.960	99.699
SK0254	open pit	LST	657421	6921814	23.90	3.39	2.09	1.72	40.70	0.71	1.03	0.273	0.115	0.035	0.008	0.058	0.148	25.480	99.659
SK0256	open pit	GOS	657458	6921794	44.80	4.51	35.40	0.33	0.36	nd	0.24	0.128	1.120	2.500	1.351	0.067	0.223	6.980	98.010
SK0257	open pit	ARK	657458	6921794	82.30	9.32	1.95	0.13	0.06	nd	3.84	0.244	0.130	0.053	0.028	0.029	0.132	1.224	99.441
SK0258	open pit	ARK	657458	6921794	73.80	14.90	2.01	0.53	0.11	0.28	1.22	0.406	0.111	1.260	0.107	0.028	0.168	4.150	99.077
SK0259	open pit	GOS	657458	6921794	68.60	10.20	3.06	0.32	0.21	nd	0.82	0.380	0.578	8.000	0.678	0.045	0.071	4.230	97.191
SK0260	open pit	GOS	657490	6921764	16.50	7.05	37.80	1.06	1.04	nd	1.54	0.267	1.070	13.400	3.857	0.062	0.227	13.630	97.503
SK0265	open pit	ARK	657540	6921735	64.30	20.50	4.28	1.24	0.27	nd	3.38	0.638	0.240	0.021	0.127	0.160	0.079	4.150	99.385
SK0267	open pit	GOS	657599	6921687	13.30	6.33	47.40	0.72	0.63	nd	0.53	0.174	0.928	11.200	2.546	0.098	0.311	13.860	98.023
SK0268	open pit	ARK	657599	6921687	58.70	23.30	3.80	2.06	0.14	0.21	6.28	1.020	0.182	0.028	0.062	0.028	0.089	3.700	99.595
SK0269	open pit	GOS	657599	6921687	28.30	16.70	37.60	0.76	0.36	0.39	0.96	0.506	0.870	0.599	1.293	0.083	0.276	10.510	99.202
SK0273	outcrop	ARK	656458	6921061	85.30	8.89	0.85	1.16	0.13	nd	1.31	0.254	0.052	nd	nd	0.013	0.101	1.810	99.862
SK0275	outcrop	ARK	655066	6922181	89.30	6.49	0.61	0.37	0.15	nd	0.81	0.115	0.128	nd	nd	0.029	0.123	1.427	99.557
SK0276	outcrop	ARK	654948	6922295	88.50	7.67	0.68	0.45	0.03	nd	1.29	0.174	0.058	nd	nd	0.007	0.091	0.966	99.917
SK0277	outcrop	ARK	654804	6922436	90.80	4.92	0.50	0.38	0.31	nd	0.49	0.110	0.152	nd	0.003	0.087	0.079	1.450	99.283
SK0279	open pit	BSA	657765	6921821	36.00	7.19	2.39	0.69	0.75	nd	1.70	0.169	0.086	0.038	34.926	0.011	0.154	15.650	99.755
SK0283	open pit	ARK	657785	6921827	51.80	12.50	2.09	0.76	2.45	nd	7.72	0.438	3.370	11.100	1.473	0.046	0.066	4.260	98.074
SK0287	open pit	ARK, GOS	657475	6921844	18.80	12.70	33.90	0.81	0.42	nd	1.76	0.481	1.020	12.800	2.674	0.088	0.125	12.140	97.719
SK0289	outcrop	ARK	654749	6921550	84.60	9.98	0.74	0.51	0.02	nd	2.04	0.249	0.108	nd	0.003	0.011	0.106	1.253	99.618
SK0290	outcrop	RHY	654589	6921551	89.00	6.90	0.75	0.40	0.12	nd	1.30	0.136	0.132	nd	0.005	0.031	0.083	0.968	99.835
SK0291	outcrop	ARK	654315	6921505	86.10	8.81	0.99	0.55	0.02	nd	1.62	0.192	0.041	nd	0.004	0.008	0.091	1.406	99.834
SK0292	outcrop	RHY	655068	6921087	91.10	5.37	0.57	0.28	0.22	nd	0.80	0.085	0.157	nd	0.004	0.152	0.014	0.719	99.479
SK0293	outcrop	RHY	655068	6921087	87.30	8.05	1.41	0.44	0.02	nd	1.33	0.130	0.086	nd	0.004	0.011	0.049	1.020	99.853
SK0296	outcrop	ARK	655231	6920432	88.70	7.78	0.56	0.33	0.02	nd	1.10	0.158	0.069	nd	0.005	0.008	0.037	1.078	99.852
SK0297	outcrop	ARK	655425	6920412	86.90	9.29	0.28	0.49	0.04	nd	1.43	0.196	nd	nd	0.004	0.005	0.039	1.191	99.869
SK0299	outcrop	ARK	655564	6920265	90.20	6.43	0.31	0.41	0.12	nd	1.16	0.164	0.126	nd	0.003	0.024	0.055	0.863	99.877
BC0101	open pit	ARK	657420	6921978	80.10	6.12	5.82	1.07	0.91	0.80	1.07	0.288	0.387	0.156	0.013	0.085	0.430	2.410	99.656
BC0102	open pit	ARK	657420	6921978	74.10	8.58	5.54	2.51	0.53	1.77	1.30	0.505	0.204	0.241	0.016	0.119	1.022	3.230	99.670
BC0103	open pit	CALCRETE	657420	6921978	19.80	3.17	1.55	2.13	43.00	0.64	0.89	0.204	0.108	0.023	0.006	0.086	0.065	28.000	99.674

nd - not detected

na - not analysed

XRF whole rock analyses

Sample ID	Location	Lithology	E	N	V [ppm]	Cr [ppm]	Co [ppm]	Ni [ppm]	Cu [ppm]	Pb [ppm]	Ag [ppm]	Ga [ppm]	As [ppm]	Rb [ppm]	Sr [ppm]	Y [ppm]	Zr [ppm]	Nb [ppm]	Cd [ppm]
0301	SD03	ARK	657485	6922181	nd	151	nd	nd	117	nd	nd	nd	nd	316	389	260	241	nd	nd
0305	SD03	ARK	657485	6922181	111	112	nd	51	69	84	nd	nd	nd	229	841	631	214	nd	nd
0307	SD03	ARK	657485	6922181	109	110	nd	nd	nd	55	nd	nd	nd	367	646	52	320	nd	nd
0311	SD03	ARK	657485	6922181	nd	122	nd	225	943	nd	nd	nd	nd	113	273	61	197	nd	nd
0313	SD03	SSS	657485	6922181	nd	242	nd	86	59	nd	nd	nd	nd	272	110	115	231	69	nd
0314	SD03	SSS	657485	6922181	90	nd	nd	320	295	nd	nd	nd	nd	159	146	41	210	29	nd
0315	SD03	LST	657485	6922181	nd	nd	nd	nd	113	nd	nd	nd	nd	194	266	72	187	37	nd
0317	SD03	SSS	657485	6922181	nd	nd	nd	135	373	nd	nd	54	nd	233	100	100	209	68	nd
0318	SD03	ARK	657485	6922181	84	187	nd	56	53	nd	nd	nd	nd	264	221	46	212	23	nd
0319	SD03	ARK	657485	6922181	nd	182	nd	168	122	nd	nd	nd	nd	283	478	38	254	nd	nd
3901	SD39	ARK	657236	6922217	nd	258	60	133	3389	nd	nd	nd	nd	199	338	27	97	nd	nd
3902	SD39	ARK	657236	6922217	nd	151	nd	nd	727	nd	nd	nd	nd	236	149	23	121	nd	nd
3905	SD39	ARK	657236	6922217	nd	222	nd	161	3111	nd	nd	nd	nd	207	291	38	154	nd	nd
3906	SD39	LST	657236	6922217	nd	nd	nd	nd	118	nd	nd	nd	nd	210	281	40	187	nd	nd
3909	SD39	LST	657236	6922217	nd	211	nd	nd	90	nd	nd	nd	nd	344	719	31	105	nd	nd
3915	SD39	LST	657236	6922217	nd	147	nd	nd	724	248	nd	nd	nd	225	271	30	180	nd	393
3916	SD39	ARK	657236	6922217	nd	608	nd	259	9969	527	nd	nd	nd	169	259	55	245	nd	nd
3917	SD39	ARK	657236	6922217	nd	nd	nd	238	57621	239	nd	nd	nd	360	477	43	319	nd	nd
3918	SD39	ARK, GOS	657236	6922217	184	102	nd	nd	7840	2584	nd	nd	nd	143	182	1803	277	nd	nd
3919	SD39	ARK	657236	6922217	nd	408	nd	nd	781	338	nd	nd	nd	67	60	201	275	nd	nd
3922	SD39	QSS	657236	6922217	nd	206	nd	116	10971	1554	nd	nd	nd	145	39	290	234	nd	nd
8001	SD80	LST	657374	6922177	nd	137	nd	58	1337	nd	156	nd	nd						
8011	SD80	ARK	657374	6922177	nd	197	nd	164	2219	nd	nd	nd	nd	263	369	34	353	nd	nd
8013	SD80	ARK	657374	6922177	nd	125	nd	296	5465	nd	nd	nd	nd	217	191	nd	244	nd	nd
8014	SD80	ARK	657374	6922177	nd	195	nd	345	6626	nd	nd	nd	nd	202	220	nd	293	nd	nd
8016	SD80	BSA	657374	6922177	nd	158	nd	508	6386	nd	nd	nd	nd	156	238	nd	303	nd	nd
8022	SD80	ARK	657374	6922177	nd	123	nd	79	2237	113	nd	nd	nd	239	190	40	252	nd	nd
8024	SD80	ARK, GOS	657374	6922177	103	164	nd	89	4618	2291	nd	nd	nd	110	72	41	296	nd	nd
8025	SD80	ARK, GOS	657374	6922177	nd	169	nd	79	4227	215	nd	nd	nd	180	106	28	175	nd	nd
8027	SD80	ARK	657374	6922177	nd	124	nd	162	7192	232	nd	nd	nd	223	138	41	nd	nd	410
BH7001	BH70	ARK	657780	6921842	nd	153	nd	222	747	nd	nd	nd	nd	198	228	31	420	nd	nd
BH7002	BH70	ARK	657780	6921842	nd	463	nd	157	815	nd	nd	nd	nd	89	155	nd	88	nd	245
BH7003	BH70	ARK	657780	6921842	nd	81	nd	190	1173	nd	nd	nd	nd	128	351	55	169	nd	304
BH7004	BH70	ARK	657780	6921842	nd	165	nd	175	894	nd	nd	nd	nd	168	229	nd	204	nd	nd
BH7005	BH70	ARK	657780	6921842	nd	158	nd	211	1134	nd	nd	nd	nd	188	242	48	267	nd	156
BH7006	BH70	ARK	657780	6921842	nd	122	nd	235	716	nd	nd	nd	nd	94	172	nd	107	nd	475
BH7008	BH70	ARK	657780	6921842	nd	791	nd	142	585	nd	nd	nd	nd	153	138	nd	93	nd	487

XRF whole rock analyses

Sample ID	Location	Lithology	E	N	V [ppm]	Cr [ppm]	Co [ppm]	Ni [ppm]	Cu [ppm]	Pb [ppm]	Ag [ppm]	Ga [ppm]	As [ppm]	Rb [ppm]	Sr [ppm]	Y [ppm]	Zr [ppm]	Nb [ppm]	Cd [ppm]
BH7009	BH70	ARK	657780	6921842	nd	101	nd	86	192	nd	nd	nd	nd	186	162	25	157	nd	nd
BH7010	BH70	SSS	657780	6921842	nd	285	nd	167	168	nd	nd	nd	nd	243	114	162	204	63	nd
BH7011	BH70	SSS	657780	6921842	nd	286	nd	184	218	nd	nd	nd	nd	214	149	141	222	60	nd
BH7012	BH70	ARK	657780	6921842	nd	136	nd	348	188	nd	nd	nd	nd	120	246	nd	nd	nd	nd
BH7013	BH70	ARK	657780	6921842	nd	150	nd	98	97	nd	nd	nd	nd	63	180	114	nd	118	263
BH7014	BH70	SSS	657780	6921842	nd	nd	nd	nd	127	nd	nd	nd	nd	nd	nd	nd	48	nd	nd
BH7015	BH70	SSS	657780	6921842	nd	162	nd	290	98	nd	nd	nd	nd	52	39	nd	53	nd	nd
BH7016	BH70	ARK	657780	6921842	nd	nd	nd	305	1237	nd	nd	nd	nd	68	82	nd	113	nd	nd
BH7017	BH70	ARK	657780	6921842	nd	nd	nd	206	1231	nd	nd	nd	nd	134	207	52	173	nd	257
4801	SD48	LST	657598	6922073	nd	526	nd	nd	137	nd	nd	nd	nd	165	197	nd	53	nd	437
4802	SD48	ARK	657598	6922073	nd	nd	nd	386	612	nd	nd	nd	nd	178	403	48	321	nd	nd
4805	SD48	LST	657598	6922073	nd	243	nd	85	91	nd	nd	nd	nd	172	460	nd	155	nd	3846
4806	SD48	LST	657598	6922073	nd	231	nd	nd	83	nd	nd	nd	nd	358	3193	36	409	nd	nd
4807	SD48	LST	657598	6922073	nd	nd	nd	nd	66	nd	nd	nd	nd	226	2473	32	313	nd	nd
4809	SD48	LST	657598	6922073	nd	109	nd	nd	61	nd	nd	nd	nd	289	1544	45	283	nd	nd
4810	SD48	LST	657598	6922073	204	142	nd	nd	122	nd	nd	nd	nd	512	196	67	457	35	nd
4812	SD48	SSS	657598	6922073	nd	63	nd	nd	29	65	nd	62	nd	496	120	180	400	72	nd
4814	SD48	LST	657598	6922073	nd	nd	nd	nd	nd	40	nd	nd	nd	170	1913	32	207	15	nd
4815	SD48	LST	657598	6922073	nd	354	nd	nd	51	nd	nd	nd	nd	476	1230	63	356	28	nd
4816A	SD48	LST	657598	6922073	nd	nd	nd	nd	nd	nd	nd	nd	nd	371	1213	52	212	nd	nd
4816B	SD48	LST	657598	6922073	nd	nd	nd	nd	nd	nd	nd	nd	nd	76	2356	57	268	nd	nd
4818	SD48	ARK	657598	6922073	119	132	nd	605	117	nd	nd	106	nd	554	1437	93	660	35	nd
4819	SD48	ARK	657598	6922073	186	328	nd	383	152	nd	nd	nd	nd	522	2686	132	536	43	nd
4820	SD48	ARK	657598	6922073	nd	149	nd	340	141	nd	nd	144	nd	423	607	nd	416	nd	nd
4821	SD48	ARK, GOS	657598	6922073	125	102	nd	533	476	nd	nd	179	nd	532	1436	104	591	48	nd
4822	SD48	ARK	657598	6922073	nd	73	nd	282	176	nd	nd	213	nd	66	194	nd	89	nd	nd
4823	SD48	ARK	657598	6922073	nd	76	nd	118	243	nd	nd	304	nd	107	167	nd	126	nd	nd
4825	SD48	ARK	657598	6922073	nd	nd	80	578	91	nd	nd	253	nd	89	54	45	81	nd	5102
4826	SD48	ARK	657598	6922073	113	538	nd	148	127	nd	nd	72	nd	509	819	76	495	31	nd
0705	SD07	ARK	657855	6921927	nd	nd	nd	335	648	nd	nd	nd	nd	160	203	nd	207	nd	455
0706	SD07	ARK	657855	6921927	nd	86	nd	257	737	nd	nd	nd	nd	102	154	nd	68	nd	676
0707	SD07	ARK	657855	6921927	nd	nd	nd	288	765	161	nd	nd	nd	198	286	nd	nd	nd	656
0708	SD07	ARK	657855	6921927	nd	nd	nd	258	788	nd	nd	nd	nd	75	95	nd	93	nd	651
0710	SD07	ARK	657855	6921927	nd	nd	nd	140	891	nd	nd	148	nd	nd	826	47	178	nd	422
0712	SD07	ARK	657855	6921927	nd	105	nd	124	769	nd	nd	109	nd	nd	267	nd	109	nd	701
0713	SD07	ARK	657855	6921927	nd	nd	nd	124	694	nd	nd	131	nd	nd	346	49	199	nd	471
0714	SD07	ARK	657855	6921927	nd	150	nd	113	695	nd	nd	308	nd	nd	708	65	275	nd	nd

XRF whole rock analyses

Sample ID	Location	Lithology	E	N	V [ppm]	Cr [ppm]	Co [ppm]	Ni [ppm]	Cu [ppm]	Pb [ppm]	Ag [ppm]	Ga [ppm]	As [ppm]	Rb [ppm]	Sr [ppm]	Y [ppm]	Zr [ppm]	Nb [ppm]	Cd [ppm]
0715	SD07	ARK	657855	6921927	nd	97	nd	103	932	nd	nd	214	nd	nd	749	65	232	nd	nd
0718	SD07	ARK	657855	6921927	nd	238	nd	171	320	nd	nd	62	nd	nd	180	nd	109	nd	nd
0719	SD07	ARK	657855	6921927	nd	104	64	nd	139	nd	nd	90	nd	nd	156	48	81	nd	nd
0726	SD07	ARK	657855	6921927	70	158	nd	252	168	nd	nd	nd	nd	283	893	49	200	nd	nd
0727	SD07	ARK	657855	6921927	nd	78	nd	241	472	nd	nd	nd	nd	59	156	39	nd	nd	592
0734	SD07	ARK	657855	6921927	nd	nd	nd	363	335	nd	nd	214	nd	273	514	51	153	nd	nd
2065	SD20	BSA	657539	6921983	nd	219	nd	288	187	nd	nd	287	nd	528	1142	75	246	nd	nd
2067	SD20	QSS, GOS	657539	6921983	nd	80	164	nd	3062	1383	nd	nd	nd	nd	nd	59	nd	nd	nd
2068	SD20	QSB, GOS	657539	6921983	nd	nd	nd	nd	7925	10807	nd	94	nd	nd	nd	128	131	nd	nd
2066	SD20	ARK, GOS	657539	6921983	nd	nd	152	nd	674	381	nd	103	nd	nd	nd	nd	179	nd	nd
2052	SD20	ARK	657539	6921983	nd	250	nd	111	998	nd	nd	nd	nd	274	285	35	104	nd	nd
4969	SD49	ARK, GOS	657535	6922042	nd	nd	nd	nd	2023	1065	nd	nd	448	nd	nd	40	nd	nd	nd
4968	SD49	ARK, GOS	657535	6922042	nd	140	nd	nd	427	6434	nd	163	nd	nd	71	1901	244	nd	nd
4952	SD49	ARK	657535	6922042	82	515	nd	nd	186	938	1428	nd	nd	201	111	67	359	28	nd
4910	SD49	ARK	657535	6922042	nd	302	nd	314	1557	134	nd	nd	nd	238	133	127	313	nd	nd
2413	SD24	QSS	657420	6921918	85	915	nd	159	298	2139	nd	nd	nd	nd	36	nd	119	13	nd
6519	SD65	ARK, GOS	657555	6921764	nd	77	nd	190	304	3114	nd	nd	nd	70	149	100	82	nd	586
SK0101	outcrop	ARK	662084	6907908	nd	128	nd	143	39	32	169	nd	nd						
SK0102	outcrop	ARK	662084	6907908	nd	nd	nd	nd	nd	nd	nd	nd	nd	84	28	nd	138	nd	nd
SK0103	outcrop	ARK	663787	6906061	214	nd	nd	72	234	82	nd	238	nd	505	33	156	nd	nd	4308
SK0104	outcrop	ARK	662242	6901289	nd	221	nd	nd	386	67	nd	nd	nd	276	571	27	107	nd	nd
SK0111	outcrop	ARK	670008	6892337	nd	nd	nd	nd	nd	nd	nd	nd	nd	158	94	28	183	nd	nd
SK0114	outcrop	ARK	665838	6898466	nd	129	nd	nd	nd	78	nd	nd	nd	175	113	37	222	nd	nd
VG0101	outcrop	LST	666470	6903120	nd	nd	nd	nd	nd	nd	nd	nd	nd	nd	855	nd	nd	nd	nd
VG0102	outcrop	ARK	666470	6903120	nd	nd	nd	nd	nd	nd	nd	nd	nd	112	237	27	372	nd	nd
VG0104	outcrop	LST	666549	6903270	nd	nd	nd	nd	nd	nd	nd	nd	nd	533	1254	22	194	nd	nd
VG0105	outcrop	LST	666549	6903270	nd	nd	nd	nd	nd	nd	nd	nd	nd	421	1063	nd	nd	nd	nd
VG0106	outcrop	ARK	668776	6904210	nd	370	nd	78	124	33	211	nd	nd						
VG0107	outcrop	LST	668705	6904133	nd	281	nd	148	1652	36	326	nd	nd						
VG0109	outcrop	LST	668696	6904116	nd	nd	nd	nd	nd	nd	nd	nd	nd	144	1249	47	378	nd	nd
SK0201	outcrop	RHY	654434	6917773	114	nd	213	388	nd	nd	nd	nd	nd						
SK0202	outcrop	RHY	654434	6917773	nd	nd	116	nd	nd	nd	nd	nd							
SK0203	open pit	ARK	657764	6921902	nd	nd	nd	204	2193	nd	nd	nd	nd	nd	132	nd	101	nd	724
SK0204	open pit	ARK	657764	6921902	nd	nd	281	236	855	nd	nd	nd	nd	nd	413	nd	nd	nd	329
SK0205	open pit	ARK	657784	6921853	nd	nd	127	nd	51	nd	nd	nd	nd	91	133	22	118	nd	nd
SK0207	open pit	ARK	657770	6921773	nd	635	nd	76	61	nd	nd	nd	nd	242	433	38	149	nd	nd
SK0208	open pit	ARK	657657	6921943	nd	nd	nd	269	381	nd	nd	nd	nd	nd	nd	nd	nd	nd	1148

XRF whole rock analyses

Sample ID	Location	Lithology	E	N	V [ppm]	Cr [ppm]	Co [ppm]	Ni [ppm]	Cu [ppm]	Pb [ppm]	Ag [ppm]	Ga [ppm]	As [ppm]	Rb [ppm]	Sr [ppm]	Y [ppm]	Zr [ppm]	Nb [ppm]	Cd [ppm]
SK02100	outcrop	ARK	654106	6920675	nd	nd	259	nd	nd	nd	nd	nd	nd	79	34	21	170	nd	nd
SK02101	outcrop	ARK	654083	6920594	nd	130	85	nd	nd	nd	nd	nd	nd	92	25	30	229	nd	nd
SK02104	outcrop	GOS	655095	6920063	311	337	nd	53	nd	147	nd	nd							
SK02106	outcrop	ARK	655027	6920013	nd	643	137	nd	nd	nd	nd	nd	nd	35	nd	36	122	nd	nd
SK02107	outcrop	ARK	654968	6919745	nd	nd	243	nd	nd	nd	nd	nd	nd	42	40	nd	229	nd	nd
SK02108	outcrop	ARK	654968	6919745	nd	nd	132	nd	nd	nd	nd	nd	nd	31	24	18	179	nd	nd
SK02109	outcrop	ARK	655047	6919636	nd	nd	104	nd	nd	nd	nd	51	nd	344	76	242	1176	113	nd
SK0211	open pit	ARK	657777	6921704	nd	nd	nd	nd	nd	nd	nd	nd	nd	227	388	34	88	nd	nd
SK02110	open pit	SSS	657810	6921762	nd	nd	106	nd	nd	271	nd	43	nd	240	155	200	1271	121	nd
SK02113	open pit	SSS	657760	6921892	nd	nd	nd	nd	nd	nd	nd	nd	nd	361	32	103	221	112	nd
SK02114	open pit	ARK	657555	6922022	nd	87	nd	211	1088	nd	nd	nd	nd	173	406	143	200	nd	237
SK02116	open pit	SSS	657545	6922040	nd	nd	111	nd	77	nd	nd	nd	nd	112	25	78	100	47	nd
SK02117	open pit	SSS	657394	6922067	nd	nd	83	nd	87	nd	nd	nd	nd	167	20	80	129	42	nd
SK02118	open pit	ARK	657499	6922061	124	432	130	nd	188	nd	nd	nd	nd	375	270	477	360	nd	nd
SK02119	open pit	ARK	657479	6921981	nd	121	178	nd	723	nd	nd	nd	nd	nd	nd	105	nd	nd	nd
SK0212	open pit	SSS	657782	6921792	nd	nd	nd	nd	nd	nd	nd	nd	nd	151	19	70	118	nd	nd
SK0213	open pit	BSA	657798	6921817	nd	nd	123	237	1847	nd	nd	nd	nd	79	209	nd	118	nd	757
SK0213B	open pit	BSA	657798	6921817	105	nd	288	292	1107	nd	nd	nd	nd	nd	279	nd	nd	nd	nd
SK0214	open pit	BSA	657730	6921817	117	126	nd	145	709	nd	nd	nd	nd	233	438	53	221	nd	nd
SK0215	open pit	BSA	657730	6921817	210	419	nd	nd	481	nd	nd	nd	nd	390	371	49	324	nd	nd
SK0216A	open pit	SSS	657761	6921841	nd	nd	98	nd	nd	nd	nd	nd	nd	112	nd	89	96	nd	nd
SK0216B	open pit	SSS	657761	6921841	nd	nd	nd	nd	55	nd	nd	nd	nd	141	nd	39	122	nd	nd
SK0218	outcrop	BAR	657260	6921664	nd	468	nd	nd	1017	3616	nd	nd	nd	nd	3209	nd	330	nd	nd
SK0217	outcrop	GOS	657299	6921655	nd	131	202	nd	302	nd	nd	nd	nd	nd	61	nd	nd	nd	nd
SK0219	outcrop	BAR	657260	6921664	nd	305	nd	nd	458	3171	nd	nd	nd	nd	2784	nd	nd	nd	1816
SK0231	outcrop	RHY	657477	6920472	nd	nd	65	nd	nd	nd	nd	nd	nd	82	23	27	299	nd	nd
SK0232	outcrop	RHY	657619	6920965	nd	nd	84	nd	nd	191	nd	nd	nd	nd	60	24	118	nd	nd
SK0235	outcrop	SSS	657695	6921154	nd	nd	82	nd	nd	166	nd	nd	nd	243	109	171	2143	156	nd
SK0236	outcrop	SSS	657694	6921157	nd	nd	70	nd	nd	70	nd	nd	nd	295	47	199	2322	178	nd
SK0237	outcrop	GOS	657702	6921169	nd	nd	nd	nd	405	567	nd	nd	nd	nd	nd	1571	196	nd	nd
SK0239A	outcrop	GOS	657558	6921170	nd	97	90	nd	nd	nd	nd	nd	nd	72	33	nd	246	nd	nd
SK0239B	outcrop	GOS	657558	6921170	nd	109	nd	nd	226	523	nd	nd	nd	126	226	403	192	nd	nd
SK0241	outcrop	ARK	657466	6921382	nd	nd	107	nd	nd	169	nd	nd	nd	nd	45	nd	135	nd	nd
SK0242	outcrop	ARK	657466	6921382	nd	nd	82	nd	35	212	nd	nd	nd	31	23	nd	137	nd	nd
SK0246	open pit	ARK, GOS	657740	6921766	156	300	115	nd	388	397	nd	nd	nd	46	608	73	291	nd	nd
SK0247	open pit	ARK, GOS	657723	6921794	nd	313	204	nd	654	1206	nd	nd	nd	70	521	58	127	nd	nd
SK0249	open pit	ARK	657707	6921830	nd	358	nd	nd	64	nd	nd	nd	nd	100	43	52	224	nd	nd

XRF whole rock analyses

Sample ID	Location	Lithology	E	N	V [ppm]	Cr [ppm]	Co [ppm]	Ni [ppm]	Cu [ppm]	Pb [ppm]	Ag [ppm]	Ga [ppm]	As [ppm]	Rb [ppm]	Sr [ppm]	Y [ppm]	Zr [ppm]	Nb [ppm]	Cd [ppm]
SK0251	open pit	LST	657421	6921814	nd	270	94	nd	543	1150	nd	nd	nd	44	309	46	195	nd	nd
SK0253	open pit	LST	657421	6921814	137	589	86	nd	nd	nd	nd	nd	nd	82	181	28	263	nd	nd
SK0254	open pit	LST	657421	6921814	nd	451	nd	78	390	nd	159	nd	nd						
SK0256	open pit	GOS	657458	6921794	nd	860	208	nd	4314	9586	nd	nd	375	65	128	105	75	nd	nd
SK0257	open pit	ARK	657458	6921794	nd	490	121	nd	182	324	nd	nd	nd	78	68	80	187	nd	nd
SK0258	open pit	ARK	657458	6921794	nd	394	212	nd	922	245	nd	nd	nd	40	60	448	177	nd	nd
SK0259	open pit	GOS	657458	6921794	nd	470	155	nd	1749	5639	nd	nd	nd	211	373	89	352	nd	nd
SK0260	open pit	GOS	657490	6921764	nd	nd	nd	nd	14351	192	nd	nd	nd	105	513	153	131	nd	nd
SK0265	open pit	ARK	657540	6921735	96	462	nd	nd	627	614	nd	nd	nd	171	47	58	282	26	nd
SK0267	open pit	GOS	657599	6921687	nd	nd	195	nd	7511	1081	nd	nd	nd	276	474	58	136	nd	nd
SK0268	open pit	ARK	657599	6921687	137	333	nd	nd	172	nd	nd	nd	nd	324	86	57	341	34	nd
SK0269	open pit	GOS	657599	6921687	nd	97	142	nd	2671	1626	nd	nd	272	55	106	66	254	nd	nd
SK0273	outcrop	ARK	656458	6921061	nd	nd	98	nd	nd	nd	nd	nd	nd	61	17	19	242	nd	nd
SK0275	outcrop	ARK	655066	6922181	nd	nd	169	nd	nd	nd	nd	nd	nd	39	25	nd	117	nd	nd
SK0276	outcrop	ARK	654948	6922295	nd	nd	121	nd	nd	nd	nd	nd	nd	42	20	nd	161	nd	nd
SK0277	outcrop	ARK	654804	6922436	nd	nd	223	nd	nd	nd	nd	nd	nd	30	20	nd	168	nd	nd
SK0279	open pit	BSA	657765	6921821	nd	nd	nd	245	953	nd	nd	nd	nd	126	300	nd	169	nd	nd
SK0283	open pit	ARK	657785	6921827	nd	547	522	nd	1183	67	nd	nd	nd	358	1957	38	216	nd	266
SK0287	open pit	ARK, GOS	657475	6921844	nd	118	nd	nd	5166	585	nd	nd	nd	119	746	64	213	nd	nd
SK0289	outcrop	ARK	654749	6921550	nd	115	163	nd	nd	nd	nd	nd	nd	91	64	22	213	nd	nd
SK0290	outcrop	RHY	654589	6921551	nd	146	111	nd	nd	nd	nd	nd	nd	63	31	nd	123	nd	nd
SK0291	outcrop	ARK	654315	6921505	nd	nd	101	nd	nd	46	nd	nd	nd	83	nd	19	144	nd	nd
SK0292	outcrop	RHY	655068	6921087	nd	209	168	nd	nd	nd	nd	nd	nd	31	38	nd	88	nd	nd
SK0293	outcrop	RHY	655068	6921087	nd	nd	120	nd	nd	nd	nd	nd	nd	64	80	nd	132	nd	nd
SK0296	outcrop	ARK	655231	6920432	nd	nd	79	nd	nd	nd	nd	nd	nd	49	63	23	171	nd	nd
SK0297	outcrop	ARK	655425	6920412	nd	nd	83	nd	nd	nd	nd	nd	nd	64	110	nd	167	nd	nd
SK0299	outcrop	ARK	655564	6920265	nd	nd	115	nd	nd	nd	nd	nd	nd	52	72	16	161	nd	nd
BC0101	open pit	ARK	657420	6921978	90	69	nd	135	nd	105	nd	nd	nd	39	123	36	149	nd	nd
BC0102	open pit	ARK	657420	6921978	109	98	nd	132	37	70	nd	nd	nd	49	209	41	195	18	nd
BC0103	open pit	CALCRETE	657420	6921978	nd	229	nd	65	nd	nd	nd	nd	nd	50	420	22	176	nd	nd

nd - not detected

na - not analysed

XRF whole rock analyses

Sample ID	Location	Lithology	E	N	W [ppm]	Ba [ppm]
0301	SD03	ARK	657485	6922181	nd	1476
0305	SD03	ARK	657485	6922181	nd	1471
0307	SD03	ARK	657485	6922181	nd	1962
0311	SD03	ARK	657485	6922181	nd	1611
0313	SD03	SSS	657485	6922181	nd	1676
0314	SD03	SSS	657485	6922181	nd	597
0315	SD03	LST	657485	6922181	nd	1988
0317	SD03	SSS	657485	6922181	nd	1480
0318	SD03	ARK	657485	6922181	nd	1662
0319	SD03	ARK	657485	6922181	nd	1033
3901	SD39	ARK	657236	6922217	390	1103
3902	SD39	ARK	657236	6922217	656	1194
3905	SD39	ARK	657236	6922217	303	1484
3906	SD39	LST	657236	6922217	263	906
3909	SD39	LST	657236	6922217	nd	821
3915	SD39	LST	657236	6922217	233	574
3916	SD39	ARK	657236	6922217	637	390
3917	SD39	ARK	657236	6922217	nd	1283
3918	SD39	ARK, GOS	657236	6922217	nd	14311
3919	SD39	ARK	657236	6922217	764	3281
3922	SD39	QSS	657236	6922217	469	1287
8001	SD80	LST	657374	6922177	nd	231
8011	SD80	ARK	657374	6922177	nd	784
8013	SD80	ARK	657374	6922177	nd	581
8014	SD80	ARK	657374	6922177	nd	520
8016	SD80	BSA	657374	6922177	nd	1152
8022	SD80	ARK	657374	6922177	nd	1365
8024	SD80	ARK, GOS	657374	6922177	nd	8989
8025	SD80	ARK, GOS	657374	6922177	nd	4030
8027	SD80	ARK	657374	6922177	nd	933
BH7001	BH70	ARK	657780	6921842	nd	626
BH7002	BH70	ARK	657780	6921842	nd	735
BH7003	BH70	ARK	657780	6921842	nd	1382
BH7004	BH70	ARK	657780	6921842	nd	907
BH7005	BH70	ARK	657780	6921842	nd	919
BH7006	BH70	ARK	657780	6921842	nd	296
BH7008	BH70	ARK	657780	6921842	nd	471

XRF whole rock analyses

Sample ID	Location	Lithology	E	N	W [ppm]	Ba [ppm]
BH7009	BH70	ARK	657780	6921842	nd	959
BH7010	BH70	SSS	657780	6921842	nd	949
BH7011	BH70	SSS	657780	6921842	nd	866
BH7012	BH70	ARK	657780	6921842	nd	494
BH7013	BH70	ARK	657780	6921842	nd	285
BH7014	BH70	SSS	657780	6921842	nd	nd
BH7015	BH70	SSS	657780	6921842	nd	218
BH7016	BH70	ARK	657780	6921842	nd	nd
BH7017	BH70	ARK	657780	6921842	nd	1456
4801	SD48	LST	657598	6922073	691	nd
4802	SD48	ARK	657598	6922073	788	182
4805	SD48	LST	657598	6922073	511	526
4806	SD48	LST	657598	6922073	1794	826
4807	SD48	LST	657598	6922073	934	2060
4809	SD48	LST	657598	6922073	991	1578
4810	SD48	LST	657598	6922073	919	1552
4812	SD48	SSS	657598	6922073	413	633
4814	SD48	LST	657598	6922073	995	334
4815	SD48	LST	657598	6922073	1880	766
4816A	SD48	LST	657598	6922073	1731	853
4816B	SD48	LST	657598	6922073	632	182
4818	SD48	ARK	657598	6922073	474	930
4819	SD48	ARK	657598	6922073	500	1491
4820	SD48	ARK	657598	6922073	887	550
4821	SD48	ARK, GOS	657598	6922073	812	713
4822	SD48	ARK	657598	6922073	687	132
4823	SD48	ARK	657598	6922073	nd	199
4825	SD48	ARK	657598	6922073	nd	440
4826	SD48	ARK	657598	6922073	422	869
0705	SD07	ARK	657855	6921927	1408	825
0706	SD07	ARK	657855	6921927	nd	nd
0707	SD07	ARK	657855	6921927	nd	247
0708	SD07	ARK	657855	6921927	1307	nd
0710	SD07	ARK	657855	6921927	853	5495
0712	SD07	ARK	657855	6921927	nd	405
0713	SD07	ARK	657855	6921927	1034	487
0714	SD07	ARK	657855	6921927	nd	1228

XRF whole rock analyses

Sample ID	Location	Lithology	E	N	W [ppm]	Ba [ppm]
0715	SD07	ARK	657855	6921927	695	767
0718	SD07	ARK	657855	6921927	616	350
0719	SD07	ARK	657855	6921927	1551	577
0726	SD07	ARK	657855	6921927	nd	597
0727	SD07	ARK	657855	6921927	nd	132
0734	SD07	ARK	657855	6921927	734	273
2065	SD20	BSA	657539	6921983	nd	2558
2067	SD20	QSS, GOS	657539	6921983	608	nd
2068	SD20	QSB, GOS	657539	6921983	nd	148
2066	SD20	ARK, GOS	657539	6921983	651	341
2052	SD20	ARK	657539	6921983	nd	909
4969	SD49	ARK, GOS	657535	6922042	nd	1119
4968	SD49	ARK, GOS	657535	6922042	476	12733
4952	SD49	ARK	657535	6922042	nd	599
4910	SD49	ARK	657535	6922042	155	2104
2413	SD24	QSS	657420	6921918	nd	1680
6519	SD65	ARK, GOS	657555	6921764	nd	418
SK0101	outcrop	ARK	662084	6907908	364	538
SK0102	outcrop	ARK	662084	6907908	1005	323
SK0103	outcrop	ARK	663787	6906061	269	nd
SK0104	outcrop	ARK	662242	6901289	372	19984
SK0111	outcrop	ARK	670008	6892337	nd	519
SK0114	outcrop	ARK	665838	6898466	464	1311
VG0101	outcrop	LST	666470	6903120	nd	nd
VG0102	outcrop	ARK	666470	6903120	684	903
VG0104	outcrop	LST	666549	6903270	nd	nd
VG0105	outcrop	LST	666549	6903270	nd	nd
VG0106	outcrop	ARK	668776	6904210	656	289
VG0107	outcrop	LST	668705	6904133	274	2799
VG0109	outcrop	LST	668696	6904116	nd	643
SK0201	outcrop	RHY	654434	6917773	1032	210
SK0202	outcrop	RHY	654434	6917773	1613	130
SK0203	open pit	ARK	657764	6921902	nd	2989
SK0204	open pit	ARK	657764	6921902	1499	9769
SK0205	open pit	ARK	657784	6921853	2679	306
SK0207	open pit	ARK	657770	6921773	690	1673
SK0208	open pit	ARK	657657	6921943	nd	418

XRF whole rock analyses

Sample ID	Location	Lithology	E	N	W [ppm]	Ba [ppm]
SK02100	outcrop	ARK	654106	6920675	4446	399
SK02101	outcrop	ARK	654083	6920594	1775	503
SK02104	outcrop	GOS	655095	6920063	6465	230
SK02106	outcrop	ARK	655027	6920013	1520	nd
SK02107	outcrop	ARK	654968	6919745	2989	353
SK02108	outcrop	ARK	654968	6919745	1629	279
SK02109	outcrop	ARK	655047	6919636	1048	717
SK0211	open pit	ARK	657777	6921704	899	1006
SK02110	open pit	SSS	657810	6921762	1037	824
SK02113	open pit	SSS	657760	6921892	263	234
SK02114	open pit	ARK	657555	6922022	nd	568
SK02116	open pit	SSS	657545	6922040	940	1202
SK02117	open pit	SSS	657394	6922067	910	1449
SK02118	open pit	ARK	657499	6922061	534	1415
SK02119	open pit	ARK	657479	6921981	592	348
SK0212	open pit	SSS	657782	6921792	388	479
SK0213	open pit	BSA	657798	6921817	1153	5915
SK0213B	open pit	BSA	657798	6921817	1223	18664
SK0214	open pit	BSA	657730	6921817	799	886
SK0215	open pit	BSA	657730	6921817	418	1535
SK0216A	open pit	SSS	657761	6921841	1501	421
SK0216B	open pit	SSS	657761	6921841	1246	428
SK0218	outcrop	BAR	657260	6921664	875	312002
SK0217	outcrop	GOS	657299	6921655	nd	6267
SK0219	outcrop	BAR	657260	6921664	nd	440087
SK0231	outcrop	RHY	657477	6920472	582	292
SK0232	outcrop	RHY	657619	6920965	754	2848
SK0235	outcrop	SSS	657695	6921154	1079	3584
SK0236	outcrop	SSS	657694	6921157	513	3193
SK0237	outcrop	GOS	657702	6921169	nd	2367
SK0239A	outcrop	GOS	657558	6921170	889	248
SK0239B	outcrop	GOS	657558	6921170	529	4837
SK0241	outcrop	ARK	657466	6921382	1760	648
SK0242	outcrop	ARK	657466	6921382	2661	451
SK0246	open pit	ARK, GOS	657740	6921766	1426	10583
SK0247	open pit	ARK, GOS	657723	6921794	299	55802
SK0249	open pit	ARK	657707	6921830	699	260

XRF whole rock analyses

Sample ID	Location	Lithology	E	N	W [ppm]	Ba [ppm]
SK0251	open pit	LST	657421	6921814	712	9412
SK0253	open pit	LST	657421	6921814	825	399
SK0254	open pit	LST	657421	6921814	390	293
SK0256	open pit	GOS	657458	6921794	706	2882
SK0257	open pit	ARK	657458	6921794	1236	2123
SK0258	open pit	ARK	657458	6921794	2125	2584
SK0259	open pit	GOS	657458	6921794	627	17286
SK0260	open pit	GOS	657490	6921764	nd	7798
SK0265	open pit	ARK	657540	6921735	269	776
SK0267	open pit	GOS	657599	6921687	nd	8853
SK0268	open pit	ARK	657599	6921687	232	754
SK0269	open pit	GOS	657599	6921687	531	1500
SK0273	outcrop	ARK	656458	6921061	945	nd
SK0275	outcrop	ARK	655066	6922181	2812	299
SK0276	outcrop	ARK	654948	6922295	893	179
SK0277	outcrop	ARK	654804	6922436	4632	168
SK0279	open pit	BSA	657765	6921821	nd	585
SK0283	open pit	ARK	657785	6921827	2676	9913
SK0287	open pit	ARK, GOS	657475	6921844	nd	12750
SK0289	outcrop	ARK	654749	6921550	2547	452
SK0290	outcrop	RHY	654589	6921551	1320	230
SK0291	outcrop	ARK	654315	6921505	1411	165
SK0292	outcrop	RHY	655068	6921087	1686	384
SK0293	outcrop	RHY	655068	6921087	1000	156
SK0296	outcrop	ARK	655231	6920432	1286	nd
SK0297	outcrop	ARK	655425	6920412	977	172
SK0299	outcrop	ARK	655564	6920265	1191	118
BC0101	open pit	ARK	657420	6921978	nd	1550
BC0102	open pit	ARK	657420	6921978	nd	1307
BC0103	open pit	CALCRETE	657420	6921978	nd	548

nd - not detected

na - not analysed

Microprobe analyses of hypogene sulphide minerals

	Sample ID	Location	Mineral	S [%]	Mn [ppm]	Fe [%]	Co [ppm]	Ni [ppm]	Cu [%]	Zn [%]	Ge [ppm]	As [ppm]	Se [ppm]	Ag [ppm]	Cd [ppm]	Sb [ppm]	Ga [ppm]	Pb [%]	Total [%]
1	4964	SD49	sphalerite	33.4389	1396	8.6017	nd	18	0.0207	57.4561	nd	nd	207	nd	1775	69	6	nd	99.8645
2	4964	SD49	sphalerite	32.9394	1163	8.033	nd	30	0.313	57.7726	nd	nd	96	71	1605	nd	426	nd	99.3971
3	4964	SD49	sphalerite	33.117	1342	8.5096	nd	nd	0.0035	57.3028	0.0033	nd	nd	88	1754	nd	nd	nd	99.2546
4	4964	SD49	sphalerite	33.7867	959	8.5394	16	120	0.022	57.9122	0.0022	nd	nd	nd	1635	22	nd	nd	100.5377
5	4964	SD49	sphalerite	33.2796	1198	8.16	nd	64	0.0148	57.5825	nd	nd	155	nd	1543	nd	nd	nd	99.3329
6	4964	SD49	sphalerite	32.9337	376	3.9541	nd	nd	0.0699	63.589	0.0014	nd	66	77	856	nd	nd	nd	100.6856
7	4959	SD49	sphalerite	33.4182	16090	7.708	nd	70	0.028	57.2524	0.018	189	199	nd	1930	152	nd	nd	100.2876
8	4959	SD49	sphalerite	33.4489	14471	8.065	71	nd	0.0292	57.5714	0.0364	144	nd	214	1515	nd	nd	nd	100.7924
9	4959	SD49	sphalerite	33.5674	6918	7.268	nd	nd	0.019	58.4219	0.0147	nd	nd	nd	1652	99	46	nd	100.1625
10	4959	SD49	sphalerite	33.6281	5021	6.6877	120	40	nd	58.7983	nd	36	44	147	1825	nd	37	nd	99.8411
11	2036	SD20	sphalerite	33.1348	1292	6.469	nd	nd	0.0027	59.3849	nd	138	38	48	1922	nd	nd	nd	99.3352
12	2036	SD20	sphalerite	33.1855	2129	6.6944	nd	nd	0.0251	58.8455	0.0249	nd	nd	nd	2314	72	29	nd	99.2298
13	2036	SD20	sphalerite	33.3014	2412	6.6614	59	100	0.0067	59.0319	0.0126	156	368	189	1578	nd	nd	nd	99.5002
14	2036	SD20	sphalerite	31.6318	2419	6.6815	nd	nd	0.0184	58.9524	nd	176	402	nd	1918	nd	nd	nd	97.7756
15	2036	SD20	sphalerite	33.1351	2828	6.7042	nd	40	0.0149	58.9934	nd	46	nd	145	1672	nd	nd	nd	99.3207
16	2036	SD20	sphalerite	33.9941	2503	6.6391	41	nd	0.0016	59.1768	nd	91	314	nd	1538	159	20	nd	100.2782
17	2036	SD20	sphalerite	33.1892	2527	6.7176	41	49	nd	58.7746	0.0048	64	375	nd	1513	9	23	nd	99.1463
18	2036	SD20	sphalerite	33.2729	2594	6.6738	43	nd	0.0157	58.6518	0.0327	128	413	nd	1876	nd	nd	nd	99.1523
19	2036	SD20	sphalerite	33.7073	2503	6.614	nd	nd	nd	58.8252	0.0041	nd	nd	nd	1465	nd	134	nd	99.5608
20	2036	SD20	sphalerite	32.321	2617	6.7734	nd	85	0.0494	58.9756	0.0022	18	nd	56	1986	nd	35	nd	98.6013
21	2036	SD20	sphalerite	33.2937	2599	6.6422	nd	126	0.0365	58.7676	nd	385	346	nd	2140	nd	204	nd	99.32
22	2036	SD20	sphalerite	33.3747	2614	6.6665	21	69	0.02	59.3679	0.0261	nd	181	nd	1453	nd	nd	nd	99.889
23	2036	SD20	sphalerite	33.3996	2695	6.7121	nd	nd	0.0306	59.2288	0.0154	nd	332	120	1866	230	nd	nd	99.9108
24	2015	SD20	sphalerite	32.9097	1654	5.7208	nd	nd	0.007	61.0762	0.0227	46	nd	139	1386	nd	nd	nd	100.0589
25	2015	SD20	sphalerite	32.947	1521	5.6254	nd	nd	0.0043	61.3343	0.0158	nd	nd	191	1450	168	nd	0.056	100.3158
26	2015	SD20	sphalerite	32.9804	1730	5.5838	nd	105	nd	61.2591	nd	27	112	63	1429	4	nd	nd	100.1703
27	2015	SD20	sphalerite	32.8388	1463	5.4421	nd	nd	0.0031	61.236	nd	37	195	nd	1696	40	nd	0.035	99.8981
28	2015	SD20	sphalerite	33.0182	565	4.2384	159	60	0.0085	63.3628	0.0048	nd	60	nd	1425	nd	nd	nd	100.8596
29	4964	SD49	galena	13.0885	297	0.6085	nd	257	0.0471	0.722	nd	nd	501	277	nd	63	nd	87.4795	102.0851
30	4964	SD49	galena	14.4518	37	2.2834	304	118	nd	0.0303	0.0314	28	85	288	nd	276	422	79.9662	96.9189
31	2036	SD20	galena	13.3839	nd	0.2373	178	nd	0.0113	3.9946	nd	245	910	4793	nd	257	nd	76.1391	94.4045
31	2036	SD20	galena	13.5416	nd	0.2394	nd	nd	0.0326	3.8619	0.0003	nd	767	4436	nd	nd	nd	86.8004	104.9965
33	2015	SD20	galena	13.4896	nd	nd	90	nd	nd	0.0153	nd	nd	387	5504	nd	103	nd	85.0753	99.1886
34	2015	SD20	galena	13.5745	nd	nd	241	182	0.0088	nd	nd	nd	253	6010	nd	nd	58	84.7039	98.9616
35	2015	SD20	galena	13.2861	nd	nd	127	nd	nd	nd	nd	407	96	7291	nd	nd	nd	84.6535	98.7317
36	4964	SD49	pyrite	52.0588	158	45.7391	nd	nd	0.0048	nd	0.0022	575	nd	102	206	215	nd	nd	97.9305
37	4964	SD49	pyrite	52.4793	32	45.8873	145	189	nd	0.1668	nd	51	nd	157	164	nd	403	nd	98.6475
38	4959	SD49	pyrite	53.0307	97	46.4465	nd	nd	nd	0.0437	0.0621	529	349	12	nd	32	nd	nd	99.6849
39	4959	SD49	pyrite	53.0278	nd	46.5602	nd	57	0.0009	0.0158	nd	155	174	nd	nd	nd	nd	nd	99.6433
40	2036	SD20	pyrite	52.9084	nd	46.4092	143	209	0.0168	0.0767	0.0324	409	nd	135	72	nd	93	nd	99.5496
41	2015	SD20	pyrite	52.5462	nd	46.2955	85	nd	nd	0.0172	nd	53	89	nd	151	nd	nd	nd	98.8967
42	2015	SD20	pyrite	53.1528	97	46.2687	nd	nd	0.0209	0.011	nd	254	94	nd	16	nd	nd	nd	99.4995
43	2015	SD20	pyrite	52.2808	114	46.4417	nd	nd	nd	0.0099	nd	82	44	nd	nd	nd	269	nd	98.7833
44	2015	SD20	pyrite	53.8304	118	46.4309	nd	59	0.0026	0.0221	0.0158	nd	15	nd	nd	66	164	nd	100.344
45	2015	SD20	pyrite	53.5208	64	46.4592	nd	nd	0.0184	nd	0.0128	207	nd	nd	nd	nd	nd	nd	100.0383
46	4964	SD49	chalcopyrite	36.2082	18	30.7324	109	190	32.4896	0.0327	nd	nd	134	238	nd	66	nd	nd	99.5384
47	4959	SD49	chalcopyrite	34.6619	62	29.9507	nd	5	36.6223	nd	nd	nd	100	295	25	nd	nd	nd	101.2836
48	4959	SD49	chalcopyrite	34.6384	73	29.4581	nd	nd	36.3482	0.035	0.0151	322	nd	12	18	74	88	nd	100.5535
49	4959	SD49	chalcopyrite	34.5514	nd	29.4592	nd	nd	36.0148	0.0665	0.0206	nd	181	89	29	149	nd	nd	100.1573
50	4932	SD49	chalcopyrite	34.23	nd	29.2055	nd	180	36.0498	nd	nd	479	nd	nd	264	nd	260	nd	99.6036
51	4932	SD49	chalcopyrite	34.1672	4	29.2417	126	nd	35.9598	0.0315	nd	53	187	96	nd	nd	70	nd	99.4538
52	4932	SD49	chalcopyrite	34.8153	29	29.443	37	28	35.6147	0.2031	nd	nd	283	120	nd	58	103	nd	100.1419

nd - not detected

Microprobe analyses of supergene sulphide minerals

	Sample ID	Location	Mineral	S [%]	Mn [ppm]	Fe [ppm]	Co [ppm]	Ni [ppm]	Cu [%]	Zn [%]	Ge [ppm]	As [ppm]	Se [ppm]	Ag [ppm]	Cd [%]	Sb [ppm]	Ga [ppm]	Pb [%]	Total [%]
1	2015	SD20	sphalerite, colloform	31.5135	nd	2872	nd	74	nd	65.9692	361	nd	84	nd	nd	nd	nd	0.1623	97.9841
2	2015	SD20	sphalerite, colloform	28.4022	nd	432	nd	56	nd	56.701	169	65	nd	nd	0.0201	nd	nd	0.0634	85.2589
3	2015	SD20	sphalerite, colloform	29.4625	nd	350	61	nd	0.0133	60.5047	288	nd	nd	68	0.0279	nd	nd	0.0141	90.0992
4	2015	SD20	sphalerite	32.2459	nd	351	nd	nd	0.0175	66.8736	nd	nd	99	nd	0.0124	nd	nd	nd	99.1944
5	2015	SD20	sphalerite, colloform	29.2377	43	134	nd	nd	nd	59.859	nd	nd	145	8	nd	nd	nd	0.2255	89.3552
6	2015	SD20	sphalerite, colloform	31.5156	nd	305	nd	58	0.0057	65.8389	66	28	nd	155	nd	nd	nd	0.1409	97.5633
7	2015	SD20	sphalerite	32.3177	60	247	nd	nd	0.0422	66.4646	nd	nd	31	28	nd	nd	502	0.0985	99.0098
8	2015	SD20	sphalerite, colloform	32.0561	141	745	30	12	0.008	66.3649	nd	28	23	60	0.0188	nd	20	0.0564	98.6101
9	2015	SD20	sphalerite, colloform	32.5555	125	597	nd	nd	0.0199	66.4799	nd	nd	nd	323	0.0061	84	23	0.1784	99.355
10	4959	SD49	galena	13.7194	nd	nd	263	nd	nd	0.0844	nd	nd	nd	nd	nd	nd	84	86.5684	100.4069
11	4959	SD49	galena	13.4575	19	149	nd	nd	0.0163	0.1736	187	505	nd	109	nd	nd	nd	86.9866	100.7309
12	4959	SD49	galena	13.3412	155	nd	nd	162	0.0104	0.1238	356	nd	nd	nd	nd	nd	107	86.1421	99.6955
13	4959	SD49	galena	13.6094	nd	nd	nd	nd	0.026	0.1373	529	103	nd	101	nd	nd	nd	87.0775	100.9235
14	4932	SD49	galena	13.5667	nd	67	116	131	0.0981	0.0497	nd	5	nd	nd	nd	44	100	86.5635	100.3243
15	4932	SD49	galena	13.6854	nd	nd	5	21	0.325	0.0091	125	nd	52	59	nd	nd	nd	85.1418	99.1875
16	2015	SD20	galena	13.6735	125	nd	nd	nd	0.0121	0.4187	nd	34	162	nd	nd	3229	nd	86.4157	100.875
17	2015	SD20	galena	13.8842	nd	nd	nd	nd	nd	3.5796	539	100	nd	13	nd	3028	nd	85.7272	103.559
18	4932	SD49	greenockite	21.9575	49	254	80	110	0.0875	1.1308	412	35	172	nd	78.8572	nd	nd	nd	102.1442
19	4932	SD49	greenockite	21.7407	nd	58	nd	nd	0.2287	0.4001	nd	23	nd	nd	79.5404	nd	365	nd	101.9545
20	4959	SD49	chalcocite	22.084	nd	17217	nd	205	79.0955	nd	nd	nd	nd	142	0.1061	86	nd	nd	103.0506
21	4959	SD49	chalcocite	21.9489	166	9005	nd	nd	77.9872	0.0442	nd	nd	265	339	0.0962	46	nd	nd	101.0586
22	4959	SD49	chalcocite	22.6491	nd	3532	26	103	79.223	0.1707	nd	nd	265	165	0.0242	162	nd	nd	102.4923
23	4932	SD49	chalcocite	21.2441	119	2058	15	128	80.5067	nd	nd	nd	nd	74	0.0081	246	nd	nd	102.0229
24	4932	SD49	chalcocite	21.1605	nd	445	nd	nd	80.9915	nd	101	nd	nd	180	0.0171	nd	nd	nd	102.2417

Microprobe analyses of sauconite

	Sample ID	Location	MgO [%]	Al ₂ O ₃ [%]	SiO ₂ [%]	P ₂ O ₅ [%]	SO ₂ [%]	K ₂ O [%]	CaO [%]	TiO ₂ [%]	MnO [%]	FeO [%]	CuO [%]	ZnO [%]	CdO [%]	BaO [%]	PbO [%]	Total [%]
1	BH7002	BH70	0.4625	2.8848	31.9913	nd	nd	0.0425	0.4201	nd	nd	0.1752	0.1887	38.1733	0.0216	nd	0.0168	74.3768
2	BH7002	BH70	0.4503	4.3935	36.0407	0.0502	nd	0.054	1.0272	nd	0.0574	0.5563	0.177	39.6934	nd	nd	nd	82.5
3	BH7002	BH70	0.6858	8.0103	37.932	nd	0.0608	0.584	1.4073	nd	0.0253	1.113	0.1791	37.9444	0.0141	nd	0.0349	87.991
4	BH7002	BH70	0.5123	6.3551	34.8752	0.0132	0.0248	0.1015	1.25	nd	0.0198	1.624	0.2622	39.5226	nd	0.0137	nd	84.5744
5	BH7002	BH70	0.8546	5.048	35.7568	0.0486	nd	0.1166	0.9246	nd	0.0078	0.7215	0.2254	39.9641	nd	nd	0.0398	83.7078
6	BH7002	BH70	0.5012	6.2839	35.8119	0.4591	0.0457	0.0822	1.805	nd	nd	1.5131	0.2581	40.0535	0.0306	nd	nd	86.8443
7	BH7007	BH70	0.3882	7.9781	32.7128	0.0546	0.0171	0.0875	0.8307	0.0208	0.0109	2.3961	0.2514	43.1916	0.0329	nd	nd	87.9727
8	BH7007	BH70	0.534	7.1699	34.2294	0.1849	0.1134	0.0895	1.5986	0.0129	0.0414	5.7732	0.2005	38.9102	nd	nd	0.0232	88.8811
9	BH7007	BH70	0.4208	4.3408	38.2105	nd	0.0115	0.078	1.0886	nd	nd	0.7116	0.1138	39.3453	nd	nd	0.0481	84.369
10	BH7008	BH70	0.4142	6.7382	35.5944	0.0351	nd	0.0795	1.0921	nd	0.106	2.3847	0.2225	40.319	nd	0.0063	0.0332	87.0252
11	BH7008	BH70	0.3658	5.9962	38.0771	0.6235	0.0111	0.0588	1.5994	nd	0.1948	1.7921	0.1766	39.9883	nd	0.0656	nd	88.9493
12	BH7008	BH70	0.1486	1.9368	14.0284	13.6021	0.0504	0.0986	14.4984	nd	0.0978	29.4871	0.2905	15.592	0.2241	nd	0.0346	90.0894
13	BH7008	BH70	0.6517	5.4154	38.2505	0.0694	0.0523	0.0542	1.3853	nd	0.0118	1.0989	0.1883	40.3275	nd	nd	0.0859	87.5912
14	BH7008	BH70	0.3302	4.3311	39.8234	0.0398	0.0139	0.0445	1.0997	nd	0.0266	0.7029	0.1199	38.573	0.0114	nd	0.0345	85.1509
15	BH7014	BH70	0.5669	26.4037	32.3176	6.9515	0.9325	0.237	10.8524	0.0564	0.089	1.9945	0.0666	4.5751	0.037	1.3741	0.2095	86.6638
16	BH7014	BH70	0.6095	11.6034	51.8896	0.4505	0.7319	0.2227	1.9798	0.0293	7.6042	2.7201	0.5472	8.3822	0.0712	1.4758	0.4069	88.7243
17	BH7014	BH70	0.6686	16.7913	13.1669	3.0043	0.7051	0.1776	7.313	0.1248	0.1371	6.6208	0.1212	17.818	nd	1.0226	0.1696	67.8409
18	BH7014	BH70	0.5656	38.4811	15.84	0.1739	0.6487	0.1555	2.0847	nd	0.0485	1.0286	0.037	25.0263	nd	0.9743	0.1518	85.216
19	BH7014	BH70	0.5973	46.2984	11.0507	0.3634	1.1185	0.2967	4.3586	0.1364	0.0992	2.7071	0.0806	6.6576	nd	2.022	0.3926	76.1791

nd - not detected

Microprobe analyses of hemimorphite

	Sample ID	Location	MgO [%]	Al ₂ O ₃ [%]	SiO ₂ [%]	P ₂ O ₅ [%]	SO ₂ [%]	K ₂ O [%]	CaO [%]	TiO ₂ [%]	MnO [%]	FeO [%]	CuO [%]	ZnO [%]	CdO [%]	BaO [%]	PbO [%]	Total [%]
1	BH7014	BH70	0.0076	0.0075	26.9636	0.1652	nd	nd	0.0062	0.0083	nd	0.001	0.0411	66.3959	0.002	nd	nd	93.5984
2	BH7014	BH70	0.0341	0.0403	27.2443	0.4494	nd	nd	0.0288	0.0089	0.0053	0.0092	nd	65.9632	nd	nd	nd	93.7835
3	BH7014	BH70	nd	nd	27.88	0.187	nd	nd	0.0104	nd	0.0093	0.0272	nd	66.5942	nd	nd	nd	94.7081
4	BH7014	BH70	0.0024	0.0072	28.1767	0.2981	0.0083	nd	0.0088	0.0058	nd	0.0142	0.0273	66.1434	nd	nd	nd	94.6922
5	BH7014	BH70	nd	nd	27.4202	0.0819	nd	nd	0.0136	0.0191	nd	0.0105	0.0038	66.4527	nd	nd	nd	94.0018
6	BH7002	BH70	nd	0.0157	27.5105	0.1976	nd	nd	0.0119	nd	nd	0.0268	nd	66.4378	nd	0.0102	nd	94.2105
7	BH7002	BH70	0.0089	0.0127	27.3305	0.1424	nd	nd	0.0051	nd	nd	0.0087	0.0022	66.9234	0.0285	nd	nd	94.4624
8	BH7002	BH70	0.0063	nd	27.0451	0.9076	nd	0.0073	0.0226	0.0131	nd	nd	0.022	66.0078	0.0157	nd	nd	94.0475
9	BH7002	BH70	nd	nd	27.0262	0.9245	0.0143	0.0038	0.0034	0.0167	0.0076	0.0042	0.0016	66.2919	0.014	nd	nd	94.3082
10	BH7002	BH70	0.0051	0.0172	27.1889	0.17	nd	nd	0.013	nd	nd	0.0157	nd	66.3149	0.0221	nd	nd	93.7469
11	BH7002	BH70	0.0063	nd	28.3635	0	0.0371	nd	0.0293	nd	nd	0.0062	nd	66.2994	0.0144	0.0126	nd	94.7688

nd - not detected

Microprobe analyses of smithsonite

	Sample ID	Location	CO ₂ [%]	MgO [%]	Al ₂ O ₃ [%]	SiO ₂ [%]	P ₂ O ₅ [%]	SO ₂ [%]	K ₂ O [%]	CaO [%]	TiO ₂ [%]	MnO [%]	FeO [%]	CuO [%]	ZnO [%]	CdO [%]	BaO [%]	PbO [%]	Total [%]
1	BH7008	BH70	34.6576	0.1205	0.0176	0.0237	0.068	nd	0.0112	0.0304	nd	0.5791	0.0236	0.1919	64.0702	0.1035	nd	nd	99.8973
2	BH7008	BH70	35.8374	0.0467	nd	0.0196	0.1548	nd	0.028	0.4344	nd	nd	nd	0.0552	63.0922	0.2522	nd	nd	99.9205
3	BH7008	BH70	36.1257	0.0672	nd	0.0032	0.0158	nd	0.0301	0.028	0.022	nd	0.0251	0.2106	63.1855	0.2344	nd	nd	99.9476
4	BH7008	BH70	35.4555	0.0062	0.0373	0.0191	0.0439	0.0563	0.0122	0.0212	0.0105	nd	0.0238	0.1749	63.9216	0.1498	0.0034	nd	99.9357
5	BH7008	BH70	36.1094	0.0258	nd	0.0046	0.1231	0.0255	0.0345	0.5653	0.0123	0.0585	0.0208	0.1021	62.616	0.2538	nd	nd	99.9517
6	BH7008	BH70	35.5305	0.1174	nd	0.0151	0.0797	0.0409	nd	0.0347	nd	0.4445	0.0324	0.2498	63.3145	0.0682	nd	0.007	99.9347
7	BH7008	BH70	36.3758	0.0893	nd	nd	nd	nd	0.0133	0.4567	nd	0.0863	0.1657	nd	62.5437	0.1247	0.0055	0.0169	99.8779
8	BH7008	BH70	35.5832	0.0309	0.0161	0.0282	0.0279	nd	nd	0.1444	0.0169	0.0453	0.1014	nd	63.8453	0.0925	nd	nd	99.9321
9	BH7008	BH70	35.3761	0.2132	nd	0.0236	0.0159	nd	0.0433	0.2769	nd	0.0221	0.1377	0.2076	63.2304	0.3381	nd	nd	99.8849
10	BH7008	BH70	36.1124	0.1763	0.0264	0.0367	nd	nd	0.0268	0.1799	nd	0.0147	0.0195	0.2092	62.8907	0.2163	nd	nd	99.9089
11	BH7008	BH70	35.9293	0.4519	nd	0.0284	0.0361	nd	0.0131	0.1466	nd	0.0217	nd	0.1584	62.9204	0.1321	nd	nd	99.838

Microprobe analyses of smithsonite

	Sample ID	Location	CO ₂ [%]	MgO [%]	Al ₂ O ₃ [%]	SiO ₂ [%]	P ₂ O ₅ [%]	SO ₂ [%]	K ₂ O [%]	CaO [%]	TiO ₂ [%]	MnO [%]	FeO [%]	CuO [%]	ZnO [%]	CdO [%]	BaO [%]	PbO [%]	Total [%]
12	BH7008	BH70	35.9391	0.3328	nd	nd	0.041	0.0447	0.0301	0.4313	nd	nd	0.0443	0.135	62.63	0.2827	nd	nd	99.911
13	BH7008	BH70	36.3504	0.0146	nd	0.0208	0.2446	nd	0.0253	0.2927	nd	0.0432	0.0973	0.3009	62.2972	0.2296	nd	nd	99.9166
14	BH7008	BH70	35.7319	0.3397	nd	nd	nd	nd	0.0215	0.1545	nd	nd	0.0894	0.0915	63.3196	0.146	nd	nd	99.8941
15	BH7007	BH70	35.7874	0.1773	nd	nd	0.0448	0.0576	0.0345	0.2832	nd	2.3591	0.111	0.0612	60.776	0.1901	nd	nd	99.8822
16	BH7007	BH70	35.0548	0.1327	nd	nd	0.1728	0.0369	0.0159	0.4391	nd	0.1609	0.0992	0.1211	63.5044	0.2011	nd	nd	99.9389
17	BH7007	BH70	35.2752	0.608	nd	nd	nd	nd	0.0108	0.0296	0.0216	0.1409	0.0496	0.0627	63.587	0.0926	0.0145	nd	99.8925
18	BH7007	BH70	36.3975	0.1418	nd	nd	0.1968	nd	0.0173	0.2289	nd	nd	0.0317	0.1709	62.4506	0.2085	nd	0.0103	99.8543
19	BH7007	BH70	36.0944	0.1608	nd	nd	0.1845	nd	0.0338	0.5384	nd	0.0146	0.0381	0.2773	62.2914	0.3113	nd	nd	99.9446
20	BH7007	BH70	35.7796	0.2522	0.0181	0.0291	0.0165	nd	0.0153	0.0808	0.0174	nd	0.0517	0.0879	63.4275	0.1155	nd	0.0423	99.9339
21	BH7007	BH70	35.7923	0.3158	nd	nd	0.0367	0.0157	0.0276	0.2767	nd	2.1556	0.0266	0.025	61.0564	0.1937	nd	nd	99.9221
22	BH7007	BH70	34.9886	0.2063	0.0197	nd	nd	nd	0.0197	0.1436	nd	nd	0.0138	0.1125	64.1925	0.1645	nd	0.0227	99.8839
23	SK0212	Open Pit	35.3807	0.0267	nd	nd	0.3611	0.0237	0.018	0.7647	nd	0.0255	nd	0.2601	62.798	0.1948	nd	nd	99.8533
24	SK0212	Open Pit	35.2611	0.0686	nd	nd	0.3161	0.0264	0.0299	0.8845	nd	nd	nd	0.2008	62.8282	0.1952	nd	0.0124	99.8232
25	SK0212	Open Pit	34.3037	0.0125	0.0349	0.0448	0.4646	nd	0.0205	0.9415	nd	3.6483	0.1614	nd	59.1743	0.1755	0.9363	0.0564	99.9747
26	SK0212	Open Pit	36.4782	0.0291	0.0105	nd	0.3236	nd	0.0156	0.7137	0.0163	nd	nd	0.1661	61.9664	0.1754	nd	nd	99.8949
27	SK0212	Open Pit	35.662	0.032	nd	nd	0.326	0.0179	0.0191	0.7107	nd	nd	nd	0.1813	62.7927	0.1751	nd	nd	99.9168
28	SK0212	Open Pit	34.6725	0.1659	nd	0.0132	0.2157	0.0205	0.0308	0.7693	nd	0.0838	nd	0.0103	63.7496	0.2065	nd	nd	99.9381
29	SK0212	Open Pit	35.866	0.0173	nd	0.0249	0.3272	0.0359	0.0168	0.7685	nd	nd	0.0212	0.1473	62.4785	0.208	nd	nd	99.9116
30	SK0212	Open Pit	34.7411	0.069	0.0015	0.0295	0.1671	nd	nd	0.569	nd	2.9359	0.1045	nd	60.3853	0.0863	0.7637	0.0215	99.8744
31	SK0212	Open Pit	34.2276	0.0336	0.0481	0.0447	0.2601	0.0523	0.0268	0.4843	nd	5.1854	0.1518	0.0304	58.0421	0.1291	1.2495	nd	99.9658
32	SK0212	Open Pit	35.1334	0.0412	0.0155	0.0714	0.3294	0.0235	0.0282	0.8667	0.0102	3.5893	0.1036	nd	59.17	0.1715	0.3688	0.0563	99.979
33	SK0212	Open Pit	36.7469	0.0201	nd	nd	0.4575	nd	0.0187	0.8732	0.0115	0.046	0.0134	0.0185	61.5816	0.1518	nd	0.0257	99.9649

Semiquantitative SEM analyses of minerals in thin sections

Sample ID	Mineralogy	Location	E	N	SiO ₂ [%]	Al ₂ O ₃ [%]	Fe ₂ O ₃ [%]	MgO [%]	CaO [%]	Na ₂ O [%]	K ₂ O [%]	TiO ₂ [%]	P ₂ O ₅ [%]	MnO [%]
SK0237	goethite	outcrop	657702	6921169	5.29	nd	92.59	nd	nd	nd	nd	nd	1.00	nd
SK0237	goethite	outcrop	657702	6921169	1.21	nd	97.89	nd	0.41	nd	nd	nd	nd	nd
SK0237	goethite	outcrop	657702	6921169	5.09	nd	92.39	nd	nd	nd	nd	nd	1.27	nd
SK0237	goethite	outcrop	657702	6921169	3.56	nd	91.99	nd	nd	nd	nd	nd	1.17	nd
SK0237	goethite	outcrop	657702	6921169	4.68	nd	93.44	nd	nd	nd	nd	nd	1.24	nd
SK0237	goethite	outcrop	657702	6921169	3.97	nd	93.66	nd	nd	nd	nd	nd	1.23	nd
<i>SK0237 (average)</i>	<i>goethite</i>	<i>outcrop</i>	<i>657702</i>	<i>6921169</i>	<i>3.97</i>	<i>nd</i>	<i>93.66</i>	<i>nd</i>	<i>0.08</i>	<i>nd</i>	<i>nd</i>	<i>nd</i>	<i>0.98</i>	<i>nd</i>
SK0287	goethite	open pit	657475	6921844	4.61	nd	83.80	nd	0.21	nd	nd	nd	1.66	5.27
SK0287	goethite	open pit	657475	6921844	3.53	nd	75.89	nd	0.35	nd	nd	nd	1.34	13.84
SK0287	goethite	open pit	657475	6921844	3.04	nd	94.56	nd	nd	nd	nd	nd	1.10	1.30
SK0287	goethite	open pit	657475	6921844	4.81	nd	84.87	nd	0.36	nd	nd	nd	2.15	4.04
SK0287	goethite	open pit	657475	6921844	4.00	nd	84.78	nd	nd	nd	nd	nd	1.56	6.11
SK0260	goethite	open pit	657490	6921764	5.89	2.06	66.37	nd	0.95	nd	nd	nd	2.02	15.66
SK0260	goethite	open pit	657490	6921764	5.91	1.87	76.99	nd	0.56	nd	nd	nd	2.77	4.77
SK0260	goethite	open pit	657490	6921764	7.12	nd	77.81	nd	0.59	nd	nd	nd	1.95	6.73
SK0260	goethite	open pit	657490	6921764	8.43	2.96	78.76	nd	0.42	nd	nd	nd	2.12	1.93
SK0260	goethite	open pit	657490	6921764	7.82	3.07	79.30	nd	0.48	nd	nd	nd	1.96	2.01
SK0260	goethite	open pit	657490	6921764	16.24	7.50	66.50	nd	0.00	nd	1.46	nd	2.14	1.46
SK0260	goethite	open pit	657490	6921764	8.24	2.84	79.79	nd	0.37	nd	nd	nd	1.95	1.66
SK0260	goethite	open pit	657490	6921764	7.83	2.97	79.15	nd	0.43	nd	nd	nd	1.92	1.85
SK0260	goethite	open pit	657490	6921764	7.42	2.62	67.58	nd	0.52	nd	nd	nd	1.50	12.37
<i>average</i>	<i>goethite</i>	<i>open pit</i>			<i>6.78</i>	<i>1.85</i>	<i>78.30</i>	<i>nd</i>	<i>0.37</i>	<i>nd</i>	<i>0.10</i>	<i>nd</i>	<i>1.87</i>	<i>5.64</i>
SK0217	hematite	outcrop	657299	6921655	0.51	nd	99.49	nd	nd	nd	nd	nd	nd	nd
SK0217	hematite	outcrop	657299	6921655	2.34	nd	97.66	nd	nd	nd	nd	nd	nd	nd
SK0217	hematite	outcrop	657299	6921655	1.86	nd	98.14	nd	nd	nd	nd	nd	nd	nd
SK0217	hematite	outcrop	657299	6921655	0.46	nd	99.54	nd	nd	nd	nd	nd	nd	nd
SK0217	hematite	outcrop	657299	6921655	4.65	nd	91.53	0.84	0.77	nd	nd	nd	nd	nd
SK0217	hematite	outcrop	657299	6921655	1.53	nd	98.17	nd	nd	nd	nd	nd	nd	nd
SK0217	hematite	outcrop	657299	6921655	5.07	nd	90.78	0.87	0.62	nd	nd	nd	nd	nd
<i>SK0217 (average)</i>	<i>hematite</i>				<i>2.35</i>	<i>nd</i>	<i>96.47</i>	<i>0.24</i>	<i>0.20</i>	<i>nd</i>	<i>nd</i>	<i>nd</i>	<i>nd</i>	<i>nd</i>
SK0283	undefined	open pit	657785	6921827	35.50	2.97	17.14	nd	nd	nd	1.96	nd	nd	7.23
SK0283	undefined	open pit	657785	6921827	14.41	0.58	1.13	nd	0.15	nd	0.41	nd	nd	1.29
SK0283	undefined	open pit	657785	6921827	36.91	4.16	13.49	nd	1.53	nd	2.46	nd	1.11	7.18
SK0283	undefined	open pit	657785	6921827	78.23	nd	6.47	nd	nd	nd	0.65	nd	1.74	2.77
<i>average</i>					<i>41.26</i>	<i>2.57</i>	<i>9.56</i>	<i>nd</i>	<i>0.84</i>	<i>nd</i>	<i>1.37</i>	<i>nd</i>	<i>1.43</i>	<i>4.62</i>
SK0260	K feldspar	open pit	657490	6921764	53.98	31.47	1.12	nd	nd	nd	11.45	1.14	nd	nd
SK0260	K feldspar	open pit	657490	6921764	51.75	33.93	0.79	nd	nd	nd	11.69	1.00	nd	nd

Semiquantitative SEM-EDX analyses of minerals in thin sections

Sample ID	Mineralogy	Location	E	N	SiO ₂ [%]	Al ₂ O ₃ [%]	Fe ₂ O ₃ [%]	MgO [%]	CaO [%]	Na ₂ O [%]	K ₂ O [%]	TiO ₂ [%]	P ₂ O ₅ [%]	MnO [%]
SK0260	K feldspar	open pit	657490	6921764	52.93	32.90	nd	nd	nd	nd	11.44	1.22	nd	nd
SK0283	K feldspar	open pit	657785	6921827	66.06	17.23	nd	nd	nd	0.68	15.72	nd	nd	nd
SK0283	K feldspar	open pit	657785	6921827	66.15	17.36	nd	nd	nd	0.68	15.59	nd	nd	nd
SK0283	K feldspar	open pit	657785	6921827	65.66	17.30	nd	nd	nd	0.54	15.67	nd	nd	nd
SK0283	K feldspar	open pit	657785	6921827	65.77	17.29	nd	nd	nd	0.63	15.81	nd	nd	nd
SK0283	K feldspar	open pit	657785	6921827	61.18	18.54	nd	nd	nd	0.00	13.72	nd	nd	nd
<i>SK0283 (Average)</i>	<i>K feldspar</i>	<i>open pit</i>	<i>657785</i>	<i>6921827</i>	<i>60.44</i>	<i>23.25</i>	<i>0.36</i>	<i>nd</i>	<i>nd</i>	<i>0.32</i>	<i>13.89</i>	<i>0.42</i>	<i>nd</i>	<i>nd</i>
SK0283	gorceixite	open pit	657785	6921827	nd	34.83	0.58	nd	2.96	nd	nd	nd	33.22	1.69
SK0283	gorceixite	open pit	657785	6921827	nd	36.55	0.52	nd	2.04	nd	0.28	nd	33.67	1.36
SK0283	gorceixite	open pit	657785	6921827	nd	35.84	0.52	nd	2.81	nd	nd	nd	33.35	1.49
SK0283	gorceixite	open pit	657785	6921827	nd	35.38	0.45	nd	1.24	nd	0.83	nd	32.44	2.01
<i>SK0283 (average)</i>	<i>gorceixite</i>	<i>open pit</i>	<i>657785</i>	<i>6921827</i>	<i>nd</i>	<i>35.65</i>	<i>0.52</i>	<i>nd</i>	<i>2.26</i>	<i>nd</i>	<i>0.28</i>	<i>nd</i>	<i>33.17</i>	<i>1.64</i>
SK0260	Zn-bearing Mn-oxide	open pit	657490	6921764	nd	nd	nd	nd	0.47	nd	0.30	nd	nd	72.57
SK0260	Zn-bearing Mn-oxide	open pit	657490	6921764	nd	nd	15.51	nd	0.96	nd	0.36	nd	nd	60.88
SK0260	Zn-bearing Mn-oxide	open pit	657490	6921764	nd	nd	9.61	nd	0.79	nd	nd	nd	nd	64.20
SK0260	Zn-bearing Mn-oxide	open pit	657490	6921764	nd	nd	17.91	nd	0.94	nd	nd	nd	nd	58.59
SK0260	Zn-bearing Mn-oxide	open pit	657490	6921764	nd	nd	nd	nd	0.28	nd	nd	nd	nd	73.38
SK0260	Zn-bearing Mn-oxide	open pit	657490	6921764	nd	nd	10.31	nd	0.89	nd	0.65	nd	nd	64.54
SK0260	Zn-bearing Mn-oxide	open pit	657490	6921764	nd	nd	17.62	nd	1.08	nd	0.41	nd	nd	58.83
SK0260	Zn-bearing Mn-oxide	open pit	657490	6921764	nd	nd	7.18	nd	0.48	nd	nd	nd	nd	68.40
SK0260	Zn-bearing Mn-oxide	open pit	657490	6921764	nd	3.81	2.74	nd	nd	nd	0.23	nd	nd	65.67
SK0260	Zn-bearing Mn-oxide	open pit	657490	6921764	nd	0.62	14.61	nd	0.40	nd	0.43	nd	nd	59.20
SK0260	Zn-bearing Mn-oxide	open pit	657490	6921764	nd	2.07	48.70	nd	1.07	nd	nd	nd	1.17	30.35
SK0260	Zn-bearing Mn-oxide	open pit	657490	6921764	nd	0.74	11.50	nd	0.90	nd	nd	nd	nd	64.39
SK0260	Zn-bearing Mn-oxide	open pit	657490	6921764	nd	1.56	13.13	nd	0.85	nd	1.04	nd	0.63	66.64
SK0260	Zn-bearing Mn-oxide	open pit	657490	6921764	nd	1.37	11.76	nd	0.81	nd	1.12	nd	nd	67.39
<i>SK0260 (average)</i>	<i>Zn-bearing Mn-oxide</i>	<i>open pit</i>	<i>657490</i>	<i>6921764</i>	<i>nd</i>	<i>0.73</i>	<i>12.90</i>	<i>nd</i>	<i>0.71</i>	<i>nd</i>	<i>0.32</i>	<i>nd</i>	<i>0.13</i>	<i>62.50</i>
SK0283	Zn-bearing Mn-oxide	open pit	657785	6921827	nd	3.18	nd	nd	nd	nd	6.75	nd	3.50	79.47
SK0283	Zn-bearing Mn-oxide	open pit	657785	6921827	nd	0.97	nd	nd	0.22	nd	1.20	nd	1.51	70.85
SK0283	Zn-bearing Mn-oxide	open pit	657785	6921827	nd	3.57	2.87	nd	nd	nd	5.04	nd	nd	77.16
SK0283	Zn-bearing Mn-oxide	open pit	657785	6921827	nd	2.72	nd	nd	0.71	nd	0.68	nd	2.83	69.99
SK0283	Zn-bearing Mn-oxide	open pit	657785	6921827	nd	1.22	nd	nd	0.57	nd	0.51	nd	1.64	69.81
SK0283	Zn-bearing Mn-oxide	open pit	657785	6921827	nd	2.97	1.44	nd	nd	nd	6.54	nd	3.25	78.04
SK0283	Zn-bearing Mn-oxide	open pit	657785	6921827	nd	3.58	1.67	nd	nd	nd	6.12	nd	3.69	77.95
<i>SK0283 (average)</i>	<i>Zn-bearing Mn-oxide</i>	<i>open pit</i>	<i>657785</i>	<i>6921827</i>	<i>nd</i>	<i>2.60</i>	<i>0.85</i>	<i>nd</i>	<i>0.21</i>	<i>nd</i>	<i>3.83</i>	<i>nd</i>	<i>2.35</i>	<i>74.75</i>
SK0287	Zn-bearing Mn-oxide	open pit	657475	6921844	nd	nd	nd	nd	0.49	nd	0.68	nd	0.87	77.30
SK0287	Zn-bearing Mn-oxide	open pit	657475	6921844	nd	nd	7.01	nd	0.43	nd	0.43	nd	0.77	66.40

Semiquantitative SEM-EDX analyses of minerals in thin sections

Sample ID	Mineralogy	Location	E	N	SiO ₂ [%]	Al ₂ O ₃ [%]	Fe ₂ O ₃ [%]	MgO [%]	CaO [%]	Na ₂ O [%]	K ₂ O [%]	TiO ₂ [%]	P ₂ O ₅ [%]	MnO [%]
SK0287	Zn-bearing Mn-oxide	open pit	657475	6921844	nd	0.70	10.51	nd	0.69	nd	0.56	nd	0.74	66.85
SK0287	Zn-bearing Mn-oxide	open pit	657475	6921844	nd	2.18	21.06	nd	0.91	nd	0.66	nd	1.41	58.44
<i>SK0287 (average)</i>	Zn-bearing Mn-oxide	open pit	657475	6921844	<i>nd</i>	<i>0.72</i>	<i>9.65</i>	<i>nd</i>	<i>0.63</i>	<i>nd</i>	<i>0.58</i>	<i>nd</i>	<i>0.95</i>	<i>67.25</i>

nd - not detected

na - not analysed

Semiquantitative SEM-EDX analyses of minerals in thin sections

Sample ID	Mineralogy	Location	E	N	ZnO [%]	BaO [%]	PbO [%]	CuO [%]	SO ₃ [%]	Total [%]
SK0237	goethite	outcrop	657702	6921169	1.12	nd	nd	nd	nd	100.00
SK0237	goethite	outcrop	657702	6921169	nd	nd	nd	nd	0.50	100.01
SK0237	goethite	outcrop	657702	6921169	1.24	nd	nd	nd	nd	99.99
SK0237	goethite	outcrop	657702	6921169	1.28	nd	nd	nd	nd	98.00
SK0237	goethite	outcrop	657702	6921169	0.64	nd	nd	nd	nd	100.00
SK0237	goethite	outcrop	657702	6921169	1.07	nd	nd	nd	nd	99.92
<i>SK0237 (average)</i>	<i>goethite</i>	<i>outcrop</i>	<i>657702</i>	<i>6921169</i>	<i>0.86</i>	<i>nd</i>	<i>nd</i>	<i>nd</i>	<i>0.08</i>	<i>99.62</i>
SK0287	goethite	open pit	657475	6921844	3.31	0.32	nd	0.83	nd	100.01
SK0287	goethite	open pit	657475	6921844	3.16	1.35	nd	0.54	nd	100.00
SK0287	goethite	open pit	657475	6921844	nd	nd	nd	nd	nd	100.00
SK0287	goethite	open pit	657475	6921844	2.72	nd	nd	1.05	nd	100.00
SK0287	goethite	open pit	657475	6921844	2.30	0.42	nd	0.61	nd	99.77
SK0260	goethite	open pit	657490	6921764	2.95	0.97	nd	1.76	nd	98.63
SK0260	goethite	open pit	657490	6921764	3.73	nd	nd	2.14	nd	98.74
SK0260	goethite	open pit	657490	6921764	3.59	nd	nd	2.20	nd	99.99
SK0260	goethite	open pit	657490	6921764	3.44	nd	nd	1.94	nd	100.00
SK0260	goethite	open pit	657490	6921764	3.34	nd	nd	2.02	nd	100.00
SK0260	goethite	open pit	657490	6921764	2.87	nd	nd	1.42	nd	99.59
SK0260	goethite	open pit	657490	6921764	3.49	nd	nd	1.66	nd	100.00
SK0260	goethite	open pit	657490	6921764	3.77	nd	nd	2.07	nd	99.99
SK0260	goethite	open pit	657490	6921764	4.28	0.95	nd	2.35	0.42	100.01
<i>average</i>	<i>goethite</i>	<i>open pit</i>			<i>3.07</i>	<i>0.29</i>	<i>nd</i>	<i>1.47</i>	<i>0.03</i>	<i>99.77</i>
SK0217	hematite	outcrop	657299	6921655	nd	nd	nd	nd	nd	100.00
SK0217	hematite	outcrop	657299	6921655	nd	nd	nd	nd	nd	100.00
SK0217	hematite	outcrop	657299	6921655	nd	nd	nd	nd	nd	100.00
SK0217	hematite	outcrop	657299	6921655	nd	nd	nd	nd	nd	100.00
SK0217	hematite	outcrop	657299	6921655	nd	nd	nd	1.66	0.55	100.00
SK0217	hematite	outcrop	657299	6921655	nd	nd	nd	nd	0.29	99.99
SK0217	hematite	outcrop	657299	6921655	nd	nd	nd	1.76	0.90	100.00
<i>SK0217 (average)</i>	<i>hematite</i>				<i>nd</i>	<i>nd</i>	<i>nd</i>	<i>0.49</i>	<i>0.25</i>	<i>100.00</i>
SK0283	undefined	open pit	657785	6921827	16.69	1.61	nd	nd	16.90	100.00
SK0283	undefined	open pit	657785	6921827	44.81	0.30	nd	nd	36.92	100.00
SK0283	undefined	open pit	657785	6921827	16.01	1.17	nd	nd	15.99	100.01
SK0283	undefined	open pit	657785	6921827	3.55	0.35	nd	nd	6.23	99.99
<i>average</i>					<i>20.27</i>	<i>0.86</i>	<i>nd</i>	<i>nd</i>	<i>19.01</i>	<i>100.00</i>
SK0260	K feldspar	open pit	657490	6921764	nd	0.84	nd	nd	nd	100.00
SK0260	K feldspar	open pit	657490	6921764	nd	0.84	nd	nd	nd	100.00

Semiquantitative SEM-EDX analyses of minerals in thin sections

Sample ID	Mineralogy	Location	E	N	ZnO [%]	BaO [%]	PbO [%]	CuO [%]	SO ₃ [%]	Total [%]
SK0260	K feldspar	open pit	657490	6921764	nd	0.51	nd	nd	nd	100.00
SK0283	K feldspar	open pit	657785	6921827	nd	0.32	nd	nd	nd	100.01
SK0283	K feldspar	open pit	657785	6921827	nd	0.26	nd	nd	nd	100.04
SK0283	K feldspar	open pit	657785	6921827	nd	0.83	nd	nd	nd	100.00
SK0283	K feldspar	open pit	657785	6921827	nd	0.50	nd	nd	nd	100.00
SK0283	K feldspar	open pit	657785	6921827	nd	6.56	nd	nd	nd	100.00
<i>SK0283 (Average)</i>	<i>K feldspar</i>	<i>open pit</i>	<i>657785</i>	<i>6921827</i>	<i>nd</i>	<i>1.33</i>	<i>nd</i>	<i>nd</i>	<i>nd</i>	<i>100.01</i>
SK0283	gorceixite	open pit	657785	6921827	3.92	22.66	nd	nd	nd	99.86
SK0283	gorceixite	open pit	657785	6921827	3.18	22.40	nd	nd	nd	100.00
SK0283	gorceixite	open pit	657785	6921827	3.49	22.50	nd	nd	nd	100.00
SK0283	gorceixite	open pit	657785	6921827	2.74	24.91	nd	nd	nd	100.00
<i>SK0283 (average)</i>	<i>gorceixite</i>	<i>open pit</i>	<i>657785</i>	<i>6921827</i>	<i>3.33</i>	<i>23.12</i>	<i>nd</i>	<i>nd</i>	<i>nd</i>	<i>99.97</i>
SK0260	Zn-bearing Mn-oxide	open pit	657490	6921764	14.80	7.73	nd	2.94	nd	98.81
SK0260	Zn-bearing Mn-oxide	open pit	657490	6921764	13.50	2.70	nd	4.21	nd	98.12
SK0260	Zn-bearing Mn-oxide	open pit	657490	6921764	16.04	3.74	nd	3.92	nd	98.30
SK0260	Zn-bearing Mn-oxide	open pit	657490	6921764	13.74	2.35	nd	3.93	nd	97.46
SK0260	Zn-bearing Mn-oxide	open pit	657490	6921764	15.15	7.98	nd	2.36	nd	99.15
SK0260	Zn-bearing Mn-oxide	open pit	657490	6921764	13.34	3.85	nd	4.98	nd	98.56
SK0260	Zn-bearing Mn-oxide	open pit	657490	6921764	13.63	2.20	nd	3.94	nd	97.71
SK0260	Zn-bearing Mn-oxide	open pit	657490	6921764	13.28	6.54	nd	3.06	nd	98.94
SK0260	Zn-bearing Mn-oxide	open pit	657490	6921764	23.64	2.05	nd	0.94	nd	99.08
SK0260	Zn-bearing Mn-oxide	open pit	657490	6921764	12.69	5.66	nd	4.88	nd	98.49
SK0260	Zn-bearing Mn-oxide	open pit	657490	6921764	6.93	1.12	nd	2.42	nd	93.83
SK0260	Zn-bearing Mn-oxide	open pit	657490	6921764	12.07	4.37	nd	4.41	nd	98.38
SK0260	Zn-bearing Mn-oxide	open pit	657490	6921764	5.50	nd	nd	8.06	nd	97.41
SK0260	Zn-bearing Mn-oxide	open pit	657490	6921764	6.01	nd	nd	8.67	nd	97.13
<i>SK0260 (average)</i>	<i>Zn-bearing Mn-oxide</i>	<i>open pit</i>	<i>657490</i>	<i>6921764</i>	<i>12.88</i>	<i>3.59</i>	<i>nd</i>	<i>4.19</i>	<i>nd</i>	<i>97.96</i>
SK0283	Zn-bearing Mn-oxide	open pit	657785	6921827	4.55	0.93	nd	1.23	nd	99.61
SK0283	Zn-bearing Mn-oxide	open pit	657785	6921827	23.08	1.32	nd	0.45	nd	99.60
SK0283	Zn-bearing Mn-oxide	open pit	657785	6921827	8.23	1.50	nd	0.96	nd	99.33
SK0283	Zn-bearing Mn-oxide	open pit	657785	6921827	6.00	15.29	nd	0.92	nd	99.14
SK0283	Zn-bearing Mn-oxide	open pit	657785	6921827	8.19	12.89	3.33	0.76	nd	98.92
SK0283	Zn-bearing Mn-oxide	open pit	657785	6921827	4.22	1.28	nd	1.02	nd	98.76
SK0283	Zn-bearing Mn-oxide	open pit	657785	6921827	4.40	1.13	nd	1.06	nd	99.60
<i>SK0283 (average)</i>	<i>Zn-bearing Mn-oxide</i>	<i>open pit</i>	<i>657785</i>	<i>6921827</i>	<i>8.38</i>	<i>4.91</i>	<i>0.48</i>	<i>0.91</i>	<i>nd</i>	<i>99.28</i>
SK0287	Zn-bearing Mn-oxide	open pit	657475	6921844	2.63	15.52	nd	1.52	nd	99.01
SK0287	Zn-bearing Mn-oxide	open pit	657475	6921844	14.18	8.52	nd	1.42	nd	99.16

Semiquantitative SEM-EDS analyses of minerals in thin sections

Sample ID	Mineralogy	Location	E	N	ZnO [%]	BaO [%]	PbO [%]	CuO [%]	SO ₃ [%]	Total [%]
SK0287	Zn-bearing Mn-oxide	open pit	657475	6921844	4.01	13.50	nd	1.55	nd	99.11
SK0287	Zn-bearing Mn-oxide	open pit	657475	6921844	1.61	11.00	nd	0.92	nd	98.19
<i>SK0287 (average)</i>	Zn-bearing Mn-oxide	open pit	657475	6921844	<i>5.61</i>	<i>12.14</i>	<i>nd</i>	<i>1.35</i>	<i>nd</i>	<i>98.87</i>

nd - not detected

na - not analysed

**Erklärung gemäß der Promotionsordnung der Mathematisch-Naturwissenschaftlich-
Technischen Fakultät der Martin-Luther-Universität Halle-Wittenberg § 5, Absatz 2 (b)**

Hiermit erkläre ich, dass ich die vorliegende Arbeit selbständig und ohne fremde Hilfe verfasst habe. Ich habe keine anderen als die von mir angegebenen Quellen und Hilfsmittel benutzt. Die den benutzten Werken wörtlich oder inhaltlich entnommenen Stellen habe ich als solche kenntlich gemacht.

10.02.2006

Katrin Kärner